Electronic characterization of graphene nanoribbons from different perspectives

Dissertation

zur Erlangung des Doktorgrades
der Naturwissenschaften (Dr. rer. nat)
der Fakultät Physik
der Universität Regensburg

vorgelegt von

Tobias Preis

aus München

im Jahr 2020

Promotionsgesuch eingereicht am:	15.07.2020
Die Arbeit wurde angeleitet von:	PD Dr. Jonathan Eroms
	Prof. Dr. Jascha Repp
	Prof. Dr. Dieter Weiss

Prüfungsausschuss:

Vorsitzender:	Prof. Dr. Jaroslav Fabian
Erstgutachter:	PD Dr. Jonathan Eroms
Zweitgutachter:	Prof. Dr. Jascha Repp
weiterer Prüfer:	Prof. Dr. Christoph Strunk

Contents

1. Introduction

After the first isolation of graphene—a single layer of carbon atoms arranged in a honeycomb structure—in 2004 [1], a sort of gold rush started in the research of two-dimensional materials. High mobilities even at room temperature [1], the ability to carry high current densities [2] and excellent thermal conductivity [3] render graphene a suitable material for future device application [4]. Considering also its high transparency [5] and outstanding flexibility [6], the usage of graphene in organic electronics seems promising as well [7]. The emergence of two-dimensional carbon as a possible transistor material comes at the right time since the miniaturization of silicon-based transistor technology is approaching its limits. Therefore, many experiments were—and are—conducted to explore the intriguing properties of graphene and graphene-related materials.
The biggest drawback of graphene regarding its electronic applications is its lack of a band gap in its pristine form [1]. This gap is needed to switch on and off the current flow in a device. One way to modify the electronic structure of graphene is to cut it into narrow strips, so-called graphene nanoribbons (GNRs). Thereby the much needed band gap arises due to quantum confinement [8].

There are many ways to fabricate such GNRs. The most promising approach for mass production of high-quality GNRs to this date is chemical synthesis [9]. In recent years, the branch of on-surface synthesis chemistry has made huge advances, enabling the fabrication of a manifold of specifically designed precursor molecules. By placing them onto a catalytic surface, GNRs with different widths and edge shapes can be tailored [10].
Since the width of the GNR directly influences its band gap [11], it is thus possible to engineer the electronic properties of the GNRs. Hereby, the addition or removal of only a single row of atoms to the GNR width can decide over the existence of a band gap. Furthermore, certain edge shapes may also lead to the emergence of edge magnetism [12, 13].
The formation of different GNRs from precursor molecules on various substrates is an intensely studied topic in surface science [14, 15]. However, little is known about the impact of single adatoms on the electronic properties of the GNRs.

In this work, the electronic properties of GNRs are modified on the atomic scale by adding single Co adatoms to the GNRs. Depending on the exact adatom position, a Kondo-like resonance can be observed in differential conductance spectroscopy.
In order to find applications for GNRs in devices, their transport properties on the mesoscopic scale are investigated as well [16–18]. Thus, we contacted GNRs with

metal leads and measured their I-V-characteristics.
In an attempt to combine the atomistic and mesoscopic worlds, we investigated how the current flow through GNRs influenced possible doping atoms on the atomic scale.

As an introduction to the topic, some theoretical basics are discussed in chapter 2. Starting with the physical properties of graphene, the characteristics of GNRs are described. Different methods of GNR fabrication are presented.
Further, the principles of scanning tunneling microscopy and atomic force microscopy are reviewed since both pose important methods to characterize the topography and electronic structure of surfaces with high resolution.

In chapter 3, the deposition of chemically synthesized GNRs on mechanically exfoliated hexagonal boron nitride (hBN) flakes is described. We observe the formation of ordered GNR domains by means of atomic force microscopy. The GNRs are contacted with different metals and their I-V-characteristics are measured under ambient conditions. Since the realization of reliable contacts is of key importance for the implementation of GNRs in electrical circuits, special focus is put on the formation of Schottky barriers at metal-semiconductor interfaces. Some GNRs are encapsulated with a second hBN flake to protect them from environmental influences, and zero-dimensional end contacts are tested.

Chapter 4 shows how the electronic properties of GNRs can be manipulated by adding single adatoms to the GNR. Here, GNRs are grown under ultra high vacuum (UHV) conditions in the chamber of a scanning tunneling microscope (STM). Subsequently, single Co atoms are added to the surface and manipulated underneath the GNRs with the help of the STM tip. The modifications of the electronic structure of the GNRs upon Co intercalation are probed by differential conductance spectroscopy. For certain intercalation sites, the appearance of a Kondo-like resonance can be observed. The experimental results are compared to density functional theory and tight-binding calculations.

The diffusion of Co atoms adsorbed on top of on-surface synthesized GNRs is studied in chapter 5. The GNRs are contacted with an STM tip and current is injected which causes a displacement of the Co adatoms. Remarkably, the Co atoms show a tendency to stay on the GNR during their dislocation, rendering the motion one-dimensional. Temperature dependent measurements are performed to extract the Co diffusion rate.

A summary of the results and a short outlook conclude this thesis.

2. Theoretical basics

This chapter will give a brief introduction into the electronic band structure and fabrication of graphene nanoribbons (GNRs) and introduce the basics of scanning probe microscopy. More specific theoretical details will be given at the beginning of the individual chapters.
We begin with a short tight-binding description of graphene. From this starting point, graphene will be confined to one dimension, yielding GNRs. In these narrow strips, quantum confinement leads to quantization of the allowed wave vectors and the development of an electrical band gap. The results are not only dependent on the width of the GNR, but also on the width of the unit cell used to describe the GNR.
To round up this part, different methods of fabricating GNRs are presented and their advantages and disadvantages are discussed.

In the second part, the fundamentals of scanning tunneling and atomic force microscopy are explained. First, an expression for the determination of the tunneling current is derived. Then, the working principle of scanning tunneling spectroscopy is sketched. Last, a short introduction into atomic force microscopy is given and two of its operational modes are introduced.

2.1. Graphene nanoribbons

To understand how the band structure of GNRs evolves form the electronic dispersion of graphene, some considerations about the lattice and band structure of graphene are presented first. Then, boundary conditions are introduced that occur at the edges of GNRs.

2.1.1. Graphene

Carbon is a very versatile element which constitutes the basis of life with its ability to form various types of complexes with diverse binding partners in different kinds of geometries. In its pristine form, it can appear in all kind of dimensionalities. Some examples are depicted in Fig. 2.1. Carbon atoms can connect to form diamond or graphite in three dimensions (3D), graphene in 2D, carbon nanotubes (CNTs) and

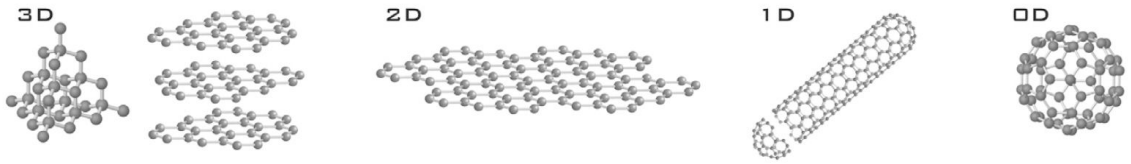

Figure 2.1.: **Allotropes of graphene.** Various forms of carbon atom arrangement in different dimensions. From 3D (diamond, graphite) over 2D (graphene) and 1D (carbon nanotubes) to 0D (fullerenes). From [19].

graphene nanoribbons (not depicted here, but discussed in detail later on) in 1D and fullerenes in 0D.
The versatility of carbon is linked to its electronic configuration which is $1s^2 2s^2 2p^2$ in its ground state [20]. However, the formation of hybrid orbitals by mixing s and p orbitals allows carbon to form different types of covalent bonds (single, double and triple) and to develop different structures [21]. Depending on its arrangement, it can hold distinctively different properties. Whereas diamond is electrically insulating, for instance, graphite is conductive.

In graphene, the 2D allotrope of carbon, the carbon atoms are sp^2 hybridized and form a planar honeycomb lattice with bonding angles of 120°. Three of the four valence electrons develop strong σ bonds with the neighboring atoms. The remaining valence electron occupies the p_z orbital which is oriented perpendicular to the graphene plane. Due to the lateral overlap with neighboring p_z orbitals, π bonds are developed. These are delocalized over the graphene plane and account for the conductivity of graphene [22].
The hexagonal lattice of graphene is depicted in Fig. 2.2 (a) and consists of two trigonal sublattices—labeled A (white atoms) and B (black atoms) [20]. The lattice vectors $\vec{a}_1 = (a_0, 0)$ and $\vec{a}_2 = (\frac{1}{2}a_0, \frac{\sqrt{3}}{2}a_0)$ span a unit cell (shaded in gray) which contains one atom of each sublattice. The distance between two neighboring carbon atoms is $a_{CC} = 1.42\,\text{Å}$ and the lattice constant $a_0 = \sqrt{3}a_{CC} = 2.46\,\text{Å}$ [23].
The corresponding reciprocal lattice is hexagonal as well. Fig. 2.2 (b) shows the first Brillouin zone (BZ) with the reciprocal lattice vectors $\vec{b}_1$ and $\vec{b}_2$ and the high symmetry points Γ at the center of the BZ, K and K' at the corners of the BZ and M halfway between them. K and K' are not equivalent due to the two distinct trigonal sublattices of graphene [22].

The band structure of graphene can be calculated using a tight-binding approach. This was done for graphite by Wallace already in 1947 [25]. In the simplest form, only interaction between nearest neighbors is taken into account. In the tight-biding model, the electrons are considered to be localized at the carbon atoms (one electron per atom) and to hop from one p_z orbital to the p_z orbital of the neighboring carbon atom. Next-nearest-neighbor hopping and Coulomb interaction between the electrons are neglected in the simplest model but can be implemented.

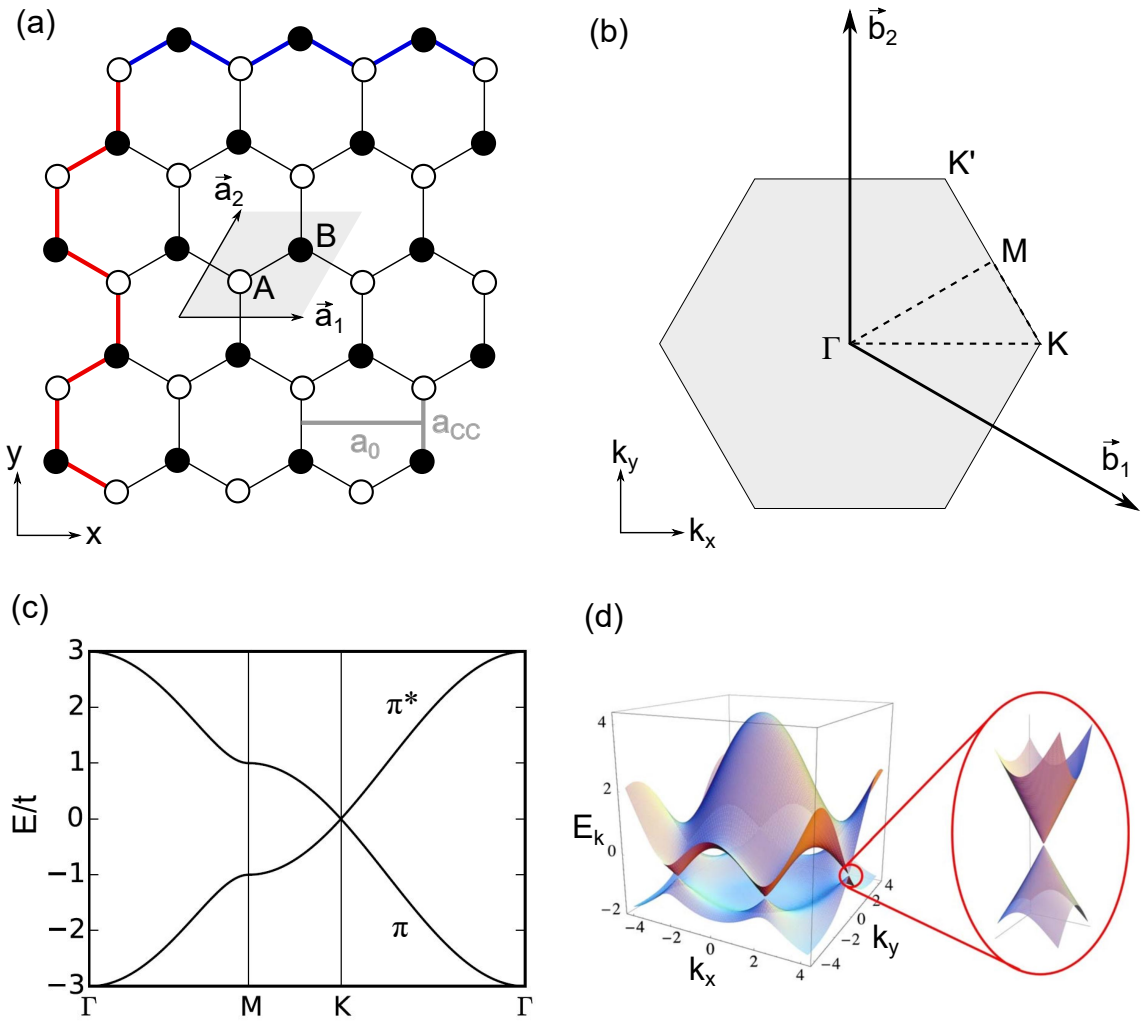

Figure 2.2.: **Lattice and electronic structure of graphene.** (a) Honeycomb structure of graphene composed of sublattice atoms A (white circles) and B (black circles) with nearest neighbor distance a_{CC}. The lattice vectors $\vec{a}_1$ and $\vec{a}_2$ span the unit cell (gray) with the lattice constant a_0. The armchair direction is emphasized by a red line, the zigzag direction by a blue one. (b) First Brillouin zone of graphene with the reciprocal basis vectors $\vec{b}_1$ and $\vec{b}_2$. The high symmetry points Γ, K, K' and M are marked. (c) Band structure along the dashed line in (b). The energy is given in units of t. From [24]. (d) 3D energy dispersion of graphene (including next-nearest-neighbor hopping) exhibiting a conical structure at the Dirac points. From [22].

The derivation of the band structure is not shown here but can be found in detail in Refs. [21, 22, 26]. In short, by writing the eigenfunctions of graphene as a linear combination of Bloch waves, one can solve the Schrödinger equation and obtain the following dispersion relation [21, 22]

$$E(\vec{k}) = \pm t\sqrt{1 + 4\cos\left(\frac{\sqrt{3}a_0 k_x}{2}\right)\cos\left(\frac{a_0 k_y}{2}\right) + 4\cos^2\left(\frac{a_0 k_y}{2}\right)} \tag{2.1}$$

Hereby, $\vec{k} = (k_x, k_y)$ is the wave vector and $t \approx 3\,\mathrm{eV}$ the nearest-neighbor hopping energy (also referred to as transfer integral or hopping parameter). The corresponding band structure can be seen in Fig. 2.2 (c) where the bonding π band (described by the "$-$" sign in Eq. 2.1 and corresponding to the valence band (VB)) and antibonding π^* band (described by the "$+$" sign, corresponding to the conduction band (CB)) are depicted along the dashed line in panel (b).
In panel (d), the 3D energy dispersion is depicted as a function of k_x and k_y. Note that for this plot also the next-nearest-neighbor interaction was taken into account which leads to an asymmetry between VB and CB [22]. In the vicinity of the K and K' points (see zoom-in), the bands have a conical form exhibiting linear dispersion. In the absence of band curvature, the electrons can be described like quasi-relativistic (massless) particles. For this reason, the K and K' points are also called Dirac points. The energy dispersion close to the Dirac points can be approximated by

$$E(\vec{k}) = \pm\hbar v_F |\vec{k}| \tag{2.2}$$

with the reduced Planck constant $\hbar$ and the energy-independent Fermi velocity $v_F = 3ta_{CC}/(2\hbar) \approx 10^6\,\mathrm{m/s}$.

2.1.2. Lattice and electronic structure of graphene nanoribbons

As evident from the last section, there is no band gap in pristine graphene which would be needed for an application as a transistor material. A gap can be introduced by cutting graphene into narrow strips which are called graphene nanoribbons. Then, quantum confinement can lead to the opening of a band gap [8].
There are two basic shapes of graphene edges [12]. One arises when cutting a graphene sheet along the blue line in Fig. 2.2 (a). Due to the zigzag arrangement of the carbon atoms along this line, the resulting edge is called zigzag edge and the corresponding GNRs are referred to as zigzag GNRs (zGNRs). Analogously, cutting graphene along the red line yields armchair edges and armchair GNRs (aGNRs). There are also other types of GNR edges but these can be considered as (often periodic) mixtures of armchair and zigzag cusps along the edge.
Usually, the width of aGNRs and zGNRs is counted in terms of graphene unit cells, and therefore in carbon dimers instead of carbon atoms. The corresponding scheme is explained in Fig. 2.3. Here, the black circles represent the carbon atoms belonging to the GNR. The gray circles indicate the imaginary neighboring atoms of the

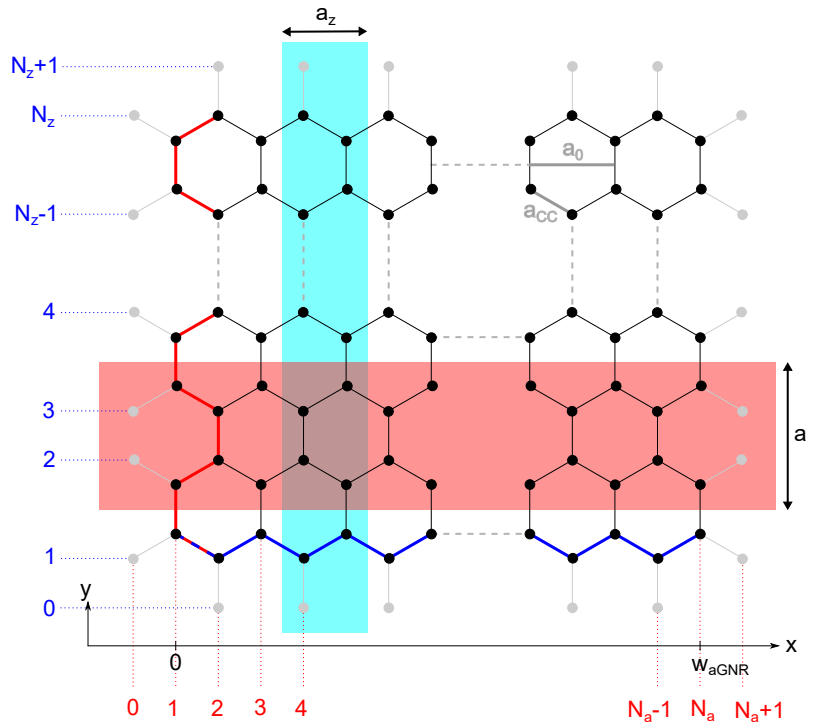

Figure 2.3.: **Lattice structure of GNRs.** Armchair and zigzag edge are marked by a red and blue line, respectively. Corresponding dimer lines are counted by the colored markers. The width of the aGNR is indicated. Unit cells of aGNR and zGNR are depicted by shaded rectangles. More details in the text.

graphene lattice. To prevent effects of dangling bonds, the carbon atoms along the GNR edges are considered to be passivated by hydrogen atoms in most theoretical descriptions. In this way, the edge carbon atoms are sp^2 hybridized as well and thus host one π electron, just like the carbon sites in the interior[1].
The red line emphasizes an armchair edge that runs along the y-direction. The red labels clarify the counting of the dimer lines and the width of the aGNR is given by

$$w_{aGNR} = \frac{1}{2}(N_a - 1)a_0 \tag{2.3}$$

with N_a being the number of carbon dimer lines parallel to the armchair direction and a_0 the lattice constant of graphene. The unit cell of the aGNR is displayed as shaded red rectangle. Accordingly, the lattice constant of an aGNR is given by a. Note that it measures $a = \sqrt{3}a_0$ and is therefore different from the graphene lattice constant.

[1]This is still only an approximation. Although certain aGNRs are predicted to be metallic, they are found to be semiconducting in experiment. The reason for this is that the hydrogen termination causes a contraction of the carbon-carbon bond at the edges of these aGNRs that leads to stronger electron hopping between these edge atoms and thus the opening of a band gap (see supplemental of Ref. [27]).

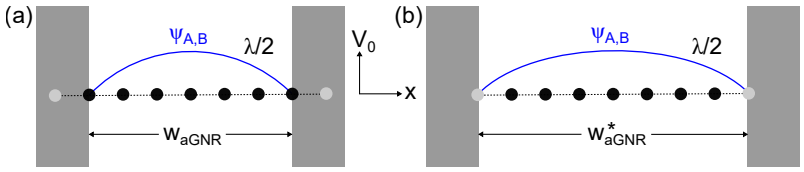

Figure 2.4.: **Particle-in-a-box model.** Cross section of a wave function $\psi_{A,B}$ (blue) across an aGNR in the ground state with wave length λ. Carbon atoms of the aGNR are displayed as black circles, imaginary next neighbors as light gray circles. The potential V_0 outside the aGNR is assumed to be infinitely high (dark gray areas). (a) and (b) depict the situations for different boundary conditions (see text).

A zigzag edge is highlighted in blue. For zGNRs, the dimer lines run in x-direction and the width is counted as indicated by the blue labels. The zGNR has a unit cell as plotted by the shaded blue rectangle and a lattice constant of $a_z = a_0$.

In the following, the width of the GNRs will be indicated by adding the number of dimer rows (N_a or N_z) as a prefix to the notation of the GNR. For instance, 7-aGNR refers to an armchair graphene nanoribbon with a width of 7 carbon dimers across the GNR.

Since GNRs share the same lattice with graphene, their band structures are very similar. However, the lateral confinement of the GNRs leads to a quantization of the wave vectors in one direction. In the following, the discretization of the wave vector for aGNRs will be discussed.
In contrast to graphene—which is assumed to be extended infinitely—aGNRs have boundaries. Here, we assume that the aGNRs have a finite size perpendicular to their edges and are infinite along their long axis. These additional constrictions pose special boundary conditions for the wave functions in aGNRs.
The wave vector in k_y direction (i. e. along the infinitely extended aGNR) is continuous. For the determination of the wave vector across the aGNR, in a first approximation, the wave functions are assumed to vanish on the outer carbon atoms of both armchair edges[2]—as displayed in Fig. 2.4 (a). Since the armchair edges host both, A and B sublattice atoms, this means that the wave functions should vanish on both sublattices at both armchair edges [22]:

$$\psi_A(x = 0) = \psi_B(x = 0) = \psi_A(x = w_{aGNR}) = \psi_B(x = w_{aGNR}) = 0 \tag{2.4}$$

Further, one can assume the potential V_0 outside the GNR to be infinitely high and treat the GNR states like a particle-in-a-box model. The wave functions $\psi_{A,B}$ then have a wavelength of $\lambda = 2w_{aGNR}/n$ with $n = 1, 2, ..., N_a$. Since wave vector and wave length are related by $k = 2\pi/\lambda$, the quantized wave vector along this direction

[2]As will be clarified below, this assumption is not very realistic. Since it is frequently used in literature, though, it will be discussed here nonetheless.

then reads

$$k_x = \frac{n \cdot \pi}{w_{aGNR}} \tag{2.5}$$

Hence, the difference between two allowed wave vectors in k_x-direction is

$$\Delta k_x = \frac{\pi}{w_{aGNR}} = \frac{2\pi}{(N_a - 1)a_0} \tag{2.6}$$

In practice, however, the electrons are not strictly localized at the positions of the carbon atoms but are delocalized due to finite size of the p_z orbital lobes. That means that the wave function is not necessarily zero on the carbon edge atoms. To take this into consideration, the boundary conditions can be modified in such a way that the wave functions vanish at the position of the imaginary neighbors of the edge atoms instead—see Fig. 2.4 (b)—and thus leave a finite amplitude on the edge sites. The width of the aGNR then becomes an effective width

$$w^*_{aGNR} = \frac{1}{2}(N_a + 1)a_0 \tag{2.7}$$

and the spacing between two allowed k_x wave vectors reads [28]

$$\Delta k_x = \frac{\pi}{w^*_{aGNR}} = \frac{2\pi}{(N_a + 1)a_0} \tag{2.8}$$

Since Eq. 2.8 models the boundary conditions for the wave functions in a more realistic way, only this convention will be used in the following[3].
At this point, it should also be mentioned that the Hamiltonian for the system is sometimes expanded around the K point [22, 29]. In that case, an additional offset for the wave vector appears in Eq. 2.5. This does, however, not affect the spacing Δk_x between allowed k_x values.

Since the k vectors of GNRs are continuous in one direction (along the GNR) and discrete in the direction perpendicular to that, one obtains a series of parallel lines when plotting the allowed wave vectors for GNRs onto the Brillouin zone of graphene [30, 31]—as is shown in Fig. 2.5. Here, the first BZ of graphene is plotted as a black hexagon. The dashed red lines are the allowed wave vectors of a 7-aGNR which are numbered by the index n from above. The red rectangle marks the first BZ of the 7-aGNR which has a width of $2\pi/a$ and a length of $2\pi/a_0$. One can now obtain the band structure of the GNR by projecting the lines of allowed k vectors onto the 3D graphene energy dispersion which is shown above the graphene BZ. This is indicated in the zoom-in. The GNR bands are therefore line cuts through

[3]The choice of the effective aGNR width may appear to be arbitrary. Since the wave function has to vanish outside the aGNR and its amplitude is defined only at the atom sites in a tight-binding model, there is a margin on the scale of a few atoms to choose appropriate boundary conditions. Letting the wave function vanish on the imaginary nearest neighbor site is the most common method used in literature.

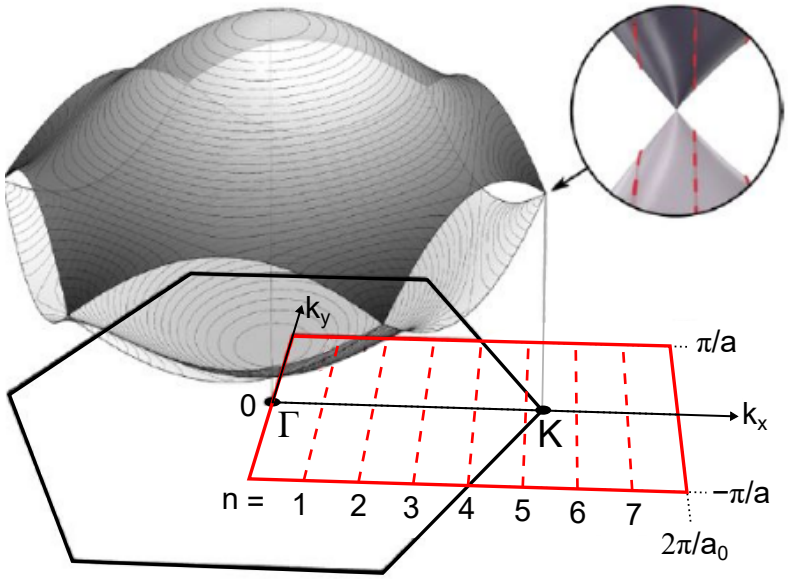

Figure 2.5.: **First Brillouin zone of 7-aGNR.** First BZs of graphene (black hexagon) and of a 7-aGNR (red rectangle). The allowed wave vectors for the 7-aGNR are plotted with red dashed lines and numbered by the index n. As depicted in the inset, the band structure of GNRs is obtained by projecting the GNR wave vectors onto the 3D graphene energy dispersion that is plotted above the graphene BZ. See also Fig. 2.6. After [30].

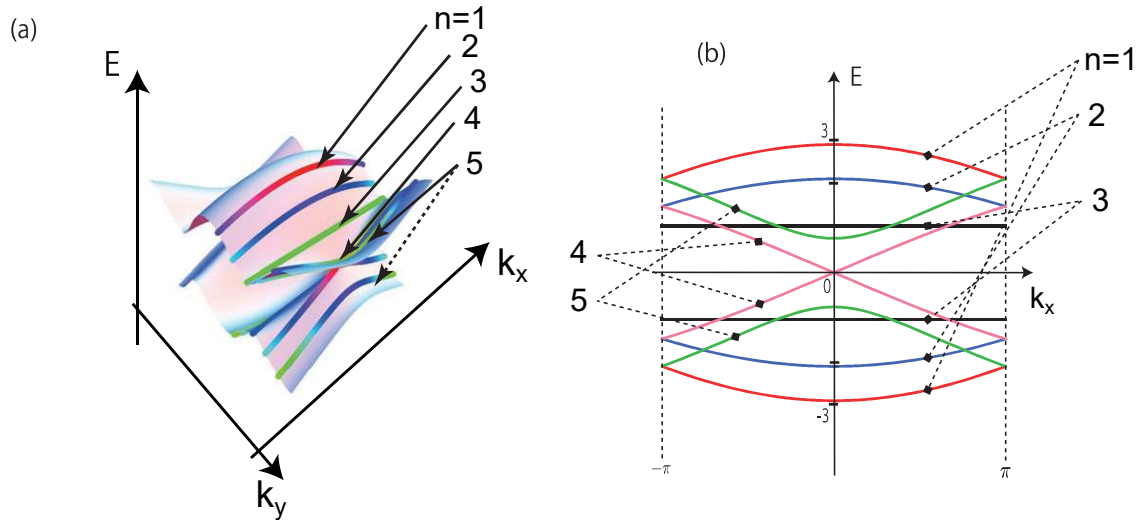

Figure 2.6.: **Band structure of 5-aGNR.** (a) Electronic dispersion of graphene and lines of allowed k vectors. (b) Cutting lines form (a) projected onto the $E - k_x$ plane. a and t are set to 1. After [32].

the 3D energy dispersion of graphene.
This can be seen even more clearly in Fig. 2.6 from Ref. [32]. Panel (a) shows the energy bands of a 5-aGNR projected onto the 3D graphene energy dispersion. The colored lines are cutting lines of the allowed wave vectors with the graphene dispersion. Projecting these line cuts onto the $E - k_x$ plane, as shown in panel (b), yields the band structure of 5-aGNRs. t and a are set to unity in this graph.
Interestingly, the bands labeled with $n = 4$ touch at $E = 0$ which makes the 5-aGNR metallic. Graphically, the closed gap results from an intersection of one of the allowed k value lines with a Dirac cone of the graphene dispersion.

The spacing Δk_x of the allowed k lines depends, as shown in Eq. 2.8, on the width of the GNR. The orientation of the lines, on the contrary, is given by the shape of the GNR edges [12]. For zGNRs, the BZ is rotated by 90° and for chiral GNRs (GNRs with mixtures of armchair and zigzag cusps) an angle between 0° and 90° results[4]. Whenever a k line cuts a Dirac cone, the corresponding GNR is metallic[5]. In the other cases, the GNRs have a band gap.
For aGNRs, it turned out that the resulting band gaps can be grouped into three different *families*, depending on the aGNR width [11]. According to their number of dimer lines across the aGNR, they are referred to as $N_A = 3p$, $3p + 1$ and $3p + 2$ family with p being an integer. The $3p + 2$ family is always metallic in the tight-binding description. $3p$ and $3p + 1$ GNRs, on the contrary, have a gap. Due to the increasing effect of quantum confinement with decreasing GNR width, the size of

[4]This is also reminiscent of the band structure of CNTs [33–35].
[5]At least in the framework of the tight-binding model. Considering effects like electron-electron interaction can open a band gap in supposedly metallic GNRs.

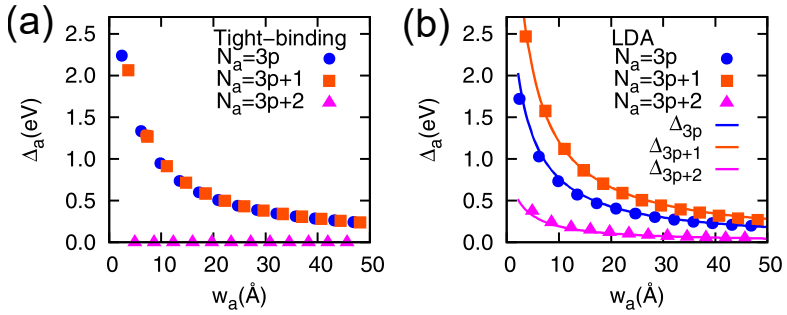

Figure 2.7.: **Band gaps of aGNRs.** Calculation of the size of the band gap with (a) tight-binding and (b) local density approximation. From [11].

the band gap E_{gap} scales inversely with the GNR width [11]:

$$E_{gap} \propto \frac{1}{w_{GNR}} \tag{2.9}$$

Fig. 2.7 shows the band gap of aGNRs in dependence on the aGNR width. The different families are marked by different colors and symbols. In the tight-binding description shown in panel (a), the $3p+2$ family has always a vanishing band gap—and thus metallic character—and the other two families possess an equally large gap that decreases with aGNR width. Panel (b) shows the band gaps obtained by local density approximation. In that case, all GNRs have a gap, with the $3p+1$ family exhibiting the largest gaps.
Further details on the calculation of the band structure and the determination of the band gaps for the different families can be found in Ref. [32].

Last, the band structure of zGNRs shall be outlined briefly. For zGNRs, the situation is slightly more complicated than for aGNRs because the transversal wave vector does not only depend on the zGNR width but also on the longitudinal wave vector. Details are not discussed here but can be found in Refs. [22, 32].
To give a short summary, tight-binding calculations lead to partially flat bands that give rise to magnetic order along the zigzag edges. This ordering can be schematically seen in Fig. 2.8 (b). The color and the size of the circles correspond to the sign and the magnitude of the local magnetic moment at this position. Note that the sign of the magnetic moments is the same for all atoms on one sublattice and opposite to the one of atoms on the other sublattice. Thus, all magnetic moments along one zigzag edge point in the same direction. The magnetic ordering will be further discussed in chapter 4. At this point, it shall only be stated that the wave functions are completely localized on one sublattice along the zigzag edge for $k_y = \pi/a_z$ and extended across the zGNR for $k_y = 2\pi/(3a_z)$ [13]. The situation in Fig. 2.8 (b) is an intermediate state where the magnetic moments are most pronounced at the zigzag edges but decay towards the zGNR center.

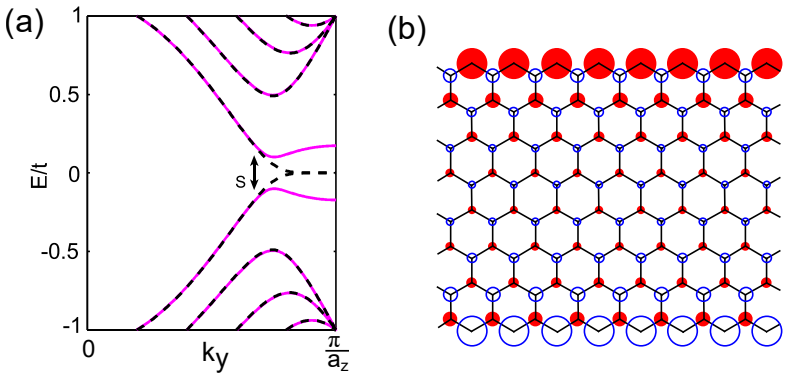

Figure 2.8.: **Local magnetic moments and band structure of zGNR.** (a) Mean-field Hubbard-model band structure (solid lines) compared with tight-binding band structure (dashed lines). (b) Corresponding distribution of the local magnetic moments. Color and size of the circles indicate sign and magnitude of the magnetic moments. From [36].

According to tight-binding calculations, zGNRs are always metallic. The introduction of Coulomb interaction in the framework of a Hubbard model, however, leads to an opening of a band gap in zGNRs as well. The difference between these two models can be seen in Fig. 2.8 (a). Using a Hubbard model still yields flat bands and therefore magnetic moments at the zGNR edges.

2.1.3. Fabrication of graphene nanoribbons

GNRs with a band gap have great potential in the semiconductor industry, since it allows to turn on and off the current flow in GNR based devices and therefore the use of GNRs as transistor material [4, 12, 37]. There are several ways to obtain GNRs. GNRs can be fabricated by etching lithographically structured graphene sheets [37], unzipping carbon nanotubes [38, 39] or cutting GNRs out of a graphene sheet with the help of an STM tip [40]. These methods are called *top-down* approaches because they start with a larger entity which is then reduced to a GNR. The disadvantage of this method is the lack of atomic precision with which the GNR edges are obtained. This negatively influences the transport properties of the GNRs [41–43].

Another approach is to grow GNRs epitaxially on the stepped surface of SiC. Such GNRs showed ballistic transport [44]. Furthermore, GNRs were grown inside etched trenches in hBN [45]. But again, both of these methods do not yield atomically precise edges.

An alternative path was opened by advances in on-surface chemistry. During the so-called *bottom-up* approach, GNRs are formed by fusing small building blocks on a catalytic metal surface [46, 47]. These surface synthesized GNRs can be fabricated

with atomic precision. Their fabrication process relies on a surface assisted bottom-up assembly of precursor molecules in UHV [46]. By choosing the right precursor molecule, almost all GNR geometries can be realized. Experiments showed the successful on-surface synthesis of aGNRs of different widths [10, 18, 30, 47–51], zGNRs [52], chiral GNRs [53], "chevron"-type GNRs [47] and "cove"-type GNRs (cGNRs) [54]. The shape of the precursor also determines the width of the GNR. Furthermore, side groups can readily be added to the GNRs [52, 55–57] and doping atoms can be incorporated in the GNR frame [48, 58–61], altering their electronic properties.

A wide range of different catalytic surfaces adds an additional tool to grow GNRs in different shapes and also in specific directions. For instance, placing the precursor molecule DBBA[6] on a Au(111) or Ag(111) surface yields 7-aGNRs whereas placing it on Cu(111) gives chiral GNRs [53]. The orientation of the substrate can also be exploited to grow GNRs in a specific direction. The narrow, parallel terraces of the Au(788) surface were used to grow arrays of parallel aGNRs for transistor application [62, 63].
An advantage of on-surface synthesized GNRs is that no solvents have to be involved in the ribbon growth. Since the process takes place in UHV, the surface stays extremely clean. Additionally, there is an enormous number of precursor molecules, allowing a huge variety of possible GNR shapes.
On the other hand, performing the synthesis in UHV demands sophisticated equipment. Additionally, the GNRs are typically grown on metallic substrates which prevents their direct electronic characterization, since the GNR states hybridize with the states of the metal substrate. This requires a transfer of the GNRs to an insulating substrate which usually involves etchants leaving residues that contaminate the GNRs [16, 18, 64]. There are possibilities to grow GNRs on the semiconducting surfaces of TiO_2 [65] and Ge(001) [66], but those GNRs cannot compete with the ones synthesized on metals in terms of edge quality.

To circumvent these problems, one can use solution-processable GNRs [17, 67–69]. They offer a large variety of different shapes as well. Additionally, they are typically longer than their on-surface synthesized counterparts and easy to process. Typically, the synthesized GNR powder is dispersed in a solvent and drop-cast onto an arbitrary surface. This method will be introduced in chapter 3.

[6]This molecule will be introduced in chapter 4.

2.2. Scanning Probe Microscopy

This section will give a short introduction into scanning probe microscopy (SPM) which is an important tool to gain insight into the atomic and electronic structure of GNRs and molecules on surfaces. The principles of scanning tunneling microscopy (STM) and atomic force microscopy (AFM) will be introduced. The invention of these two microscopes in the 1980s [70, 71] enabled the direct determination of surface structures in real space and therefore boosted the analysis of surfaces with atomic resolution. Furthermore, it enabled the investigation of (single) adatoms and molecules on surfaces in terms of their geometry and electronic configuration. In SPM, a probe is scanned in close proximity over a sample surface. Whereas STM measures a current between probe and sample, AFM senses the forces between probe and surface. The resulting signals can be transformed into information about the sample topography and electronic structure, as will be explained in the next sections.

2.2.1. Scanning Tunneling Microscopy

The functionality of STM is based on the quantum mechanical tunneling effect. The principle of tunneling is sketched for one dimension in Fig. 2.9 (a). An electron wave function ψ can penetrate a barrier with height Φ (much) higher than its own energy. Classically, the barrier would reflect the particle, but the electron can tunnel through it. In the barrier region, the wave function decays with the decay constant $\kappa = \sqrt{2m_e\Phi}/\hbar$, where m_e denotes the electron mass.

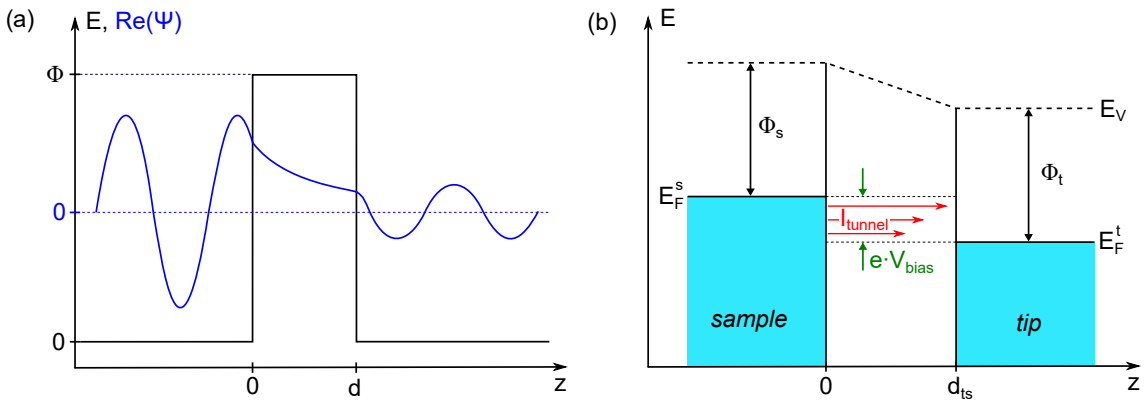

Figure 2.9.: **Tunneling at a barrier and energy level alignment in STM.** (a) A wave function ψ (blue) penetrates a tunneling barrier of height Φ. (b) Energy level alignment in an STM tunneling junction with tip-sample distance d_{ts}. A bias voltage V_{bias} is applied across the junction which causes a tunneling current I_{tunnel}. Fermi level and work function of sample (E_F^s, Φ_s) and tip (E_F^t, Φ_t) and vacuum energy E_V are indicated.

When bringing together two electrodes very closely, electrons can tunnel through the vacuum gap from one electrode into the other. In STM, one of the electrodes is a conductive probe—called *tip*—the other one is referred to as *sample*. When applying a bias voltage V_{bias} across the junction, a net tunneling current I_{tunnel} arises. A scheme for the energy level alignment in this situation can be seen in Fig. 2.9 (b). E_F^s and E_F^t mark the Fermi energies of sample and tip, respectively. Their respective work functions—i. e. the energy required to remove an electron from the material to the vacuum—are labeled with Φ_s and Φ_t. For reasons of simplicity, it is assumed that $\Phi_s \approx \Phi_t \approx \Phi$. The vacuum level is denoted with E_V and tip and sample are separated by a distance d_{ts} along the z direction.

To find an explicit expression for the tunneling current, one can follow the description of tunneling introduced by Bardeen [72]. He determined the tunneling current for a metal-insulator-metal junction already in 1961 using a perturbative approach. In this picture, sample and tip are assumed to be separable and their wave functions, ψ_μ for the sample and χ_ν for the tip, can be treated independently. The proximity of sample and tip is considered as a perturbation for the states of the respective other electrode. Thus, the following expression for the tunneling current can be derived:

$$I_{tunnel} = \frac{2\pi e^2}{\hbar} V_{bias} \sum_{\mu,\nu} |M_{\mu\nu}|^2 \delta(E_\mu - E_F)\delta(E_\nu - E_F) \tag{2.10}$$

with e the charge of an electron, $\delta(E)$ the Dirac delta function and $M_{\mu\nu}$ the tunneling matrix element between states ψ_μ from the sample and χ_ν from the tip:

$$M_{\mu\nu} = \frac{\hbar^2}{2m} \int_\Omega (\psi_\mu \nabla \chi_\nu^* - \chi_\nu^* \nabla \psi_\mu) \cdot d\vec{S} \tag{2.11}$$

Here, the surface integral $d\vec{S}$ integrates over an area Ω separating tip and sample.

In order to adjust this expression to STM, Tersoff and Hamann [73] evaluated $M_{\mu\nu}$ by modeling the tip as a locally spherical potential well. This potential has a curvature of radius R with its center at position $\vec{r}_0$. The model assumes elastic tunneling from occupied to unoccupied states—i. e. conservation of energy—and is valid in the limit of small voltages and temperatures only. By expanding the wave functions of sample and tip and inserting them into Eq. 2.11, the expression obtained for the tunneling current reads

$$I_{tunnel} = \frac{32\pi^3 e^2 V_{bias} \Phi^2 \rho_t(E_F) R^2}{\hbar \kappa^4} e^{2\kappa R} \sum_\mu |\psi_\mu(\vec{r}_0)|^2 \delta(E_\mu - E_F) \tag{2.12}$$

The sum is also referred to as local density of states (LDOS) of the sample at the Fermi level at the position of the tip:

$$\sum_\mu |\psi_\mu(\vec{r}_0)|^2 \delta(E_\mu - E_F) \equiv \rho_s(E_F, \vec{r}_0) \tag{2.13}$$

The decay constant κ in the vacuum region is affected by the applied bias voltage as

$$\kappa = \sqrt{\frac{2m(\Phi - e \cdot V_{bias})}{\hbar^2}} \tag{2.14}$$

When measuring at liquid helium temperatures, the limit of small temperature is fulfilled. Sometimes, however, higher bias voltages are used. The Tersoff Hamann model can therefore be extended to finite bias voltages. By assuming that the matrix tunneling element is independent of energy, the equation for the tunneling current reads [74]

$$I_{tunnel} = \frac{4\pi e}{\hbar} \int_0^{eV} \rho_t(E_F - eV + \epsilon)\rho_s(E_F + \epsilon)|M|^2 d\epsilon \tag{2.15}$$

with $\rho_s(E)$ and $\rho_t(E)$ the density of states (DOS) of sample and tip, respectively. The integral takes into account that all states in the interval between E_F and E_F+eV contribute to tunneling. The DOS of the tip is assumed to be constant over the energy range of interest and can thus be extracted from the integral. Furthermore, $M \propto \psi(\vec{r}_0)$ and $\rho_s(E, \vec{r}_0) = |\psi(\vec{r}_0)|^2 \rho_s(E)$. Therefore, Eq. 2.15 yields

$$I_{tunnel} \propto \rho_t(E_F) \int_0^{eV} \rho_s(E_F + \epsilon, \vec{r}_0) \tag{2.16}$$

From this equation, one can see that the tunneling current is proportional to the integrated local density of states in the sample. That implies that one can map the electronic structure of a sample by means of STM. By considering that the DOS in a metal usually varies smoothly, the changes in electronic structure on a surface can also be related to a change in the geometrical sample topography. Additionally, one always has to keep in mind that the tunneling current is a convolution of tip DOS and sample DOS. Therefore, careful preparation of the STM tip is required in experiments to guarantee a flat DOS of the tip around E_F.
Furthermore, one can see that the tunneling current is proportional to the sample wave function ψ which decays exponentially to the vacuum. Thus, I_{tunnel} depends critically on the tip-sample separation:

$$I_{tunnel}(z) \propto \exp(-2\kappa z) \tag{2.17}$$

For typical metals ($\Phi \approx 5\,\text{eV}$ [74]), a change of 1 Å in tip-sample separation changes I_{tunnel} by roughly one order of magnitude. This fact forms the basis of the high spatial resolution of STM.
The derived theory is based on the assumption of a spherically symmetric tip (with *s*-wave character). Imaging with a *p*-wave tip—as in the case of CO tip functionalization—and the correspondingly changed imaging contrast will be discussed in section 4.1.2.

STM has two operating modes to map surfaces. In the *constant height* mode, the tip is scanned in x and y direction over a surface whereby the tip height z is kept unchanged—see Fig. 2.10 (a)—and the tunneling current is recorded. During this,

the tunneling current is measured. Due to its high sensitivity on z, atoms on the surface with diameters of 2–3 Å lead to an increase in I_{tunnel} by a factor of 100–1000. The disadvantage of this scan mode is that for highly corrugated surfaces this can lead to a loss of the tunneling signal or—worse—that the tip runs into the sample surface.

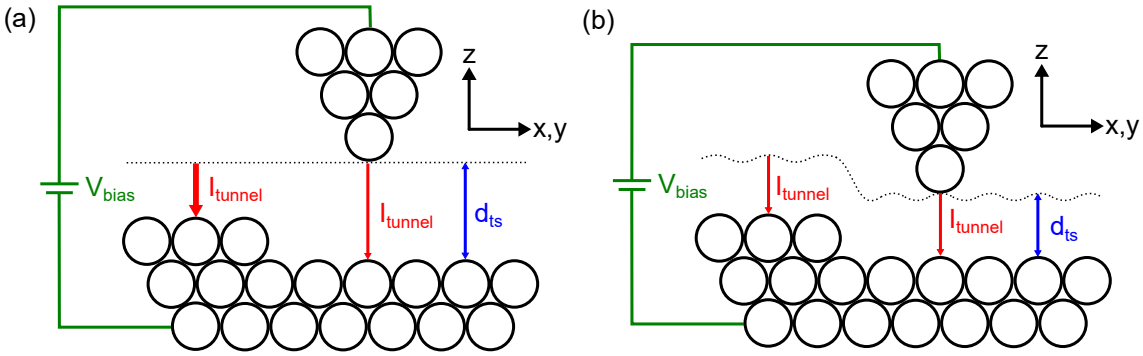

Figure 2.10.: **STM operating modes.** (a) Constant height mode. The tip is scanned in x and y direction across the sample without changing z. Simultaneously, I_{tunnel} is measured. The tip-sample distance d_{ts} varies. (b) Constant current mode. The tip is scanned in x and y direction over the sample. z is regulated in order to keep the tunneling current I_{tunnel} constant. Images after [75].

To avoid these so-called crashing events, the *constant current* mode can be used. Here, z is regulated via a feedback loop in order to maintain a constant tip-sample separation and therefore a constant tunneling current (see Fig. 2.10 (b)). Extension and retraction of the tip give information about the sample topography in that case.
The scanning in x and y direction as well as the control of z are usually done via piezoelectric elements. These elements—typically ceramics in a plate or tube shape—can change their dimensions on the Å scale upon applying a voltage to them.

2.2.2. Scanning Tunneling Spectroscopy

Apart from mapping a surface at a constant voltage (i. e. at a fixed energy), one can also probe the DOS of the sample as a function of energy with an STM. Since the tunneling current is proportional to the integral over the sample LDOS (see Eq. 2.16), its derivative with respect to the current—also called dI/dV or differential conductance—directly reflects the sample LDOS:

$$\frac{dI}{dV} \propto \rho_s(E_F + eV, \vec{r}_0) \tag{2.18}$$

To obtain a dI/dV spectrum, the STM tip is spatially fixed at a certain position over the sample and a bias voltage sweep is performed. By measuring the resulting tunneling current, the LDOS can not only be studied at E_F, but at arbitrary energy levels. The corresponding technique is referred to as scanning tunneling spectroscopy (STS). A peculiarity about STS is that it can probe both, empty and occupied states of the sample.
To obtain a better signal-to-noise ratio for the differential conductance spectra, a lock-in amplifier can be employed. In this case, a sinusoidal modulation voltage V_{mod} is added to the bias voltage with a fixed modulation frequency ω. This leads to a periodic modulation of the tunneling current. By Taylor expanding the current as function of the bias voltage and inserting the modulation voltage, one obtains

$$I(V + V_{mod} \cdot \sin(\omega t)) = I(V) + \frac{dI(V)}{dV} \cdot V_{mod} \cdot \sin(\omega t) + ... \tag{2.19}$$

One can thus easily extract the dI/dV signal and hence the LDOS of the sample.

2.2.3. Atomic Force Microscopy

Like in STM, a sharp tip is scanning a sample surface in AFM. In contrast to STM, however, AFM can also map insulating surfaces. Instead of a tunneling current, the forces between tip and sample yield information about the sample topography. Here, only a brief overview of the basics of AFM and its different operating modes is given. More details can be found in Refs. [74, 76].
To conduct AFM studies, a sharp tip is mounted to a cantilever and brought in vicinity of the sample surface (see Fig. 2.11 (a)). The interaction between tip and sample then leads to a deflection of the cantilever. Various types of cantilevers are employed in AFM—depending on the type of measurement that is performed.
One distinguishes between *static* (also called *contact*) and *dynamic* (*non-contact*) operation mode. In static AFM, the tip is dragged over the sample surface. The interaction with the sample leads to a deflection of the cantilever which is then used as the measurement signal. In dynamic AFM, the cantilever is driven to oscillate at or close to its resonance frequency. Due to the tip-sample interaction, the frequency and the amplitude of the cantilever oscillation can change. These quantities are then used as imaging signal in *frequency modulation* (FM) or *amplitude modulation* (AM) mode.

To derive a theory for frequency modulated AFM (FM-AFM), the cantilever is modeled as a spring of mass m^* and stiffness k_0 (see Fig. 2.11 (b)). The cantilever is treated as a harmonic oscillator that oscillates at its eigenfrequency

$$f_0 = \frac{1}{2\pi}\sqrt{\frac{k_0}{m^*}} \tag{2.20}$$

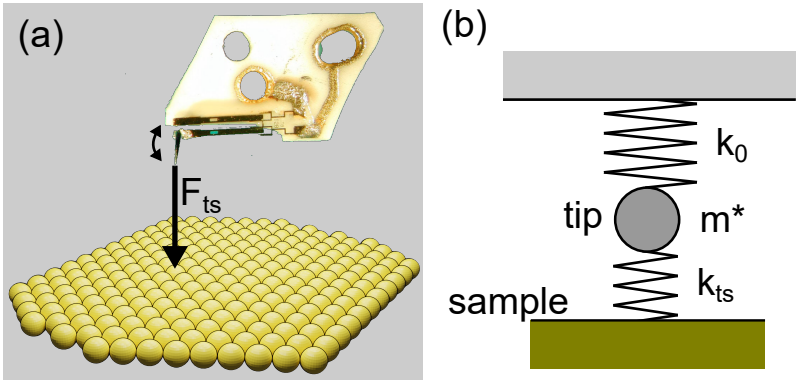

Figure 2.11.: **Model for tip-sample interaction.** (a) AFM tip mounted on a qPlus sensor oscillating over a surface. F_{ts} results from interactions between tip and sample. Picture of qPlus from [76]. (b) The cantilever is modeled as a mass m^* attached to a spring of stiffness k_0. The coupling between tip and sample is taken into account as an additional spring of stiffness k_{ts}.

For small oscillation amplitudes, the tip-sample force F_{ts} can be modeled as an additional spring of stiffness k_{ts}. Then, the oscillation frequency of the cantilever becomes

$$f = \frac{1}{2\pi}\sqrt{\frac{k_0 + k_{ts}}{m^*}} \tag{2.21}$$

By assuming $k_{ts} \ll k_0$ (i. e. stiff cantilevers) the square root can be Taylor expanded. Hence, one obtains for the frequency shift

$$\Delta f = f - f_0 = f_0 \frac{k_{ts}}{2k_0} \tag{2.22}$$

Since $\partial F_{ts}/\partial z = -k_{ts}$, it follows

$$\Delta f = -\frac{f_0}{2k_0}\frac{\partial F_{ts}}{\partial z} \tag{2.23}$$

By determining the frequency shift of the cantilever oscillation, one thus measures the force *gradient* perpendicular to the sample surface—i. e. in direction of the cantilever oscillation.
Various forces can contribute to F_{ts}. The individual contributions are, e. g., van der Waals force, electrostatic force, magnetic force and chemical forces. Whereas the van der Waals force and the electrostatic force are long-ranged and attractive in nature, the Pauli repulsion (a chemical force) is short-ranged and repulsive. A detailed description of the individual forces can be found in Refs. [74, 76].

FM-AFM is a non-invasive technique. The tip is kept oscillating with a constant amplitude[7] in close vicinity to the sample but is not touching the surface. Static

[7]Which is established by feedback loops.

AFM, on the other hand, concedes tip-sample contact which can lead to damaging of both, tip and sample.
An intermediate way of operation is the so-called *tapping mode* [77] (also referred to as *intermittent mode*). This mode is based on AM-AFM. Here, a cantilever is actuated at a fixed frequency f_{drive} which is close to but different from its resonance frequency f_0. The oscillation amplitudes for the cantilever are typically much larger than in FM-AFM [77]. When the tip starts to make contact with the surface, its oscillation amplitude decreases. A scheme is depicted in Fig. 2.12 (a). The reduction

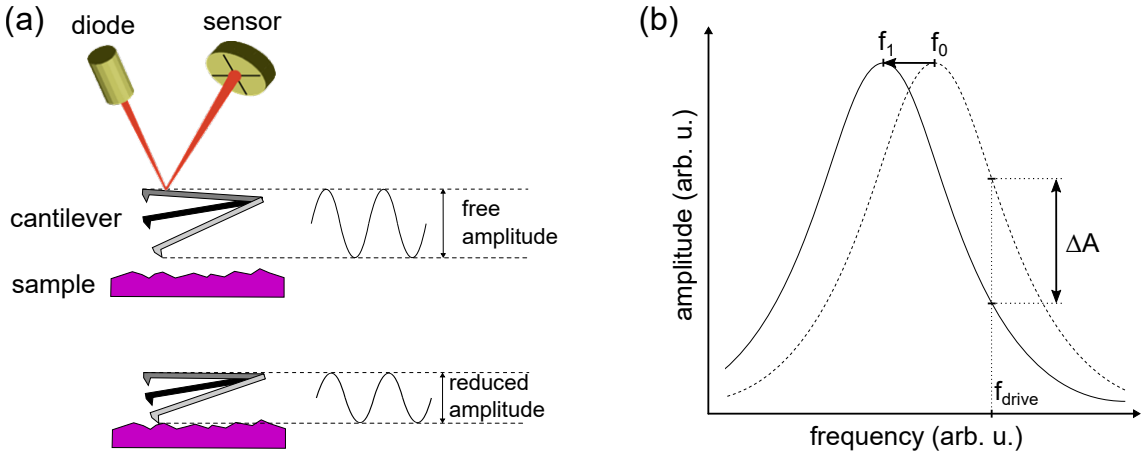

Figure 2.12.: **Amplitude modulated AFM.** (a) Schematic illustration of the tapping mode. A cantilever oscillates over a sample surface. Upon decreasing the tip-sample distance, the tip-sample interaction leads to a decrease of the oscillation amplitude—which is detected with a laser diode and a photo sensor. Image after [78]. (b) The cantilever is kept oscillating with the driving frequency f_{drive}. When approaching the surface, its resonance curve shifts (from dashed to solid curve) leading to a decrease of the amplitude by ΔA.

of the oscillation amplitude can be registered (for instance) with a laser diode and a position sensitive photo sensor—as indicated in the figure. For this purpose, the cantilever has to be coated with a reflecting material.
The reason for the decrease in oscillation amplitude can be understood from panel (b). As long as the tip is still far away from the sample, the cantilever has a resonance curve with eigenfrequency f_0 (dotted line). When the tip is approached towards the sample, the tip-sample interaction leads to a shift of the resonance frequency of the cantilever to f_1 (solid line). Since the driving frequency f_{drive} is kept fixed during the approach, the oscillation amplitude drops by an amount ΔA. Note that tapping mode is more gentle than contact mode because the tip makes contact with the sample only during a short time of the oscillation cycle.

The choice of AFM operating method depends on the requirement and circumstances of the experiment. In this thesis, two different modes are deployed. Tapping

mode is employed to image solution-processed GNRs deposited on hBN flakes. The cantilevers used for this purpose are made out of coated Si. Furthermore, on-surface synthesized GNR are characterized in UHV conditions at low temperatures by means of FM-AFM. In that case, a qPlus sensor is utilized [79]. Apart from its higher stiffness it also allows the simultaneous recording of tunneling currents which is needed for STM operation.

3. Transport measurements on cGNRs on hBN

In this chapter, solution-processable "cove"-type GNRs (cGNRs) are investigated. They are dispersed in a solvent and drop-cast onto hexagonal boron nitride (hBN). By means of ambient AFM investigations, a formation of ordered cGNR domains on the hBN flakes is found. Using electron beam lithography, the cGNRs are contacted with different metals. Mostly, standard top contacts were applied, but also zero-dimensional end contacts were attempted. The I-V-characteristics of the cGNR devices are dominated by the Schottky behavior of their contacts. By fitting the data with the thermionic field emission model, the height of the Schottky barriers is extracted.

The main results of this chapter are published in [80]. Two master students, Andreas Lex [81] and Christian Kick [82], made considerable contributions in the device fabrication and measurement of the cGNR samples. Some of the images shown in this chapter are similar or identical to images from the publication or their master's theses.
The samples with zero-dimensional contacts as well as the characterization of further molecules, namely DBOV-TDOP, in the outlook section were done together with the student intern Dhruv Mittal.

For understanding the measured I-V-curves, the principles of Schottky barrier formation are of key importance. Therefore, a short theoretical introduction into this topic will be presented at the beginning of this chapter.

3.1. Theory of Schottky barriers

The GNRs investigated in this chapter are of semiconducting nature and they are contacted by different metals. In general, bringing a metal and a semiconductor into contact causes a bending of the semiconductor bands and leads to the formation of a Schottky barrier. This phenomenon is well described in literature and therefore, the metal-semiconductor junction will be treated only shortly here. More details can be found, e. g., in Refs. [83–87].

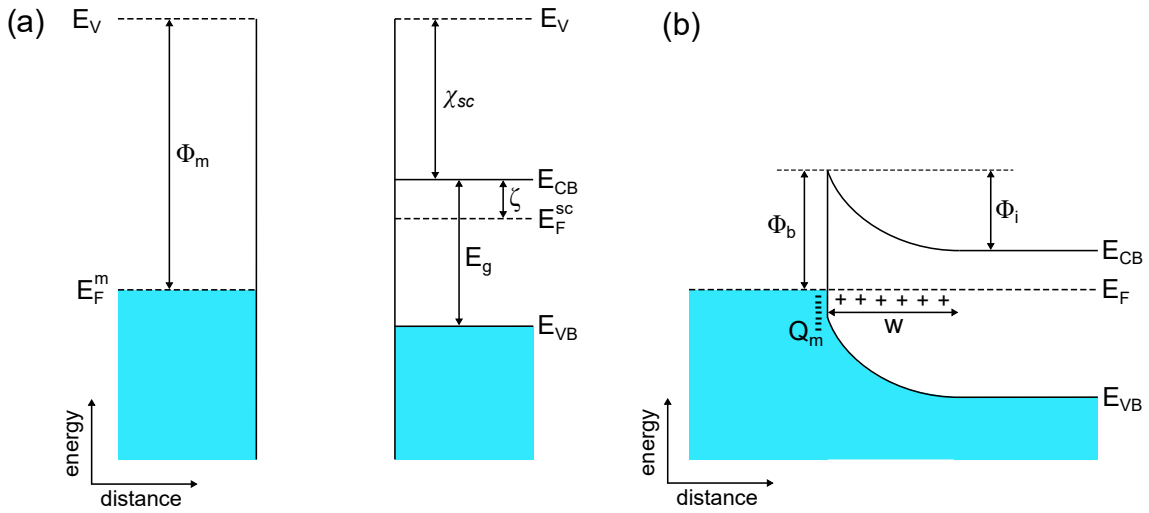

Figure 3.1.: **Schottky barrier formation.** (a) Energy level alignment for a normal metal (left) and an n-doped semiconductor (right). E_F^m and E_F^{sc} refer to the Fermi levels of metal and semiconductor, respectively, and Φ_m to the work function of the metal. χ_{sc} is the electron affinity of the semiconductor, E_g its band gap, E_{CB} the bottom of the conduction band, E_{VB} the top of the valence band, ζ the distance between E_F^{sc} and E_{CB} and E_V the vacuum level. (b) Upon joining metal and semiconductor, electrons flow into the metal causing a charge Q_m at the metal surface and a depletion layer of width w in the semiconductor. The semiconductor bands bend upwards by an amount Φ_i—called the built-in potential—and a Schottky barrier of height Φ_b emerges at the interface. After [86].

3.1.1. Formation of a Schottky barrier

Fig. 3.1 (a) shows an energy band diagram for a metal on the left hand side and an n-doped semiconductor on the right hand side. Both materials are separated by vacuum and far enough apart so that they do not disturb each other. E_V refers to the vacuum level. The metal states are occupied up to the Fermi level of the metal E_F^m and the work function of the metal is denoted by Φ_m.
For the semiconductor, E_{CB} denotes the bottom of the conduction band and E_{VB} the top of the valence band. E_g refers to the band gap and E_F^{sc} to the Fermi level of the semiconductor. Its electron affinity (i. e. the distance between bottom of conduction band and vacuum energy) is indicated with χ_{sc}, and ζ is the distance between Fermi level and conduction band edge. Often, the work function of the metal is larger than the electron affinity of the semiconductor and the two Fermi levels are not aligned.
When bringing metal and semiconductor into contact, as shown in panel (b), the Fermi levels start to equalize. Charge transfer occurs until a thermal equilibrium is established. For n-type semiconductors, electrons from the semiconductor flow into the metal and lead to the accumulation of a charge Q_m at the metal surface. At

the same time, the area in the semiconductor close to the interface gets depleted of free charge carriers and only positively charged ion cores remain. In this so-called depletion region of width w, an electric field evolves due to the charge imbalance that counteracts the flow of electrons from semiconductor to metal. Assuming a homogeneous distribution of the uncompensated donor ions in the depletion region, the electric field in this region will increase linearly with distance from the edge of the depletion region towards the interface and therefore lead to a parabolic band bending. The amount of the band bending is expressed by the built-in potential Φ_i. The resulting potential barrier is referred to as Schottky barrier and has a height of

$$\Phi_b = \Phi_m - \chi_{sc} \tag{3.1}$$

Since Schottky [88] and Mott [89] were the first to describe this relation theoretically, Eq. 3.1 is also known as Schottky-Mott approximation.
Analogously, a Schottky barrier forms for holes when joining a p-type semiconductor and a metal with $\Phi_m < \chi_{sc}$. The corresponding band diagram is not shown here but can be found in the literature [83, 84, 86].

3.1.2. Modifications to Schottky barriers

Experimentally obtained values for Schottky barriers, however, were found to deviate from Eq. 3.1. The discrepancies were explained by the presence of an interface layer of thickness δ between metal and semiconductor [90]. In this layer, interface states form, which are continuously distributed in energy at the semiconductor surface and can be characterized by a neutral level Φ_0 that is measured from the top of the valence band of the semiconductor. When these states are occupied up to Φ_0 and empty above, the surface is electrically neutral. In general, Fermi level and neutral level do not coincide. This means that a net charge at the semiconductor surface exists—which in turn causes an image charge in the metal surface[1]. Thus, a dipole layer develops altering the potential difference at the interface [84, 90]:

$$\Phi_b = \gamma(\Phi_m - \chi_{sc}) + (1-\gamma)(E_g - \Phi_0) \tag{3.2}$$

with

$$\gamma = \frac{\epsilon_i}{\epsilon_i + e^2 \delta D_{it}} \tag{3.3}$$

being a parameter that is indirectly proportional to the density of interface states D_{it}. ϵ_i refers to the permittivity of the interface layer and e to the electron charge. If there are no interface states, $\gamma = 1$ and the Schottky-Mott approximation results from Eq. 3.2. For a very high density of interface states, on the contrary, γ becomes

[1] When an electron is placed in front of a metal at a distance x_e, a positive charge will be induced on the metal surface. The attractive force between electron and induced charge—also known as image force—is equivalent to the force that would exist between the electron and an equal positive charge located at $-x_e$ which is called image charge.

very small and $\Phi_b = E_g - \Phi_0$ follows. In this case, only a small change of the Fermi level leads to a large charge transfer at the interface (due to the high density of interface states), establishing an equilibrium in the junction. For this reason, the Fermi level is said to be *pinned* by the high density of interface states. The barrier height is independent of the metal work function and is determined completely by the surface properties of the semiconductor.

Historically, the existence of interface states was first proposed by Bardeen [91]. He suggested that dangling bonds at the surface of a semiconductor lead to surface states in the gap of the semiconductor which also persist when bonds to a metal surface are formed[2].
Cowley and Sze [90] developed a model in which metal and semiconductor are separated by a thin interfacial layer, as mentioned above. Practically, this interfacial layer might stem, e. g., from oxidation at the respective surfaces during the fabrication process. The layer is thin enough so that electrons can tunnel through it.
An alternative approach to explain the presence of interface states was given by Heine [92]. He proposed that the wave functions of electrons in the metal at the interface do not abruptly terminate but decay into the semiconductor where they create metal-induced gap states (MIGS). The exchange of charge between metal and semiconductor leads to the dipole layer that alters the Schottky barrier height. Presently, the MIGS-model is the most frequently invoked model in literature to describe Schottky barriers [87].
More details on the different models and their limitations are discussed in the review of Tung [87].

Moreover, one should mention that the Schottky barrier may also be influenced by a voltage applied across the metal-semiconductor junction. The electric field in the junction paired with the image charge effect lead to a lowering of the Schottky barrier height and make it dependent on the applied external voltage. More details can be found in Ref. [86].

3.1.3. Transport across the Schottky barrier

There are several ways how charge carriers can get from the semiconductor into the metal or vice versa. Here, the case of a degenerately doped n-type semiconductor is discussed with E_F^{sc} lying in the conduction band. When a voltage is applied across the junction, the Fermi level of the semiconductor can be shifted up or down with respect to the Fermi level of the metal. An upwards shift of E_F^{sc} is referred to as applying a voltage in *forward* direction, as depicted in Fig. 3.2 (a). In this situation, electrons from filled conduction band states can penetrate the Schottky barrier by tunneling. The corresponding process is referred to as field emission (FE) and is the dominating process at low temperatures.

[2]Even though adsorbed foreign atoms may reduce the density of surface states by completing

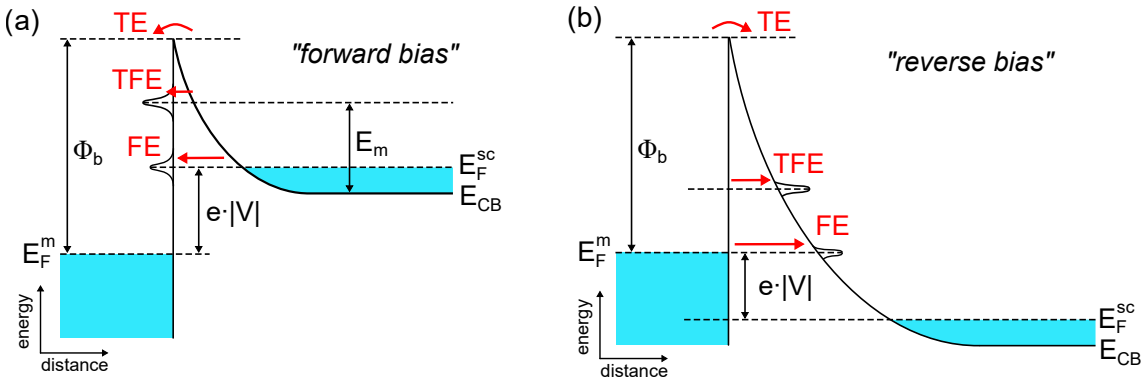

Figure 3.2.: **Transport mechanisms.** A metal-semiconductor junction is depicted with an applied voltage V under (a) forward bias and (b) reverse bias. The semiconductor is degenerately doped and E_F^{sc} is situated in its conduction band. Electrons can pass the barrier via tunneling (field emission, FE), thermally activated tunneling (thermionic field emission, TFE) or by thermally overcoming the barrier (thermionic emission, TE). After [93].

At higher temperatures, electrons can get thermally excited up to an energy E_m above E_{CB}. For these electrons, the barrier is much thinner and therefore the tunneling process is enhanced. This mechanism is called thermionic field emission (TFE).
Upon further increasing the temperature, electrons have enough energy to directly overcome the barrier—which is referred to as thermionic emission (TE).
Further effects like recombination are not discussed here.
Applying a voltage in forward direction is usually accompanied by a strong increase in current across the junction because the barrier for electrons from the semiconductor is effectively lowered.

When changing the sign of the applied voltage, one speaks of running the current in *reverse* direction. This scenario is displayed in Fig. 3.2 (b). E_F^{sc} is lowered with respect to E_F^m and electrons flow from the metal to the semiconductor. The processes to overcome the barrier (FE, TFE, TE) are as described above. One has to note that the height of the Schottky barrier Φ_b that electrons in the metal see stays always the same—regardless of the voltage applied across the junction[3].

It is most common to describe the I-V-characteristics of a Schottky barrier by the TE model. In this case, only thermal activation over the barrier is considered and the current density J per unit area through a metal-semiconductor contact is given by [83]

$$J = AT^2 \exp\left(-\frac{\Phi_b}{k_B T}\right) \exp\left(\frac{qV}{\eta k_B T}\right) \left[1 - \exp\left(-\frac{qV}{k_B T}\right)\right] \tag{3.4}$$

broken bonds.
[3]... neglecting the effect of image charge lowering.

Here, A denotes the Richardson constant, T the temperature, Φ_b the height of the Schottky barrier, k_B the Boltzmann constant, q the charge, V the voltage applied across the barrier and η the ideality factor. η describes how the barrier height changes when a voltage is applied across it and $\eta = 1$ for ideal junctions. Deviations from the ideal behavior result from effects like the presence of an interface layer or image force lowering. Under large *reverse* bias, the current across the barrier is constant. The main component that is missing in the TE model is the tunneling of electrons through the barrier. Tunneling becomes the dominating process under reverse bias [94] and is especially important for nanostructures [95].

In the TFE model, tunneling of electrons that are thermally activated to a higher energy E_m (still below the barrier) and have therefore an enhanced tunneling probability are considered. For the reverse direction, the TFE model yields a current density of [93, 94]

$$J = \frac{AT\sqrt{\pi q E_{00}}}{k_B} \exp\left(\frac{-\Phi_b}{qE_0}\right) \exp\left[V\left(\frac{q}{k_B T} - \frac{1}{E_0}\right)\right] \times \sqrt{q(V-\zeta) + \frac{\Phi_b}{\cosh^2(qE_{00}/k_B T)}} \tag{3.5}$$

with the variables defined as above. Additionally, ζ is the distance between band edge and Fermi level and $E_0 = E_{00}\coth(qE_{00}/k_B T)$. Here,

$$E_{00} = \frac{\hbar}{2}\sqrt{\frac{N_d}{m_e^* \epsilon_s}} \tag{3.6}$$

with $\hbar$ the reduced Planck constant, N_d the donor concentration, m_e^* the effective electron mass and ϵ_s the permittivity of the semiconductor.
This equation is valid for voltages $V > 3k_B T/q$ [95] (which is roughly 75 mV at room temperature). The reverse bias increases the field in the junction and thus the probability for an electron to tunnel from the metal to the semiconductor [93].
As a rule of thumb, TE dominates when $k_B T \gg E_{00}$, FE prevails for $k_B T \ll E_{00}$ and TFE is the main mechanism when $k_B T \approx E_{00}$ [83].

In the case of a metal-contacted semiconducting nanostructure (as the GNRs presented in this chapter), a metal-semiconductor-metal (MSM) junction forms with two Schottky barriers, one at each metal-semiconductor interface. A corresponding scheme is presented in Fig. 3.3 (a). In panel (b), an equivalent circuit is shown. The Schottky contacts that form at the metal-semiconductor interfaces are represented by diode symbols. Since electrons passing through the MSM junction see one Schottky barrier in reverse direction and the other one in forward direction, this setup is called *back-to-back* configuration. Source and drain are applied at the two metal leads and the nanostructure is depicted as a resistor.
Panel (c) displays a band schematics for the MSM junction under an applied source-drain voltage V_{sd}. E_F^{source} and E_F^{drain} denote the Fermi levels for source and drain contact, respectively. Φ_{b1} and Φ_{b2} are the Schottky barrier heights at the metal-semiconductor interface of contact 1 and 2. Note that Φ_{b1} and Φ_{b2} can be different

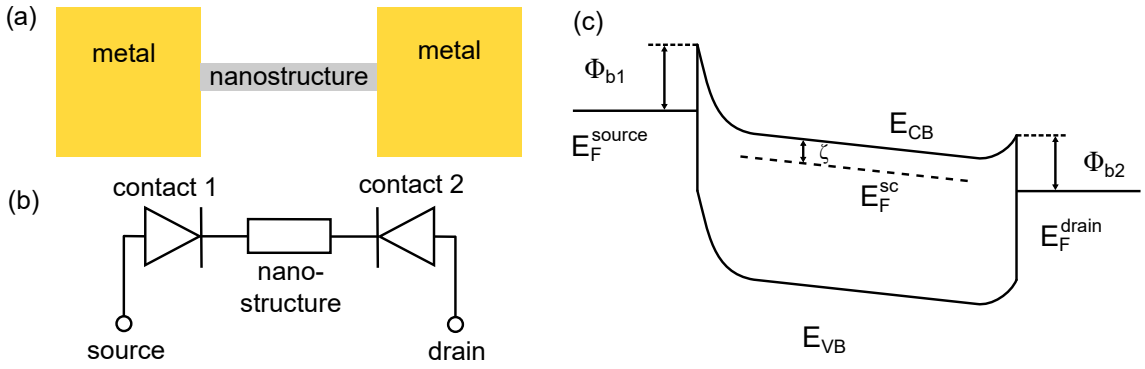

Figure 3.3.: **Back-to-back configuration.** (a) Schematic for a semiconducting nanostructure (e. g. a GNR) contacted by metal leads on both sides and (b) its equivalent circuit. (c) Band structure of the MSM contact under applied bias. Contact 1 is in reverse direction, contact 2 in forward direction. After [94].

for reasons that will be discussed later in this chapter. An electron moving from source to drain contact first passes contact 1 in reverse direction, travels through the nanostructure and then sees a lowered barrier at contact 2 in forward direction. In this configuration, the current is mainly limited by the Schottky barrier in reverse direction. Therefore, the experimentally obtained I-V-curves in this chapter will be fitted by the TFE model from Eq. 3.5 in reverse direction to extract parameters like the Schottky barrier height. This was shown in literature to yield good results for metal-contacted semiconducting nanostructures [94–96].
Last, it should be noted that also models specifically designed for fitting Schottky barriers in back-to-back configuration can be found in literature [97, 98]. These models, however, mainly focus on thermionic emission over the barrier and thus underestimate the tunneling occurring in reverse direction. Therefore, the TFE model was preferred in the analysis conducted here. An analysis of some I-V-curves with the back-to-back model can be found in the master's thesis of Andreas Lex [81].

3.2. Sample preparation

The chemical structures of the GNRs investigated in this chapter can be seen in Figs. 3.4 (a) and (b). The GNRs have a modified zigzag shape with additional

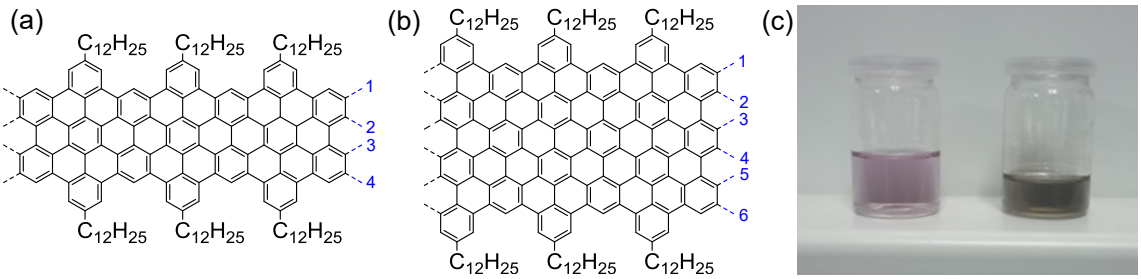

Figure 3.4.: **4- and 6-cGNRs.** (a)–(b) Chemical structure of "cove"-type GNRs of 4 and 6 carbon dimers in width, respectively. Both have alkyl side chains attached for better solubility. (c) Dispersion obtained after sonicating 4-cGNR powder in THF (left) and 6-cGNR powder in chlorobenzene (right).

benzene rings along the edges. Owing to the cove shape of their edges, they are called "cove"-type GNRs (cGNRs). As indicated in the figure, their width is 4 carbon dimers for the 4-cGNRs (a) and 6 carbon dimers for the 6-cGNRs (b). Their band gap is predicted to be 2.0 eV and 1.5 eV, respectively [99, 100]. The alkyl side chains are attached for better solubility and were shown to have no substantial effect on the electronic structure [101].
The synthesis of the cGNRs was carried out by Akimitsu Narita and coworkers at the Max Planck Institute for Polymer Research in Mainz. The detailed process relies on the Diels-Alder polymerization and can be found in [67, 102]. As a result, not single cGNRs, but many cGNRs agglomerated as a black powder are produced.
This powder was put in a solvent to disperse the cGNRs. Tetrahydrofuran (THF) was used for 4-cGNRs and chlorobenzene for 6-cGNRs. Hereafter, the mixture was sonicated for at least 1 hour, until the powder was mostly dispersed. The dispersion turned violet for the 4-cGNRs and gray for the 6-cGNRs, as can be seen in Fig. 3.4 (c).
The violet color of the 4-cGNR dispersion stems from a strong absorbance of the dispersed 4-cGNRs in the green spectral range [67, 100]. Therefore, mainly the red and blue portions of the visible light can pass the dispersion, yielding the violet appearance. The absorbance of the 6-cGNRs, on the other hand, is much broader [100, 102], turning the dispersion gray. The influence of the solvent on the spectrum is expected to be minor, whereas aggregation of the cGNRs could lead to a change of the optical properties [103, 104].

Subsequently, hBN was exfoliated on a freshly cleaned Si/SiO_2 chip using the Scotch tape method [1]. hBN has a hexagonal lattice structure with alternating B and N atoms and a lattice mismatch with graphene of only 1.7 % [105, 106]. It was shown

to greatly increase the mobility of graphene due to its atomic flatness and screening of charged impurities that are trapped in SiO_2 [107, 108]. This makes hBN an excellent support material.
The cGNR-dispersion was drop-cast onto the hBN-Si/SiO_2 chip lying on a 60°C hot plate. The hot plate is used to evaporate the solvent which leaves only the cGNRs on the surface. Dipping the chip into solution for one minute with subsequent drying on the hotplate was also performed and yielded similar results.
When the dispersion on the chip evaporates, it forms a droplet that diminishes until it eventually vanishes. The dispersion left most residues at the spot that dried last. Therefore, it is advantageous to tilt the chip slightly when drying it in order to get the residues close to the edges of the chip instead of somewhere in the center.

3.3. Sample characterization by means of AFM

To investigate the cGNR adsorption on the sample, the hBN flakes of interest were examined with an ambient condition atomic force microscope in tapping mode after depositing the dispersion on the chip.

Figs. 3.5 (a) and (c) show AFM phase images of 4-cGNRs on hBN. The first observation is that the cGNRs appear to be wiggled. This stands in striking contrast to the deposition of 4-cGNRs on an HOPG surface where the cGNRs were found to be parallel, straight lines [67]. The wiggled structure can most likely be explained by the small lattice mismatch of the cGNR carbon backbone and the underlying hBN substrate of roughly 1.7%. The cGNRs presumably buckle in order to match the carbon atom positions with the boron and nitrogen positions of the hBN. This effect has been predicted for 7-aGNRs on hBN with molecular dynamics simulations—see Fig. 3.5 (e) [109]. Here, we assume a similar effect to take place. The fact that the cGNRs are very mobile on hBN, as will be discussed later, could facilitate the wiggling of the cGNRs.
Furthermore, the alkyl side chains of the cGNRs could affect the ordering on the hBN. They might adsorb non-homogeneously on the substrate and contribute to the formation of the wiggled cGNR appearance. The single alkyl side chains could not be resolved by AFM.
One should also mention at this point that—although the formation of a monolayer of cGNRs on the hBN flake is assumed—the adsorption of more than one layer of cGNRs cannot be ruled out with the given measurement resolution.

Another interesting observation is the formation of domains in which the cGNRs are parallel to each other. A domain formation of cGNRs on HOPG was already seen in Ref. [67] where 4-cGNRs adsorbed as straight, parallel lines. On hBN, we could observe the formation of multiple domains with different directions. The domain sizes varied between 50 nm to over 2 µm, both in length and width.

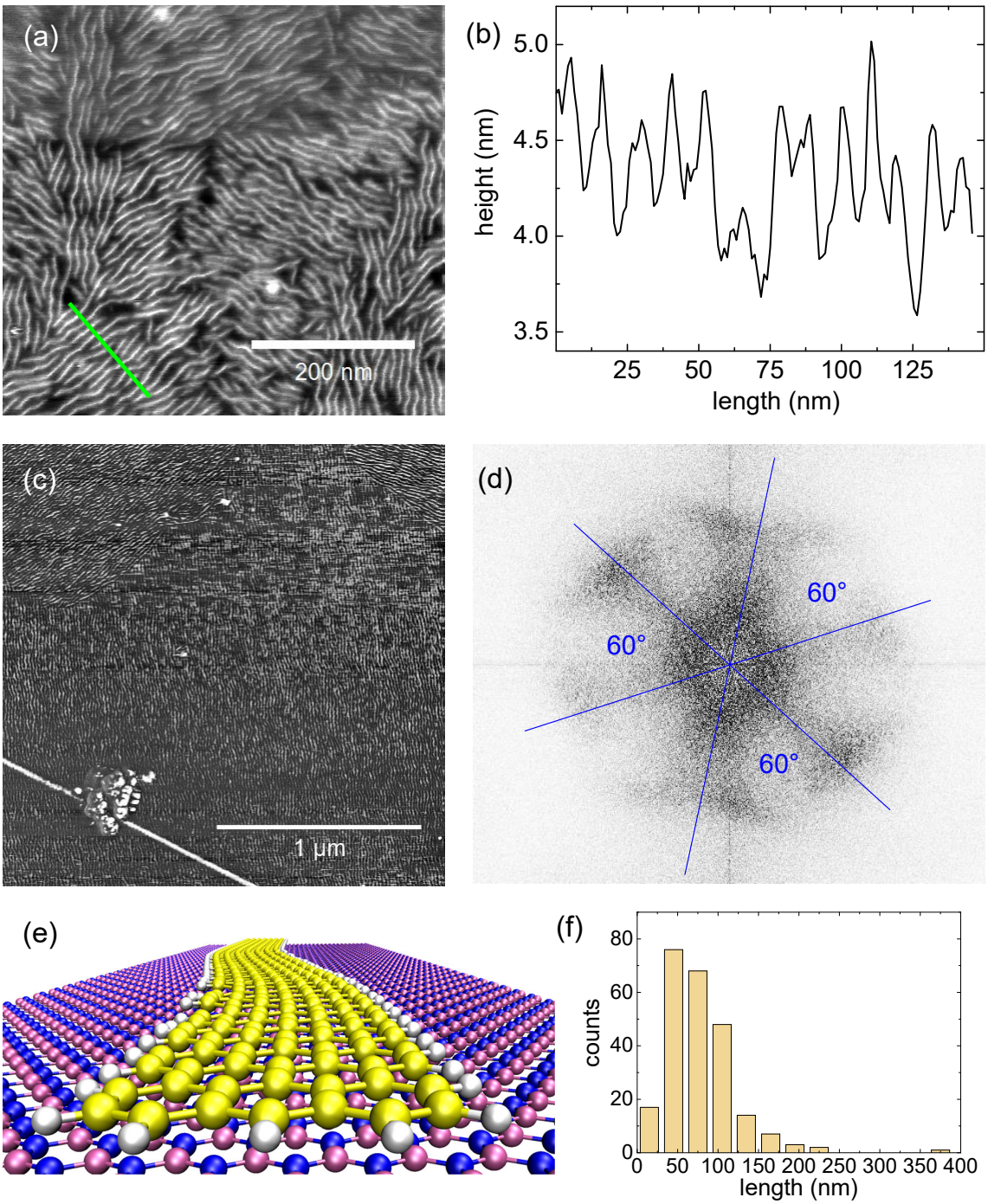

Figure 3.5.: **AFM investigation of 4-cGNRs on hBN.** (a) AFM phase image. Small domains of 4-cGNRs with single cGNR lengths of up to 370 nm can be seen. (b) Height profile along the green line in (a). (c) AFM phase image of 4-cGNRs of a different batch of samples, exhibiting larger domain sizes. (d) Typical 2D-FFT of an AFM phase image revealing three preferential directions of the cGNR adsorption on hBN. (e) Molecular dynamics simulation of a 7-aGNR (C atoms represented by yellow balls) on hBN (pink and blue balls) showing wiggled ribbon adsorption due to registry mismatch between ribbon and substrate. From [109]. (f) Length distribution of the 4-cGNRs shown in (a).

For further characterization, Fig. 3.5 (b) shows a height profile taken along the green line marked in Fig. 3.5 (a). The apparent width of the 4-cGNRs is roughly 5 nm. Theoretically, the ribbon backbone (without alkyl side chains) is only 1.4 nm wide. The discrepancy can be explained by considering the attached alkyl side chains and the limited sharpness of the AFM tip.
The alkyl side chains can be regarded as a string of 12 singly bonded C atoms with a C–C bond distance of 1.42 Å. Each C atom is passivated by two hydrogen atoms and forms tetrahedral bonding angles of 109.5° to its neighbors. The alkyl chains are attached perpendicularly to the long cGNR axis on both cGNR sides. This yields a broadening of the cGNR by $2 \cdot 12 \cdot 1.42\,\text{Å} \cdot \sin(109.5°/2) = 2.8\,\text{nm}$. Adding the length of the alkyl chains to the cGNR backbone width, one obtains a total width of 4.2 nm, showing good agreement with the experimentally acquired value. The slight deviation from the exact value might be explained by the limited sharpness of the AFM tip.
The apparent height of the 4-cGNRs lies between 0.3 nm and 1.0 nm. The variation in measured cGNR height is probably also due to fluctuating tip sharpness or buckling because of the wiggled adsorption on hBN. For comparison, the layer-to-layer distance in graphite is 0.33 nm [110].
The distance between two neighboring 4-cGNRs (center-to-center) is 10–12 nm. This is by far larger than the distance between 4-cGNRs on HOPG measured with STM by Narita *et al.* [67]. They obtained straight, parallel 4-cGNRs with a center-to-center distance of 1.8 nm. In their case, the 4-cGNRs with their alkyl chains partially overlapped with neighboring 4-cGNRs. Here, the alkyl chains presumably fit in between the cGNRs. The spacing between the 4-cGNRs might be larger here due to their wiggling on the hBN surface.
The single 4-cGNRs reach lengths of up to 370 nm. A length distribution of the 4-cGNRs from Fig. 3.5 (a) is shown in Fig. 3.5 (f). The average length is 76 nm with standard deviation of 42 nm.

Fig. 3.5 (c) shows 4-cGNRs on hBN from a different batch of samples, exhibiting domain formation as well. The same 4-cGNR powder was used and the sample was prepared in the same way as for (a). Nevertheless, the domain size of these 4-cGNRs is much larger than in (a).
To track down possible reasons for the varying domain sizes, dispersions with different amounts of 4-cGNR powder in the solvent were studied, but no clear influence of the concentration on the domain size could be detected.
The duration of the sonication did not influence the domain size as well[4].
The aging of the dispersion does also not affect the domain sizes, although older solvents might leave slightly more residues on the cGNR films.
Possibly, different qualities of the hBN crystals have an influence on the cGNR

[4]With two exceptions: When the dispersion was sonicated for too long, the cGNRs broke into little ribbon fragments, yielding smaller domains. On the other hand, if the sonication time was too short, the cGNRs did not go into dispersion at all (no coloring of the solution was visible in that case), and no cGNRs adsorbed on the hBN flakes.

domain formation. Additionally, varying times between hBN exfoliation and deposition of the cGNRs might play a role as well.
Altogether, the reason for the formation of different domain sizes remains open.

The ordered cGNR domains on hBN are found to be rotated by 60° with respect to each other. This becomes especially clear when looking at the two-dimensional Fast Fourier Transform (2D-FFT) of an AFM image. Fig. 3.5 (d) shows a typical 2D-FFT of cGNRs on hBN. The highest intensity in this plot lies along three major axes corresponding to three major domain directions. Blue lines serve as guides to the eye and underline that the domains are oriented by 60° towards each other. The angle distribution is broadened because of the wiggled structure of the cGNRs on hBN.
A possible reason for the directional alignment is the similarity of the graphene backbone of the cGNR with the hBN lattice structure. As already mentioned, both have a hexagonal lattice with only a small lattice mismatch. The interaction of B and N atoms with the π-electrons of the hexagonal carbon lattice leads to an alignment of the cGNRs along the hBN lattice [109, 111, 112]. Together with the three-fold symmetry of the hexagonal lattice this results in 60° angles.
The occurrence of parallel ordered domains facilitates the implementation of cGNRs in electrical devices, since it is possible to deliberately contact multiple cGNRs with a given orientation at the same time. Additionally, the cGNR domains align mostly with the crystallographic axes of the hBN flakes, as will be discussed in more detail below. This can be utilized when fabricating cGNR devices.

The sample characterization and fabrication process for 6-cGNRs works analogous to the one for 4-cGNRs.
The only difference is that 6-cGNR powder did not go into dispersion in THF, even after heat treatment on a hot plate and over-night sonication. Therefore, the 6-cGNR powder was dispersed in chlorobenzene (C_6H_5Cl) instead, yielding a gray color of the dispersion (see right hand side of Fig. 3.4 (c)).

Fig. 3.6 (a) shows an optical microscope image of an hBN flake on a Si/SiO_2 substrate after drop-casting 6-cGNR dispersion onto it. When exfoliating hBN on SiO_2, it often cleaves in angles in multiples of 30°, following its crystallographic axes (along the zigzag or armchair edge of its hexagonal lattice [113]). Two of those axes are indicated with black dashed lines.
Fig. 3.6 (b) is a zoomed-in AFM phase image of the area highlighted in panel (a). One can identify two domains enclosing an angle of 60°. When comparing the optical microscope image with the AFM image, one can see that the directions of the cGNR domains are aligned in parallel to the crystallographic axes of the hBN flake. This could enable the fast identification of cGNR domain directions by optical microscopy analysis of the hBN flake edges instead of time consuming AFM imaging.

The optical micrograph in Fig. 3.6 (a) exhibits stains on the hBN flake as well as on the SiO_2 surface. These are residues from the chlorobenzene solvent which leaves more remnants than THF.

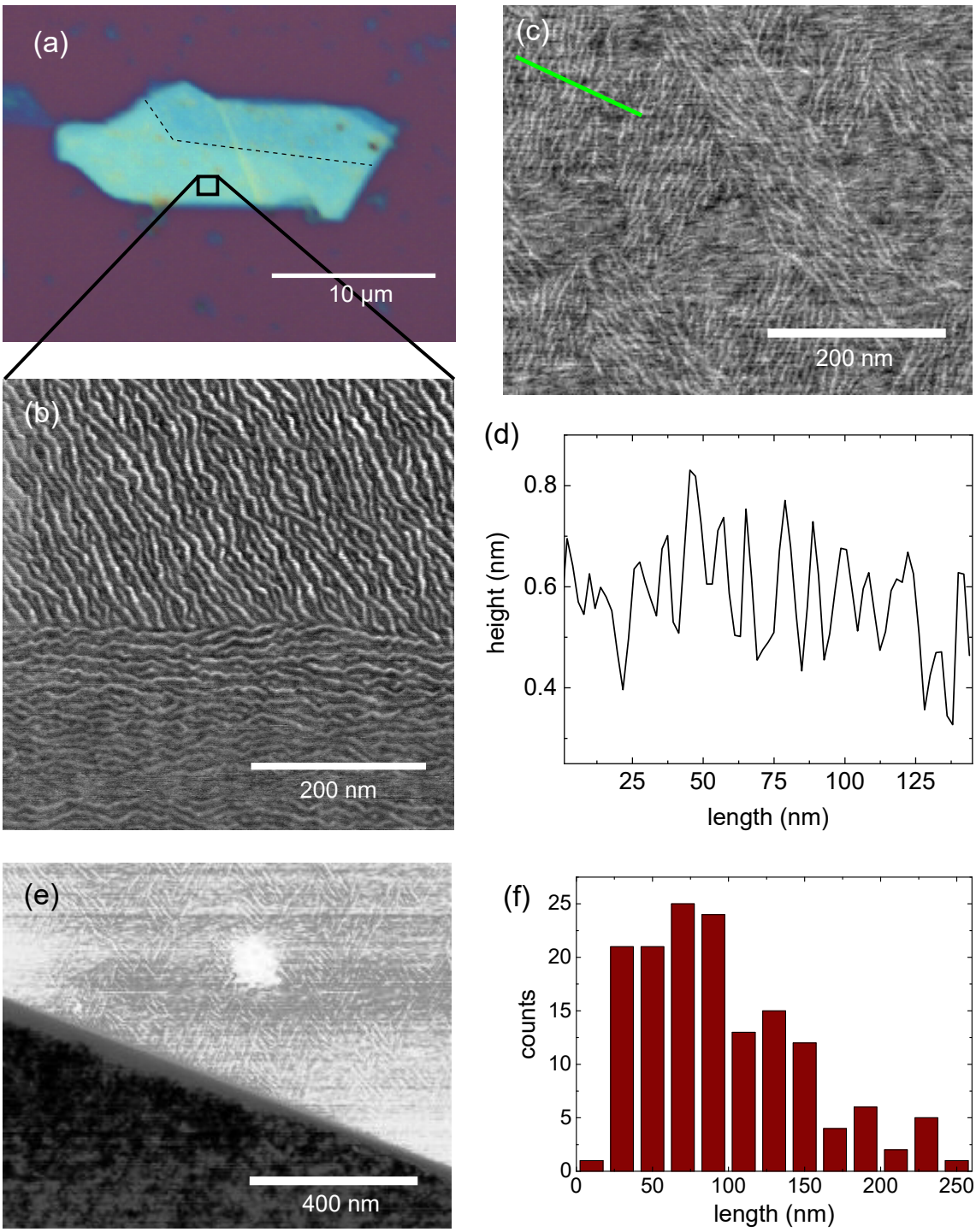

Figure 3.6.: **6-cGNRs on hBN.** (a) Optical micrograph of an hBN flake on Si/SiO_2. (b) AFM phase image of 6-cGNRs (area highlighted in (a)). (c) AFM phase image of a different 6-cGNR sample showing smaller domains. (d) Height profile along green line in (c). (e) AFM topography image of a sample edge: The cGNRs adsorb only on the hBN flake (top right area) whereas the SiO_2 surface (bottom left area) stays free of cGNRs. (f) Length distribution of the 6-cGNRs shown in (b).

The AFM image (Fig. 3.6 (b)) on this flake is, however, surprisingly clean. Apparently, there are some areas that are left free from residues.

Nevertheless, the cleanliness of the surface has a crucial effect on how well the cGNRs could be resolved by AFM. A higher degree of solution residues leads to lower image quality. Furthermore, the AFM tip shape is an important factor in obtaining well resolved cGNR images (the sharper the tip, the cleaner the image). Using the standard AFM tapping mode tips[5], the cGNRs could only be resolved when using completely new tips and carefully optimizing the scanning parameters. Imaging was easier when using super sharp tips[6].
For AFM imaging, the tapping mode was used, where tip and sample repeatedly come into contact. Therefore, the tip is worn down over time which reduces the resolution.

The domain sizes for the 6-cGNRs on hBN reach from 60 nm to over 1.2 µm, for both, length and width. An example for smaller 6-cGNR domains can be seen in Fig. 3.6 (c), which stems from another batch of samples, prepared after the same procedure.
The 6-cGNR lengths ranged up to 240 nm. A histogram for the length distribution of Fig. 3.6 (b) can be seen in Fig. 3.6 (f), showing an average length of 97 nm with standard deviation of 53 nm. These values are comparable to the results obtained for 4-cGNRs. The 6-cGNRs seem to be longer on average than the 4-cGNRs. This is probably due to the many short 4-cGNR segments present in Fig. 3.5 (a) which might stem from a too long sonication process. The 4-cGNRs, on the other hand, provide the longest single ribbons with measured lengths of up to 370 nm.
Fig. 3.6 (d) shows the height profile along the green line marked in Fig. 3.6 (c). The apparent width of the 6-cGNRs is roughly 6 nm, again wider than the theoretically expected value of 1.8 nm [102]. As expected, the 6-cGNRs are a little wider than the 4-cGNRs.
The 6-cGNRs are separated by 8–14 nm (center-to-center distance), which is roughly the same spacing as for the 4-cGNRs (10–12 nm).
With values of 0.5–0.7 nm, their apparent height is less deviant than for the 4-cGNRs (0.3–1.0 nm).
Resolving the 6-cGNRs with AFM was more challenging than finding 4-cGNRs and the images tended to be noisier. This is presumably because the 6-cGNR solvent chlorobenzene left more residues on the sample than the 4-cGNR solvent THF.

A further interesting observation is that the cGNRs stick readily to the hBN surface whereas they do not adsorb on the SiO_2 surface at all. This can be clearly seen in Fig. 3.6 (e). Only the area of the hBN flake (top right corner) is covered with cGNRs whereas the SiO_2 surface (bottom left area) stays free of cGNRs.
This makes hBN an appealing substrate for GNR based devices because in previous experiments, the SiO_2 surfaces had to be carefully functionalized to enable GNR ad-

[5]model "TESPA" from Bruker
[6]model "SHR300" from BudgetSensors

sorption [17, 68]. Here, hBN enables GNR adsorption and triggers oriented domain formation at the same time.

Since dirt and residues left by the solvent hamper the quality of the AFM images, it is desirable to get rid of the contamination. Commonly, samples are cleaned by thermal annealing. However—as already mentioned—the cGNRs are quite mobile on the atomically flat hBN surface, especially at elevated temperatures. Fig. 3.7 shows

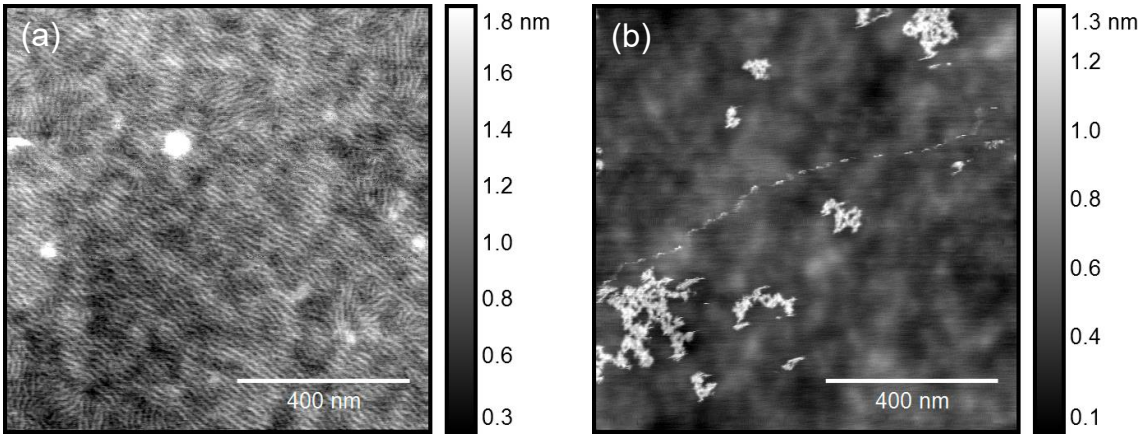

Figure 3.7.: **Annealing of 4-cGNRs on hBN.** AFM topography images. (a) Before the annealing process, the hBN flake is covered homogeneously with 4-cGNRs. (b) After annealing to 450°C for two hours in a low pressure atmosphere, the 4-cGNRs have apparently formed agglomerates and the bare hBN surface is visible.

that annealing a 4-cGNR covered hBN flake to 450°C in a low pressure forming gas atmosphere for two hours[7] leads to an apparent agglomeration of 4-cGNRs and uncovers the underlying bare hBN surface. The texture seen in the background of both AFM images probably stems from the SiO_2 substrate which can still be seen through the 25 nm thick hBN flake used here (c. f. Ref. [114]). Nevertheless, the hBN substrate is much flatter than the bare SiO_2 surface [108, 115].
In UHV experiments, the superlubricity of 7-aGNRs on a Au(111) substrate was already reported [116]. In our case, the high mobility of the cGNRs at elevated temperatures could be explained by the atomic flatness of hBN.
To prevent the agglomeration of cGNRs, the samples were not annealed.

[7] Ramp up to maximal temperature at 8 mbar, annealing at 8 mbar for 90 min and finally at 100 mbar for another 30 min.

3.4. Fabrication of contacts

For transport measurements, the cGNRs have to be contacted. To this end, contacts were structured by electron beam lithography (EBL) and metal evaporation.
The process steps employed for the contact fabrication can be seen in Fig. 3.8 and are explained in the following. (a) After exfoliating hBN (cyan) onto heavily p-doped Si/SiO_2 (gray/violet), the cGNR dispersion is drop-cast onto the sample, yielding a coating of the hBN flake with cGNRs (black)—as described in the previous section. (b) Subsequently, the sample is covered with a thin layer of the e-beam resist CSAR (green) by spin coating. (c) EBL is performed and (d) the exposed resist is removed by dipping the sample in a developer. (e) Hereafter, metal contacts (golden color) are evaporated thermally and with e-beam. Pd, NiCr/Au or Cr/Au served as contact materials. (f) Eventually, redundant e-beam resist and metal were removed in the lift-off step by putting the sample in resist remover on a hotplate. Pd was deposited without any adhesion layer, and therefore, special care had to be taken during the lift-off step not to damage the fine metal structures. The detailed process parameters can be found in the appendix.

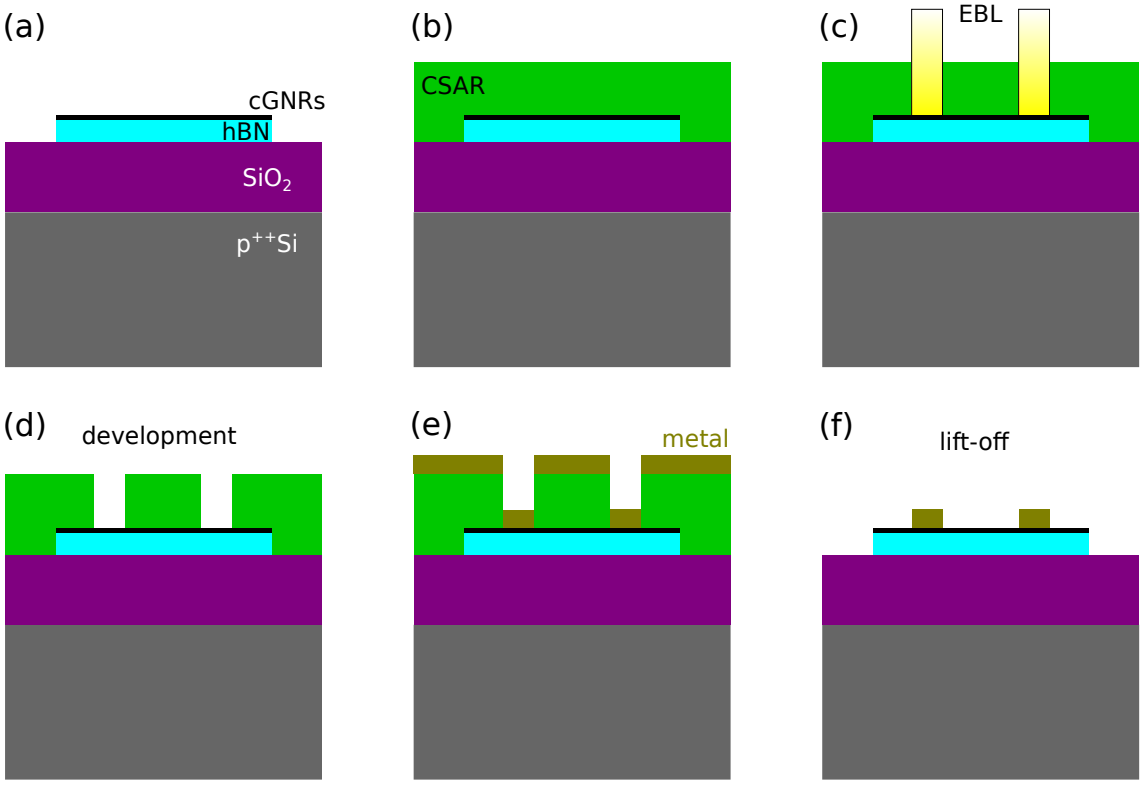

Figure 3.8.: **Process steps for contact fabrication.** Details are given in the text.

Contacting very small objects—such as the cGNRs presented here—by employing EBL brings along a couple of challenges. First, alignment on the sub 100 nm scale is an issue due to the limited precision of the scanning electron microscope (SEM) used to perform EBL. Therefore, contacting specific cGNRs that were previously identified by AFM is not always possible. As a work around, one can place the contact leads in such a way that they are perpendicular to one of the cGNR domain directions (see Fig. 3.9). This way, one can contact an entire domain (or even several different ones) in which the cGNRs are perpendicularly aligned to the contact leads. Additionally, domains oriented by 60° with respect to the leads will be contacted. In that case, only the longest cGNRs can span the gap between two contact leads.

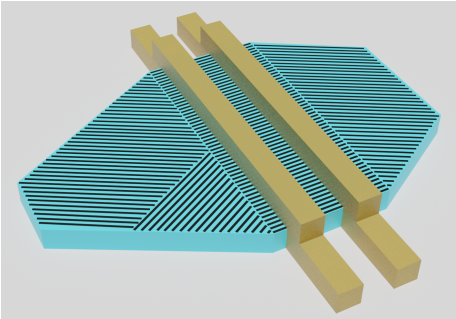

Figure 3.9.: **Orientation of contacts.** Scheme of an hBN flake (blue) with differently oriented cGNR domains (black). Contact leads (golden) are placed in such a way that they are perpendicular to one domain direction.

For this reason, it is desirable to minimize the distance between two contact leads as much as possible. The limiting factor in this aspect is caused by the proximity effect: The electron beam—used to expose only parts of the e-beam resist—is scattered within the resist layer and also partially backscattered from the substrate, which leads to exposure of neighboring resist areas. This causes over-development of the contact structures which can lead to shorts between contacts or failure during the lift-off process. One can gain precision by using thinner resist layers. The minimum resist thickness is, however, dependent on the thickness of the contacts. To ensure successful lift-off, the resist layer should not fall below two to three times the height of the contacts. The lower bound for the height of the contacts, on the other hand, is given by the hBN flake thickness to assure integrity of the contacts when passing the flake edges.

To increase the chances for successful cGNR contacting, several contact leads were placed in parallel, using an intertwined comb structure (see Fig. 3.10, right). The thickness of the contact metals varied between 15–50 nm and the spacing of the contact fingers between 70–120 nm. The width of the fingers was in the range 100–120 nm and their length 2–3 µm.

Fig. 3.10 shows images of a typical sample structure with 6-cGNRs on hBN and 15 nm thick Pd contacts. On the left hand side, one can see rectangular contact pads, connected by leads to the central hBN flake (blue color). The pads exhibit some scratches from the needles of a probe station which were used to measure the I-V-characteristics of this device. For better orientation on the sample, the chip is provided with a Cr/Au coordinate system.

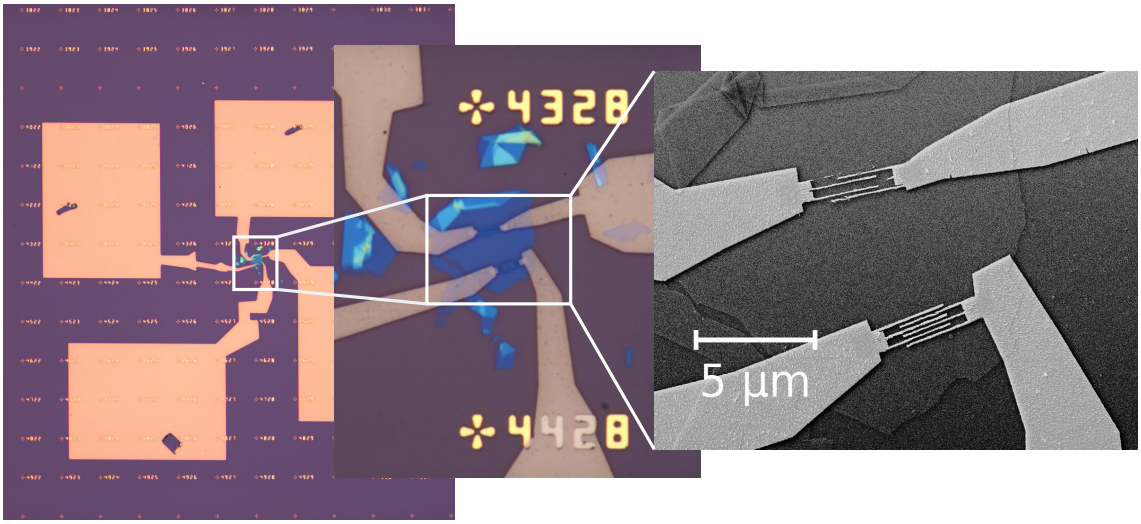

Figure 3.10.: **Typical sample design.** Left: Overview optical microscope image of a complete device after measurement. Middle: Zoom into the central area of the device. Distance between markers: 50 µm. Right: SEM image of the contact area showing the intertwined comb structure of the contacts.

The middle image shows the center part of the structure. Since the thickness of the Pd layer is only 15 nm, the contacts appear transparent. The contact fingers in the central region are barely visible. The distance between two numbered markers is 50 µm.
On the right hand side, a magnified SEM image of the contact area is visible. At the upper contact pair, two fingers are missing due to a partially failed lift-off, documenting the vulnerability of the fabrication process.

Slight differences in the resist height[8] lead to an over- or underexposure during EBL. This can result in fused contact combs, which was one of the main issues during device fabrication. Sometimes, these shorts could be repaired by cutting shorted fingers with the help of a focused ion beam (FIB). Fig. 3.11 shows such an example. The contact material is Pd with a thickness of 15 nm. In the top part, three fingers (two from the right, one from the left) are fused together due to a partially unsuccessful lift-off. By cutting trenches (marked with white arrows) in the hBN substrate with the help of FIB, the clumped fingers were severed from the intact contact leads.
To ensure that the Ga^+ ions (used as focused ion beam source) are not deposited on the substrate creating shorts themselves, reference samples with FIB cut contact pairs without cGNRs were fabricated, yielding no electrical conduction.
Furthermore, one can observe in Fig. 3.11 that step edges in the hBN flake can cause disruption in the leads as (almost) happening in the central finger region.

[8] arising from the spin coating step, Fig. 3.8 (b)

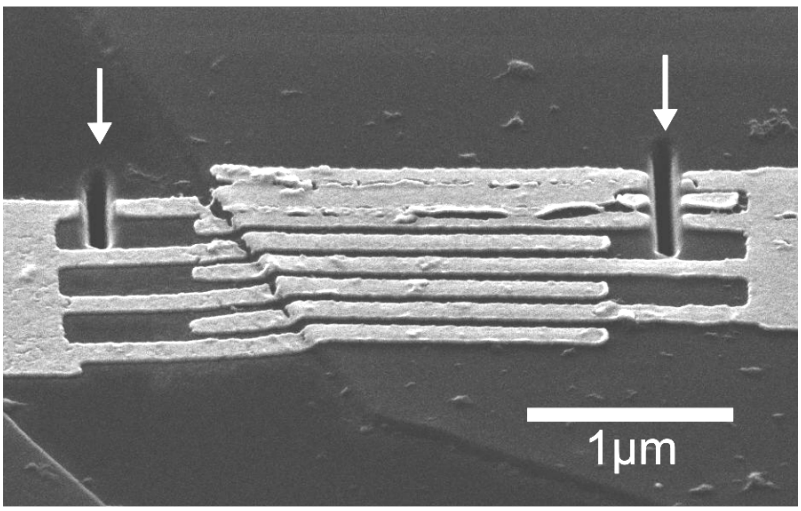

Figure 3.11.: **FIB cutting of fused contact combs.** Some shorts could be repaired by cutting through fused contact lines with the help of a focused ion beam (trenches indicated by white arrows).

A further attempt to improve the contacts and the device quality was to encapsulate the cGNRs with a second hBN flake and apply side contacts. In the case of graphene, 1D side contacts have proven to be reliable and of high quality [117]. For cGNRs, side contacting means to contact the short ends of the cGNRs, thus reducing the dimensionality of the contacts even further, leading to 0D contacts. This method of fabricating contacts has also been used to contact CNTs [118].
An additional advantage of encapsulating the cGNRs is that they are protected from environmental influences like adsorbates from the air.

For the encapsulated cGNRs, the fabrication process was modified. After identifying an hBN flake with homogeneous cGNR coverage, a second hBN flake was placed on top of the first hBN flake, sandwiching the cGNRs. The principle of this technique is shown in Fig. 3.12 and works as follows. (a) A polypropylene carbonate (PPC) film is spin coated onto a Si/SiO_2 chip and hBN is exfoliated on top of it. Then, the

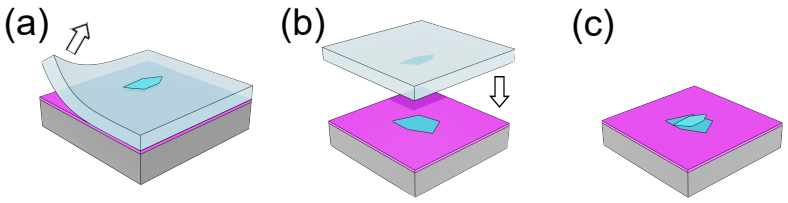

Figure 3.12.: **Stacking process.** Fabrication steps for the encapsulation of cGNRs with hBN flakes.

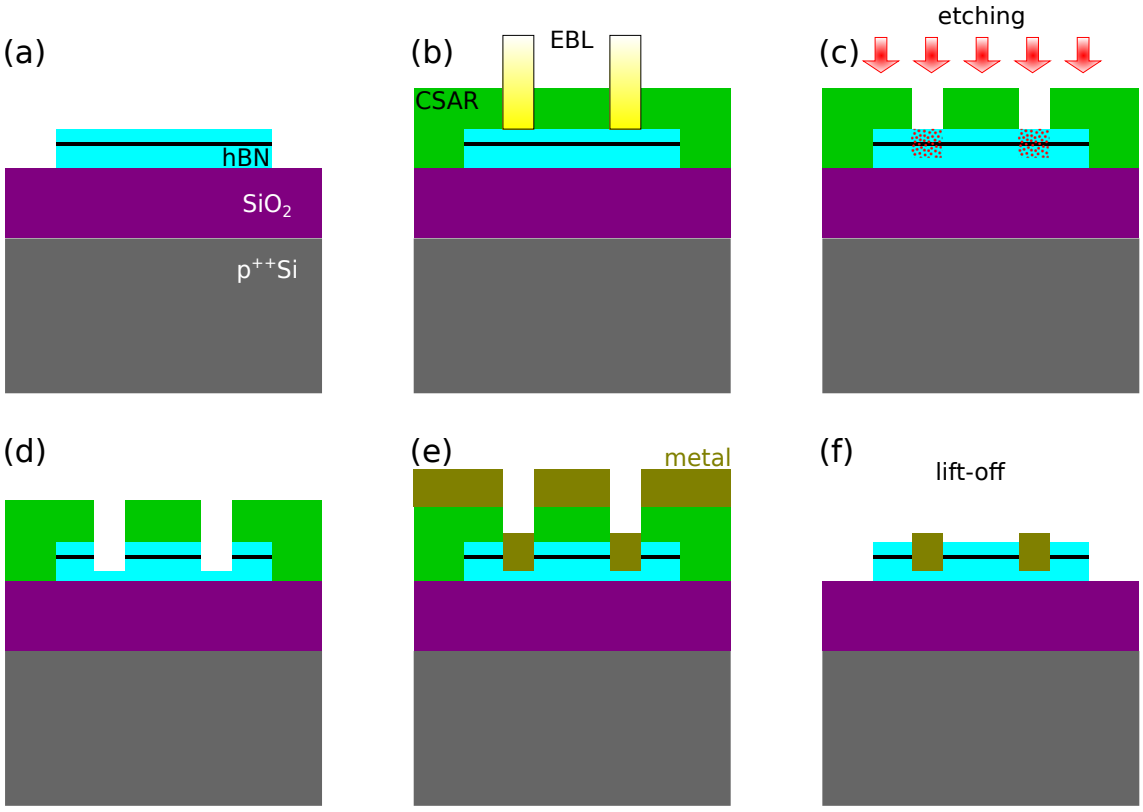

Figure 3.13.: **Contact fabrication for encapsulated cGNRs.** Details are given in the text.

PPC film is carefully peeled off the substrate by using an adhesive tape[9]. (b) The PPC film is flipped over and mounted to a transfer setup in an optical microscope. Another hBN flake—exfoliated on a Si/SiO_2 chip and covered with cGNRs—serves as target flake. The two flakes are brought into contact by carefully lowering the PPC film. (c) After contact formation, the PPC film is dissolved by exposure to chloroform. More details for the stacking procedure can be found in the PhD thesis of Martin Drienovsky [119].

The further procedure is shown in Fig. 3.13. Panel (a) depicts an hBN-cGNR-hBN stack. (b) CSAR e-beam resist is spin coated onto the sample and EBL is performed. (c) After development, the sample is placed into a reactive ion etching (RIE) chamber and the sample is etched with a mixture of CHF_3 and O_2 plasma. (d) The CSAR resist acts as a hard mask during etching, leading to trenches in the hBN-cGNR-hBN stack after the process. (e) The contact metal is deposited directly after the etching process to establish side contacts to the cGNRs. Only Cr/Au was used for the encapsulated cGNRs. (f) Redundant e-beam resist and

[9]To avoid that the surface of the hBN comes into contact with the sticky surface of the adhesive tape, a hole is cut in the tape leaving the area around the hBN flake untouched.

Figure 3.14.: **Encapsulated sample.** Optical image of an encapsulated and side contacted 4-cGNR sample. Areas of stacked hBN flakes are highlighted with dashed lines. The distance between two markers is 50 µm.

metal are removed during the lift-off step.

Fig. 3.14 shows an optical micrograph of a sample with encapsulated and side contacted 4-cGNRs. The large hBN flake was placed on top of two smaller hBN flakes whose outlines are highlighted by dashed lines. Cr/Au served as contact material. The reddish structure on top of the contact leads is presumably contamination appearing after measurement and storage in ambient conditions for a couple of weeks.

3.5. Transport characterization

After successful contact fabrication, the cGNRs were measured electrically using a probe station at ambient conditions. In this section, the results for non-encapsulated devices will be presented.

The schematics of the measurement setup is sketched in Fig. 3.15. A source-drain voltage V_{sd} is applied across the cGNRs and a resistor to protect the cGNRs from high currents. The drain current I_d is recorded and the heavily p-doped Si substrate can be used as back gate electrode by applying a back gate voltage V_{bg}. The SiO_2 layer is 285 nm thick and the thickness of the bottom hBN flakes varies between 10–40 nm.

Fig. 3.16 shows the I-V-characteristics of a Pd contacted 6-cGNR device (labeled sample **6-1**, blue triangles) as well as a NiCr/Au contacted 4-cGNR device (sample **4-1**, black squares) and a Pd contacted 4-cGNR device (sample **4-2**, red dots). The drain current I_d is plotted versus the source-drain voltage V_{sd} and is in the range of tens to hundreds of nA.
The NiCr/Au contacted 4-cGNRs exhibit the steepest current onset when increasing the source-drain voltage. The Pd contacted 4- and 6-cGNRs look very similar on the negative voltage side and differ only slightly on the positive side. This is quite

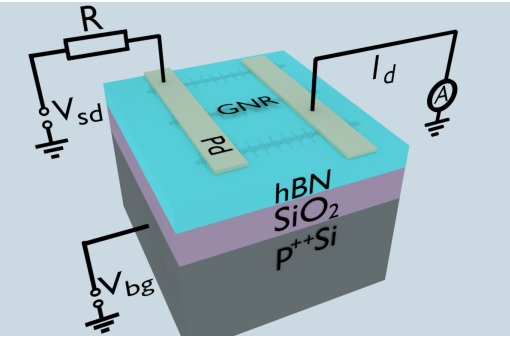

Figure 3.15.: **Measurement setup.** The cGNRs are contacted with metal leads. A source-drain voltage V_{sd} is applied across a resistor and the drain current I_d is measured. A back gate voltage V_{bg} can be applied at the p-doped Si layer of the substrate.

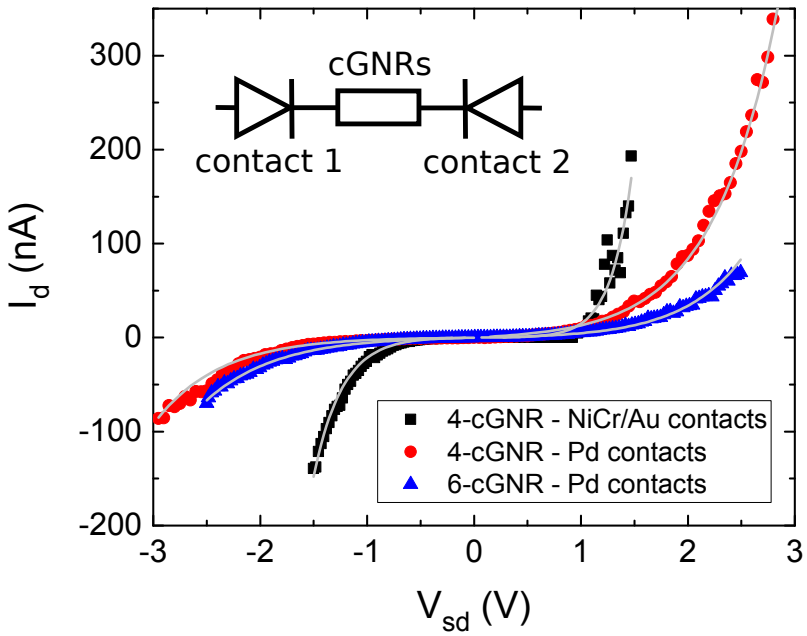

Figure 3.16.: ***I-V*-curves.** Experimental data (symbols) of 4- and 6-cGNR devices contacted with NiCr/Au or Pd and corresponding TFE fits (lines). Inset: Scheme for two Schottky contacts connected back-to-back over the cGNRs (represented by a resistor).

surprising, since their different band gaps should be reflected in the I-V-curves.
Moreover, the I-V-curve for the 6-cGNRs is fairly symmetric. On the other hand, the curves for the 4-cGNRs are asymmetric which is untypical for this two-terminal geometry.
Taking all these effects into account, it seems likely that the measurements are dominated by the Schottky behavior of the contacts.

The Schottky barriers form at both cGNR ends where the metallic leads come into contact with the semiconducting cGNR(s)[10]. These two Schottky barriers are connected back-to-back. This is sketched in the inset of Fig. 3.16 where the cGNRs (one or many) are depicted as a resistor.
The contacts at both cGNR ends can be quite distinct, though. First, the overlap area between metal and cGNRs can differ at both sides, leading to a different current injection/extraction area. Further, residues stemming from the fabrication process might be distributed unevenly over both sides. The alkyl side chains might also play a role here by flipping over and acting as an extra insulating layer between cGNRs and metal. Therefore, the shape of the I-V-curves and the drain currents of the devices presented in this chapter vary considerably.

Determination of the number of cGNRs in the junction

The experimental data in Fig. 3.16 are fitted with the thermionic field emission model (see Eq. 3.5). Since the detected current is limited by the current leaking through the Schottky diode in reverse direction, the fits to the I-V-curves (gray lines) are performed to the negative and positive voltage regions separately, and always for the reverse direction of the Schottky diode.

Eq. 3.5 displays a current density. Therefore, one has to multiply the expression for J with the contact area in order to fit the model to the experimental data.
Since the overlap between cGNRs and metal is unknown, the cross sectional area of a cGNR is taken as the contact area. It is assumed to be the width of the cGNR backbone times the layer distance in graphite. That yields $0.23\,\mathrm{nm}^2$ for the 4-cGNRs and $0.39\,\mathrm{nm}^2$ for the 6-cGNRs. This area needs to be multiplied with the number of cGNRs in the junction.

As already mentioned, it is uncertain how many cGNRs have been contacted at the same time. Even by carefully planning the sample design and executing the lithography with great diligence, it is impossible to fabricate contacts with precision on the nanometer scale due to aberrations of the SEM.
Since it is not possible to check the contact formation after metal deposition by AFM, the number of successfully contacted cGNRs had to be estimated.
To do so, the device was examined by SEM after measurement. There, the actual

[10]The determination of the number of cGNRs in the junction will be addressed later.

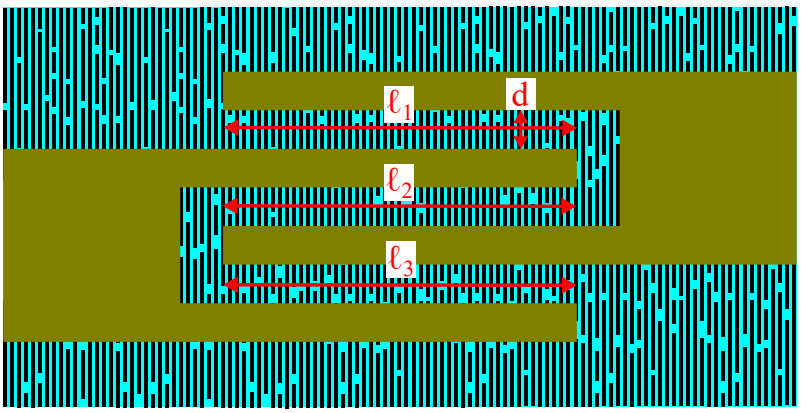

Figure 3.17.: **Determination of the effective contact length.** The effective contact length l^* is the combined length of the segments in which cGNRs (black stripes) can cross the gap between two contact leads (golden fingers): $l^* = l_1 + l_2 + l_3$. The distance d between the contact leads is indicated as well.

distance d between the contact leads was measured as well as the effective contact length l^* (see Fig. 3.17 for clarification).

The cGNRs on hBN exhibit three different domain orientations. One of them is perpendicular to the contact leads[11] which means that only cGNRs with lengths L larger than d can span the gap between two contact leads.
cGNRs in the other domains are rotated by 60° with respect to the contacts. In that case, the cGNR length has to be larger than $d/\cos(60°) = 2d$ to connect both leads.
Since all three domain orientations are equally probable to occur, it is assumed that for one third of the effective contact length the cGNRs have to be longer than d, and for two thirds the cGNRs have to be longer than $2d$.
From the length distribution of the cGNRs (see Figs. 3.5 (f) and 3.6 (f)) one can determine the number of cGNRs with $L > d$ and $L > 2d$ and therefore obtains the probability P that a cGNR gets contacted. This has to be done separately for every domain orientation and the results have to be summed up to get the total probability.
When multiplying the probability with the effective contact length divided by the spacing of the cGNRs (on average 11 nm for both, 4- and 6-cGNRs), one obtains the expected number of cGNRs in the junction[12].

[11] This is achieved by designing the EBL according to the cGNR domains previously determined by AFM.

[12] Note that the real number of cGNRs in the junction is probably lower than this value because the cGNRs are not necessarily centered in the gap between the contacts (i. e. a cGNR that is sufficiently long to span the gap could be mostly lying underneath one of contacts, and thus its remaining length might be too short to reach to the other contact). One could therefore also speak of the maximum expected number.

As an example, the calculation for the expected number of cGNRs in the junction of sample **6-1** is done here. An SEM image of its contact fingers is displayed in Fig. 3.11. From this image, one can determine the distance d between the contact leads to be 70 nm and the effective contact length l^* to be 6.3 µm. Thus, for one third of this effective contact length (= 2.1 µm), the 6-cGNRs have to be longer than $d = 70$ nm and for two thirds (= 4.2 µm), the 6-cGNRs have to be longer than $2d = 140$ nm. From evaluating the length distribution in Fig. 3.6 (f), it turns out that 65.3% of the 6-cGNRs are longer than 70 nm and 20% are longer than 140 nm. The spacing between the 6-cGNRs is 11 nm.

Therefore, the expected number N of 6-cGNRs in the junction is given by

$$N = \frac{\text{effective contact length}}{\text{spacing between 6-cGNRs}} \cdot P(\text{cGNR length} \geq \text{spacing between contacts})$$

$$N = \frac{\frac{1}{3} \cdot 6.3\,\mu\text{m}}{11\,\text{nm}} \cdot 65.3\% + \frac{\frac{2}{3} \cdot 6.3\,\mu\text{m}}{11\,\text{nm}} \cdot 20\% = 201$$

The same method was used to determine the expected number of 4-cGNRs in the junctions of samples **4-1** and **4-2** (Fig. 3.16). Here, up to 526 cGNRs are expected to be contacted at the same time. Even though the 4-cGNRs were a bit shorter on average, i. e. less likely to be contacted, the effective contact length was longer for these samples, thus leading to the higher number of potentially contacted 4-cGNRs.

Fitting procedure

The TFE fits to the experimental data were performed by manually adjusting the parameters Φ_b, E_{00} and ζ from Eq. 3.5 for a single cGNR in the junction. Since changing the contact area has the same effect as changing the Schottky barrier height [94], the fitting was repeated for the maximum expected number of cGNRs in the junction. In most cases, only Φ_b had to be changed to obtain a matching fit curve whereas the values for E_{00} and ζ remained the same. The difference between the values for Φ_b obtained by fitting for one cGNR in the junction and for the maximum expected number of cGNRs in the junction was taken as uncertainty margin.

Further, it has to be noted that strictly speaking, the Richardson constant A used in Eq. 3.5 is dependent on the effective electron mass m_e^* [83, 84]:

$$A = \frac{4\pi m_e^* k_B^2 q}{h^3} \tag{3.7}$$

with h being the Planck constant. The effective electron mass, however, is unknown for this contact configuration.
On the basis of DFT calculations, Ivanov *et al.* [100] predicted an effective electron mass of $m^*_{4-cGNRs} = 0.24 \cdot m_0$ for the 4-cGNRs and $m^*_{6-cGNRs} = 0.16 \cdot m_0$ for the

6-cGNRs, with m_0 being the free electron mass. These calculations were done without considering the alkyl side chains. Instead, the GNR edges were passivated with hydrogen. For aGNRs, however, it was shown that the effective mass can vary with different edge functionalizations [120]. Therefore, the data were fitted using both, the free electron mass and the reduced values obtained by Ivanov and coworkers. Here, only the values obtained by fitting with the free electron mass are presented. When fitting with the reduced effective masses, the Schottky barriers are ∼30% lower, whereas the values for E_{00} and ζ stayed unchanged.
In spite of the unknown effective electron mass, the large variation in possibly contacted cGNRs is the main source for uncertainty in the evaluation of the barrier height, exceeding also further uncertainties like thermal broadening.

Finally, the difference between fitting with the TFE model (Eq. 3.5) and the TE model (Eq. 3.4) is briefly discussed. As pointed out in more detail in section 3.1.3, the TFE model should be suited better to fit back-to-back configurations (as present here) because it takes into account tunneling through the Schottky barrier. Indeed, the TFE model yielded superior fitting which becomes apparent when plotting the drain current as a logarithmic function of the source-drain voltage. Fig. 3.18 reproduces the I-V-curve for sample **6-1** in the range of positive voltages only. In panel (a), the current is plotted on a linear scale and both, the TFE and the TE fits seem to match reasonably well to the experimental data points. When plotting the same data on a logarithmic scale in panel (b), however, one can observe that the TE fit yields either good fitting for higher voltages and deviates for the lower voltages (as depicted here) or good fitting for lower voltages and deviates for higher voltages (not shown here). The TFE fit, in contrast, matches for all voltage ranges.

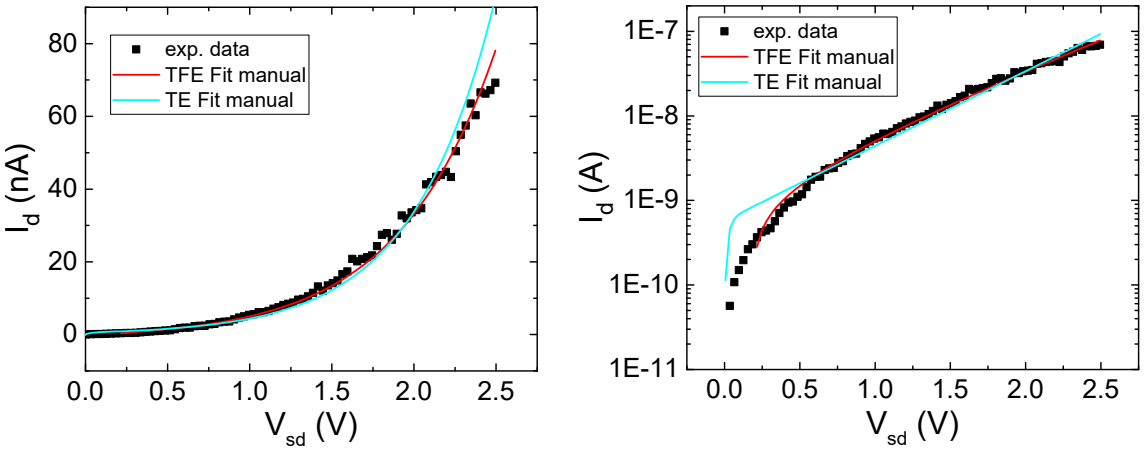

Figure 3.18.: **Fitting procedures for sample 6-1.** Manually optimized TFE and TE fit curves to experimental data on a (a) linear and (b) logarithmic scale. The TFE model yields better matching over the entire measurement range.

Turning back to the I-V-curves in Fig. 3.16, the TFE fits match the experimental data quite nicely. The fitting results can be found in Table 3.1. For the positive voltage side, the NiCr/Au contacted sample **4-1** has a substantially higher Schottky barrier ($\approx$ 220 meV) than the Pd contacted devices ($\approx$ 110 meV for sample **4-2** and $\approx$ 150 meV for sample **6-1**). On the negative voltage side, the heights of the Schottky barriers are roughly the same ($\approx$ 150 meV for all three devices). The Schottky barrier heights obtained here are in line with experiments on CNTs known from literature [85].
E_{00} is almost twice as high for the NiCr/Au contacts as for the Pd contacted cGNRs, irrespective of cGNR type. A higher value for E_{00} corresponds to a faster increase in I_d as the voltage is increased. ζ lies in most of the devices between 0.2–0.4 V, meaning the Fermi energy lies quite close to the band edge.

From the point of reliability, Pd seems to be the better contact material. Sample **4-1** is the only device with working NiCr/Au contacts, which is why no data for 6-cGNRs with this contact material are shown in this thesis.

Device degradation

Next, the long-term stability of 6-cGNR devices was tested. Fig. 3.19 shows data of two Pd contacted 6-cGNR devices measured directly after fabrication and two weeks later. Forward and backward sweep direction of the source-drain voltage are shown. Apart from slight deviations in the first measurement of sample **6-2**, the measurements are free of hystereses.

On the first run, the I-V-curve of sample **6-2** (black squares) has a pronounced s-shape whereas the curvature of sample **6-3** (green dots) is less prominent. Both devices exhibit fairly symmetric I-V-characteristics. The drain currents are higher than for sample **6-1** which might be explained by a higher number of 6-cGNRs spanning the gap between the metal leads or better contacts.
The TFE fits produce lower values for the Schottky barrier heights for these devices in comparison to the previously measured ones (see Table 3.1). The fits yield a Schottky barrier height of $\Phi_b \approx (50 \pm 150)$ meV for sample **6-2** on both voltage sides and $\Phi_b \approx (20 \pm 110)$ meV for sample **6-3**, also on both voltage sides.
Apparently, the TFE fits to the low barrier height sample **6-3** do not trace the experimental data in the low voltage regime as nicely as the TFE fits to the other I-V-curves, because of its less prominent curvature. The shape parameter E_{00} is in this case lower (5 mV for sample **6-2** and 4 mV for sample **6-3**) than for the previous devices.

After storing the devices two weeks under ambient conditions, their I-V-characteristics were measured again. Now, the drain current for both samples decreased by roughly a factor of three. The drop in drain current in the second run could be explained by degradation of the cGNRs, degradation of the contacts or contamination

Sample	volt.	Φ_b	E_{00}	ζ
4-1 (NiCr/Au)	pos.	(218 ± 194) meV	17 mV	0.2 V
	neg.	(156 ± 175) meV	14 mV	0.3 V
4-2 (Pd)	pos.	(106 ± 175) meV	9 mV	0.2 V
	neg.	(150 ± 168) meV	9 mV	0.1 V
4-3 (Pd)	pos.	(231 ± 168) meV	9 mV	0.6 V
	neg.	(256 ± 175) meV	9 mV	0.1 V
4-4 (Cr/Au, end contacted)	pos.	(87 ± 131) meV	7 mV	0.4 V
4-5 (Cr/Au, encapsulated)	pos.	(106 ± 137) meV	7 mV	0.3 V
6-1 (Pd)	pos.	(147 ± 146) meV	9 mV	0.4 V
	neg.	(137 ± 144) meV	8 mV	0.2 V
6-2 (Pd)	pos.	(47 ± 146) meV	5 mV	0.05 V
(1st measurement)	neg.	(55 ± 145) meV	6 mV	0.4 V
6-2 (Pd)	pos.	(53 ± 147) meV	4 mV	0.05 V
(2 weeks later)	neg.	(53 ± 147) meV	4 mV	0.7 V
6-3 (Pd)	pos.	(15 ± 110) meV	4 mV	0.2 V
(1st measurement)	neg.	(15 ± 110) meV	4 mV	0.2 V
6-3 (Pd)	pos.	(36 ± 108) meV	4 mV	0.3 V
(2 weeks later)	neg.	(41 ± 109) meV	4 mV	0.4 V
6-4 (Pd, 64 cGNRs in junction)	pos.	(90 ± 90) meV	7 mV	0.4 V

Table 3.1.: **Fitting results.** Summary of the fitting results for all devices presented in this chapter. The parameters Φ_b, E_{00} and ζ were obtained by using the TFE model from Eq. 3.5 to fit the experimental data. All fits were performed to the positive and negative voltage side separately (indicated in the column "volt.") assuming a single cGNR in the junction. Considering the maximum expected number of cGNRs in the junction yielded the uncertainty margins.

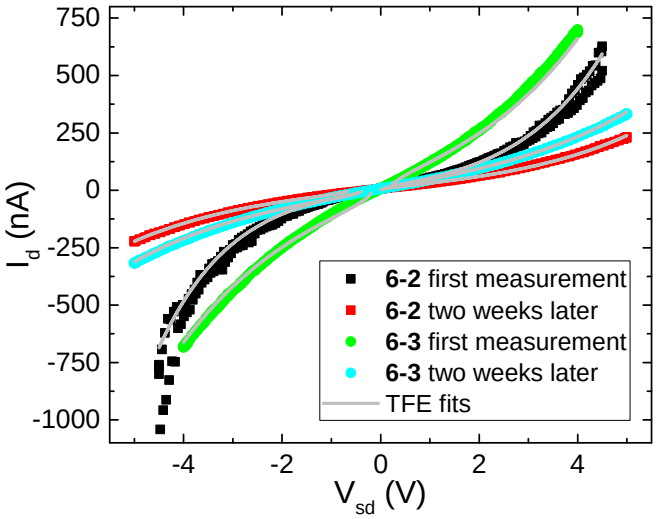

Figure 3.19.: **Device degradation** Two Pd contacted 6-cGNR devices (samples **6-2** and **6-3**) measured directly after fabrication (black and green) and after storing them for two weeks in ambient conditions (red and cyan). Gray lines are TFE fits to the experimental data.

of the cGNRs by particles in the air.
When repeating the TFE fitting procedure, the E_{00} value for sample **6-2** decreased to 4 mV, reflecting the slower increase of current with voltage, but the Schottky barrier height stayed the same. For sample **6-3**, on the other hand, the E_{00} value stayed the same, but the height of the Schottky barrier increased to roughly (40 ± 110) meV.
Thus, a decrease in current can be related to both, an enhanced Schottky barrier height or a changed barrier shape (i. e. a lower barrier shape parameter E_{00}).

Back gate dependence

Next, the back gate response of the devices was tested. As an example, Fig. 3.20 shows a Pd contacted 6-cGNR device (sample **6-4**) measured at three different back gate voltages. The three I-V-curves are (almost) identical and no effect of the applied back gate voltage could be detected. Similarly, the other devices showed no back gate dependence.

A possible explanation of the lacking gate dependence could be Fermi level pinning at the Schottky contacts. Furthermore, the distance from the cGNRs to the Si back gate is much larger than the spacing between the electrodes (see scheme in Fig. 3.21). Therefore, screening could greatly reduce the gate coupling.

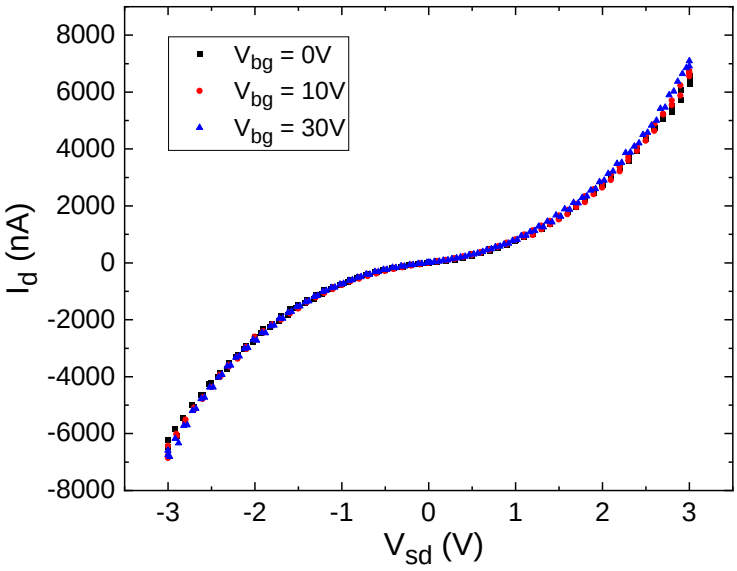

Figure 3.20.: **Back gate dependence.** I-V-curves of Pd contacted 6-cGNRs (sample **6-4**) show no dependence on the applied back gate voltage.

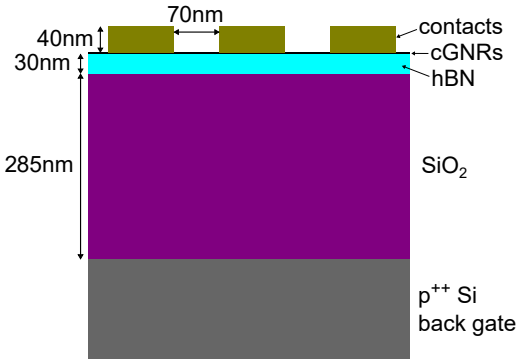

Figure 3.21.: **True to scale model of a typical contact configuration.** The relevant distances are indicated in the drawing.

Remarkably, the drain current is one order of magnitude higher than for the previously studied devices. Furthermore, the I-V-curve is symmetric.
When trying to perform the TFE fitting for a single cGNR in this junction, the fit followed the experimental data only when choosing a Schottky barrier height of $\Phi_b \approx 0\,\text{meV}$. On the one hand, this could mean that the Schottky barrier is really (vanishingly) low for this sample, thus explaining the high drain current.
On the other hand, it could also mean that the TFE equation is not suited to model these high drain current curves. For some reason—possibly due to doping—the Fermi level might be shifted in such a way, that it is more likely for electrons (or holes) to overcome the barrier. Here, the Fermi level could lie in the conduction band (valence band in the case of hole transport), whereas it was situated in the band gap for the previous samples.
Moreover, the number of actually contacted cGNRs could be much higher in this

case than for the other samples. By contacting more cGNRs, the contact area increases which has the same effect as lowering the Schottky barrier [94]. Therefore, instead of having only a few cGNRs with a low Schottky barrier in the junction, it is also possible to have many cGNRs with a moderate Schottky barrier. When assuming the maximum expected number of 6-cGNRs in the junction (64 for this device), the fit agrees well with the experimental data (fit not shown here), yielding a Schottky barrier height of 90 meV and a shape factor of $E_{00} = 7$ mV.

The back gate dependence was also tested for the 4-cGNR devices. Fig. 3.22 (a) shows the I-V-curve of a Pd contacted 4-cGNR device (sample **4-3**). The curve is asymmetric with respect to the source-drain bias. Here, the drain current measures only a few nA which is two to three orders of magnitudes lower than for the previous samples. Accordingly, relatively high Schottky barriers result. The TFE fits match

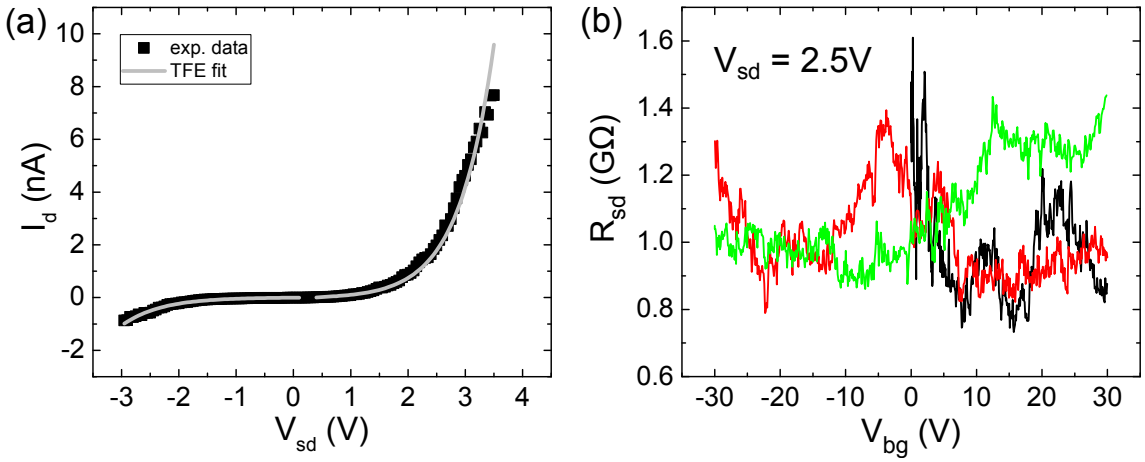

Figure 3.22.: ***I*-*V*-characteristic and gate response of Pd contacted 4-cGNRs.** (a) I-V-measurement of sample **4-3** at zero gate voltage and TFE fits to the experimental data. (b) Back gate sweeps at $V_{sd} = 2.5$ V exhibiting no clear gate dependence.

the experimental data quite nicely and yield Schottky barrier heights of $\Phi_b \approx (230 \pm 170)$ meV for the positive voltage side and $\Phi_b \approx (260 \pm 170)$ meV for the negative one. The shape factor was $E_{00} = 9$ mV and thus similar to the other Pd contacted 4-cGNR device. A possible explanation for the lower drain current might be that more residues stayed between 4-cGNRs and metal leads and therefore lowered the contact quality.

Fig. 3.22 (b) displays consecutive back gate sweeps of this device at a fixed source-drain voltage of $V_{sd} = 2.5$ V. The sweeps reveal run-to-run variations, but no clear back gate dependence.
Usually, one can extract the doping level by measuring the source-drain resistance R_{sd} of the sample in dependence of the back gate voltage V_{bg}. Here, unfortunately,

no information could be extracted from the back gate sweeps. Therefore, neither the doping level nor the mobility of the investigated cGNRs could be determined.

Comparison to literature

The results for 4-cGNRs are in line with previous experiments from literature whereas no transport measurements have been performed for 6-cGNRs so far. In preceding studies, 4-cGNRs prepared from organic solvents and aGNRs of different widths obtained by on-surface synthesis exhibited device currents in the range of 1 nA to 1 µA for a source-drain bias of 1 V, which is in agreement with the observations made here [16–18, 69].
Zschieschang *et al.* [68] measured drain currents for 4-cGNRs prepared from solution of up to tens of µA. However, their devices showed signs of agglomerated cGNRs, leading to a greatly reduced band gap. This could explain a lower Schottky barrier and correspondingly higher drain currents.

3.6. Encapsulated cGNR devices

The large variation in the magnitude of the drain currents and the shape of the I-V-curves of the previously presented samples show that the contact fabrication needs to be improved in order to get more uniform and reliable contacts. One approach towards this direction is the implementation of side contacts.
With this method, a heterostructure with different layers (e. g. graphene encapsulated between hBN) is fabricated with the help of the stacking process (see Fig. 3.12). Then, the structure is etched and metalized. The metal forms a contact to the encapsulated material only at the edge which was exposed during the etching process. Applying this technique to cGNRs, only the ends of the cGNRs are contacted, producing 0D *end contacts*.

One of the main advantages of this technique is that the cGNRs stay free of EBL resist. Therefore, less residues should be left between cGNRs and metal leads producing a better contact. Additionally, the top hBN flake protects the cGNRs from adsorbates from air and therefore keeps them pristine.

Moreover, it was shown for CNTs that the contact behavior is different when the CNTs were contacted only at their ends or when the contacts partially overlapped with the CNTs [85, 121, 122]. For the end contacted CNTs, a covalent bond formation was predicted and the contacts were shown to be basically unaffected by Fermi level pinning [121]. This might also play a role when contacting cGNRs. The cGNRs were so far contacted by placing the contacts over a domain of oriented cGNRs of different lenghts. Most of the cGNRs were presumably partially buried under the

contact metal whereas some could potentially only be end contacted. When encapsulating the cGNRs and applying etched end contacts, only one type of contact (the end contact) is established.

Opposing to these very appealing properties of the etched end contacts stands the complicated fabrication process. Due to the high precision that is needed for the contact placement (including the low spacing between the contact fingers), it is not possible to use the standard fabrication recipe for encapsulated graphene for the cGNRs. Usually, the EBL resist used as hard mask during the etching process is removed and the sample is cleaned to remove etching residues. Subsequently, the sample is again covered with resist, EBL is performed and the sample is metalized. Here, the structures are so fine that it is impossible to align the lithographies for etching and metalization. Therefore, the metalization was performed directly after the etching step, omitting resist removal and cleaning of etching residues in between.

Despite the delicate fabrication process, some first devices with edge contacts could be produced. Unfortunately, the samples did not yield reproducible I-V-curves, but failed after only a few voltage sweeps. Therefore, no gate dependence could be tested.
For the encapsulation process, only 4-cGNRs were used since they exhibited the longer single ribbons.
Cr/Au turned out to be the best contact material for the end contact configuration. In two out of three Cr/Au contacted devices, a drain current could be measured whereas not a single Pd end contacted device was functional.

Fig. 3.23 shows the I-V-characteristics for end contacted 4-cGNRs on hBN (sample **4-4**). These cGNRs were not fully encapsulated, but the contacts were fabricated using the same procedure as for encapsulated cGNRs, i. e. the cGNRs were etched and end contacted (see inset for contact configuration). Cr/Au served as contact material for this device.
One can see that the I-V-curve has a rectifying character. On the positive voltage side, the drain current increases exponentially reaching µA values. For this voltage range, the experimental data were fitted with the TFE model. Despite the noisy data, the fit matches quite well and yields a relatively low Schottky barrier of $\Phi_b \approx (90 \pm 130)\,\mathrm{meV}$. The shape parameter $E_{00} = 7\,\mathrm{mV}$ is comparable to the ones of the standard-contacted 4-cGNR devices.
On the negative voltage side, no stable current is transmitted.
The curve is quite noisy for source-drain voltages $|V_{sd}| > 3.5\,\mathrm{V}$ which is probably due to bad contact between metal and cGNRs. Especially on the negative voltage side, there are some spikes in the curve where I_d seems to follow an exponential behavior, but then the current drops back to nearly zero. This could be due to rearrangement between cGNRs and metal in the contact area or the fact that the contact between metal and cGNR gets lost due to the increasing source-drain voltage. The sweep was performed starting at $+5.5\,\mathrm{V}$ down to $-7\,\mathrm{V}$.

The rectifying behavior might be explained by different Schottky barrier heights at

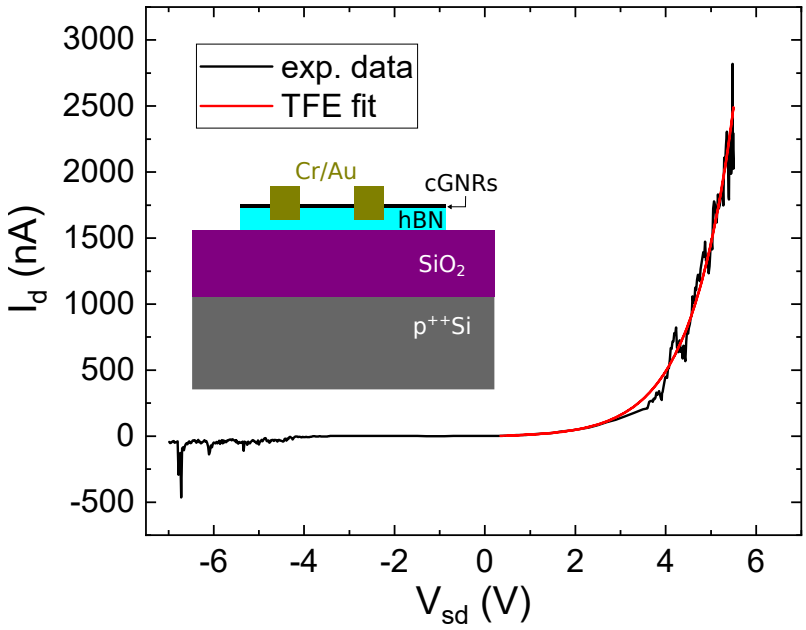

Figure 3.23.: **End contacted 4-cGNRs on hBN.** I-V-curve of sample **4-4** exhibiting high current on the positive voltage side. Red line is the TFE fit for this region. The inset illustrates the contact configuration.

both cGNR ends or by destruction of the cGNR–metal contacts during the voltage sweep.
If the barrier at one contact is substantially higher than at the other one, it has the following effect (c. f. also section 3.1.3): When the bias voltage is applied such that the contact with the higher barrier is in forward direction, the current is limited by the lower Schottky barrier contact in reverse direction. If this second barrier is low enough, a notable current can flow. When the bias voltage, however, is applied in opposite direction, i. e. such that the higher barrier contact is in reverse direction, the current flow can be completely suppressed.

A situation that might cause this behavior is sketched in Fig. 3.24. When the contact metal is evaporated under an angle, the EBL resist casts a shadow leading to (almost) no metal deposition at one side of the etched trench. This effect is enhanced by the undercut of the resist that is caused by the proximity effect during EBL. For one side of the contact (blue circle), this has no negative effects. But for the other side (red circle), the shadow cast by the resist leads to a gap between metal and cGNRs. Since the evaporation process takes place at room temperature, the incident hot metal atoms can still diffuse over the surface and close the gap between metal and cGNR—as depicted in Fig. 3.24 (a). For this reason, the non-etched and non-encapsulated cGNR devices from the previous section showed a current response for both bias voltage polarities.
When an etching step is involved, however, the situation gets more complicated, as

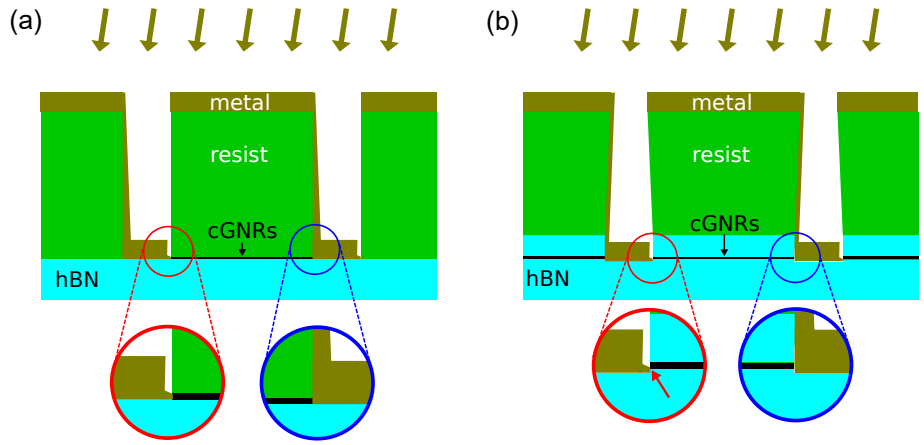

Figure 3.24.: **Metalization of a tilted sample.** Scheme illustrating that a slight tilt in the evaporation angle can lead to a bad contact between metal and cGNRs. Situation for (a) standard and (b) encapsulated and etched devices.

depicted in Fig. 3.24 (b). Since the etching rate is highly non-linear and changes during the etching process, it is almost impossible to stop the etching exactly at the point when the upper hBN flake is etched away and the cGNRs are uncovered. Instead, a (more or less) small trench is etched in the bottom hBN flake, creating a step edge between the bottom of the etching trench and the encapsulated cGNRs. This step edge could prevent proper contact formation at one side of the cGNRs (see red arrow). The finite size of the evaporation source, however, leads to a widening of the incident metal atom stream. Thus, there is still a chance that contact to the cGNRs can be made.

An alternative explanation might be that the Cr used as adhesive layer in the metalization process could oxidize before the Au is evaporated[13]. Thus, an additional tunneling barrier would arise at the interface between cGNRs and metal contact. This increases the thickness of the tunneling barrier that electrons have to penetrate to participate in the current transport.

Fig. 3.25 finally shows the I-V-characteristics of a fully encapsulated 4-cGNR device with Cr/Au end contacts (sample **4-5**). This device also exhibits rectifying behavior and therefore only the positive voltage side of the I-V-curve is displayed. The voltage sweep was performed from 0 V to 4 V, this voltage was kept for some seconds, and then lowered back to 0 V. The sweep direction is indicated with arrows in the graph. In the forward sweep direction, the drain current stays close to zero up to a voltage of roughly 3.5 V and then suddenly jumps to 170 nA. A possible explanation for this behavior is that a small layer of resist residues, etching residues or contamination

[13]The oxidation might happen directly after Cr deposition (although the vacuum in the evaporation chamber is in the range of 10^{-7} mbar and Au evaporation starts only a few minutes after Cr deposition) or the Cr might already be partially oxidized before deposition on the surface.

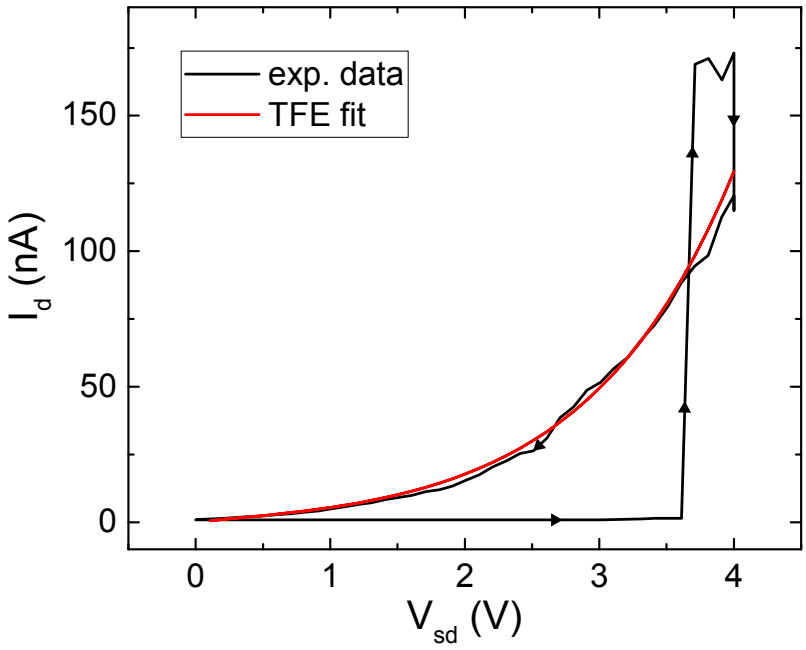

Figure 3.25.: **hBN encapsulated 4-cGNRs.** I-V-curve of sample **4-5**. The current follows an exponential trace only for the backsweep direction. The red line is the TFE fit to this region.

from air stayed between cGNRs and metal before starting the measurement. When ramping up the voltage, this layer could have been burned away which caused a sudden increase in the drain current.
On the back sweep, the drain current has an exponential decay and can be fitted with the TFE model. It is not obvious why the drain current dropped by approximately 50 nA before starting the back sweep. A possible reason is that—while keeping the current at roughly 170 nA for some seconds—some of the 4-cGNRs could have been damaged or the contact to some of them might have got lost. The TFE fits yield a Schottky barrier height of $\Phi_b \approx (110 \pm 140)$ meV, being slightly higher than for sample **4-4**. Still, the Schottky barrier is lower than for most standard-contacted 4-cGNR devices.

3.7. Conclusion and outlook

Even though there are still some difficulties in the fabrication of high quality contacts, the approach presented here seems suitable to characterize the adsorption and electronic properties of solution-processed cGNRs. hBN as a flat and clean substrate plays a key role in this regard.

Concerning the standard-contacted samples, the 6-cGNR devices have mostly sym-

metric I-V-curves, whereas the presented 4-cGNR devices tend to be more asymmetric. In general, TFE fitting yielded higher Schottky barriers for the 4-cGNRs. The strong variation in Schottky barrier heights is presumably due to a differing number of contacted cGNRs or different levels of contamination between cGNRs and metal contacts. The 6-cGNRs were more stable and transport measurements could be performed repeatedly without changing the shape of the I-V-curves. For the 4-cGNRs, on the other hand, the devices stopped working after only a few runs.

Despite the challenging fabrication process, encapsulated 4-cGNRs could be successfully contacted. Cr/Au appears to be a promising contact material for the encapsulated cGNRs. The end contacts, however, could not fulfill the expectations regarding reliability and higher sample quality so far. Possibly, a layer consisting of residues from EBL resist or etching, or contamination from air could have formed between cGNRs and metal. An additional gentle etching step with O_2 plasma before the metalization could possibly reduce residues and improve the contact quality. Furthermore, letting the sample rotate during the metalization might yield more homogeneous contacts to both cGNR ends.

An option for achieving better contact to non-encapsulated cGNRs is to first structure the contacts on the substrate, and then deposit the cGNRs. However, simply pre-structuring metal contacts on hBN with the help of EBL and subsequent cGNR deposition was not possible, because residues from the EBL resist remained on the surface hindering the adsorption of cGNRs on hBN.
A workaround might be to use (fewlayer) graphene contacts. One can fabricate very tiny gaps in the nm range into graphene sheets with the help of electroburning [123, 124]. During this process, a relatively high current is sent through a graphene sheet[14]. The graphene gets hot and a chemical reaction of carbon atoms with oxygen is triggered. This leads to local breakage of the graphene sheet, leaving a small gap between the carbon atoms. Solution deposited cGNRs could bridge this gap. Through the introduced heat of the electroburning process, the graphene sheet gets also cleaned from EBL resist that is used for pre-structuring and contact fabrication. This technique was already successfully applied to make contact to electro spray deposited 4-cGNRs [69] and bottom-up synthesized GNRs [125].

Another possibility to obtain small gaps in graphene sheets is to cut trenches into freshly exfoliated graphene with the help of a FIB. The beam diameter of the FIB can reach down to a few nm. Following this method, no EBL resist has to be used.

To tackle the issue of lacking gate dependence, one could decrease the distance from the back gate to the cGNRs. One possible approach is to use exfoliated (fewlayer) graphene as a back gate electrode and place hBN on top of it. Then, the distance between back gate and cGNRs is determined by the thickness of the bottom hBN flake which is usually in the range of 10–40 nm.

[14] Sometimes a pre-structured narrow point is added to ensure the electroburning takes place at a specific point.

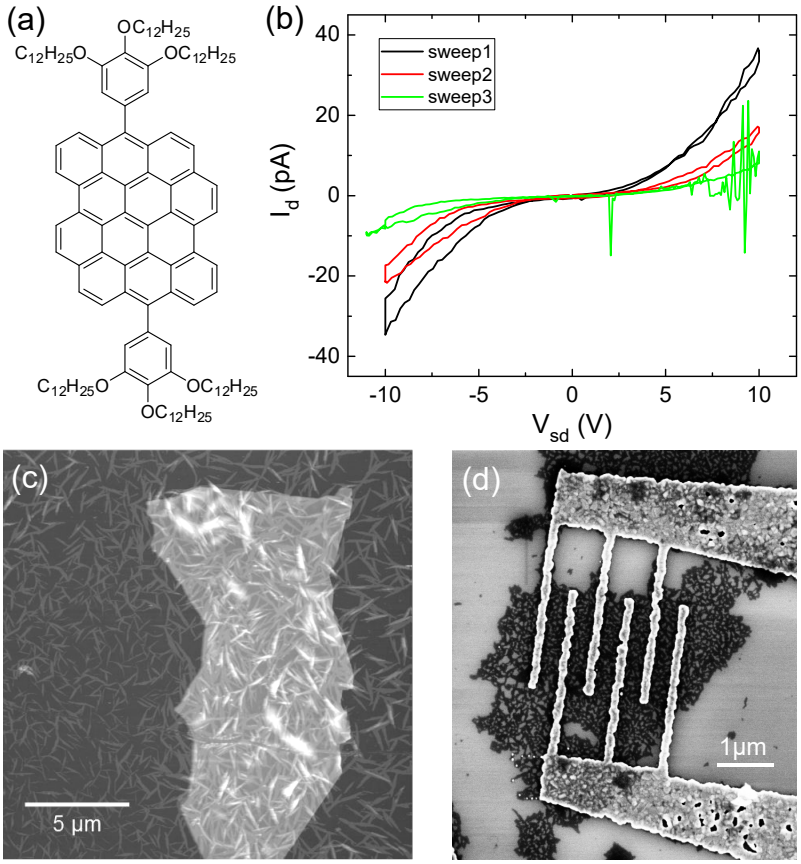

Figure 3.26.: **Towards organic electronics.** (a) Chemical structure of DBOV-TDOP molecules. (b) Three consecutive I-V-sweeps of a contacted molecule film. (c) AFM topography image of DBOV-TDOP molecules on hBN and SiO_2. (d) SEM image of Pd contacted molecule film.

Apart from the investigation of cGNRs, the methodology presented in this chapter is also suited to step further in the direction of organic electronics.
Fig. 3.26 sums up some first results on this path. 3,4,5-tridodecyloxyphenyl-dibenzo-[*hi,st*]ovalene (DBOV-TDOP) molecules (see Fig. 3.26 (a)), synthesized from the group of Akimitsu Narita at the Max Planck Institute in Mainz [126], were dispersed in solution and drop-cast onto exfoliated hBN on a Si/SiO_2 substrate. AFM images (see Fig. 3.26 (c)) reveal that the molecules stick not only to the hBN but also to the SiO_2 surface. Fig. 3.26 (d) shows an SEM image of Pd fingers contacting a patch of DBOV-TDOP molecules on SiO_2. I-V-curves of these molecules were taken and are presented in Fig. 3.26 (b). The measured current is very low and drops from run to run, showing that the contact quality still needs to be improved.

4. Tailoring end states of graphene nanoribbons by magnetic dopants

As was shown in the previous chapter, surface contamination can hamper the exploration of the intrinsic properties of GNRs. Therefore, it is desirable to minimize the amount of adsorbates on the sample. One possibility to achieve this goal is to directly synthesize the GNRs under UHV conditions. Like this, the GNRs are not exposed to any solvents which might leave residues on the GNRs.
In this chapter, 7-aGNRs are synthesized on a Au(111) surface in an UHV-STM chamber using the recipe of Cai *et al.* [47]. Subsequently, magnetic Co atoms are evaporated onto the sample. The Co atoms exhibit a Kondo effect on the Au surface. With the help of an STM tip, the Co atoms are manipulated towards the 7-aGNR, whereupon they get buried underneath the GNR. The interaction between the 7-aGNR and the Co states is investigated using scanning tunneling spectroscopy. Different intercalation sites of the Co atom are studied. Density functional theory (DFT) and tight-binding calculations are compared to the experimental findings.

The measurements in this chapter were done together with Sujoy Karan and the DFT calculations were performed by Tobias Frank.

4.1. Theoretical basics

First, the electronic structure of GNRs shall be reviewed. Special attention is paid to the states emerging from the zigzag configuration of graphene edges. Furthermore, STM imaging with a CO-terminated tip is briefly discussed. The difference in STM contrast formation in comparison to imaging with a pure metal tip is explained. Last, the Kondo effect is introduced and a short overview of recent experiments is given.

4.1.1. Electronic states in GNRs

One of the most appealing properties of GNRs for possible applications is their tunable band gap. Depending on the geometrical width, the edge shape, but also the environment, large variations in the electrical properties of GNRs are possible.

7-aGNRs, for instance, were shown to exhibit a band gap of 2.3 eV–2.7 eV when investigated on a Au(111) surface by means of STS [28, 127]. Slight variations of reported band gap values result partly from the varying definitions of the band gap. While Ruffieux *et al.* [28] measured the gap as the distance between the onsets of conduction and valence bands, Koch *et al.* [127] defined the gap as peak-to-peak distance between resonances at the conduction and valence band edges, thus leading to higher values.
Additionally, shorter GNRs have slightly higher band gap values due to additional quantum confinement [128].
However, the experimental values are substantially smaller than the theoretically predicted 3.8 eV for a free standing 7-aGNR obtained by first-principles calculations [8]. The lower band gap seen in experiments can be ascribed to screening by the metal surface [28]. The placement of a GNR onto a metal surface leads to a surface polarization which acts back on the energy levels of the GNR and lowers the band gap [129, 130].
Separating the GNRs from the metallic substrate by introducing an insulating spacer layer leads to the decoupling of the electronic structures of GNRs and conductive substrate. It was shown that the experimental band gap of 7-aGNRs increases from 2.4 eV to 2.7 eV upon intercalation of a monolayer of Si atoms between the Au(111) substrate and the 7-aGNRs [131]. In another experiment, 7-aGNRs were manipulated onto NaCl monolayers on a Au(111) surface with the help of a STM tip [132]. Here, the measured band gap of the decoupled 7-aGNRs was found to be 2.9 eV.
These experimental findings are in accordance to calculations addressing the role of a substrate layer for the band gap formation [130].

The reported band gap values, both experimental and theoretical, classify 7-aGNRs clearly as semiconductors, if not as insulators. One possibility to get a lower band gap is to use GNRs with zigzag edge configuration. According to simple tight-binding calculations, zGNRs are always metallic [13]. Taking into account electron-electron interactions, however, leads to a band gap opening in zGNRs [11, 133]. An additional peculiarity of zGNRs is that they are predicted to host magnetic moments [12, 13].
The zigzag configuration of the carbon atoms along the zGNR edges gives rise to flat bands located at the Fermi level in the band structure, as was shown by different levels of theory [12, 134]. This behavior is not unique to carbon, but appears generally in honeycomb structures, when the edge atoms see a different chemical environment than their bulk counterparts [135]. For the zGNRs, the inner carbon atoms bond to three other carbon atoms, whereas for the edge atoms, one bonding partner is replaced by a hydrogen atom.
The flat bands lead to a high DOS at the Fermi level and the corresponding wave functions are highly localized at the zGNR edges [12, 13, 134].
The high localization of the electrons at the edges longs for the inclusion of electron-electron effects. Therefore, Coulomb interaction was integrated into the theoretical

investigations of zGNRs [8, 11, 36]. As a result, the opening of a band gap was reported and a special ordering of the spins was obtained: The electrons favor a ferromagnetic (FM) ordering along the zigzag edge [11, 136] which can be rationalized in the framework of the Stoner criterion [137]. Since the flat bands lead to a low kinetic energy of the electrons, the gain in magnetic energy by FM ordering can overcome the cost to align the spins and therefore the FM ordering causes a lowering of the total energy.
Considering the spin orientation of opposing zGNR edges, it turned out that an antiferromagnetic (AF) ordering is energetically most favorable [138]. That means that in the ground state all spins along one zigzag edge are aligned in the same direction, but opposite to the spins at the other zigzag edge. This is because the atoms of opposing zGNR edges belong to different sublattices. That leads to a constructive interference effect of the magnetic tails of the polarized edge states in the zGNR center which enhances the magnetic moments in the center for the AF configuration (see Fig. 4.1 (a)). In the case of FM ordering across the edges, destructive interfer-

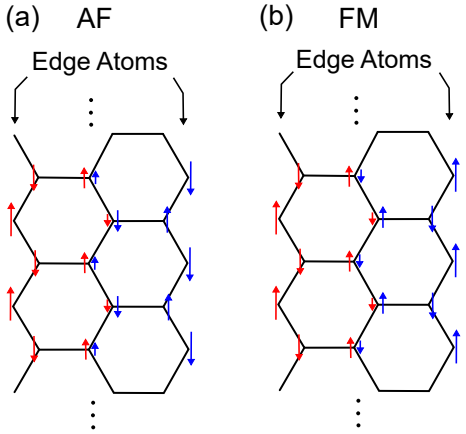

Figure 4.1.: **Interedge coupling in zGNRs.** AF (a) and FM (b) coupling of edge states across a narrow 3-zGNR. Red and blue arrows represent sign and magnitude of magnetic moments along the zigzag edges and their tails decaying towards the GNR center. After [136].

ence takes place in the zGNR center (see Fig. 4.1 (b)), yielding a lower energy gain [136]. Therefore, the total energy of the AF configuration is lower than that of the FM case, but only by a few meV per carbon edge atom [136, 138].
The AF spin alignment across the zGNR leads to a cancellation of the magnetic moments of opposing edges and renders the zGNR spin neutral. This is in accordance to Lieb's theorem for bipartite lattices which predicts magnetic moments only for an imbalance of sublattice sites [139].

Interestingly, the staggered sublattice potentials from magnetic ordering open a gap in the band structure for the AF ground state whereas the FM configuration is metallic [11, 36, 133, 138].

To investigate the zigzag edge related states experimentally, STS is frequently used. The real-space resolution of an STM allows to probe states at specific sample positions (i. e. the zigzag edge sites) and acquiring dI/dV spectra allows to determine the corresponding local density of states (LDOS).
Therefore, the enhanced LDOS at the Fermi level as well as the splitting of the

zero-energy peak can experimentally be measured by means of STS. The observed spectroscopic features of zigzag edge related states, however, vary.
The presence of edge states was shown for zigzag edges at stepped HOPG surfaces where they manifest as a peak in dI/dV spectra at a voltage of $-30\,\mathrm{mV}$ [140]. No spin splitting was found in this case.
First observations of spin-split edge states were made at the zigzag cusps of chiral GNRs on a Au(111) surface made out of unzipped CNTs [141]. Here, an energy splitting of 25–50 meV was reported for GNR widths ranging from 8–20 nm and an inverse correlation between edge state splitting and GNR width was shown.
A larger splitting, namely up to 0.3 eV, was found for zGNRs that were cut by STM lithography out of a CVD grown graphene sheet transferred onto a Au(111) surface [142]. Furthermore, the authors observed a sudden transition from semiconducting to metallic GNR behavior as the GNR width was increased above 7 nm which was rationalized by a transition from antiferromagnetic to ferromagnetic spin coupling across opposite zigzag edges.
Li *et al.* [143] also described an inverse relation between band gap and zGNR width, using zGNRs that were etched out of graphene on SiC. They reported band gap values of up to 1.1 eV for 1.1 nm wide zGNRs and a constant gap of 0.12 eV for zGNRs broader than 3 nm.
However, direct evidence for the magnetic moments the edge states are carrying is still lacking.

Nakada *et al.* [12] predicted that as few as three zigzag cusps are enough to give rise to edge states.
The chemical structure of the precursor molecules used to synthesize 7-aGNRs [47] produces not only atomically perfect armchair edges along the ribbon, but also yields three zigzag cusps at its short edges. Therefore, the 7-aGNR should host electronic midgap states localized at the zigzag edges.

Indeed, the occurrence of an end state[1] was reported for 7-aGNRs on Au(111) [127, 144]. dI/dV spectra taken at the corners of the 7-aGNR exhibit a peak at a voltage of approximately 30 mV which is absent when taking spectra along the armchair edges or the 7-aGNR center. It is only present at the zigzag edge and decays within a distance of roughly 1.5 nm from the zigzag termini [132]. Therefore, this peak is ascribed to the 7-aGNR end state and often referred to as Tamm state [127, 145].
However, no splitting of the end state was observed. For magnetism induced by adatoms on extended graphene it was shown that doping can cause a transition from a magnetic state with peak splitting to a non-magnetic state with a single, degenerate energy level [146]. Also for GNRs it was predicted that the coupling between the edge localized magnetic moments can be controlled by doping the GNR and that high doping levels can quench the magnetic moments [147, 148]. 7-aGNRs on a Au(111) substrate were reported to be hole doped [144] leading to a shift of the

[1] Due to their existence at the short zigzag ends of the 7-aGNRs, the edge states will be referred to as end states here.

end state peak above the Fermi level[2], arousing the assumption that the magnetic ordering is quenched in this configuration. Ijäs *et al.* [151] found that even doping by a single charge carrier is enough to quench the AF order.
On the other hand, the peak splitting for charged 7-aGNRs is very small (in the order of meV) [144, 151], so it might also be that the splitting is present, but can not be observed with the given experimental resolution.

When decoupling the 7-aGNRs from the metallic Au(111) substrate by manipulating them onto NaCl monolayers, Wang *et al.* [132] reported a splitting of the end state peak of 1.9 eV. This is presumably due to a reduction of the substrate work function caused by the NaCl monolayer [152]. Thereby, the decoupled 7-aGNRs are not hole doped anymore (or only slightly), but neutral instead, thus facilitating an AF ordering and correspondingly the opening of a gap.
It should be stressed, however, that this splitting is of Coulombic nature. The magnetic splitting between the AF, singlet-like ground state and the FM, triplet-like configuration is much smaller and could be observed with an applied magnetic field [153].

Su *et al.* [154] reported a splitting of the zigzag end state peak of a 7-aGNR on Au(111) of roughly 50 mV upon the fusion of a manganese phthalocyanine (MnPc) molecule to the GNR end. The splitting could be switched off by adsorbing a H atom on top of the MnPc. In that case, differential conductance spectra showed a single end state peak located at −150 mV instead. Apparently, the MnPc changes the doping of the 7-aGNR zigzag edge from hole doped (end state peak at 30 mV) in the pristine case over nearly neutral (split end state peak) for fused MnPc to electron doped (end state peak at −150 mV) for H adsorption on the fused MnPc.

Apart from the peak in dI/dV spectra, the end state manifests itself also directly in STM topography images. An example is given in Fig. 4.2. Panel (a) sketches the atomic structure of a 7-aGNR with a length of roughly 4.3 nm. All C atoms of the left zigzag terminus are saturated with a single H atom. The middle of the right zigzag terminus, on the other hand, hosts two H atoms. In the STM image in panel (b) one can see that the left zigzag terminus appears a little broader than the middle part of the 7-aGNR and exhibits a finger-like structure when imaged with a metal tip [127, 128, 144, 155].
It should be noted that the end state is not present for all 7-aGNR ends on Au(111). A fraction of the 7-aGNRs is lacking the finger-like structure and the 7-aGNR termini look rather rectangular instead, like the right end of the GNR shown in Fig. 4.2 (b). This is accompanied by a lack of an end state related peak in dI/dV spectra. The featureless 7-aGNR end appearance was—at least for some cases—shown to stem from double hydrogenation of the middle carbon atom of the zigzag edge [128, 155]. Since an additional hydrogen atom at the zigzag edge lowers the total energy of the 7-aGNR, and free hydrogen atoms are present on the surface due to the ribbon growth process, some 7-aGNR termini naturally host an additional hydrogen atom.

[2]This can be explained by the higher work function of Au with respect to graphene [49, 149, 150].

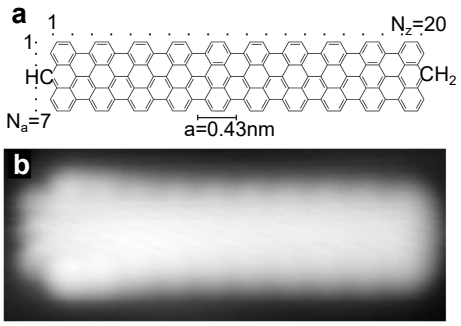

Figure 4.2.: **7-aGNR.** (a) Atomic structure of a 7-aGNR with an additional H atom at the middle of the right zigzag edge. (b) STM topography image of such a GNR. At the left zigzag terminus, a finger-like structure related to the end state can be seen which is absent at the right terminus. Image adapted from [128].

This extra hydrogen atom, however, unbalances the zigzag configuration at the edge and suppresses the formation of a related end state. By applying a voltage pulse with the STM tip, the additional hydrogen atom can be removed and the end state can be restored [155].

The effect of different GNR zigzag end terminations can be rationalized by looking at the electronic structure of GNRs given by Clar's theory [156, 157]. According to the Clar rule, the Clar structure of a hydrocarbon with the highest number of aromatic sextets is most stable and most representative of its π-electron structure. In Fig. 4.3 (a) the Clar structure of a CH_2-terminated 7-aGNR can be seen. This structure is unique and accommodates two aromatic sextets per unit cell.
For CH-terminated 7-aGNRs, on the other hand, there exist more possibilities to draw a Clar structure. Two of these possibilities are given in Fig. 4.3 (b)[3]. Structure

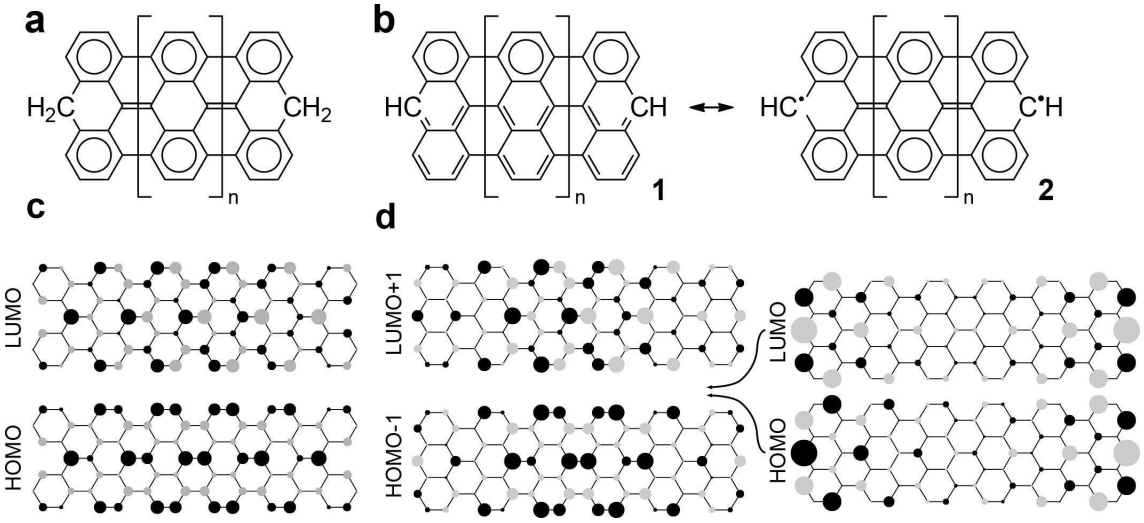

Figure 4.3.: **Electronic structure of 7-aGNRs.** (a) Clar structure for CH_2 termination. (b) Clar structures for CH termination. (c) Tight-binding orbitals of a CH_2-terminated 7-aGNR consisting out of 6 anthracene rings. The size of the circles is proportional to the electron density and the color indicates the sign of the wave function. (d) Same as in (c), but for CH-termination. Image from [128].

1 shows the case of normal bonding for single H termination. Only one aromatic sextet per unit cell exists. This makes this structure less stable than the CH_2-terminated case.
In the singly hydrogen terminated case, a higher number of aromatic rings—namely two per unit cell—and therefore higher stability, can be reached by breaking a π-bond at the middle of the zigzag edge and a rearrangement of double bonds. This scenario can be seen in structure **2**. In this way, a radical is created and the 7-aGNR hosts an unpaired electron at each zigzag end (illustrated as a dot close to the C atom in the Clar formula).
Thus, the atomic configuration at the GNR end is a competition between the energy gain by aromatic stabilization—favoring structure **2**—and the cost of breaking a π-bond—favoring structure **1**. This competition is dependent on the ribbon length and structure **2** is dominant for 7-aGNRs longer than 3 anthracene units [128].

Talirz *et al.* [128] performed tight-binding calculations for GNRs with both, doubly and singly hydrogenated zigzag ends. The frontier orbitals are shown in Figs. 4.3 (c) and (d). For the CH_2-termination in (c), the central carbon atom at the zigzag edge is bound to two hydrogen atoms and therefore does not contribute an electron to the π-system. Accordingly, the middle carbon atom is simply removed within the tight-binding approximation—corresponding to a cove defect at the zigzag edge. The electron density is mostly distributed over the central part of the GNR.
For the CH-termination, on the other hand, each GNR end accommodates an unpaired electron, giving rise to a HOMO (highest occupied molecular orbital) and LUMO (lowest unoccupied molecular orbital) that are localized near the zigzag termini and decay exponentially towards the GNR center—and correspond to the previously discussed end state of zigzag edges.

Due to the fact that 7-aGNRs are well studied, easy to synthesize and offer atomically precise edges with short zigzag cusps at their termini, they pose a viable test ground to further investigate the zigzag edge related end states in graphene structures. Especially the circumstance that the end states are energetically separated from the bulk states of the 7-aGNRs seems beneficial [132].

4.1.2. STM imaging with a CO-terminated tip

To achieve atomic resolution in AFM experiments, often a CO molecule is attached at the apex of the tip [158]. In general, tip termination strongly influences the mechanism of image contrast formation in STM experiments. Fig. 4.4 (a) displays experimentally recorded (top row) and DFT simulated (bottom row) dI/dV maps of a 7-aGNR terminus. Panel (I) shows an image recorded with a pure metal tip. Five fingers can be seen at the GNR end. The DFT simulations for a metal tip in panel (II) confirm this structure. In panel (III), a GNR terminus imaged with a

[3]For more possible configurations see, e. g., [155].

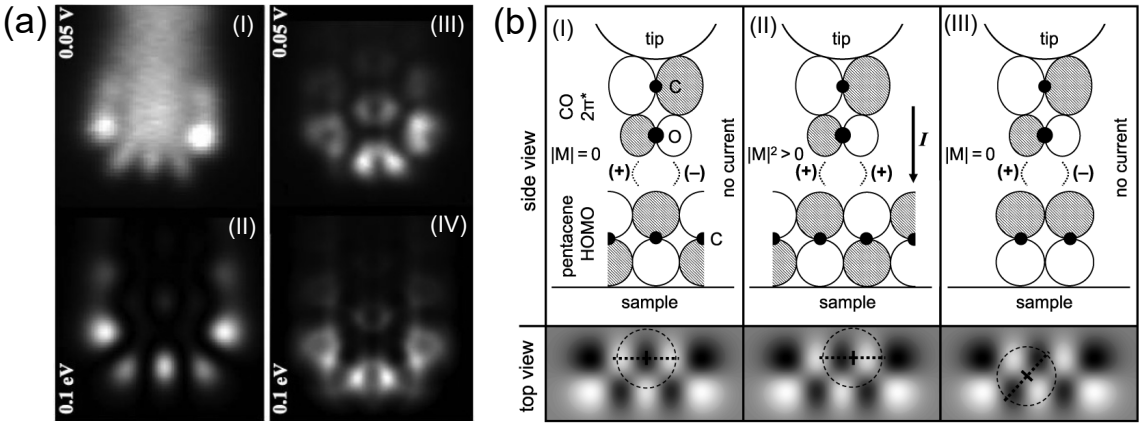

Figure 4.4.: **Imaging with *p*-wave STM tip.** (a) Experimental dI/dV maps of a 7-aGNR terminus imaged with a pure metal tip (I) and a CO-terminated tip (III). For comparison, DFT simulations of the same configurations are shown in (II) and (IV). Images from [151]. (b) Schematics for tunneling between the orbitals of a CO-terminated tip and the HOMO of a pentacene molecule. More details are given in the text. Images from [159].

CO-terminated tip is displayed. Here, instead of five fingers three V-shaped features pointing away from the 7-aGNR can be observed. This observation can also be made in the DFT simulated image of panel (IV).

The reason for the different contrast is the different orbital character of the CO-terminated tip compared to the pure metal tip. Whereas the metal tip has mainly s-wave character, for the CO-terminated tip mostly p_x and p_y orbital of the CO molecule contribute to the imaging contrast.
Fig. 4.4 (b) shows a schematic for the contrast formation for imaging the HOMO of a pentacene molecule with a CO-functionalized tip. In the bottom row, top views of the pentacene HOMO are shown. Black and white color correspond to different signs of the wave funtion. The dotted line indicates the cross section of the sample that is illustrated in the top row. There, a side view of an STM tip with a CO molecule attached is depicted over some horizontally aligned carbon atoms of the pentacene molecule. The orbitals for CO and pentacene are depicted by large spheres and the colors correspond to the sign of these orbitals.
For panel (I), the CO tip is positioned above the center of a pentacene orbital lobe. Due to symmetry reasons, the contribution of positive and negative CO orbitals to the tunneling current cancel out each other and the matrix overlap integral $|M|$ is zero, meaning no current flow.
In the case of panel (II), the tip is located between two lobes of the pentacene HOMO. In this situation, the symmetry between CO orbitals and pentacene orbitals matches and current can flow.
Panel (III) depicts the case in which the tip is placed above the crossing of two nodal

planes. Opposing orbital lobes do not exhibit a phase change. Therefore, positive and negative contributions of the CO tip cancel out and no current flows.
If the HOMO of pentacene was imaged with a pure metal tip, bright features—meaning current flow—at the positions of the lobes shown in the bottom row of Fig. 4.4 (irrespective of their sign) would be measured, separated by dark areas of no current flow. In contrast, an image obtained for a CO-terminated tip would exhibit bright features at the nodal planes between two lobes of the HOMO. Further details can be found in [159].
To sum up, since the p-orbitals have a nodal plane at the maximum position of the s-orbital, the contrast formation in imaging is—roughly speaking—inverted [159].

4.1.3. Kondo effect

Next, another zero-bias resonance will be discussed, namely the Kondo effect. The Kondo effect arises when magnetic impurities are added to a metal and is a long-studied phenomenon. The structure of this section is mostly following the review of Ternes [160].

When a normal metal is cooled down, its resistance decreases due to freezing of lattice vibrations at lower temperatures. Impurities and structural defects in the metal lead to a saturation of the resistance at a certain value. In the 1930s, experiments on metals containing magnetic impurities revealed that the resistance increases again below a certain threshold [161]—as illustrated in Fig. 4.5 (a). This effect was explained in 1964 by Jun Kondo [162] by an increased effective scattering cross section for conduction electrons due to the magnetic impurities.
The process leading to the increase in resistance is sketched in Figs. 4.5 (b) and (c) and takes place only below a certain temperature, the so-called Kondo temperature T_K. Above T_K, the conduction electrons of the metal of different spins (represented by small arrows) move around and scatter at the magnetic impurity (blue sphere, spin indicated by large arrow). Below T_K, the conduction electrons of the metal form the so-called Kondo screening cloud around the magnetic impurity which screens the magnetic moment of the impurity and increases the scattering cross section.
Renewed interest [163] in the Kondo effect arose in the late 1990s after the first experimental demonstration of the single-impurity Kondo effect in quantum dots [164] and by means of STS [165, 166].

Although the Kondo effect is a complex phenomenon, it can be described in a simplified manner with the Anderson single-impurity model [168]. In this model, the full electronic structure is simplified by assuming only a single orbital state, which can be empty or filled with one or two electrons. Fig. 4.5 (d) sketches this situation for a magnetic atom on a metal surface. The states in the metal are filled up to the Fermi level E_F. The singly occupied state of the magnetic impurity is located at an energy ε_i below the Fermi level and separated by the Coulomb repulsion energy U from the state occupied with two electrons. Hybridization between electronic states

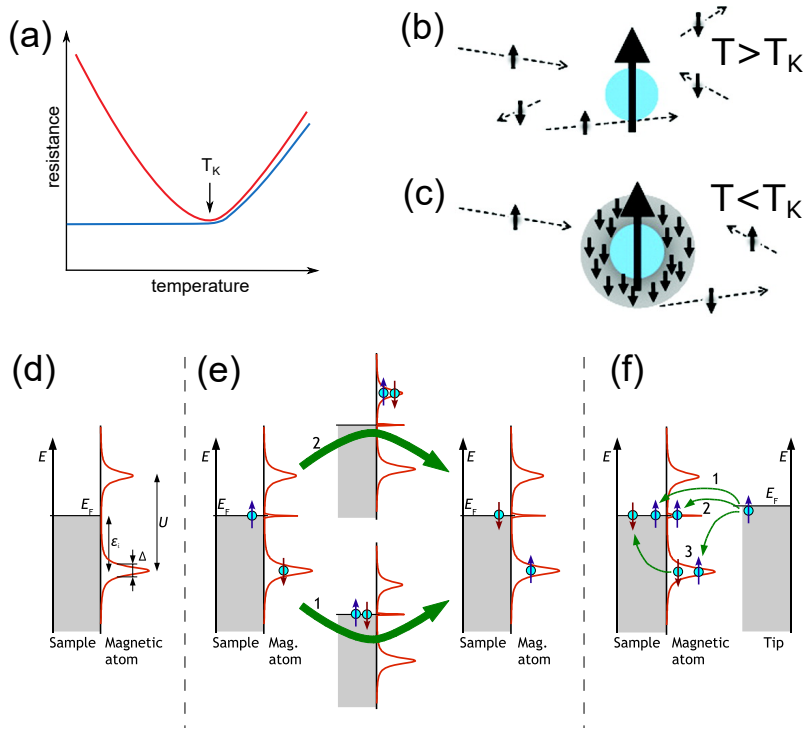

Figure 4.5.: **Kondo effect.** (a) Resistance behavior of a normal metal (blue) and a metal with magnetic impurities (red) upon sample cooling. T_K denotes the Kondo temperature. (b) Magnetic impurity surrounded by conduction electrons above T_K. (c) Formation of screening cloud below T_K. (d) Anderson single-impurity model: Magnetic adatom sitting on a metal surface. (e) The spin of the singly occupied impurity state can be flipped via a virtual state in which the adatom is either empty (path 1) or doubly occupied (path 2). This process gives rise to a sharp resonance at the Fermi level, the so-called Kondo resonance. (f) Electrons from an STM tip can tunnel directly into empty sample states (1), into the Kondo resonance (2) or via a spin-flip through the magnetic impurity (3). Images adapted from (a) [163], (b) and (c) [167] and (d)–(f) [160].

in the host metal and the impurity lead to the peak broadening Δ.
Fig. 4.5 (e) depicts the situation where the magnetic impurity state is singly occupied with its electron having a certain spin direction (left panel). Classically, one has to pay an energy to bring in a second electron or remove an electron from the state. The cost is at least $|\varepsilon_i|$ to get the electron from the impurity into an empty metal state and $|U - \varepsilon_i|$ to bring in another electron from an occupied state in the metal into the impurity state. But quantum mechanically, due to the Heisenberg uncertainty principle, an electron can tunnel out of the impurity for a very short time $t \approx h/|\varepsilon_i|$, forming a virtual state (middle panel, path 1). During this timescale (in the order of fs), an electron from the metal can tunnel back into the empty impurity

state[4]. During this process, the spin of the electron on the impurity can be flipped (right panel). The coherent superposition of many such events gives rise to a sharp resonance right at the Fermi level, called Kondo resonance. Since the interaction between many particles has to be considered in this process, the Kondo resonance is a many-body phenomenon. The conduction electrons from the metal and the electron from the impurity form a many-body singlet.

The width of the Kondo resonance is temperature dependent. At a system temperature of $T = 0\,\mathrm{K}$, the Kondo temperature can be extracted from the energy width of the Kondo resonance by [160]

$$T_K = \frac{\mathrm{FWHM}}{2k_B} \tag{4.1}$$

where FWHM is the (temperature dependent) full width at half maximum of the resonance and k_B the Boltzmann constant.
This result can be expanded in the framework of the Fermi liquid theory to higher temperatures (as long as $T \ll T_K$) [160, 169, 170]:

$$\mathrm{FWHM} = \sqrt{(\alpha k_B T)^2 + (2k_B T_K)^2} \tag{4.2}$$

with α being a parameter. Theory predicts $\alpha = 2\pi$, while experimentally values for α around 5 were obtained [170–172].
It is worth noting that different forms of Eq. 4.2 can be found in literature which is due to different definitions of T_K [173].

STS appears to be a suitable tool to investigate the Kondo effect, since occupied and unoccupied states close to E_F can be sensitively probed and due to its high spatial resolution. In STS, the Kondo resonance can appear as a peak, a dip or can have an intermediate asymmetric form [160, 174]. The line shape depends on the tunneling path the electrons take from the STM tip to the substrate.
Three different paths are sketched in Fig. 4.5 (f). The electrons can tunnel directly from the tip into empty bulk states (path 1). They can also tunnel into the Kondo resonance close to E_F (path 2). Or they tunnel via the state of the magnetic atom, which might include a spin flip (path 3).
Since tunneling is a coherent quantum mechanical effect, there will be interference between tunneling paths 1 and 2. Path 3 is not contributing to the interference because the electron ends up in a different spin state.
The interference of the tunneling channels leads to a Fano line shape [175] of the differential conductance spectrum which can be described by

$$dI/dV = A + B \cdot \frac{(q + \varepsilon)^2}{1 + \varepsilon^2} \tag{4.3}$$

[4] Analogously, a second electron can tunnel into the impurity for $t \approx h/|U - \varepsilon_i|$ and one of the two electrons on the impurity can tunnel back to the metal within this time (path 2).

with the normalized energy

$$\varepsilon = \frac{2(eV - E_K)}{\mathrm{FWHM}}. \tag{4.4}$$

A and B are fitting parameters for the background and the peak amplitudes, respectively, e is the elementary charge, V the applied tunneling voltage, E_K the position of the obtained peak with respect to the Fermi energy and q the form factor. For $q = 0$, the line shape is a Lorentzian dip and for $q \to \infty$ it is a Lorentzian peak. Intermediate q values yield an asymmetric curve form.
A dip in the resonance (i. e. a q close to 0) means mainly direct tunneling into the metal. A peak shape (i. e. large q values), on the other hand, signifies mostly indirect tunneling via the Kondo resonance. The spectral shape of the measured dI/dV spectrum is dependent on the relative ratio of the different tunneling channels [160].

A quantitative analysis of the Kondo resonance, however, is difficult. The STS signal rarely fits perfectly to a Fano shape over a larger voltage range. The reasons for the challenging analysis are, on the one hand, the intrinsic properties of the Kondo system, since it is strongly affected by temperature and magnetic field. Furthermore, the interference between the different tunneling channels is not trivial to disentangle. Fits to experimental data with Eq. 4.3 usually result in different parameter sets depending on the assumed background signal and the data window taken into account. On the other hand, also instrumental broadening plays an important role. Finite sample and tip temperatures as well as the lock-in technique used to acquire the dI/dV spectra lead to a broadening that affects the width of the Kondo resonance.
One can also use a Frota function to fit the experimental differential conductance curves [176]. Whereas Frota functions yield better results for larger voltage fitting windows, Fano functions were shown to be superior at higher lock-in modulation voltages [173]. For this reason, we adhered to fit the experimental data with a Fano function (Eq. 4.3) over a small voltage range. Furthermore, the evaluation of the Kondo resonance with a Fano function is widespread in the community which makes it easier to compare the results to other groups.

Another factor that influences T_K is the number of neighboring metal atoms the magnetic impurity has. A higher number means an increase in hybridization and therefore an increase in T_K. This is why the Kondo temperature in a specific metal with magnetic impurities in the bulk is higher than in the scenario where the impurities are adsorbed on the metal surface instead [165]. Also the type of surface reconstruction matters because it leads to a different number of neighboring atoms [177].
Furthermore, the distance of the magnetic impurity to the metal substrate plays an important role for the occurrence of the Kondo effect. This was shown for Co atoms on graphene on Ru(0001) [178]. Graphene on Ru(0001) forms a moiré pattern leading to a corrugation of the graphene layer and therefore different distances from the graphene layer to the Ru substrate. Only for Co adsorption at specific positions of this moiré lattice a Kondo resonance could be observed. The authors

of this study attribute the different strengths of the coupling between the Co atom and the substrate due to the graphene corrugation to be the reason that the Kondo effect can or cannot be observed for different Co adsorption positions.
The local electronic structure is decisive for the existence of the Kondo effect and T_K. It was shown that also ligands in metal-organic complexes change the amount of hybridization between an embedded magnetic impurity and the metal substrate. Zhao *et al.* [179] investigated Co atoms inserted in phthalocyanine molecules on a Au(111) surface. The coupling between the embedded magnetic atom and the metallic substrate was still strong enough for the Kondo effect to be present. The orbitals of the phthalocyanine host molecule, however, inhibited direct tunneling from the STM tip to the substrate. Hence, instead of the dip feature typical for Co on Au(111) [165], a peak in STS was observed, accompanied with a larger q value and also an increase of T_K from 70 K for a single Co atom to 208 K for an embedded Co atom.

To distinguish the Kondo effect from other anomalies around the Fermi level, the Kondo nature of a zero-bias resonance is usually verified by conducting a temperature dependent experiment and measuring the resonance broadening, and by performing measurements in a magnetic field and observing a splitting of the resonance. Additionally, the determination of T_K via the resonance broadening is inaccurate, which is why cross-checking with temperature and magnetic field dependent measurements is desirable [180].

There are plenty of recent STM experiments addressing the Kondo effect in a metal-organic surrounding. Some of them shall be briefly summarized now.
Iancu *et al.* [181] reported the emergence of a Kondo effect upon intercalation of Co underneath an organic network of trimesic acid[5] on a Au(111) surface. The Co atom trapped between metallic surface and organic molecules led to a hybridization between Co orbitals and organic ligands resulting in a delocalized Kondo state.
In the work of Pacchioni *et al.* [182] Fe atoms were sandwiched between a Cu(111) surface and polyphenyl dicarbonitrile molecules[6]. The Fe atom was intercalated underneath the middle benzene ring of the polyphenyl chain. The outcome was a spatially strongly anisotropic Kondo effect with a Kondo dip at one side of the Fe intercalated benzene ring and a Kondo peak at its other side. This was rationalized by the existence of two screening channels originating from different Fe d-orbitals. This, again, shows the high sensitivity needed to thoroughly detect and interpret Kondo resonances.
With the help of an STM tip, Zhou and coworkers [183] manipulated picene[7] molecules across a Au(111) surface with single Co atoms adsorbed on. Upon the manipulation process, Co got buried underneath the molecule. dI/dV spectra at the position of the buried Co produced a peak in the spectrum that was attributed to

[5] Trimesic acid is basically a benzene ring with three carboxyl (COOH) groups attached to it.
[6] A chain of three lined up benzene rings connected with a single bond and terminated with a CN group at each end.
[7] five carbon rings lined up in an armchair-like manner

the Kondo effect. Up to three Co atoms were incorporated in one picene molecule which resulted in a broadening of the Kondo resonance—presumably by spin coupling between the closely spaced magnetic Co atoms.
Also experiments including GNRs were performed. Li *et al.* [184] measured a Kondo resonance at a porphyrine-based magnetic molecule not only directly on a Au(111) surface, but also when the molecule was adsorbed on top of 7-aGNRs grown on Au(111). Apparently the GNRs were mediating the spin coupling between magnetic molecule and surface. The measured signal intensities, however, were very small.
The Kondo temperature of the experiments presented so far varied between 50 K and 150 K. These relatively high values are due to the fact that the magnetic impurities are surrounded by organic molecules fostering the hybridization between magnetic atom and its environment.
A Kondo effect was also shown to exist at the junction of two fused chiral GNRs grown on a Au(111) surface without the presence of a magnetic impurity [185]. T_K was determined to be 6 K in this case. The origin of the magnetization of the carbon atoms, giving rise to the Kondo resonance, stems from two states inside the band gap of the GNR that arise due to the atomic configuration of the junction. A prerequisite for this effect to work is that these two states lie very close to E_F, one above and the other one below it.
This requirement is not fulfilled for the end states of 7-aGNRs on a Au(111) surface because the 7-aGNRs are hole doped by the substrate [144].

4.2. Sample preparation

The 7-aGNRs used in this work were grown in the preparation chamber of the STM apparatus (see appendix B for the setup), following the recipe introduced by Cai *et al.* [47]. The schematic for the growth process is shown in Fig. 4.6. A Au(111) single crystal was used as catalytic substrate and cleaned by repeated Ne^+ sputtering and annealing cycles. Subsequently, 10,10´-dibromo-9,9´-bianthryl (DBBA) monomers (see Fig. 4.6 (a) for the chemical structure) were used as precursor molecules and thermally sublimed onto the freshly prepared Au(111) surface kept at 70 °C. Fig. 4.6 (b) shows the stick and ball model of a DBBA monomer upon adsorption on a Au(111) surface. Gray depicts carbon, white hydrogen and red bromine. The underlying Au surface atoms are represented by large white spheres. The adsorption geometry of the DBBA molecule is non-planar. The two anthracene units are tilted with respect to each other. This tilt is due to steric hindrance induced by the H atoms that are attached to the unsaturated C atoms.
Upon heating the sample to 200°C, the catalytic effect of the Au(111) surface leads to the cleavage of the Br atoms from the rest of the precursor [186, 187] (see Fig. 4.6 (c)). This is referred to as dehalogenation and leaves a biradical intermediate on the surface. The unsaturated bonds are marked with yellow dots in panel (c) and render

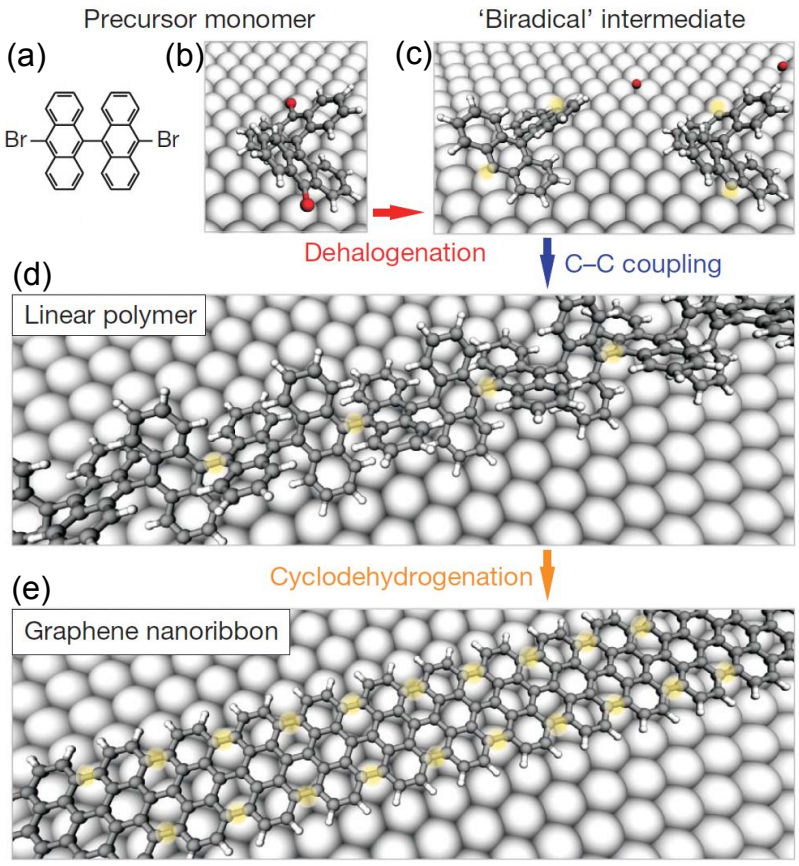

Figure 4.6.: **Growth of 7-aGNRs.** The ribbons are grown from DBBA precursor molecules on a Au(111) surface. Details are given in the text. Graphic adapted from [47].

the bianthryl rest highly reactive. The Br atoms either aggregate on the surface (at step edges) or are incorporated in the anthryl molecules and desorb at higher temperatures [14, 188].
Additionally, the elevated temperature makes the precursor molecules more mobile on the surface. Therefore, the radicals diffuse over the surface until they meet another radical with which they couple forming a C–C bond. Through this so-called C–C coupling[8], the single precursor molecules are linked to long linear polymer chains (see Fig. 4.6 (d)). The sites where two distinct precursors are joined are highlighted with yellow dots in the graph. The individual anthracene units are still tilted with respect to each other. This tilt is crucial for the formation of the linear chains. In a planar geometry, the anthracene units could not come close enough to each other to form a bond because of the steric repulsion of the H atoms. Only the tilt allows for a sufficient convergence of two precursor units [15].

[8] Also referred to as Ullmann coupling [189] due to the similar reaction scheme to an Ullmann reaction.

Finally, the temperature is raised to 400°C, initializing the cyclodehydrogenation process. Hereby, the H atoms in between the anthracene units are cleaved off, leading to a C−C bond formation between the anthracene units and rendering the GNR flat (see Fig. 4.6 (e), yellow dots) [190]. The length of the 7-aGNRs is determined during the first heating step (C−C coupling) and limited by the following factors. First, the purity of the precursor molecules has a decisive influence on the GNR length. Defective precursor units terminate the chain formation process and therefore lead to shorter GNRs. But also the heating temperature plays a role. Too high temperatures lead to a premature dehydrogenation of some of the DBBA precursor molecules producing atomic hydrogen on the surface which in turn can passivate the polymerized chains and therefore terminate the growth process [155]. Last, longer heating times increase the probability for the formation of longer polymer chains and therefore longer GNRs. The 7-aGNRs presented here reached lengths of up to 40 nm.

After the growth of the 7-aGNRs, the sample is put in the STM chamber and cooled down to 9 K. Subsequently, single Co atoms are deposited onto the cold sample surface using an electron beam evaporator. Fig. 4.7 shows an overview image of a prepared sample. The 7-aGNRs appear as light gray strips of different lengths.

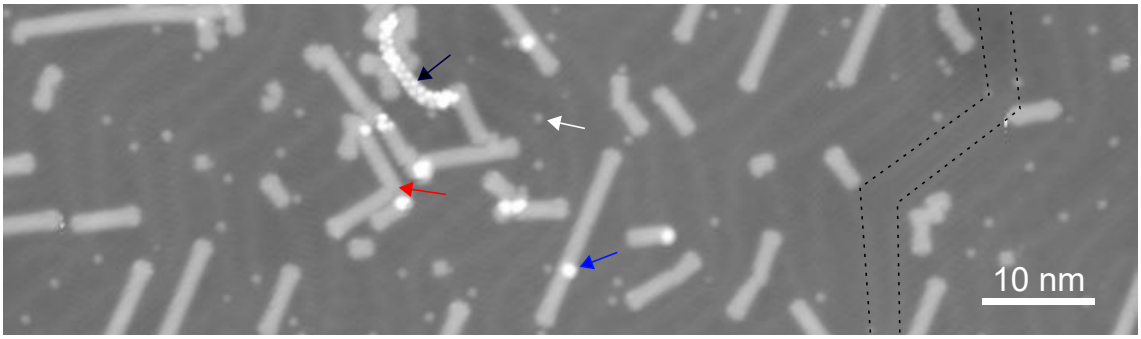

Figure 4.7.: **Overview image.** 7-aGNRs (light gray strips) and Co atoms (little round spots, see white arrow) adsorbed on a Au(111) surface. Some GNRs are fused (red arrow) and some Co atoms adsorbed on top of the GNRs (blue arrow). The black arrow marks a non-cyclodehydrogenated GNR. Parts of the herringbone reconstruction are marked by dashed black lines. $V_{bias} = 100\,\text{mV}$, $I_{tunnel} = 11\,\text{pA}$.

Most of the GNRs are separate from each other, but some of them are also fused (see red arrow).
The herringbone reconstruction of the Au(111) surface can be seen in the background (dashed black line) indicating the cleanliness of the surface.
Most of the Co atoms land on the Au surface and appear as round spots (see white arrow). Sometimes, the Co atoms adsorb also on top of a 7-aGNR (see blue arrow). In this case they appear brighter and larger. Some of the 7-aGNRs are not completely flat because the cyclodehydrogenation did not (fully) take place [190].

As a result, some carbon rings still point upwards and appear as bright, round spots. One example for such a situation is marked with a black arrow. Upwards-pointing rings can be distinguished from the on-top-adsorbed Co atoms by measuring their apparent width and height.

To characterize the 7-aGNRs with CO-functionalized tips, the sample preparation process was slightly modified. After the synthesis of the 7-aGNRs, the sample was first kept in the preparation chamber and cooled down to room temperature. Subsequently, a small amount of NaCl was deposited using a thermal evaporation source which leads to the formation of NaCl islands on the sample. Then, the sample was put into the STM chamber and cooled down to 9 K. After the deposition of Co atoms, CO gas was introduced into the STM chamber via the load-lock upon which single CO molecules adsorbed on the sample surface. The CO molecules could be picked up from the NaCl islands by the STM tip.

4.3. First sample characterization

The GNRs were investigated by imaging as well as by spectroscopic means, i. e. by taking dI/dV spectra. All bias voltages V_{bias} are given as sample bias with respect to the tip. Due to instrumental uncertainties, V_{bias} is always to be understood with an error of ± 1 mV. All AFM images shown in this chapter are taken with a CO-functionalized tip in non-contact (frequency modulated) AFM mode. For STM topography images—unless stated differently—a pure metal tip was used. Differential conductance spectra were also recorded with a pure metal tip using the lock-in technique and a modulation frequency of 170 Hz with amplitudes of 2–7 mV. The measurement temperature was 9 K.

4.3.1. End states of 7-aGNRs

To start with, the ends of 7-aGNRs are investigated. Since they are well characterized in literature [28, 47, 127, 131, 132, 144, 151, 155] they serve as a good tool to test our setup.
Fig. 4.8 (a) shows a high-resolution STM image of a 7-aGNR end. A finger-like structure is visible at the GNR terminus. There are three lobes along the short zigzag edge of the GNR and two additional, slightly brighter lobes at its corners. This structure stems from the well-known end state and is attributed to the zigzag configuration of the GNR edge [127, 155].
The dI/dV measurements presented in Fig. 4.8 (b) give information about the electronic structure of the GNR. The spectra are offset for clarity. The blue line shows the dI/dV spectrum taken at the GNR center (blue circle in the STM image). The voltage range presented here lies within the band gap of the 7-aGNR [28]. Therefore, the spectrum resembles the reference spectrum on the pristine Au(111) surface

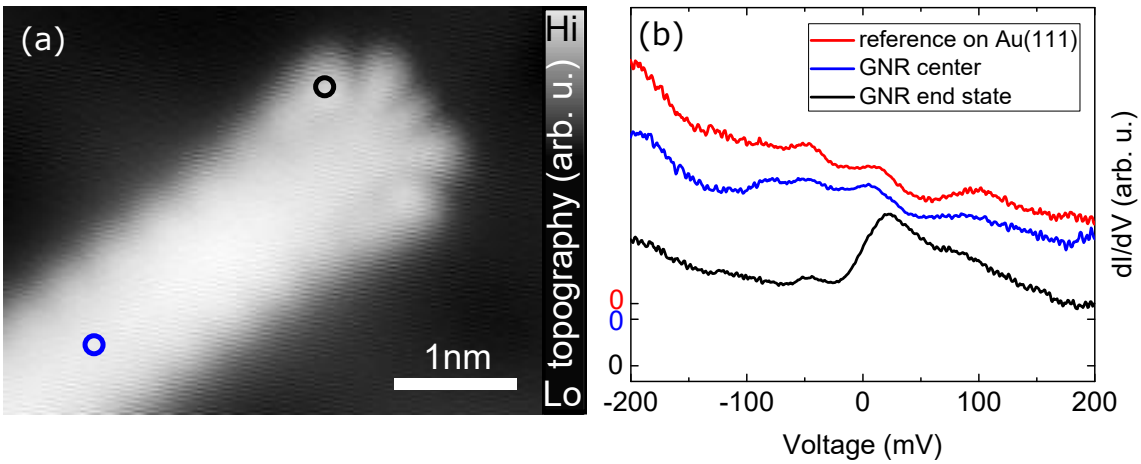

Figure 4.8.: **GNR end state.** (a) High-resolution STM image of a 7-aGNR end showing a finger like structure at the GNR terminus. Colored circles indicate place of the dI/dV spectra. $V_{bias} = 2\,\mathrm{mV}$, $I_{tunnel} = 48\,\mathrm{pA}$. (b) dI/dV spectra taken at the GNR corner (black), in the center of the GNR (blue) and on the bare Au(111) surface (red). Note the different baselines for each spectrum.

(red curve, spectrum taken outside of STM image frame) because the GNR states hybridize with the Au states. When taking a spectrum at the corner of the GNR, however, a peak centered at $(22 \pm 4)\,\mathrm{mV}$ with a full width at half maximum (FWHM) of $(42 \pm 19)\,\mathrm{mV}$ emerges, corresponding to an enhanced LDOS at this location. Its energy position is close to the literature value of the end state (or Tamm state) of 30 mV [127, 144, 151, 191]. The intensity is most pronounced at the GNR corners and fades out within a range of roughly 1 nm from the zigzag edge.

The uncertainty margins were determined in the following way. The dI/dV spectra were recorded for decreasing as well as increasing voltages. The voltage value V_m—at which the peak maximum occurred in the sweep with increasing voltage—was taken as peak maximum position. The difference of this peak position to the peak position obtained by sweeping with decreasing voltage was used as uncertainty. Such a difference can emerge, for example, from creep of the piezo element controlling the position of the STM tip during the spectrum. If the peak was rather blunt or plateau-like, the width of the plateau was added to the uncertainty margin. Of course, the uncertainty in V_{bias} of $\pm 1\,\mathrm{mV}$ was also included.
For the determination of the FWHM, the voltage position V_l at the middle of the left flank of the peak was subtracted from V_m and then multiplied by 2: $\mathrm{FWHM} = (V_m - V_l) \cdot 2$. The uncertainty margin for the FWHM was obtained by identifying the voltage position V_r for the middle of the right flank of the peak. Then, the uncertainty was determined as $(V_r - V_l) - 2 \cdot (V_m - V_l)$. This procedure was chosen since many spectra were slightly asymmetric with a broader right flank. Another 2 mV were added to this uncertainty due to uncertainties in determination of the

middle positions of both peak flanks.
The same holds true for the description of all further peak maxima and FWHM values throughout this chapter.

To get further insight into the structure of GNR ends, constant-height AFM images with a CO-terminated tip were taken. One of these can be seen in Fig. 4.9 (a). The chemical structure of the GNR becomes visible showing defect free armchair edges (top and bottom) as well as a zigzag edge (left). The zigzag edge is slightly bent towards the Au surface and therefore appearing darker than the other edges in the image. This is presumably because of its higher reactivity.

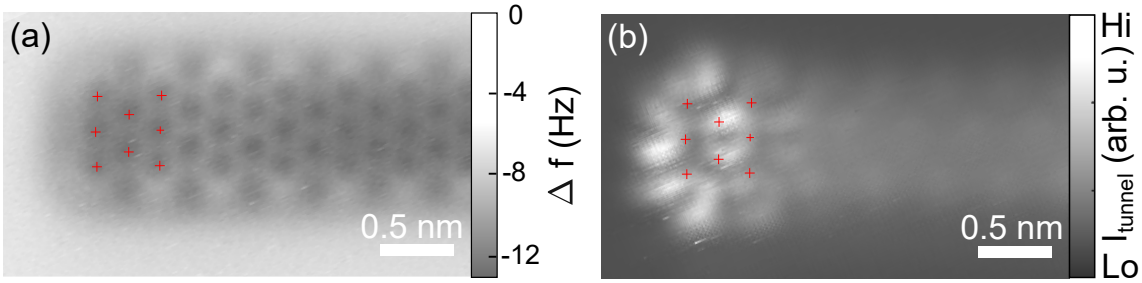

Figure 4.9.: **Structure of pristine GNR end.** (a) Constant-height AFM image of a pristine GNR end. (b) Simultaneously recorded current map by applying a small bias voltage during the constant height scan. Red crosses mark the centers of the carbon hexagon rings.

During the constant height scan, a small bias voltage of roughly 1 mV was applied to the sample, allowing electrons to tunnel between electronic states in the GNR close to E_F and tip states. The corresponding current flow was recorded, yielding the current map shown in Fig. 4.9 (b).
One has to note that the current map was recorded with a CO-terminated tip. As already mentioned, this changes the orbital symmetry of the tip from *s*-wave for metal tips to *p*-wave character and correspondingly also changes the imaging contrast [159]. Therefore, the electronic structure of the current map looks different from the constant current image obtained by standard STM imaging. Instead of the finger-like structure in the standard STM image, three V-shaped bright features appear at the GNR terminus in the current map.
Nonetheless, one can draw direct conclusions about the distribution of LDOS in the GNR. Since the end state is the only state with pronounced LDOS around the Fermi level, one can immediately deduce its spatial distribution from the current map. The current flow (and correspondingly the LDOS) is highest in the area of the GNR zigzag end and therefore illustrating that the end state is localized at and distributed along the whole zigzag edge. Due to hybridization with the Au substrate, there is also finite LDOS along the rest of the GNR, but the intensity is much lower.

4.3.2. Variation in the appearance of GNR end states

The appearance of the end state in dI/dV spectra can vary and one has to carefully interpret the observed peak shapes. The broadening of the end states will be discussed in more detail in a later section (see 4.6). For the time being, it is enough to mention that a common feature of all end states is the emergence of a maximum in the voltage range around 20–30 mV. Differences between the spectra taken at different GNR ends can be explained as follows.
First of all, the shape of the end state depends on the STM tip, since the dI/dV spectrum reflects the LDOS of the sample convoluted with the DOS of the tip. Therefore, the tip has been carefully prepared before recording dI/dV spectra. Additionally, all tips have been characterized by probing well-known states, like the Au surface state, to ensure that no tip artifacts corrupt the measurements.
Furthermore, even when using the same tip, spectra on different GNR ends (even different sides of the same GNR) can yield differently shaped end state peaks. An example is given in Fig. 4.10, where two subsequent spectra on two adjacent GNR ends are shown, using the same tip and the same parameters for taking the spectra. For GNR 1 (right GNR, black line) the intensity of the spectrum is higher than for the second GNR and the line shape is clearly a peak. Its maximum lies at (15 ± 3) mV and its FWHM measures (23 ± 6) mV. GNR 2 (left GNR, red line), on the other hand, exhibits lower signal intensity, almost obscuring the peak shape, and appears to be more asymmetric. Here, the peak is maximal at (24 ± 3) mV. The FWHM is difficult to determine due to the asymmetry, but can be roughly estimated as (50 ± 46) mV.

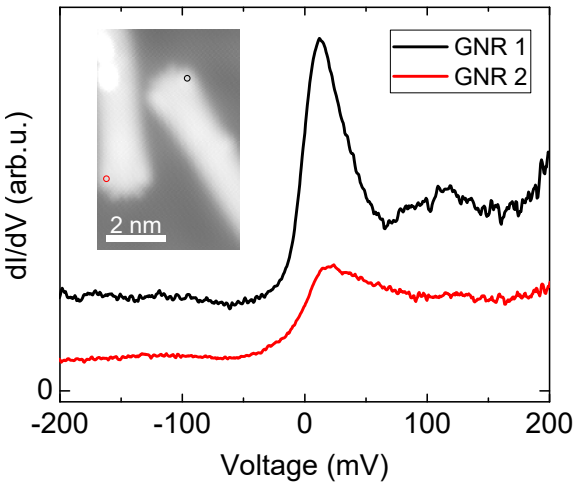

Figure 4.10.: **Different appearances of end states.** Two dI/dV spectra of adjacent GNRs (shown in the inset, $V_{bias} = 100$ mV, $I_{tunnel} = 11$ pA) recorded with the same tip and same spectroscopic parameters. The appearance of the end state can vary from GNR to GNR.

A possible explanation for the different shapes could be the interaction of the GNR with the underlying gold substrate. The Au(111) surface atoms rearrange into the herringbone reconstruction. Here, the surface is divided into regions where the top-layer Au atoms are ordered in face-centered-cubic (fcc-type) stacking and hexagonal-close-packed (hcp-type) stacking. The boundaries of these regions are connected by areas in which the surface Au atoms take bridge positions with respect to the

underlying layer. These are called wall sites. This leads to a corrugation of the surface with vertical displacements in the bridge regions of approximately 0.2 Å. The GNR ends can rest on differently reconstructed surface areas which might lead to slightly different adsorption heights of the GNR ends with respect to the Au surface. This, in turn, could lead to subtle changes in the hybridization between GNR and Au surface, thereby explaining the different end state peak shapes.

4.3.3. *dI/dV* spectra on Co atoms on Au(111)

As discussed in the theory section, the interaction of a magnetic impurity with the spins of the surrounding conduction electrons gives rise to a sharp Kondo resonance in the DOS at the Fermi level [162]. For the case of Co on Au(111), a well-known Kondo system, the resonance appears as a dip at the Fermi level in the dI/dV spectra with a Kondo temperature of 70 K [174].

Fig. 4.11 (a) shows an STM image of a Au(111) surface with a 7-aGNR and different adatoms adsorbed on the Au(111) surface. The adatoms are either Co atoms, evaporated with an e-beam evaporator, or Au atoms, brought to the surface by gently crashing the STM tip onto the surface. In STM images, these two kinds of adatoms appear indistinguishable. Therefore, one has to carefully keep track of which atoms were deposited from the tip.
Before the experiment started, the STM tip—actually consisting of a PtIr wire—was poked repeatedly into the Au surface and is therefore well covered with Au layers at its apex. By choosing the right poking parameters, small Au clusters as well as single Au atoms can be dropped from the tip onto the surface. To monitor which atoms were deposited from the tip, overview STM images were taken before and after the tip pokes and compared to each other. Co atoms that were already present beforehand resided at the same position also after the tip poke. The additionally appearing atoms in the overview image after the poke could thus be identified as Au atoms stemming from the tip.

When taking dI/dV spectra, the elements exhibit distinctly different behavior (see Fig. 4.11 (b)). The black line describes the spectrum taken on a Co atom (black circle in the STM image). It shows a clear dip at (3 ± 4) mV, i. e. the Fermi level, and a full width at half minimum of (18 ± 3) mV which can be ascribed to the Kondo effect and is absent for the Au atom (red line and circle).
By inserting the FWHM measured here into Eq. 4.2, a Kondo temperature of $T_K = (100 \pm 18)$ K is obtained. Additionally, T_K is determined by fitting the dip in the experimental dI/dV curve with Eq. 4.3 with a non-linear least squares fit (the corresponding fit curve can be seen in A.1 in the Appendix). Using an α parameter of 2π [170] yields $T_K = (106 \pm 10)$ K. The results obtained by the manually extracted FWHM and the fitting procedure differ because of the slight resonance asymmetry. Both values deviate from the literature value of 70 K for Co on Au(111) reported by Madhavan *et al.* [165]. The reason is probably thermal broadening that was not

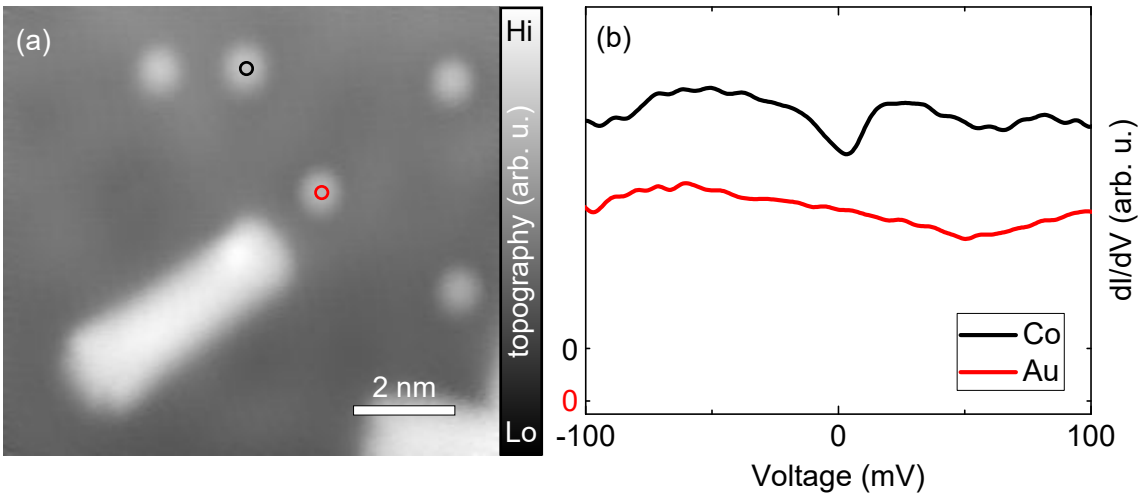

Figure 4.11.: ***dI/dV* on Co and Au atoms on a Au(111) surface.** (a) Fourier filtered STM image of a GNR and different adatoms on Au(111). Co and Au adatoms look indistinguishable with the STM. $V_{bias} = 100\,\mathrm{mV}$, $I_{tunnel} = 48\,\mathrm{pA}$. (b) Smoothed dI/dV spectra taken on a Co (black circle) and a Au (red circle) adatom. Co exhibits a Kondo dip at 0 V.

sufficiently considered in our case. This is especially relevant since the measurement temperature in our system is 9 K, and therefore slightly higher than the 4 K used by Madhavan and coworkers. Following Gruber *et al.* [173], a temperature broadening of $3.5k_bT$ is assumed which yields a broadening of 3 meV at $T = 9\,\mathrm{K}$. Adding this widening to the uncertainty margins produces a FWHM of $(18 \pm 6)\,\mathrm{mV}$ and consequently a T_K of $(100 \pm 37)\,\mathrm{K}$, which includes the literature value.

Therefore, the broadening was included in all further uncertainty specifications. The minimum uncertainty for the FWHM is thus $\pm 5\,\mathrm{mV}$ ($\pm 3\,\mathrm{mV}$ from thermal broadening and $\pm 2\,\mathrm{mV}$ from the determination of the left and right peak flank, as described before).

The different spectroscopic behavior of Co and Au can be explained by the electron configurations of these elements. While Co has the $[\mathrm{Ar}]3\mathrm{d}^7 4\mathrm{s}^2$ configuration, meaning its 3d shell is not fully occupied and hosting unpaired electron spins, Au has the $[\mathrm{Xe}]4\mathrm{f}^{14}5\mathrm{d}^{10}6\mathrm{s}^1$ configuration and a fully filled 5d shell. Therefore, a Co adatom has a magnetic moment which is screened by the electrons of the Au(111) substrate whereas a Au adatom is non-magnetic.

It should be mentioned that not every Co atom displays a clear, symmetric Kondo dip. The shape of the Kondo resonance depends on the adsorption position of the Co atom with respect to the herringbone reconstruction on the Au(111) surface [174]. For Co atoms lying on fcc or hcp regions, the Kondo dips look similar and relatively symmetric, whereas the dip is quite asymmetric for Co adsorption at wall sites.

4.4. Assembly of Co-GNR-complexes

Both, the GNR end state and the Kondo resonance of Co, host states close to the Fermi level. Therefore, it is interesting to investigate what will happen when a Co atom is brought in the vicinity of a GNR end. How will the states interact? With the help of an STM tip, single Co atoms can be manipulated across the metal surface [192, 193]. Taking use of this, we manipulated Co atoms towards the 7-aGNR zigzag ends. It turned out that, even in close vicinity, the intrinsic properties of end state and Co Kondo resonance did not change. However, when we tried to push the Co atom even further towards the GNR, the Co atoms got buried underneath the GNR which, then, changed the spectroscopic fingerprint of the system.

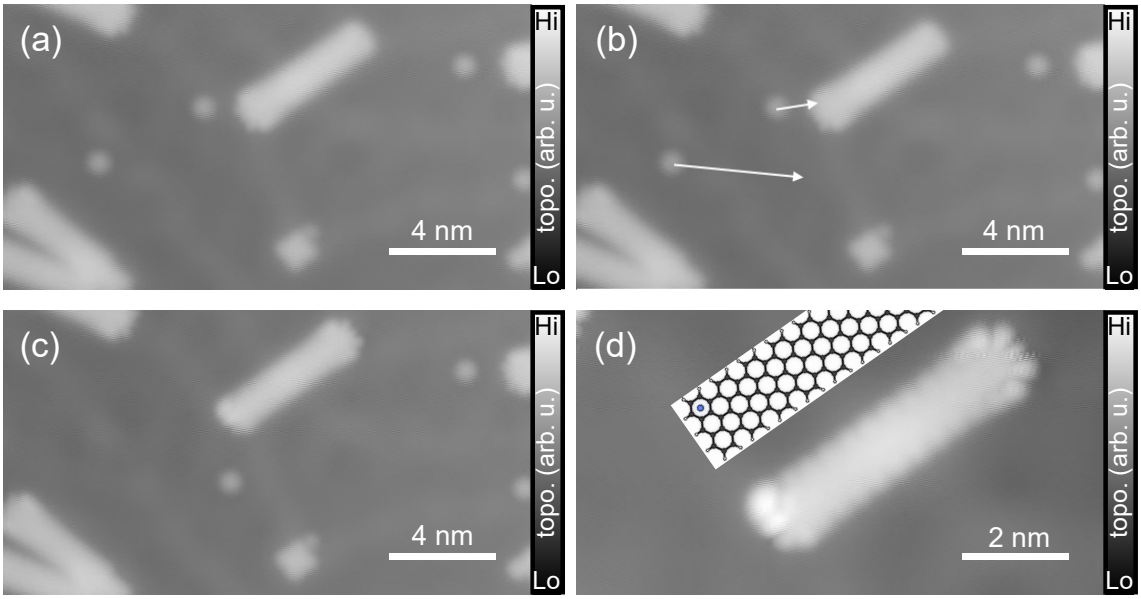

Figure 4.12.: **Assembly of Co-GNR-complexes.** (a)–(c) Manipulation of Co atoms across the surface and underneath the GNR. $V_{bias} = 100\,\mathrm{mV}$, $I_{tunnel} = 11\,\mathrm{pA}$. (d) High-resolution STM image of the Co-GNR-complex. Inset shows magnified sketch of the Co intercalation position. Black spheres depict C atoms, white H and blue Co. $V_{bias} = 2\,\mathrm{mV}$, $I_{tunnel} = 48\,\mathrm{pA}$.

Fig. 4.12 shows an example for the assembly of a Co-GNR-complex with the Co atom being placed at the GNR corner. Panel (a) displays the initial configuration with two Co atoms lying close to a GNR. Panel (b) indicates the paths along which the STM tip manipulates the Co atoms. The result of the manipulation can be seen in panel (c). One Co atom (lower arrow) was manipulated across the Au(111) surface and lies now closer to the GNR. For the other Co atom (upper arrow), the manipulation process led to an intercalation of the Co between the GNR and the Au(111) surface.
Note that also the GNR moved a little bit during the intercalation procedure. In this

case the GNR got displaced by 0.9 nm through the manipulation process. This phenomenon occurred frequently during the assembly of Co-GNR-complexes and looks like GNR and Co atom "snap-in-place" into a most favorable common configuration.

Furthermore, the finger-like structure of the end state appeared at the right, pristine GNR end after the manipulation process. A possible reason is that an additional hydrogen atom—attached to the center carbon atom of the right GNR zigzag end and suppressing the end state—got cleaved off during the intercalation process.
It is also possible that the changed adsorption position of the GNR with respect to the Au(111) surface leads to the appearance of the prior suppressed end state. Mishra *et al.* [194] found that special nanographene molecules with short zigzag edges get pinned to the elbows of the Au(111) herringbone ridges. The spin at this zigzag site—present for other molecule adsorption positions in their experiment—was found to be quenched which was tentatively explained by a bonding of the molecule zigzag edge to an under-coordinated Au atom at the elbow site.
Therefore, the disappearance of the end-state-associated finger-like structure in our GNR experiment could also be related to a bonding of the GNR zigzag end to certain sites of the Au surface, like the wall sites. Especially, when taking the radical character of a GNR with a higher number of aromatic rings and therefore higher GNR stability into consideration, a bonding to the Au substrate does not seem impossible.
Likewise, the reappearance of the finger-like structure observed here might result from a bond breaking between Au surface and GNR zigzag end due to the "snap-in-place" motion and thus a recovery of the unpaired electron at this GNR end.
Fig. 4.12 (d) shows a high-resolution STM image of the Co-GNR-complex. The typical finger-like structure of the GNR end state can be clearly seen at the right (pristine) GNR end. The opposite (left) end of the GNR, however, shows a bright, roundish protrusion at its corner. This is the position where the Co atom is buried, as sketched in the inset above the GNR. The Co atom is believed to sit underneath the center of the corner carbon ring as this is the energetically most favorable adsorption position for most adatoms on graphene [195, 196]. Calculations for various transition metal atoms adsorbed on aGNRs of different widths indicated that binding to the outermost carbon ring—i. e. the one at the armchair edge—is energetically most stable [197].

The appearance of the intercalated Co atoms in STM images is distinctly different from the one of the Co atoms that reside on top of the GNRs (c. f. Fig. 4.7). This serves as further proof that the Co atoms do not jump onto the GNR upon manipulation but get buried between GNR and Au surface instead.
Whereas the configuration of Co atoms on top of GNRs is intrinsically present on the sample due to the fabrication procedure, the spontaneous burial of Co atoms underneath the GNR is quite unlikely at the given sample temperature.

We built up Co-GNR-complexes with different intercalation positions of the Co atom. Co atoms were positioned at various locations along the armchair edge of the

GNR. It turned out that the Co atoms always got intercalated underneath the outer carbon rings of the GNR armchair edge.
It was not possible to place a Co atom underneath the middle carbon ring of the GNR zigzag edge. All trials resulted in picking up the GNR with the STM tip. This might be related to the higher reactivity of the GNR zigzag edge.

To properly refer to the intercalation position of the Co atom along the GNR edge, the nomenclature illustrated in Fig. 4.13 is introduced.

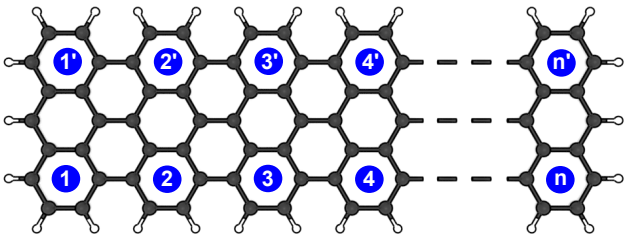

Figure 4.13.: **Nomenclature of Co-GNR-complexes.** The outer carbon rings of the armchair edges are counted starting from the left side. The positions at the upper edge are branded with a dashed number.

The GNR is depicted with its armchair edges horizontally aligned. Starting from the left side, the outer carbon rings of the armchair edges are counted and their numbers indicate the corresponding position. Dashed numbers refer to the upper armchair edge. In the case of the GNR shown in Fig. 4.12, for instance, the Co is buried at the top left corner corresponding to position (1'), therefore yielding a Co-(1')-GNR-complex.

4.5. *dI/dV* characterization of Co-GNR-complexes

To study the interaction of the Co atom with the 7-aGNR, different Co-GNR-complexes were investigated. Co atoms were placed at various locations along the GNR armchair edge and dI/dV spectra were recorded.
We start with a Co atom buried at the middle of a GNR armchair edge and then describe configurations where the Co atom is placed closer towards the zigzag edge. Finally, the situation for a Co atom positioned at the corner of the GNR will be discussed. The spectroscopic fingerprint of the Co-GNR system changes for the different scenarios. Subsequently, GNR-complexes with Co atoms at multiple corners will be presented. At the end, the experimental data are compared to DFT and tight-binding calculations.

4.5.1. Co at middle of armchair edge

First, a Co atom was placed at the GNR armchair edge. The intercalation position was chosen in such a way that the distance between Co atom and zigzag end was

sufficiently large to prevent interaction among them. In this manner, the influence of the end states on the intercalated Co atom is minimized and the interaction between the Co atom and the pure GNR armchair edge can be probed. It turned out that a Co atom buried at least 4 outer carbon rings away from the zigzag edge—i. e. at position (4) or (4') and onwards—yields the same spectroscopic features as a Co atom buried at the middle of the armchair edge several nm away from the zigzag end. Position (4) corresponds to a distance of 1.4 nm from the zigzag edge, matching the decay length of the end state reported in Ref. [132].

As a first example for Co at the middle of the armchair edge, a Co-(4)-GNR-complex will be presented. Fig. 4.14 (b) shows an STM topography image of such a structure. The Co atom intercalated at position (4) at the lower armchair edge appears as

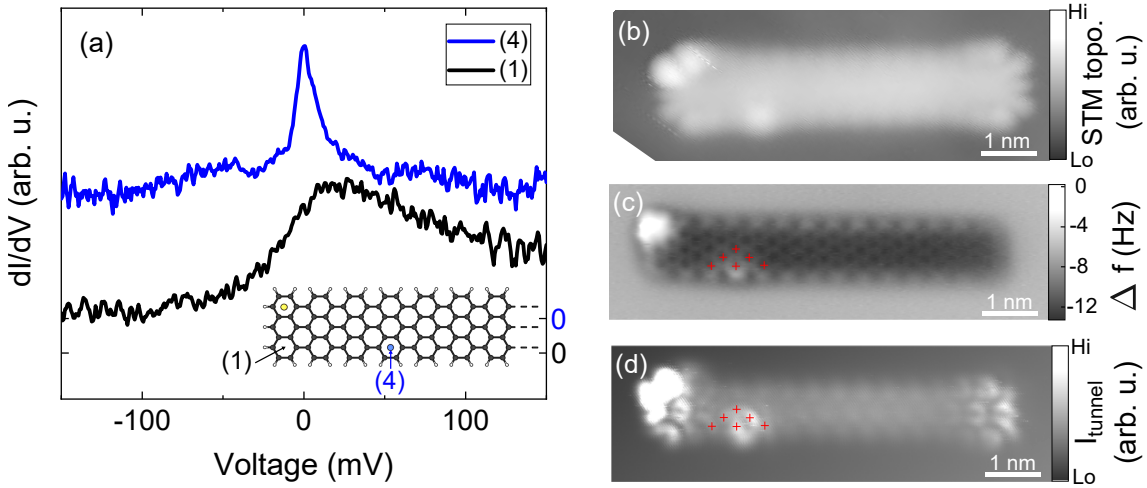

Figure 4.14.: **Co at 4th position.** (a) dI/dV spectra of a Co-(4)-GNR-complex. The inset sketches the intercalation sites of Au and Co atom and indicates the positions the spectra were taken at. (b) STM image ($V_{bias} = 4\,\mathrm{mV}$, $I_{tunnel} = 50\,\mathrm{pA}$), (c) AFM image and (d) current map of the complex. Red crosses in (c) and (d) mark the same positions.

bright, round protrusion. The right GNR end exhibits the typical finger-like structure, indicating the presence of an end state. The left GNR terminus also shows the finger-like structure, but the uppermost two fingers are much brighter than the lower three. This is due to the intercalation of a Au atom at position (1') and will be discussed in section 4.5.6. An example for a Co-GNR-complex without intercalated Au atom will be given at the end of this section.
From the STM topography image alone it is difficult to resolve the exact Co intercalation position. To unambiguously determine the Co location, an AFM image with a CO-terminated tip was recorded, shown in Fig. 4.14 (c). From this atomically resolved image, one can see that the 4th ring along the lower armchair edge reveals higher repulsion than its surrounding confirming a burial of Co at this position.

Further, the Au intercalated corner (1') also exhibits a strong repulsion. This will be discussed in more detail later in section 4.5.6. In short, the GNR corner bends more upwards than the center of the armchair edge.

To investigate the electronical properties of the complex, differential conductance spectra, some of them depicted in Fig. 4.14 (a), were recorded at various GNR locations. The inset sketches the configuration and shows the intercalation sites of Au and Co. Color coded arrows in the inset indicate the positions where the spectra were taken.
The spectrum at the GNR corner—position (1), black line—shows a weakly pronounced end state peak. As discussed in section 4.3, the end state curve shapes can vary. Here, the peak is relatively broad with a FWHM of (66 ± 8) mV. It is centered at (20 ± 5) mV and the line shape is asymmetric.
It should be underlined that the spectra taken at the GNR armchair edge are usually featureless around E_F. However, the dI/dV curve taken at position (4)—at which the Co atom is intercalated—exhibits a pronounced zero-bias peak. The curve is qualitatively different from the one obtained at the corner. The dI/dV spectrum changed its shape and became more symmetric. It is also narrower, now showing a FWHM of (9 ± 7) mV. The uncertainty margin already includes thermal broadening. Furthermore, its maximum position shifted to (0 ± 3) mV.

The peak center position at 0 mV and the narrow line shape paired with the presence of the magnetic Co atom give reason to interpret the peak as a Kondo resonance. The FWHM leads to a Kondo temperature of $\mathrm{T}_K = (44 \pm 44)$ K. A fit to Eq. 4.3 yields a T_K of (78 ± 4) K (the corresponding fit curve can be seen in A.1 in the Appendix). As already mentioned, the Kondo effect is usually verified by conducting temperature and magnetic field dependent measurements and observing the peak broadening or splitting, respectively. Here, none of these methods could be applied. On the one hand, the STM setup is not equipped with a magnet. On the other hand, the Kondo temperature of this system is so high that a raise up to the Kondo temperature would have led to significant thermal drifts of the STM tip. Drift in z-direction would corrupt the dI/dV signal and drift in x and y would face the high spatial sensitivity of the Kondo signal.
However, the assumption of a Kondo related nature of the emerging peak seems justified since Co atoms are known to exhibit a Kondo feature on the given surface and a Kondo effect was shown for similar systems [181, 183].

Apparently, the interaction between Co atom and GNR does not lead to a quenching of the Kondo effect inherent to the Co atom. The interaction between Co and GNR bulk states seems to be quite weak instead. Since the GNR does not possess any states around the Fermi level—apart from the end states at the zigzag termini—there is little hybridization expected between the Kondo resonance caused by the Co atom and GNR bulk states.

Thus, the Kondo feature stemming from the interaction of Co atom and Au(111) surface can still be observed. The shape of the Kondo feature in the Co-GNR-complex,

however, is distinctly different from the one of an isolated Co atom. Instead of the dip observed for the single Co atom on the Au(111) surface, the curve displays a peak when the Co is buried underneath the GNR. This can be explained by a modification of the tunneling channel for the electrons from the tip to the surface (c. f. section 4.1.3). The peak or dip shape is a consequence of the quantum interference between the direct tunneling path of tip electrons into the sample (dip shape) or indirectly via the Kondo resonance caused by the magnetic atom (peak shape) [160, 174].
Hence, the dip shape points to a stronger direct tunneling channel into the host substrate present for the isolated Co atoms, whereas the tunneling via the orbitals of the Co atom predominates in the case of the Co-GNR-complexes. This difference in tunneling paths is not surprising, taking into consideration that the distance between tip and substrate is significantly increased if an organic molecule is inserted between tip and surface. This makes direct tunneling to the substrate less probable. Overall, the line shape is always an interference effect between different tunneling channels.

During the constant height AFM scan, a very small bias voltage was applied to the sample yielding the current map shown in Fig. 4.14 (d). One can see that the LDOS is enhanced at the right GNR end indicating the distribution of the end state at this zigzag edge.
At the left GNR terminus, the end state is only partially visible in the current map. At the bottom left GNR corner, the end state signature can be seen. The V-shaped appearance instead of a finger results from the CO-functionalization of the tip used during the AFM scan. The rest of the left GNR zigzag edge appears very bright because of the intercalated Au atom at position (1'). Due to the upwards bending of the top left GNR corner, this part of the GNR is closer to the tip—which is scanning in constant height across the GNR—and hence more current flows.
Enhanced LDOS can also be found at the site of the intercalated Co atom. A roundish feature is visible at position (4), penetrating slightly towards the GNR center. It holds a nodal plane at its center. Comparing the atomically resolved AFM image with the current map by placing red marker crosses at identical positions (namely at the center of hexagons) reveals that this nodal plane coincides with a C–C bond of the GNR frame. Apparently, the tunneling path from Co atom to STM tip is partially impeded by the GNR lying in between.
Remarkably, the high LDOS at the roundish feature is very localized and seems to be spatially well separated from the high LDOS at the left GNR end by a region of lower LDOS. This confirms the aforementioned assumption that a Co atom intercalated at position (4) is sufficiently far away from the zigzag edge to avoid coupling between these two.

In total, 8 different Co-GNR-complexes with a Co atom buried at the middle of the armchair edge were built. The exact intercalation position was only determined once with atomic precision by AFM imaging. For the other cases, the Co atom had the same distance to the GNR zigzag terminus or was even further separated from

it, as was evident from STM topography images.
Differential conductance spectra taken at the intercalated Co atom positions yielded consistent results. A relatively narrow, Kondo-like resonance was observed at the Co intercalation site for all cases. The mean value of the peak maximum is (3 ± 3) mV and the average FWHM (20 ± 8) mV. Here, the uncertainty margins refer to the standard deviation and show that the complex presented in Fig. 4.14 had a resonance width below average.

Last, an example of another Co-GNR-complex with a Co atom intercalated at the middle of the armchair edge is shown. This time, no additional Au atom was intercalated at the GNR corner. The inset of Fig. 4.15 depicts an STM image of the complex. The Co atom is buried at the middle of the upper armchair edge. At

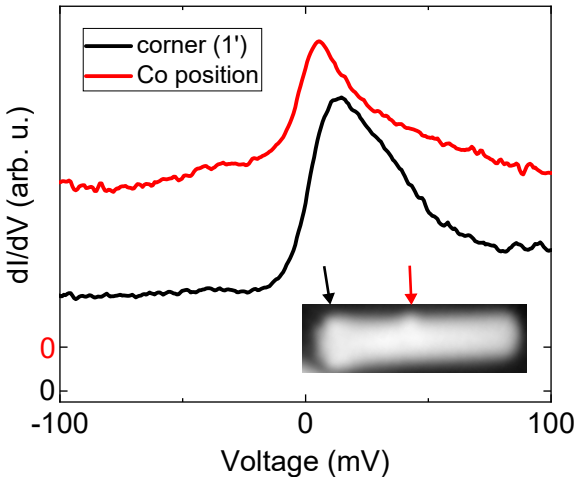

Figure 4.15.: **Co at the middle of the armchair edge.** dI/dV spectra of another Co-GNR-complex with a Co atom intercalated at the upper armchair edge. Red spectrum taken at the intercalated Co atom position, black spectrum at the pristine GNR corner (1'). Inset shows an STM image of the complex (V_{bias} = 100 mV, I_{tunnel} = 11 pA). Positions of the spectra are indicated by arrows.

the left GNR terminus, one can see the finger-like structure of the end state. At the right terminus, this end state signature is missing, possibly indicating a doubly hydrogenated carbon atom at the middle of the right zigzag edge.
The dI/dV spectra shown in the main panel of Fig. 4.15 are both a little asymmetric which might be related to the STM tip. The black spectrum, taken at the upper left GNR corner, reveals the typical end state peak with a peak maximum at (15 ± 7) mV and a FWHM of (30 ± 15) mV. At the position of the intercalated Co atom (red spectrum), on the other hand, the peak maximum shifted to (5 ± 5) mV. The curve became also narrower and now exhibits a FWHM of (18 ± 16) mV.

4.5.2. Co at 3rd position

After presenting the case of an intercalated Co atom that is well separated from the GNR zigzag edge, the situation will be discussed in which the Co atom is buried closer to the zigzag terminus. To do so, a Co atom was manipulated underneath the third hexagon counted from the zigzag end, creating a Co-(3)-GNR-complex.

Fig. 4.16 (a) shows an STM image of a GNR end with a Co atom buried at position (3) along with a sketch that indicates the intercalation site and the locations where dI/dV spectra were taken.
At the zigzag edge, the finger-like structure of the end state is present. At the lower armchair edge at position (3), there is a faint protrusion visible which is absent at the opposing position (3') at the upper edge. This protrusion stems from the intercalated Co atom. Its appearance is not as pronounced as that of a Co atom buried at the middle of the armchair edge.

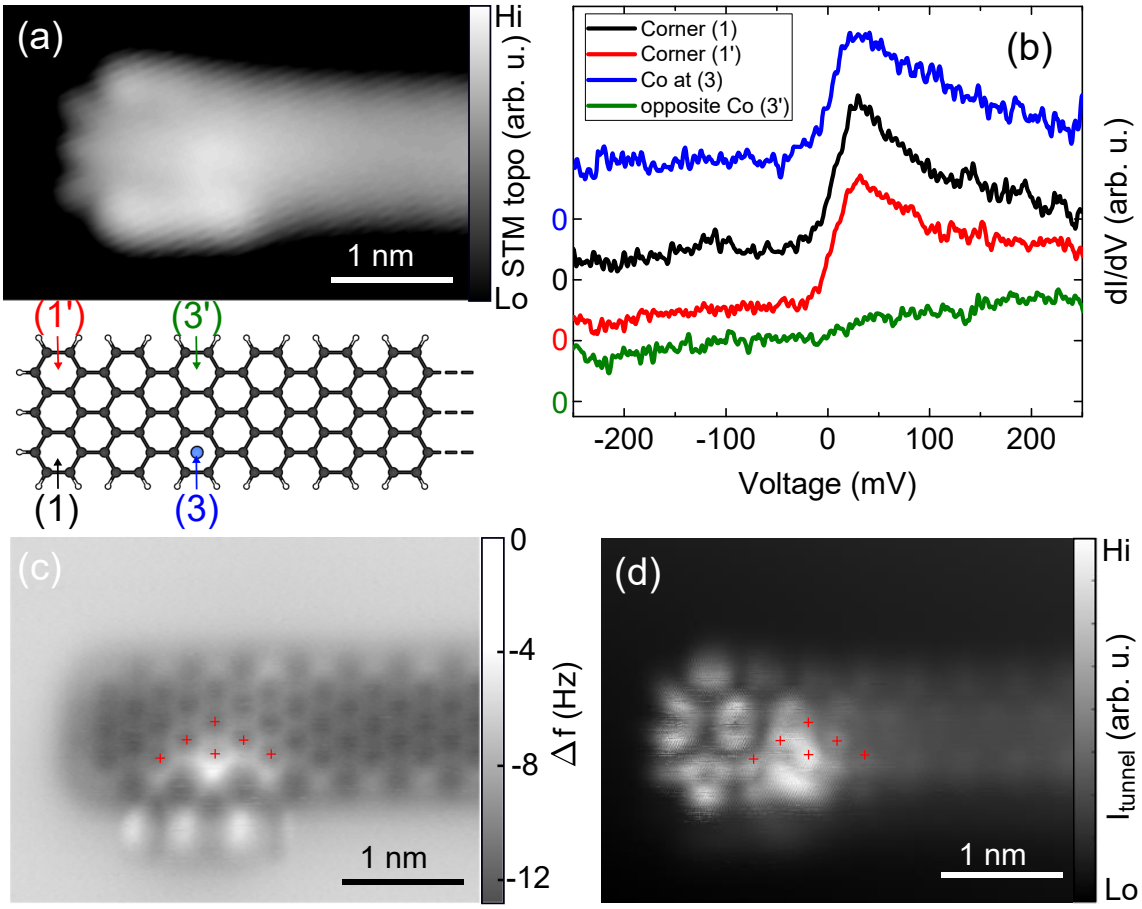

Figure 4.16.: **Co at 3rd position.** (a) Upper panel: STM image ($V_{bias} = 20\,\mathrm{mV}$, $I_{tunnel} = 48\,\mathrm{pA}$, low pass filtered). Lower panel: Sketch of Co intercalation position. (b) dI/dV spectra taken at positions indicated in (a). (c) Constant height AFM image of another Co-(3)-GNR-complex. The fourfold protrusions below the GNR are presumably artifacts from a trapped H atom. (d) Current map of the area shown in (c). The red crosses in (c) and (d) mark the same positions.

To verify the exact Co intercalation position, an AFM image with a CO-terminated tip of a Co-(3)-GNR-complex was recorded. This image can be seen in Fig. 4.16 (c) and clearly shows the 3rd carbon ring along the lower armchair edge as Co interca-

lation site.
The fourfold feature below the GNR is a measurement artifact. Presumably a hydrogen atom got trapped in the vicinity of the buried Co atom. During the scanning process, the AFM tip might have pushed or dragged the H atom along the fast scanning direction, which lies horizontally. Thereby, the H atom could have jumped to the energetically most favorable positions which—in this case—are the four spots below the lower GNR edge.

Fig. 4.16 (b) shows dI/dV spectra taken at the positions indicated in panel (a). The spectra at the GNR corners (positions (1) and (1'), black and red curve, respectively) exhibit the GNR end state peak which is a little asymmetric here. The maxima of both end state peaks are located at (30 ± 3) mV and the curves possess a FWHM of (52 ± 35) mV which is in line with previous observations. The high uncertainty in the determination of the FWHM stems from the asymmetry of the line shape.
When taking a spectrum at the clean armchair edge (position (3'), green line), the dI/dV curve is featureless, as expected.
The spectrum at the Co intercalation site (position (3), blue line), however, is not shifted to 0 mV as for Co atoms placed at the middle of the armchair edge. Instead, its maximum lies at (31 ± 15) mV and it has a FWHM of (54 ± 56) mV, practically identical as for the spectra taken at the GNR corners. Also the shape of the dI/dV curve resembles the one of the end state peaks.

It is not obvious, why the Kondo resonance cannot be observed for the Co-(3)-GNR configuration. There are multiple possible reasons.
One approach is to argue that the Kondo effect is quenched.
As discussed in the theory part, the Kondo effect is known to be very sensitive to the coupling of the magnetic impurity to the substrate. In our situation, the coupling of the Co atom to the Au substrate could be changed by the presence of the GNR and therefore the Kondo effect could become quenched.
A possible way the GNR might influence the coupling of Co and Au(111) is by its own electronic structure. Therefore, we take a look at the current map shown in Fig. 4.16 (d). One can see the V-shaped fingerprints of the end state located at the left GNR zigzag terminus. Additionally, a pronounced, roundish feature with a nodal plane is visible at the lower armchair edge. By relating AFM image and current map with the help of red marker crosses, the position of this feature is found to be the site of the intercalated Co atom and the nodal plane coincides with the lattice structure of the GNR.
Interestingly, it seems as if the end state extends along the lower armchair edge up to the intercalated Co atom site. The extension is manifested in a higher LDOS at the lower edge compared to the upper edge and the end state peak can also be found in dI/dV spectra at position (2) (not shown here). This means that there might be hybridization between the Kondo resonance and the end state.
Further evidence for this hypothesis can be found in the following. Upon taking a closer look at the bright protrusion in the current map caused by the Co atom, subtle differences between site (3) and site (4) can be found. Whereas for Co placed at

position (4) the enhanced LDOS seems to be located mostly within the GNR frame, it apparently spreads more to the GNR periphery for position (3): The round feature is shifted slightly more outwards of the GNR frame rather than to its center. To make this point clearer, a comparison of both, Co-(3)-GNR and Co-(4)-GNR, ends is shown in Fig. 4.17 and the atomic lattice is overlaid for better orientation. The

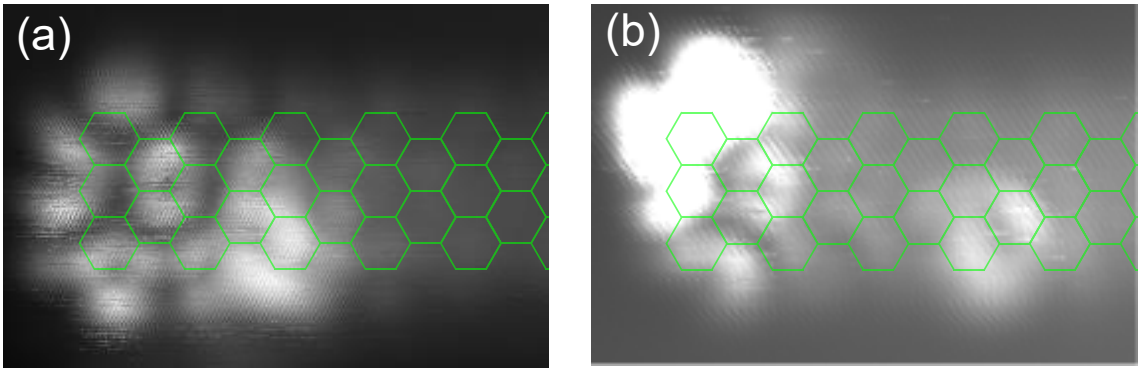

Figure 4.17.: **Nodal structure.** Zoom-in into the current maps of (a) the Co-(3)-GNR-complex and (b) the Co-(4)-GNR-complex. The atomic lattice of the GNR is overlaid with green lines.

reason for this slightly different appearance might be that position (3) lies just at the border where the end state fades out. In the vicinity of the zigzag terminus, the GNR gets broader in STM images, as can be seen in the finger-like structure of the end state. When coupled to the end state, the Co states could also spread out a little. That might be the reason why the round feature in the current map extends more towards the GNR periphery than for a Co atom placed at position (4) and hints towards hybridization of Co states and end state.
This hybridization might prevent the Kondo effect from appearing. The GNR—which is p-doped on the Au(111) surface—could try to take back some charge from the Co atom. This, in turn, might change the hybridization of Co and Au surface and therefore quench the Kondo resonance. When taking dI/dV spectra of this region, hence the end state would be dominant.

On the other hand, one could assume that the coupling between Co atom and Au surface is not substantially changed by the presence of the GNR and the Kondo effect is present. The question to answer in this approach is why the Kondo resonance is not visible.
One way is to argue that the GNR with its end state is spatially closer to the STM tip than the Co atom. This might result in primarily probing the end state instead of the Kondo resonance.
On the other hand, the Kondo resonance was shown to be relatively insensitive to the tip-sample distance [165]. Furthermore, as will be shown in the next section, the intercalation of Co at the GNR corner does not necessarily yield an end-state-like

spectrum.
Another way to argue is that the observation of the Kondo effect by the STM tip could be hindered by the electronic structure of the GNR present between tip and Co atom.
The orbital structure of the GNR could influence the current path from the STM tip to the Co atom and the substrate. It is possible that there is a nodal plane of the GNR orbitals which coincides with position (3) where the Co is buried. Therefore, the coupling between the tip orbitals and the spin-carrying Co *d*-orbitals might be suppressed.
As was already pointed out, Wang *et al.* [132] indeed showed a confinement of the end state to an area of roughly 1.5 nm from the zigzag end. That means position (3) is at the crossover point of the end state to be present and to vanish and it seems plausible that a nodal plane of GNR orbitals could appear here. This can also be concluded from tight-binding [128] and DFT [198] calculations.
Therefore, when taking a dI/dV spectrum at position (3) only the end state of the nearby zigzag end might contribute to a signal around the Fermi energy, whereas the states from the Co atom are masked.

Overall, 3 different Co-(3)-GNR-complexes were assembled. They all showed qualitatively the same behavior, i. e. an apparent extension of the end state up to the position of the intercalated Co atom and an end-state-like peak in dI/dV curves taken at the Co intercalation site. Only one of those complexes showed signs of a trapped H atom in the vicinity of the GNR. Thus, the H atom as source for the end-state-like peak appearance can be ruled out.

4.5.3. Co at corner position

Now, the Co atom will be placed even closer to the zigzag edge. Experimentally, it was not possible to create a complex with a single Co atom at position (2).
Therefore, the next configuration that will be discussed is that of a Co atom placed at the GNR corner. Fig. 4.18 shows the left end of a Co-(1)-GNR-complex and its spectroscopic characterization. In the upper part of panel (a) an STM topography image is displayed (see Fig. 4.12 (d) for a high-resolution STM image of an entire Co-(1)-GNR-complex). The finger-like structure typical for the end state is gone at this GNR end. Instead, the corner of the intercalated Co atom looks bright and roundish.
Panel (c) shows a constant-height AFM image recorded with a CO-terminated tip. One can see that the carbon ring at site (1) shows the highest repulsion confirming that the Co atom is intercalated at the corner position.

The height by which the Co-intercalated GNR corner is lifted with respect to the rest of the GNR was determined. For this purpose, the STM feedback loop was switched off and then the tip was moved to the center of the GNR. Subsequently, the tip was lowered towards the sample surface and the frequency shift sensed by

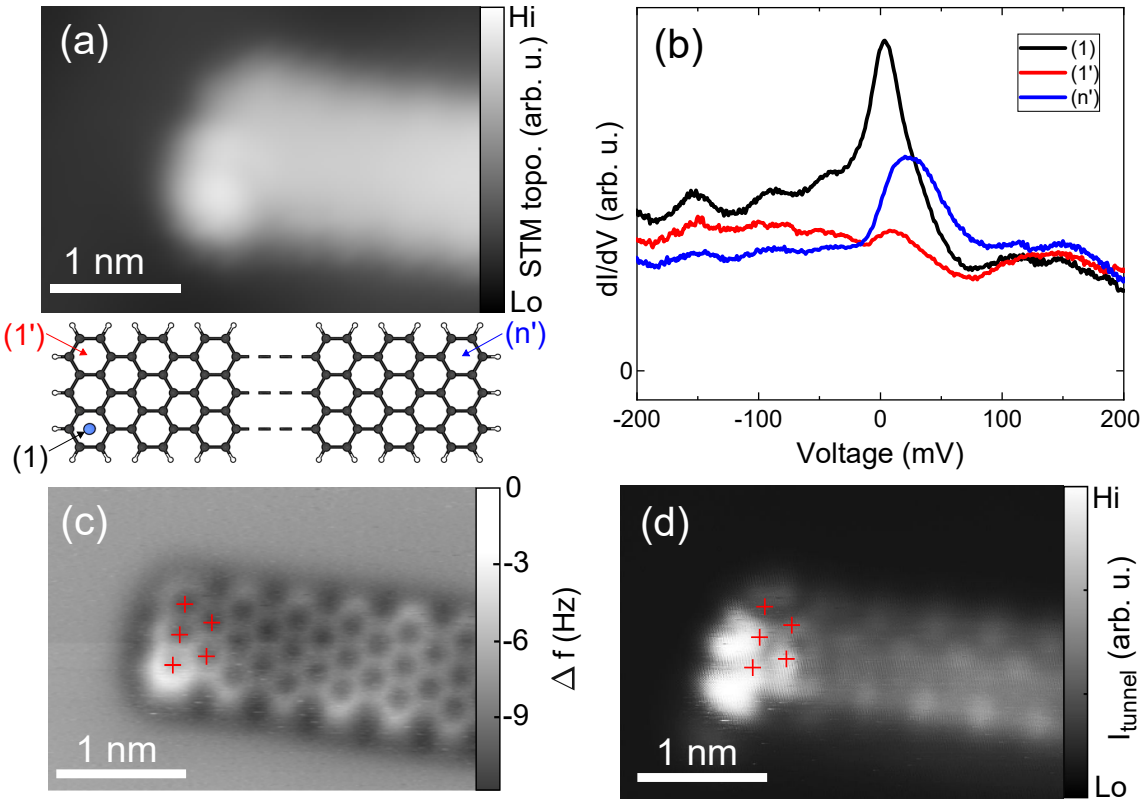

Figure 4.18.: **Co at corner position.** (a) STM image of a Co-(1)-GNR-complex (V_{bias} = 3 mV, I_{tunnel} = 50 pA, low pass filtered). The sketch illustrates the configuration. (b) dI/dV spectra taken at positions indicated in the sketch in (a). (c) Constant height AFM image and (d) current map of the complex shown in (a).

the AFM channel was recorded. The corresponding data are plotted in Fig. 4.19 as a blue line. Note that positive z values are measured from the STM set point and mean that the tip is approaching the surface. One can see a minimum in the Δf-z line at a distance of 2.7 Å corresponding to a transition from the attractive to the repulsive tip-sample-interaction regime [199].
When taking the same spectrum above the Co intercalated corner (black line), the frequency shift reaches its minimum at a distance of 2.4 Å from the set point. Thus, the STM tip needs to be lowered less by a distance of 0.3 Å to enter the repulsive regime. Accordingly, this difference poses an approximation of how much the GNR is pushed upwards by the presence of the Co atom. Interestingly, the spectrum above the pristine corner (red line) shows a minimum at 2.6 Å. That means that the pristine corner is also slightly pushed upwards, but not as strongly as the Co intercalated corner. Presumably, due to the stiffness of the GNR, the Co atom causes a small distortion of the GNR end.

Next, the dI/dV spectra shown in Fig. 4.18 (b) were taken at the positions indicated by color coded arrows in the lower part of panel (a). First of all, the spectrum taken

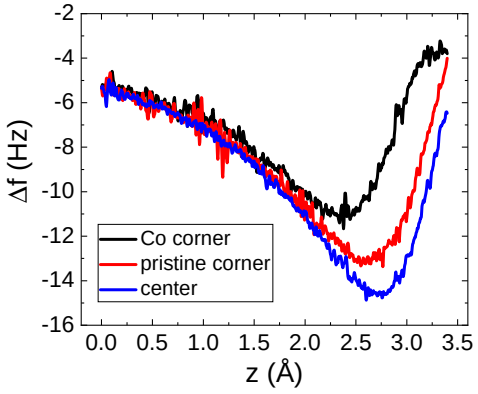

Figure 4.19.: **Δf-z spectra.** Frequency shift as function of tip height recorded at the Co intercalated corner (position (1), black line), the pristine corner (position (1'), red line) and the center of the GNR (blue line). Positive z values refer to a decreasing tip-sample separation.

at the corner (n') of the right, pristine GNR end (blue line, corner outside of STM frame) displays the well-known end state. The peak is centered at (21 ± 3) mV and has a FWHM of (42 ± 15) mV.
At the Co intercalated corner, the shape of the differential conductance spectrum reveals a change. The maximum position of the peak shifted to (1 ± 3) mV and the peak got narrower with a FWHM of (28 ± 14) mV. The line shape now resembles the Kondo-like line shape observed for Co intercalation at the middle of the armchair edge, although exhibiting a slightly broader FWHM here.
Interestingly, the adjacent corner at site (1') yields an essentially featureless spectrum, i. e. the end state peak is missing at this corner.

We now turn for a moment to the current map that was recorded simultaneously to the AFM image and is shown in Fig. 4.18 (d). Here, one can see pronounced LDOS at the site of the intercalated Co atom. With the help of the red marker crosses it becomes clear that the enhanced LDOS is not only localized at the Co corner but also spreads over its neighboring two carbon rings and also outwards of the GNR.
At position (1'), however, there is low LDOS—comparable to the LDOS at the bulk of the GNR. This is consistent with the observation that no end state was found at this site in the dI/dV spectra.

It is not clear why the end state is disappearing at one corner when a Co atom is intercalated at the corner close by.
One possible reason is that the zigzag edge might be slightly bent by the intercalation of a Co atom at one corner. Therefore, strain could lead to the disappearance of the end state. However, as will be shown in the next section, the intercalation of a Au atom at the corner does preserve the end state.
More probable seems to be the reasoning that end state and Co states hybridize to *one* state that is localized at the Co intercalated corner and therefore missing at the other corner. Indications for this hybridization can be found in the current map:
First, remnants of the V-shaped feature typical for the end state (recorded with a CO tip) are visible at the middle of the zigzag edge.
A second indication is the spatial distribution of the end state observed in STM

images. There, one can see that the GNR ends exhibiting the end state appear broader than their counterparts lacking the end state. Here, the enhanced LDOS at corner (1) is not only located within the GNR frame but spreads relatively far towards the GNR periphery. Thus, a hybridization of Co state and end state seems likely.

A possible reason for the localization of the resonance at one corner only can also be found in the framework of the Smoluchowski effect. This effect generally refers to the redistribution of the electron cloud on metal surfaces with strong corrugations. To minimize the kinetic energy of the electrons, the charge distribution at a surface corrugation—like a step edge or an adatom—is smoothed out (see Fig. 4.20). This leads to the formation of an effective dipole at the place of the adatom.

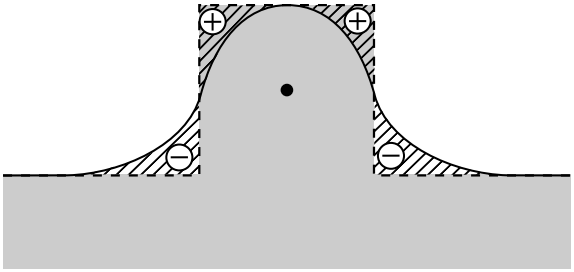

Figure 4.20.: **Smoluchowski effect.** The electron charge distribution (gray) of a surface with an adatom on top (black point) is shown with a rectangular distribution (dashed outline) and smoothed by the Smoluchowski effect (solid outline). The change in charge distribution (shaded areas) induces a local dipole (indicated by round charges).

In the case of a Co-(1)-GNR-complex, the intercalated Co atom might induce a dipole, thus deflecting the potential along the GNR. This could result in a local potential minimum at the Co intercalated corner and therefore restrict the hybridized state—consisting of end state and Co state—to one corner only.

The peak shape of the dI/dV curve taken at position (1) can now be revisited. The maximum at nearly 0 mV points towards a Kondo resonance induced by the magnetic Co atom buried at the corner. Its FWHM, however, is broader than that of a Co buried at the middle of the armchair edge. This might be a result of the hybridization between the narrow Kondo resonance and the wider end state taking place at the corner.
Extracting the Kondo temperature from the FWHM yields $T_K = (160^{+164}_{-84})\,\mathrm{K}$ for the corner position. The high (and asymmetric) uncertainty margin stems from the peak asymmetry and thermal broadening. A fit of Eq. 4.3 to the dI/dV curve from Fig. 4.18 (b) gives $\mathrm{T}_K = (200 \pm 7)\,\mathrm{K}$ (the corresponding fit curve can be seen in A.1 in the Appendix). The much lower uncertainty for the fit results from the restricted data window from $-20\,\mathrm{mV}$ to $+20\,\mathrm{mV}$ that is used to fit the curve here.
Both of these values are substantially higher than the Kondo temperature obtained for a Co at the middle of the armchair edge.

In total, 7 different Co-(1)-GNR-complexes were assembled, all showing qualitatively

the same spectroscopic fingerprints. The average maximum position was at (0 ± 4) mV exhibiting a mean FWHM of (30 ± 10) mV. The uncertainty margins refer to the standard deviation from the mean value.
The FWHM measured here is roughly 50 % higher than for the Co intercalated at the middle of an armchair edge. This might be due to a hybridization between GNR end state and Co Kondo resonance for the Co-at-the-corner position. Accordingly, the Kondo temperature obtained here is also higher than for the Co-(4)-GNR-complex.

4.5.4. Adding Co to 2nd corner

Next, we investigated the influence of several Co atoms intercalated at the same GNR.
For this purpose, we manipulated a Co atom towards the unoccupied corner (1) of a Co-(1')-GNR-complex (the one that is shown in Fig. 4.12), thus creating a 2-Co-(1,1')-GNR-complex. Regarding the nomenclature, the "2" in front signalizes the number of Co atoms intercalated at the GNR. The intercalation positions are given in the brackets.
Fig. 4.21 (b) and (c) show the addition of a second Co to the GNR end. In panel (b), an STM image of the situation before the manipulation is shown. A single Co atom can be seen adjacent to the end of a Co-(1')-GNR-complex. The white arrow describes the path of the STM tip during manipulation. Panel (c) displays the GNR after successful intercalation of the second Co atom.

In panel (a), a high-resolution STM image of the whole complex can be seen alongside a sketch indicating the positions of the intercalated Co atoms and the locations where differential conductance spectra were taken. Corner (1) and corner (1') now both exhibit the same roundish appearance typical for a Co buried at the GNR corner. The pristine GNR end shows the finger-like end state structure.

dI/dV spectra reveal the typical end state peak at the pristine GNR corners. The curve at position (n) has its maximum at (27 ± 4) mV and a FWHM of (44 ± 8) mV and the line at position (n') peaks at (22 ± 4) mV with a FWHM of (36 ± 12) mV. The two spectra are very similar, as could be expected, with a little lower signal intensity for corner (n).
The slight elevations at −40 mV and +100 mV are also visible in the background spectrum (not shown here) and are therefore considered to stem from the tip.
The spectra taken at the Co intercalated corners look less alike. First of all, both exhibit the side bumps at −40 mV and +100 mV. Furthermore, the spectrum at corner (1') provides a maximum at (3 ± 4) mV and a FWHM of (18 ± 14) mV, thus appearing like a Kondo resonance. The line shape at corner (1) has its maximum more or less at the same position, i. e. (6 ± 5) mV. However, it is clearly broader with a FWHM of (46 ± 7) mV and exhibits also overall lower signal intensity.
The peak position and the fact that a Co atom is intercalated give reason to interpret

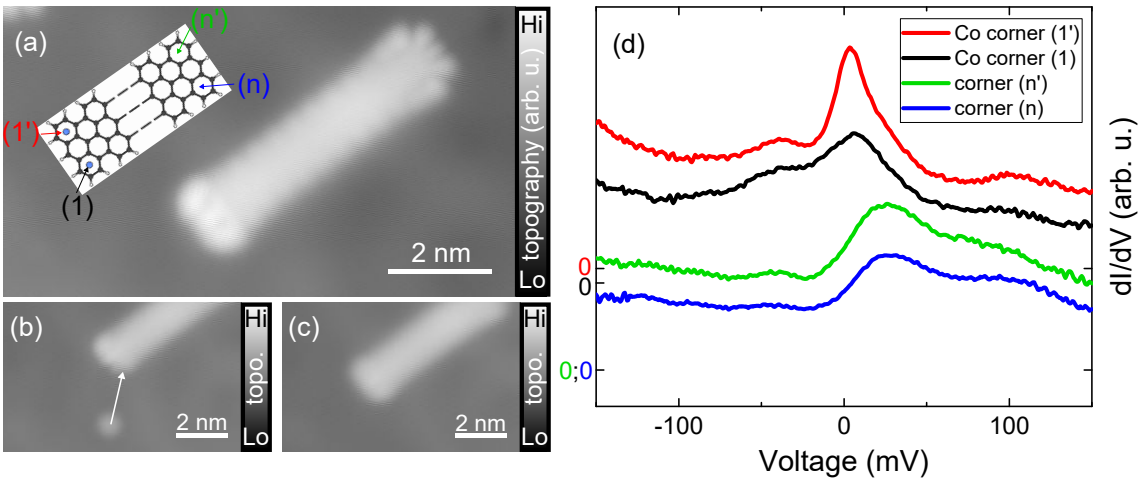

Figure 4.21.: **2 Co atoms at the corners.** (a) High-resolution STM image of a 2-Co-(1,1')-GNR-complex with Co atoms intercalated at sites (1) and (1'). The inset shows the positions of the Co atoms and color coded arrows point to the locations where dI/dV spectra were taken. $V_{bias} = 2\,\mathrm{mV}$, $I_{tunnel} = 48\,\mathrm{pA}$. (b) shows the GNR end before and (c) after the manipulation process. $V_{bias} = 100\,\mathrm{mV}$, $I_{tunnel} = 11\,\mathrm{pA}$, images low pass filtered. (d) dI/dV spectra taken at the positions indicated in (a).

the line shape at corner (1) as a Kondo resonance that is substantially broadened. Furthermore, both Co intercalated corners appear identical in STM images, thus suggesting that the Co intercalation affected both corners in the same way.
The reason for the stronger broadening of the Kondo resonance of corner (1) remains unclear. It has to be noted that both spectra taken at the corners of the lower armchair edge yield a lower signal intensity than at the upper edge. Possibly, the tip shape or the position of the GNR with respect to the substrate are accountable for the lower signal intensity and the larger state broadening, as will be discussed later.

In total, two 2-Co-GNR-complexes were fabricated. The other one, a 2-Co-(1,1')-GNR-complex, is shown in Fig. 4.22.
Panels (b) and (c) depict the manipulation process. A high-resolution STM image of the complex can be seen in panel (a), together with a sketch indicating the intercalation sites of the Co atoms (blue spheres) and places of dI/dV spectra. Corner (1) and corner (1') at the right GNR end exhibit the same roundish appearance as the previously discussed 2-Co-GNR-complex. The pristine GNR end shows the finger-like end state structure.
Close to the left GNR end, at the lower armchair edge, two defects can be seen. These are presumably dehydrogenated armchair lobes.

A dI/dV spectrum at position (n) reveals the typical end state peak. It has its maximum at $(10 \pm 3)\,\mathrm{mV}$ and a FWHM of $(32 \pm 74)\,\mathrm{mV}$. The spectrum is quite

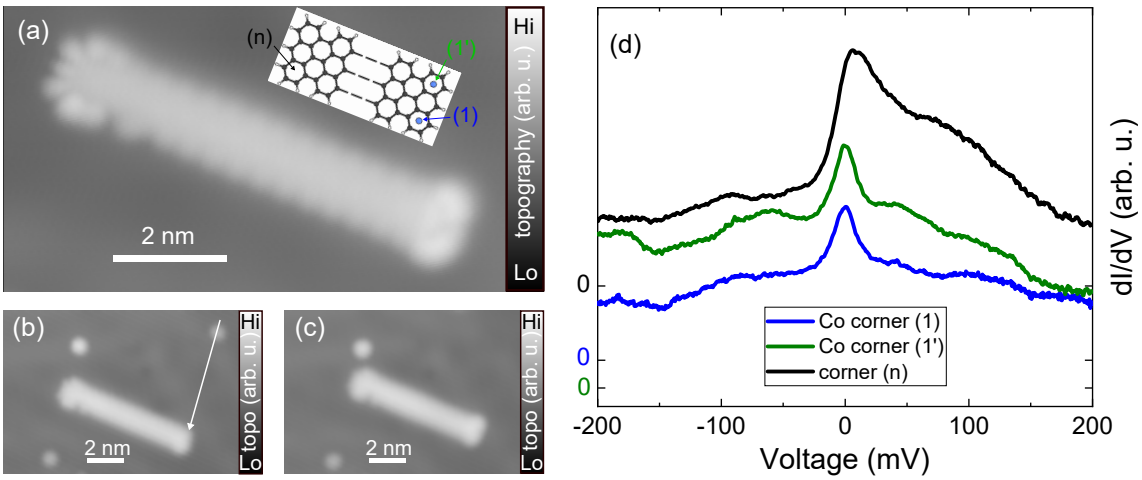

Figure 4.22.: **Second 2-Co-GNR-complex.** (a) High-resolution STM image of a 2-Co-(1,1')-GNR-complex with Co atoms intercalated at sites (1) and (1'). The inset shows the positions of the Co atoms and arrows point to the locations where dI/dV spectra were taken. $V_{bias} = 2\,\mathrm{mV}$, $I_{tunnel} = 48\,\mathrm{pA}$, image low pass filtered. (b) shows the GNR before and (c) after the manipulation process. $V_{bias} = 100\,\mathrm{mV}$, $I_{tunnel} = 11\,\mathrm{pA}$, images low pass filtered. (d) dI/dV spectra taken at the positions indicated in (a).

asymmetrically broadened which might be related to the STM tip. The two shoulders on the right flank, broadening the peak, can also be observed in the spectra taken at the Co intercalated corners—less pronounced though in the latter case.

The spectra taken at the Co intercalated corners resemble both Kondo resonances and are very similar to each other. At corner (1') the curve provides a maximum at $(2 \pm 3)\,\mathrm{mV}$ and a FWHM of $(18 \pm 10)\,\mathrm{mV}$. Corner (1) basically provides the same line shape with its maximum at $(3 \pm 3)\,\mathrm{mV}$ and a FWHM of $(18 \pm 8)\,\mathrm{mV}$. The signal level of the spectrum at corner (1) is lower than for corner (1'). Possibly, an asymmetric tip or the position on the substrate might be accountable for this difference in signal intensity.

Unlike the previously discussed complex, the two spectra at the Co intercalated corners look almost identical here and both are substantially less broadened. A possible reason for this behavior might be the adsorption geometry of the two GNRs with respect to the Au(111) surface.
Both 2-Co-GNR-complexes presented in this section are oriented along the hexagonal-close-packed direction of the Au surface atoms. A scheme for this configuration is given in Fig. 4.23 (a). The GNR (black mesh) is placed on the Au atoms (yellow circles) in such a way that the corner hexagons of the GNR zigzag edge are placed above hollow sites of the Au surface. In this way, two intercalated Co atoms, one at each GNR corner, are located underneath the center of the carbon hexagon rings

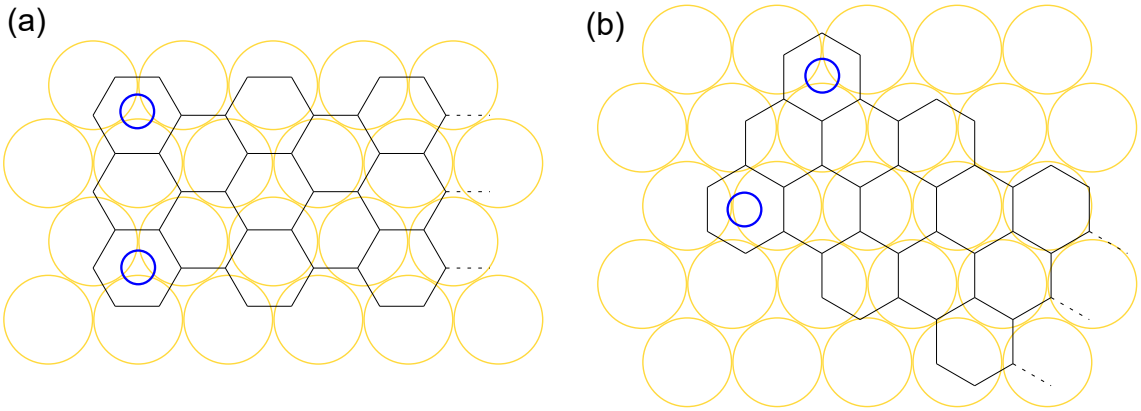

Figure 4.23.: **Orientation of GNR with respect to Au(111) surface.** Model of the hexagonal-close-packed atoms of the Au(111) surface layer (yellow circles) and a 7-aGNR (black mesh) adsorbed on it. The blue circles symbolize Co atoms intercalated at the GNR corners. The GNR is depicted (a) in parallel and (b) perpendicular to the direction of close-packed atoms of the Au(111) surface.

and at the hollow sites of the Au surface at the same time.
In panel (b), a GNR is sketched that is oriented perpendicular to the hexagonal-close-packed direction. In that case, only one of the Co atoms coincides with a hollow site whereas the second Co atom has to sit close to a bridge site. Therefore, this position is energetically unfavorable.
One has to add that the distances in Fig. 4.23 are the literature values for a Au–Au nearest neighbor distance of 2.9 Å and a C–C bond length of 1.4 Å, like in graphene. In a real system, slight deviations due to relaxations because of the intercalated Co atom or the H termination of the GNR edges might occur [200].
Both 2-Co-GNR-complexes are oriented along the hexagonal-close-packed direction (as in Fig. 4.23 (a)), but a possible difference is that the GNR from Fig. 4.21 ends on a herringbone reconstruction crest, whereas the GNR from Fig. 4.22 is lying entirely in a fcc packed region. Therefore, slight asymmetries in the positions of the two Co atoms with respect to both, the GNR and the Au(111) surface, might be more pronounced for the first complex and therefore explain the enhanced broadening of one of the corner states.

4.5.5. Adding Co to 3rd corner

Further, an additional Co atom was added to an unoccupied corner of the 2-Co-complex from Fig. 4.21. The assembly and characterization of this new 3-Co-(1,1',n)-GNR-complex is shown in Fig. 4.24. Panel (b) displays an STM image before the manipulation. A Co atom can be seen adjacent to the 2-Co-(1,1')-GNR-complex. The white arrow indicates the path along which the Co atom is manipulated. The

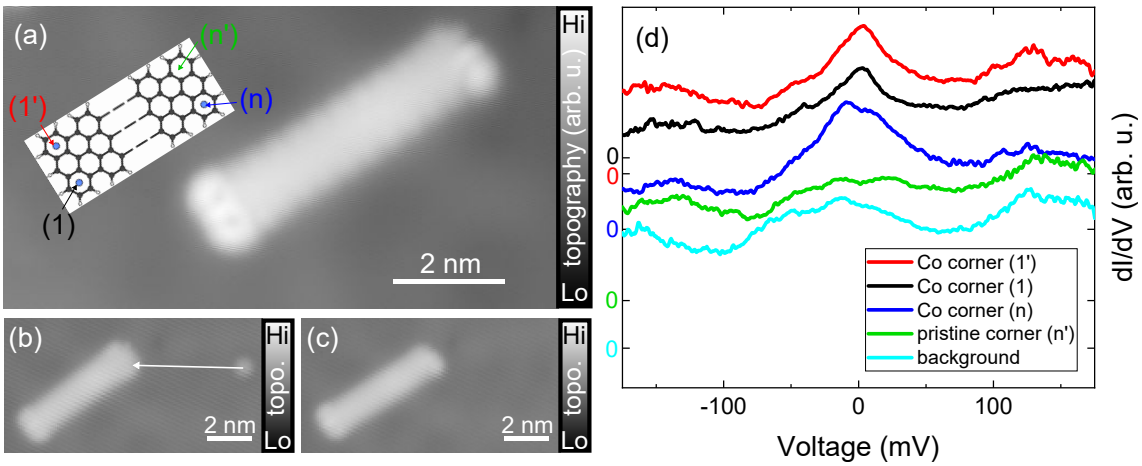

Figure 4.24.: **3 Co atoms at the corners.** (a) High-resolution STM image of a 3-Co-(1,1',n)-GNR-complex. Inset indicating the positions of the Co atoms and the recorded dI/dV spectra. $V_{bias} = 2\,\mathrm{mV}$, $I_{tunnel} = 48\,\mathrm{pA}$. (b) and (c) show the manipulation process. $V_{bias} = 100\,\mathrm{mV}$, $I_{tunnel} = 11\,\mathrm{pA}$. (d) dI/dV spectra taken at the positions indicated in (a) and reference spectrum on Au(111).

result of the successful intercalation is shown in panel (c).
Panel (a) depicts a high-resolution STM image of the 3-Co-(1,1',n)-GNR-complex. The inset sketches the Co intercalation positions and points to the sites of the dI/dV spectra presented in panel (d). The right, singly intercalated GNR end exhibits a bright, roundish feature at corner (n), as typical for a Co buried at the corner position. The left GNR end, intercalated with 2 Co atoms at its corners, shows the same roundish shapes at its corners.

In panel (d), differential conductance spectra taken at this complex are presented. To start with, the turquoise line shows a reference spectrum of the pristine Au(111) surface recorded next to the 3-Co-GNR-complex. Note the little ridges at $-10\,\mathrm{mV}$ and $+120\,\mathrm{mV}$, as they appear also in the other spectra and are related to the STM tip.
The spectra at the doubly Co intercalated edge look rather similar and both exhibit a Kondo-like peak shape, though being quite broadened. The black curve at position (1) has its maximum at $(1 \pm 4)\,\mathrm{mV}$ and a FWHM of $(24 \pm 10)\,\mathrm{mV}$. The red spectrum at site (1') shows a peak at $(3 \pm 4)\,\mathrm{mV}$ and its FWHM measures $(50 \pm 16)\,\mathrm{mV}$, therefore being even broader. Both peaks exhibit an untypically broad left shoulder. This can be explained by the presence of an additional bump in the spectra at $-10\,\mathrm{mV}$ due to the STM tip which is also visible in the reference spectrum on the pristine Au(111) surface.
Furthermore, the signal intensity at site (1) is lower. The effect of lower signal intensity for the lower armchair edge was already observed in the previous section for the same complex before the 3rd Co atom was added and is probably related to an

asymmetry of the STM tip or the position of the GNR on the surface.
At the other GNR end, the green line of the spectrum at the pristine GNR corner (n') is following the shape of the background spectrum, i. e. no states peculiar to the GNR are probed here. This is in line with the absence of an end state for the pristine corner of a singly Co intercalated GNR end as already described in section 4.5.3.
The blue spectrum, taken at the site of the buried Co atom (n) of the singly intercalated GNR end, on the other hand, displays a double peak structure. The left one of the peaks, situated at roughly $-10\,\mathrm{mV}$ can be assigned to the already discussed tip related state. The second peak lies at $(4 \pm 4)\,\mathrm{mV}$, and therefore in the same bias range as the other Kondo peaks discussed for Co intercalation at a corner. Due to the double peak structure the peak is relatively broad with a FWHM of $(76 \pm 21)\,\mathrm{mV}$.

These observations show that intercalating a Co atom at a GNR corner always leads to the same result (i. e. a Kondo peak), independently of the configuration at the other GNR end—be it two intercalated Co atoms or a pristine end. That indicates that both GNR ends are electronically decoupled and independent of each other.

It was not possible to add a 4th Co atom to the 3-Co-GNR-complex. The attempt led to a pick up of the whole GNR structure.

4.5.6. Au atom at corner position

To investigate the role of the intercalated atom, a nonmagnetic Au atom instead of Co was buried underneath the corner of a GNR. Single Au atoms were brought onto the Au(111) surface by gentle tip indentations into the surface as described in section 4.3.3, carefully discerning between Co atoms already present on the surface and freshly added Au atoms. The Au-GNR-complexes were built in the same way as the Co-GNR-complexes (illustrated in Fig. 4.12) by tip-induced manipulation.

Fig. 4.25 shows an STM image of a GNR with a Co atom intercalated at corner (1) and a Au atom intercalated at corner (n'). The two corners look qualitatively differ-

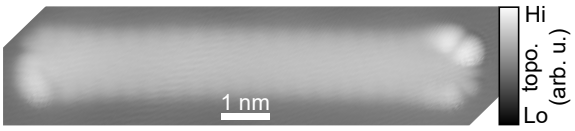

Figure 4.25.: **Au and Co at one GNR.** STM image of a GNR with an intercalated Co (bottom left corner) and Au (top right corner) atom. $2\,\mathrm{mV}$, $I_{tunnel} = 48\,\mathrm{pA}$.

ent. The Co corner (1) appears more roundish whereas the Au corner (n') exhibits the finger-like structure typical for the end state. Furthermore, the Au intercalated corner appears brighter in the STM image pointing towards either higher LDOS or enhanced height at this region. Both of these options would result in an increased

current flow from sample to STM tip and therefore appear brighter in the STM topography channel.

To characterize the impacts of the intercalated Au atom on the electronic properties of the GNR, dI/dV-spectra were recorded at a Au intercalated GNR corner and compared to a pristine GNR end. Fig. 4.26 (a) shows an STM image of a Au-(n')-

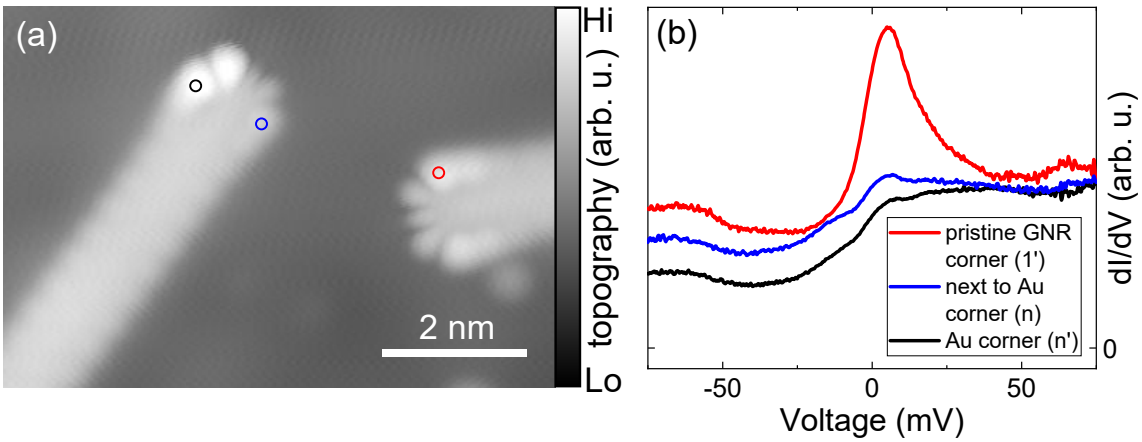

Figure 4.26.: **Au at corner position.** (a) STM image of a Au-(n')-GNR-complex (left) next to a pristine GNR end (right). $V_{bias} = 2\,\text{mV}$, $I_{tunnel} = 48\,\text{pA}$. (b) dI/dV spectra taken at the positions indicated by colored circles in (a).

GNR-complex (left) next to a pristine GNR end (right). The colored circles indicate the locations of the dI/dV spectra displayed in panel (b).
The spectrum taken at corner (1') of the pristine GNR (red curve) exhibits an end state peak. The peak maximum lies at $(6 \pm 3)\,\text{mV}$ and the FWHM of $(16 \pm 8)\,\text{mV}$ is relatively narrow in this case.
At the Au intercalated corner (n') (black line), however, a clear peak is missing in the spectrum. The same holds true for the corner (n) next to the intercalated Au atom (blue curve). One can see an increase in signal intensity from negative voltages towards 0 (i. e. a left flank), but the signal is not decreasing towards higher voltages (i. e. no right flank is present). There is, however, a tiny peak located at $(7 \pm 3)\,\text{mV}$, so at the same energetic position as the end state peak at the pristine GNR corner. This hints towards the presence of the peculiar GNR end state at the Au intercalated GNR end—as also evidenced by the survival of the finger-like structure in the STM image.
Obviously, the Au atom at the corner weakens the signal from the GNR end state. A possible reason for this behavior could be the distortion of the zigzag edge by the upwards bending of the GNR due to the intercalated Au atom. Additionally, the hybridization of the GNR end with the metal surface might be changed by the presence of the extra Au atom.

Evidence for the strong upwards bending of the GNR zigzag end by the Au atom can

be found in the AFM image of the Co-(4)-GNR-complex in Fig. 4.14 (c). There, the Au intercalated corner appears very bright, pointing towards high repulsion. This observation is less pronounced for a Co buried at the corner (c. f. Fig. 4.18 (c)). One can conclude that the repulsion of the Au atom acting on the GNR corner is stronger than the one exerted by a Co atom at the corner position. This might be due to the fact that the atomic radius of Au is larger than that of Co and Au thus occupies more space underneath the GNR. Additionally, Au is more inert than Co. Therefore, Au atom states might hybridize less with the GNR end state, thus resulting in higher repulsion between atom and GNR corner.
Furthermore, different levels of hybridization could explain the different appearances of the Co and Au intercalated corners (as seen in Fig. 4.25). Strong hybridization between Co atom and end state leads to the roundish appearance observed at the Co-intercalated corner, as discussed in section 4.5.3.
The weaker hybridization between Au and GNR, on the other hand, preserves the peculiar finger-like appearance of a pristine GNR end. The presence of the end state at a Au intercalated corner can be also observed in dI/dV spectra, as shown in Fig. 4.26, although only faint remnants of the end state peak can be found in the spectra.

The conclusion can be drawn that the simple presence of an intercalated atom is not enough to convert the end state into a zero-bias resonance. Apparently, the Au atom does not cause a zero-bias anomaly as does the Co atom. This is further indication that the resonance is caused by the magnetic properties of the Co atom and therefore related to the Kondo effect.

4.5.7. DFT calculations

To help to understand the experimental results, DFT calculations were performed by Tobias Frank and the results will be presented in this section.
To model our system, a 7-aGNR with a length of 8 anthracene units was placed on three layers of Au atoms in a (111) surface configuration. The GNR was saturated with hydrogen atoms. In experiment, the GNRs had varying lengths, most of them being longer than this model. The end states of the GNR, however, have been shown to barely depend on the GNR length[9] [132]. Therefore, it is justified to use this model for DFT simulations, since DFT calculations of longer GNRs including a substrate is computationally too expensive. The intercalated Co atom was placed on a hcp position of the Au(111) surface. The GNR was shifted in such a way that the Co atom resided in the center of one of its outer hexagon rings, which is consistent with the experiment.

A Co atom was placed at four different intercalation sites: site (1), (2), (3) and (4). In Table 4.1 the total energy of the system for the different configurations can

[9]apart from overlapping of end states of opposite zigzag edges for very short GNRs

configuration	μ_{Co}	$\Delta E[eV]$
Co-(1)-GNR	1.727	0.0000
Co-(2)-GNR	1.758	0.1436
Co-(3)-GNR	1.765	0.1812
Co-(4)-GNR	1.764	0.2149

Table 4.1.: **System energetics and magnetic moment of Co atom for different Co-GNR-complexes.** The magnetic moment of the Co atom μ_{Co} is given in units of μ_B. The system total energy difference ΔE is measured with respect to the lowest state of the Co-(1)-GNR configuration. The end states of the GNR are in antiferromagnetic configuration and the magnetization of the Co atom was antiparallel to the left zigzag edge.

be found. The energetically most favorable site is the corner position. This is in accordance with our experiment, since we created in total 7 different complexes with a Co atom sitting stably at the corner position. It is also consistent with previous work, in which Zhou *et al.* [183] observed intercalation of Co atoms preferably underneath the outermost carbon hexagon rings of picene molecules.
Experimentally, it was not possible to create a complex with a Co atom at position (2). At a first glance, this is a bit surprising because DFT predicts that the total energy of a Co at site (2) is lower than for site (3). The calculations, however, do not address the energy barriers between the intercalation sites. So, it could be that a very low energy barrier separates position (2) from position (1), as sketched in Fig. 4.27. In this case, a Co atom at site (2) could easily overcome its left barrier

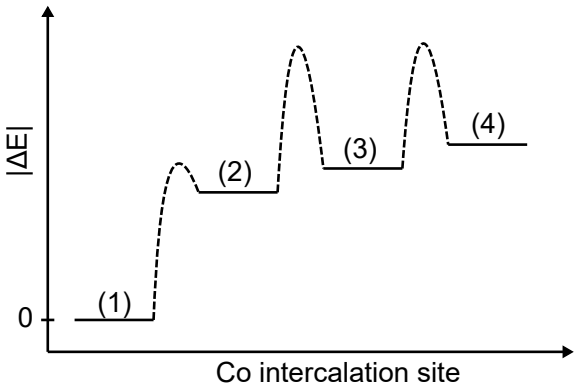

Figure 4.27.: **Energy barriers.** The energy levels from DFT for Co intercalation are drawn for different sites along the GNR armchair edge. Dashed lines mark the possible shapes of energy barriers between the levels.

and move to the more favorable position (1). Co atoms residing at position (3) or (4), however, would have to overcome larger barriers to move to a neighboring site. Therefore, no Co atoms buried at site (2) have been observed in experiment. Intercalation at all other sites, though, was possible and stable.

Furthermore, DFT can compute the distances between Au surface, intercalated Co atom and GNR. The distance between GNR and Au surface was determined to be

3.1 Å away from the Co atom and 3.3 Å close to the Co atom. The difference of approximately 0.2 Å in height is close to the experimentally obtained value of 0.3 Å. Thus, the calculations corroborate that the Co atom is indeed situated underneath the center of the carbon hexagon ring.

DFT also yields a higher repulsion of the GNR corner by an intercalated Au atom than for a Co atom, as was observed in experiment (c. f. Fig. 4.25). Fig. 4.28 shows the relaxed DFT structures of (a) a Co atom placed underneath a corner ring of the GNR and (b) the same configuration for a Au atom instead. The Au atom causes a

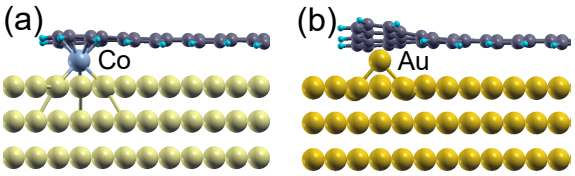

Figure 4.28.: **Au vs. Co at GNR corner.** DFT calculated side views of (a) Co-(1)-GNR-complex and (b) Au-(1)-GNR-complex, both on Au(111), revealing larger GNR distortion for (b).

much stronger upwards bending of the GNR. The reason is that the orbitals of the Co atom hybridize with the GNR. Au, on the other hand, is very inert and therefore prevents a strong hybridization of the atom with the GNR.

The DFT calculations predict the magnetic moment of the Co atom to be 1.7–1.8 μ_B for all intercalation positions, meaning that it always hosts two unpaired electrons. That implies that the Kondo effect should, in principle, be always present for all Co-GNR-complexes. This seems to be in contrast to the experiment because no Kondo peak for a Co-(3)-GNR-complex could be observed. An explanation might be that the Kondo effect is present for a Co at site (3), but cannot be observed by the STM tip due to the orbital structure of the GNR. Thus, the GNR might act—figuratively speaking—like a stencil masking the Kondo effect at certain positions.

Furthermore, the Co atom induces a magnetization of opposite kind in the carbon atoms which it is bound to. This can be seen for the exemplary case of a Co-(4)-GNR-complex in Fig. 4.29. A GNR—consisting of 8 anthracene units and

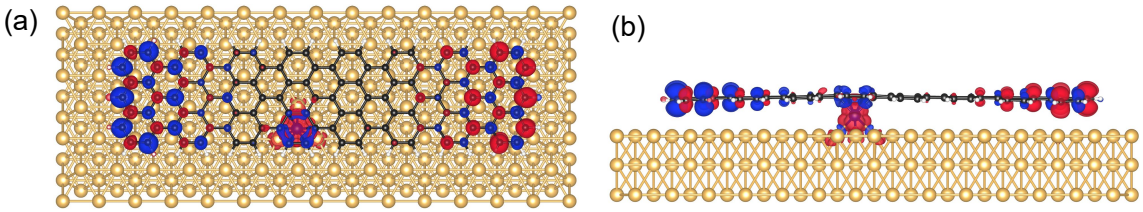

Figure 4.29.: **Magnetization density of Co-(4)-GNR-complex.** (a) Top view and (b) side view of a 8 anthracene units long 7-aGNR on Au(111) with a Co atom intercalated at position (4). Red and blue spheres represent isosurfaces of magnetization densities of $\pm 0.001\,\mu_B/\text{Å}^3$, respectively.

terminated with hydrogen—is lying on three layers of gold. The red and blue spheres are isosurfaces of the magnetization density. The GNR zigzag ends are coupled AF in this case, but the FM configuration yielded almost identical results. The carbon atoms surrounding the Co atom at position (4) display—unlike the other carbon atoms in the GNR center—a magnetization. The sign of the magnetization is opposite to the one of the Co atom.

To investigate the coupling of the Co atom to the GNR end states, the LDOS of different Co-GNR-complexes was calculated. The LDOS for a Co atom at position (4) and at the corner is shown in Fig. 4.30. Positive and negative DOS correspond

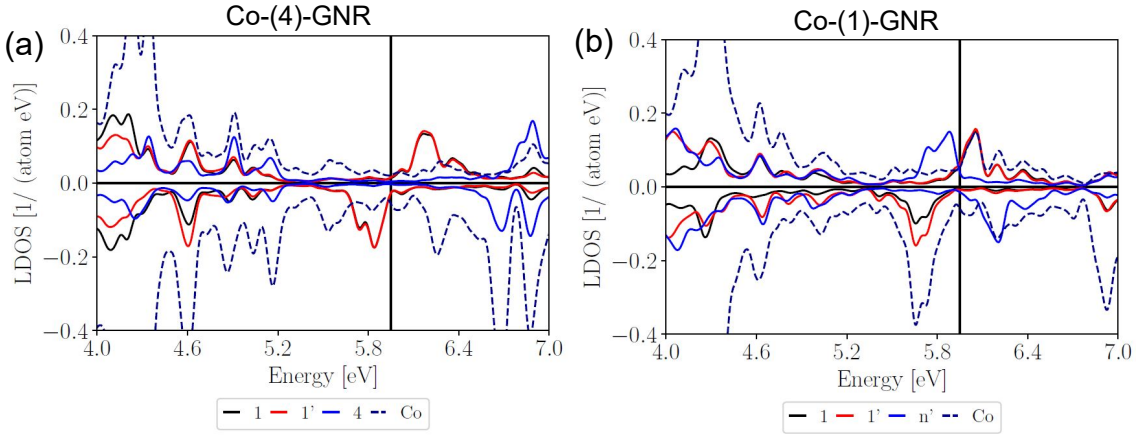

Figure 4.30.: **LDOS for different Co-GNR systems.** (a) LDOS for a Co-(4)-GNR-complex. (b) LDOS for a Co-(1)-GNR-complex. The DOS was projected onto different positions, as indicated by color coded lines. Positive DOS corresponds to spin-up electrons, negative DOS to spin-down electrons. The vertical line denotes the position of the Fermi energy.

to spin-up and spin-down electrons, respectively, and the Fermi energy is marked by the vertical line. The DOS was projected onto different positions, as indicated underneath the LDOS plot. 1 means that the LDOS was projected onto the 6 carbon atoms of the ring surrounding position (1). The same applies to 1', 4 and n'. Co refers to the LDOS directly at the position of the Co atom.
The LDOS lines for 1 and 1' reflect the occupation of the end state peak. For the Co-(4)-GNR-complex in panel (a) the LDOS for 1 (black line) and 1' (red line) are almost identical around the Fermi level. Slightly below the Fermi level, the LDOS for these positions has a peak on the negative side, meaning that the end state is occupied with spin-down electrons. The spin-up states above E_F are unoccupied. Just below the Fermi level, the Co atom hosts mainly spin-down electrons, as evident from negative LDOS in this area. The magnitude of the LDOS is, however, lower than for the end state. There is almost zero LDOS at the ring surrounding the intercalated Co atom, signalizing no (low) hybridization between GNR and Co states.

The Co-(1)-GNR-complex in panel (b) exhibits an AF coupling of its two end states. The end state at the left GNR end (rings 1 and 1') hosts spin-down electrons, whereas the right end (ring n') is occupied with spin-up electrons. In this case, the LDOS at the Co atom is relatively high and negative. Interestingly, the positions of the LDOS peaks for 1 and 1' are not—as one would expect—at the same energetic positions as the peak for n'. Instead, the peaks for 1 and 1' are shifted to slightly lower energies and match the energy of the LDOS peak of the Co atom. This is a clear indication of the influence of the Co atom on the end state in this configuration.
However, the absence of the end state peak at position (1') that was observed in experiment could not be reproduced here.

To describe the electron distribution within the Co-GNR-complexes, the LDOS was integrated over an interval of ±100 mV around the Fermi energy. This corresponds to the density from states around the Fermi energy which should be important for transport.
Fig. 4.31 shows vertical cuts through the integrated LDOS of different Co-GNR-complexes. The cut was made through the center of the Co atom. The first obser-

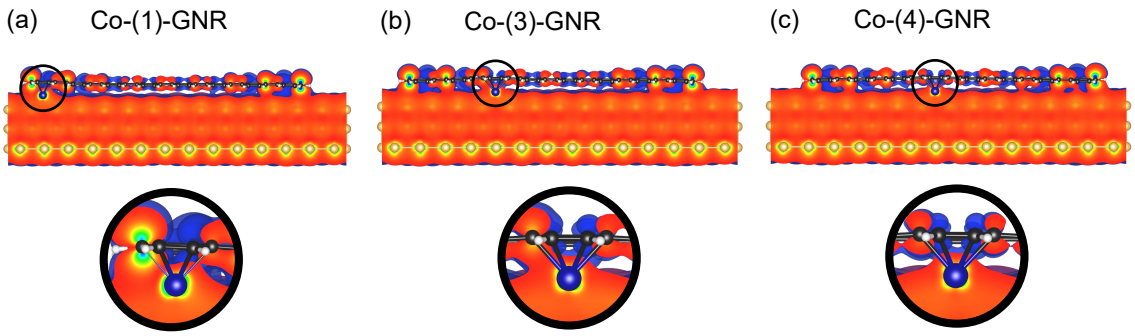

Figure 4.31.: **Integrated electron density.** Vertical cut through the integrated LDOS for a (a) Co-(1)-GNR, (b) Co-(3)-GNR and (c) Co-(4)-GNR-complex. The lower row shows a magnified view of the encircled areas above. The integration interval was ±0.1 eV with respect to E_F.

vation is that most density is located at the p_z-shaped end state.
Further, one can distinguish three different coupling scenarios. For the Co-(1)-GNR-complex shown in panel (a), the Co atom and the GNR end state are strongly coupled as evidenced by the overlap of density between the Co atom and the GNR end. This can be clearly seen in the magnified view in the lower part of panel (a).
For the Co-(3)-GNR-complex in panel (b), on the other hand, the coupling appears to be asymmetric. There is overlap of the density between Co and the carbon atoms at its left side, i. e. towards the end state, but low overlap to the right carbon atoms, i. e. towards the GNR center.
Last, panel (c) shows the situation for the Co-(4)-GNR-complex. There is low overlap in density between Co and GNR and therefore low hybridization between them.

These findings might explain the different observations in experiment for Co intercalation at different sites. For position (4), low hybridization between Co and GNR takes place and the STM tip can sense the unperturbed Kondo resonance of the Co atom. At site (3), there is asymmetric hybridization between Co atom and GNR which might be the reason why the much more pronounced end state is probed instead of the Kondo resonance. Of course, the orbital structure of the GNR might also play a role. At the corner, there is strong hybridization between Co and GNR end state, which is why a broadened zero-bias resonance is observed.

4.5.8. Tight-binding calculations

In addition, we performed a tight-binding analysis of some GNR configurations. The intercalation of a Co atom underneath the GNR leads to an interaction between Co atom and the carbon atoms it is placed next to. Although no covalent bonds are formed, coupling between Co and carbon atoms might lead to an alteration of the p_z-orbital of the respective carbon atoms. In the framework of a simple tight-binding model, the removal of a p_z-orbital is equivalent to taking out an atom from the GNR frame. Therefore, we systematically investigated the effect of taking out different carbon atoms from the rings along the GNR armchair edge—i. e. the positions where the Co atoms were intercalated.

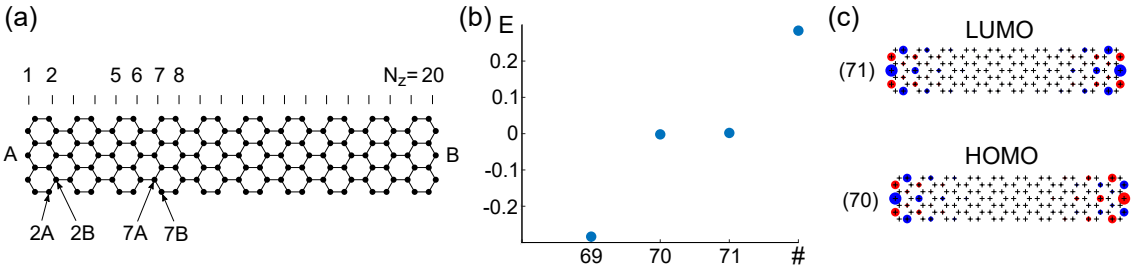

Figure 4.32.: **Tight-binding setup.** (a) Model used for the tight-binding calculations containing 140 carbon atoms. Left GNR zigzag edge consists out of A atoms only, right edge out of B atoms. (b) Energy of the states closest to E_F in units of the nearest-neighbor hopping integral t. (c) Real space distribution of the wave functions of HOMO and LUMO of the GNR.

To this end, we employed a tight-binding model considering only nearest-neighbor interaction with hopping integral t ($\approx 3\,\mathrm{eV}$ [22]). The on-site energy is zero, meaning that the Fermi level is always located at $E = 0$. We used a model of a 7-aGNR with a length of 10 anthracene units (corresponding to 20 carbon dimers along the armchair direction) containing 140 carbon atoms (see Fig. 4.32 (a) for a sketch). This length is, although being 2 anthracene units longer, comparable to the model used for DFT calculations. It is also long enough to avoid mixing of the states

from the intercalated Co atom with the end state of the second GNR zigzag edge. We denote the carbon atoms at the left GNR zigzag edge as belonging to the A sublattice and the ones at the right zigzag edge to the B sublattice. The atom positions along the GNR armchair edge are counted in terms of carbon dimers N_z along the armchair direction. They are labeled with N_z and the sublattice they belong to. In the sketch, some atom positions along the lower armchair edge are tagged for clarity.
The electronic structure of the GNR was calculated. In total, the GNR contains 140 carbon atoms, each contributing with one p_z-orbital—i. e. one electron—to the π-system of the GNR. Therefore, we obtain 140 states. 70 of them are doubly occupied with a spin-up and a spin-down electron[10] and 70 are empty. The states are sorted by energy and plotted as a function of their state number in Fig. 4.32 (b). The energy scale is given in units of t. We obtained two states lying close to zero-energy. State #70 is situated slightly below E_F and therefore represents the doubly occupied HOMO of the GNR. State #71 lies a little above E_F and constitutes the empty LUMO. All states below E_F are doubly occupied, all above E_F are empty.
Fig. 4.32 (c) shows the real space distribution of the wave functions for HOMO and LUMO. Both are localized at the GNR ends and decay towards the GNR center. These states can be related to the GNR end state. Regarding the doubly occupied HOMO, each GNR terminus hosts one electron.

Next, we removed single carbon atoms from the GNR. This was done to simulate a possible influence of the hybridization between the states of the intercalated Co atom and individual carbon atoms. Since the Co atoms were buried along the outer rings of the GNR armchair edge, only atoms from the lower GNR armchair edge were removed. The positions of the carbon atoms that were removed are labeled with the number of the corresponding zigzag dimer line and the sublattice the atom belonged to. Fig. 4.32 (a) shows some exemplary cases for the labeling.
First of all, the removal of a carbon atom decreases the total number of atoms to 139 and consequently reduces also the count of states to 139. This uneven number of states means that at least one state has to be singly occupied. Fig. 4.33 shows an overview of selected scenarios in which a carbon atom was removed from different GNR sites. Panels (a)–(d) depict the removal of a carbon atom from the corner ring, (e)–(f) from the 3rd ring and (i)–(l) from the 4th ring. Each panel is structured in such a way that it shows at its left hand side the energy of the states plotted versus their number and at the right hand side the spatial distribution of the wave functions of the three states closest to E_F.
State #69 is always doubly occupied and state #71 empty. State #70 is singly occupied and thus constitutes a SOMO (singly occupied molecular orbital). The SOMO lies exactly at E_F for all configurations and is filled with one electron. The appearance of a spin-polarized zero-energy state is in accordance to Lieb's theorem, since by taking out one carbon atom a sublattice imbalance is created [139].

[10]Spin-up and spin-down electrons are not discerned in the calculations. Therefore, all states are doubly degenerate.

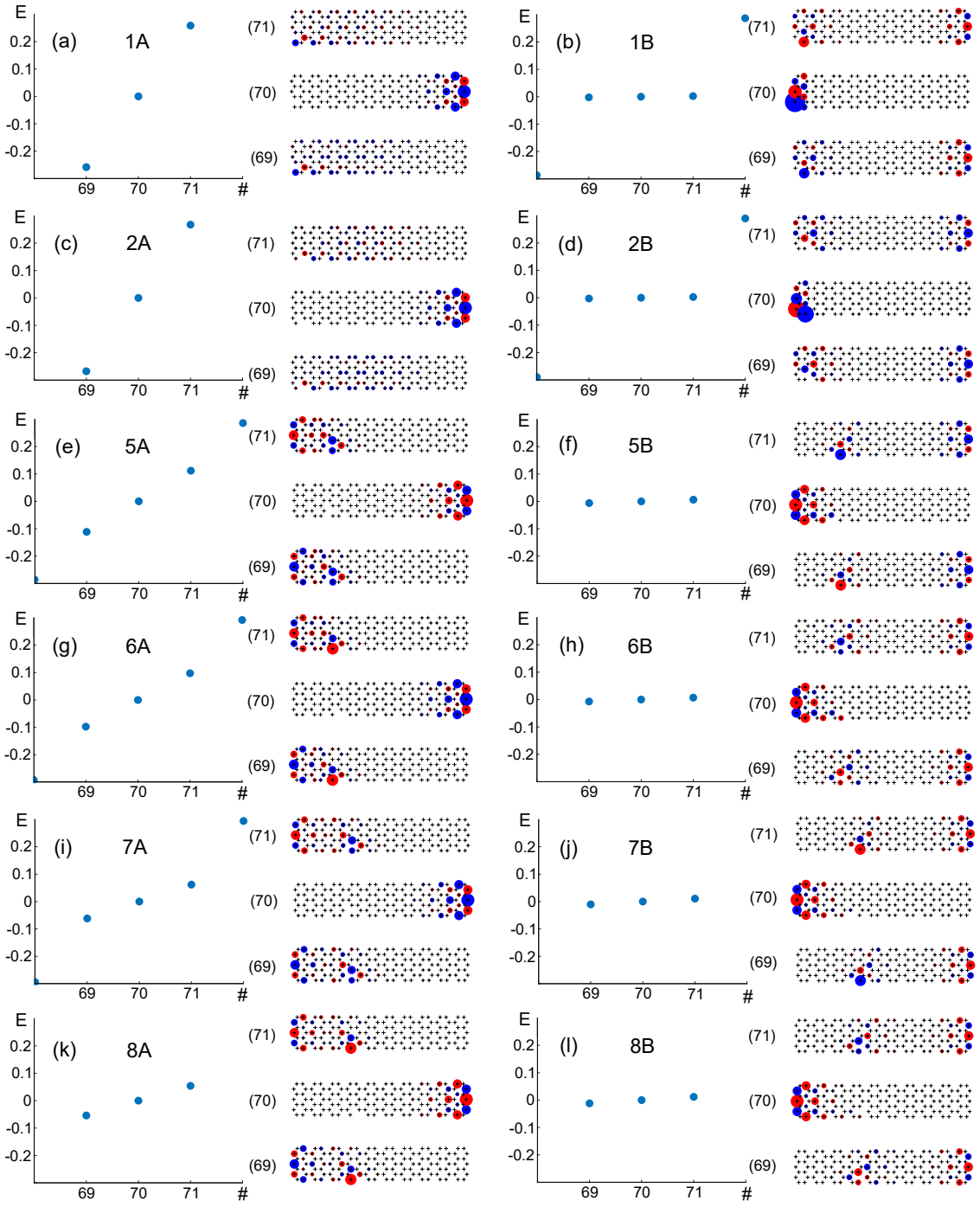

Figure 4.33.: **GNR with one atom missing.** Energy and real space distributions of GNRs with different atoms missing. The atom is missing (a)–(d) at the corner ring, (e)–(h) at the 3rd ring, (i)–(l) at the 4th ring. The energy scale is in units of t. More details are given in the text.

There is a clear difference between removing an A atom or a B atom regarding the splitting of the energy states as well as the spatial distribution of the wave functions.

We first consider the case that an atom is taken from the corner ring. When the atom is removed from the A sublattice (panels (a) and (c)), the GNR end state living on the A sublattice at the left GNR terminus is suppressed. State #70—formerly the HOMO of the intact GNR and now representing the SOMO—lies at zero-energy and hosts one electron that is located at the B atoms of the right GNR terminus. States #69 and #71 appear to be normal GNR bulk states, although being localized slightly towards the position of the defect.
On the other hand, when taking out the atom from the B sublattice (as shown in panels (b) and (d)), three states appear around E_F. The SOMO (state #70) lies at zero-energy and is located at the left GNR terminus. Its occurrence might be related to the sublattice imbalance at this end. State #69 lies closely below E_F and is doubly occupied. One electron is occupying the B lattice at the right GNR terminus and the second electron resides on A atoms of the left GNR end. Although the left end is influenced by the vacancy, this state appears to be the GNR end state. State #71 constitutes the empty, antisymmetric counterpart of state #69.
There is a resemblance between the experimentally obtained current map of a Co-(1)-GNR-complex and the tight-binding calculations presented here. In the current map, the LDOS is mainly localized at the Co intercalated corner, like in the SOMO of panels (b) and (d). One could interpret this in a way that the intercalated Co atom weakens the contribution of the p_z-orbitals of the 1B or 2B carbon atom to the π-system of the GNR and thus creates a state localized mainly at the bottom left GNR corner. Of course, the simplified tight-binding model does not depict the real situation (the Co atom rather influences all carbon atoms of the ring instead of bonding to one specific atom), but it could hint towards the state the system is actually in.

For a carbon atom removed from the 3rd carbon ring, as shown in panels (e)–(h) of Fig. 4.33, the situation looks slightly different. When taking out an atom from sublattice A (panels (e) and (g)), the three states closest to E_F are still energetically split. The SOMO with zero-energy is located at the right GNR terminus. The spatial distribution of states #69 and #71, however is interesting. They seem to be a mixture of the GNR end state at the left GNR terminus and the state created around the site of the vacancy.
For B atoms removed from the 3rd carbon ring (panels (f) and (h)), the SOMO resides again at the left GNR end. States #69 and #71 are distributed over the right GNR end and the A atoms in the surrounding of the vacancy. The location on the opposite sublattice than the removed carbon atom is in accordance to Lieb's theorem.
Again, an analogy between experiment and theory can be found. The current map of a Co-(3)-GNR-complex indicates a hybridization between GNR end state and Co induced state at position (3) and suggests the extension of the end state along the armchair edge up to site (3). In the tight-binding calculations shown in panels (e)

and (g) this conjecture is strengthened. The wave functions of states #69 and #71 are indeed located at the left GNR end and around the vacancy at the 3rd ring and seem to merge.

Last, panels (i)–(l) are discussed where an atom is removed from the 4th carbon ring. For an atom taken out from the A sublattice, panels (i) and (k) show that the SOMO is occupying the right GNR end. The real space wave functions for states #69 and #71 still overlap, but their amplitude between the left zigzag terminus and the vacancy is lower than for the 3rd ring scenario.
The situation for an atom taken out from the B sublattice, as shown in panels (j) and (l), is basically identical to the one described for the 3rd ring.
These findings can be compared to the experimental observations. The current map of a Co-(4)-GNR-complex exhibits a spatial separation between the Co state at position (4) and the end state located at the GNR zigzag terminus. The calculations also yield states localized around the vacancy and the GNR termini. There is a finite overlap in the real space wave functions between states around the vacancy and the GNR end. From experiment one can conclude that this overlap is not strong enough to cause hybridization between these two states.

To sum up, the tight-binding calculations are in accordance with experimental observations and may be used to qualitatively explain the shape of the measured current maps. In particular, they suggest a hybridization between GNR end state and vacancy related states at the 3rd carbon ring along the armchair edge.

4.6. End state broadening

At the end of this chapter, an experimental observation regarding the GNR end state shall be discussed. As was already pointed out, the position and the FWHM of the end state can vary from GNR to GNR (c. f. Fig. 4.10). Furthermore, the appearance of dI/dV spectra also depends on the STM tip shape. All tips have been carefully prepared and calibrated, but nonetheless variations in the linewidth can occur.
Fig. 4.34 shows an assembly of spectra that were taken at the pristine corners of 18 different GNRs during the experiment. Every point in the graph represents the FWHM of a specific end state plotted versus the peak maximum position. The color coding shall be neglected for the moment. The data seem to suggest that the further the state is shifted from E_F the broader it is. The points appear to exhibit, at least roughly, a linearly increasing trend. A dashed line with slope 0.5 is inserted as a guide to the eye.

It was shown that the energy broadening of surface states can be related to their lifetime [201, 202] (see the reviews of Refs. [203, 204] for more details). The Fermi liquid theory—applied to a homogeneous two-dimensional electron gas—predicts that the

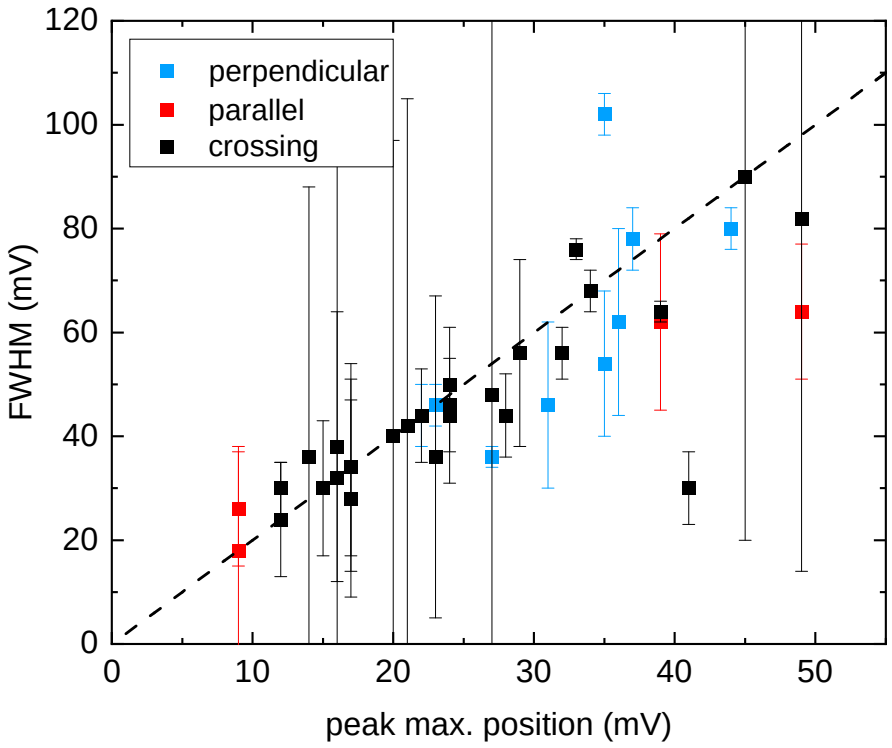

Figure 4.34.: **End state broadening.** FWHM of different end state peaks plotted vs. the peak maximum position. Colors indicate different GNR orientations with respect to the herringbone reconstruction. The black dotted line is a guide to the eye.

broadening of the state depends on the energy position of the peak with respect to the Fermi level [205]. Theoretically, the peak broadening should be proportional to $(E - E_F)^2$, with E being the energy position of the peak maximum. This behavior was confirmed also by STM experiments—however, with slight discrepancies from the parabolic shape which were attributed to STM tip effects [206, 207]. In our case, the data points have such high uncertainties that the detailed functional dependence of the increase of the FWHM with the peak maximum position can hardly be extracted.

For a Au(111) surface, another possible source of deviations can be found in the surface reconstruction. Chen *et al.* [208] found that the herringbone reconstruction acts as a superlattice for the surface state electrons, therefore modifying their electronic density. There is an electronic potential energy difference between fcc and hcp regions which presumably stems from variations in local atomic concentrations in the different regions. This leads to slightly different appearances of the surface

state in hcp and fcc regions.
Therefore, we investigated the influence of the orientation of the GNR with respect to the Au lattice of the substrate on the broadening of the end state. An easy way to determine the registry between GNRs and surface is via the herringbone reconstruction. The wall sites of the herringbone are aligned perpendicular to the close-packed direction of the Au atoms. To emphasize different orientations, the data points in Fig. 4.34 are color coded. Blue means that the spectrum was taken at a GNR that was oriented perpendicular to the herringbone wall sites (i. e. along the close-packed direction of the Au lattice), red parallel to the herringbone (and therefore perpendicular to the close-packed direction) and black that the GNR was crossing the herringbone under an angle different from 90°. As one can see, there is no clear distinction between those cases. It also does not make a difference whether the GNR end lies on or off the ridges of the herringbone wall sites (graph not shown here). This leads to the conclusion that the relation between FWHM and peak maximum position is independent of the GNR orientation with respect to the Au lattice.

One has to note, however, that the investigation of the end state spectra was not the main aim of this experiment. Hence, the spectra have not been taken in an optimized way to judge on such a trend with many different tips. This might contribute to the large uncertainty and scattering of the data points. Speculations about whether the data obey a linear or rather a parabolic trend are too early at this stage. To further investigate the relationship between peak position and FWHM of the GNR end state, one could perform another experiment in a slightly different way. The best strategy would be to prepare a sample with a rather high density of GNRs and without Co atoms. A larger overview scan should be taken and a tip suitable for STS should be prepared. Then, all GNR ends could be investigated spectroscopically with the same tip which ensures high comparability among the spectra.

As a side note, the shape of the Kondo peak seemed to vary less. A mean value of (27 ± 11) mV for the peak maximum position and (49 ± 20) mV for the FWHM for the GNR end state spectra compares to a mean value of (3 ± 3) mV for the peak maximum position and (20 ± 8) mV for the FWHM in the case of spectra taken at Co atoms intercalated at the middle of the armchair edge. The uncertainty margins represent the standard deviation here. This indicates that tip influence alone is not responsible for the varying end state peak broadening. It further corroborates our assumption that there are two different types of features with different origins, namely one related to GNR end states and the other related to the Kondo effect.

4.7. Conclusion and outlook

In this chapter, 7-aGNRs were synthesized under UHV conditions on a Au(111) surface. Subsequently added Co atoms were intercalated underneath different sites along the armchair edges of the 7-aGNRs. The Co-GNR-complexes were investigated by means of STS. Whereas Co atoms on Au(111) showed a Kondo dip in differential conductance spectra, the Co-GNR-complexes exhibited a peak. This was rationalized by different tunneling channels existing between STM tip and surface. The shape of the peak was dependent on the intercalation position along the GNR armchair edge.
Co atoms buried at the middle of the armchair edge displayed a Kondo-like resonance centered at (3 ± 3) mV with a FWHM of (20 ± 8) mV. The Co states appeared to be well separated from the GNR end state, if the Co atom was intercalated at least 4 carbon rings away from the GNR zigzag edge.
A Co atom inserted at the GNR corner also yielded a zero-bias resonance, with its maximum at (0 ± 4) mV and a FWHM of (30 ± 10) mV. The peak shape resembled a Kondo resonance, but it was broader than for the case of a Co atom at the middle of the armchair edge. The larger FWHM is presumably due to a hybridization between the Co atom states and the slightly wider GNR end state. It seems like a Co atom at the corner imprints its Kondo nature to the end state, resulting in a broadened zero-bias resonance at one GNR corner.
A Co atom placed at position (3) apparently constitutes an intermediate configuration. Differential conductance spectra taken at this site had the same appearance as the end state peak. No signs of a Kondo resonance could be found, but it seemed like the end state was extended along the armchair edge up to the intercalated Co atom.
Au atoms intercalated at the corner of the GNR did not cause any Kondo-like resonance but only weakened the observation of a GNR end state.

Kondo temperatures were obtained by manually extracting the FWHM and by a non-linear least squares fit of the dI/dV spectra to a Fano function. Differences in the obtained T_K values resulted mainly because of an asymmetric peak broadening and a small voltage window used for the fit function. Due to thermal and instrumental broadening, T_K could only be determined with large uncertainties.

Placing several Co atoms underneath the corners of one and the same GNR resulted in the observation of a Kondo-like resonance at every intercalation site. Up to three Co atoms were intercalated underneath one GNR.

DFT calculations confirmed considerations about the intercalation geometry and provided three different coupling scenarios for a Co atom along the armchair edge. However, there were also discrepancies between DFT and experiment. The localization of the resonance to only one corner for a Co atom intercalated at a corner position, for instance, was only observed in experiment and not found by DFT.

Within the framework of tight-binding calculations, individual atoms were removed from different GNR sites to simulate a possible impact of the Co atom on the π-system of the GNR. Although the model is simplified, the results are in good agreement with the phenomenological appearances of the Co-GNR-complexes.

Temperature and magnetic field dependent measurements are necessary to further investigate the properties of this Kondo system.
One could also try to intercalate magnetic atoms with different orbital occupations to study the hybridization of the GNR with different d-orbitals.
Furthermore, using another substrate could be considered. Ag(111) was shown to provide electron doping for graphene nanoflakes [209]. Also 7-aGNRs are proposed to be n-doped on this surface [210]. This would shift the GNR end state below the Fermi level and make it occupied. Thus, a splitting of the end state peak upon interaction with the magnetic adatom might be observable.

Last, the FWHM of the GNR end state peak was investigated as a function of its energy position with respect to the Fermi level. The end state apparently follows a trend that is compatible with Fermi liquid theory but needs to be examined further. To this end, an experiment with the focus on the examination of the GNR end states could be performed, putting emphasis on taking spectra with the same STM tip to ensure good comparability among the spectra.

5. Current-induced diffusion

One of the goals of this thesis was to connect the mesoscale transport of GNRs with their atomistic properties. In this chapter, we investigate how a current flow through a GNR influences adatoms on the GNR on the atomic scale. To this end, the current-induced diffusion of Co atoms, both, adsorbed on GNRs on a Au(111) substrate and on the bare Au(111) surface, is investigated.

The work in this chapter was done in collaboration with Sasha Vrbica from the group of Jan van Ruitenbeek from Leiden University in the Netherlands. They did preliminary STM experiments on Co adatom diffusion and current induced forces on epitaxial graphene on a Si/SiO_2 substrate. However, remnants from the sample processing as well as the corrugation of graphene on a SiO_2 surface hindered clear observation of Co diffusion. Therefore, a cleaner system was needed.

The motivation behind the original project was to find out more about the fundamentals of electromigration. Electromigration means that an electrical current flowing through a material exerts a force on atoms in the material or on its surface and eventually leads to a displacement of these atoms. This phenomenon is important in the semiconductor industry since it can lead to the creation of hillocks and shorts in current carrying leads and may therefore cause device failure [211, 212]. Even though first hints of electromigration were observed already in 1861 [213], this phenomenon is experimentally poorly investigated on the atomic scale. Braun *et al.* [214] reported electromigration of single adatoms on a metal surface observed by STM. This study motivated us to conduct further STM measurements in that direction to shed light on the atomic diffusion of single atoms adsorbed on GNRs.

As was pointed out in the previous chapter, on-surface synthesized GNRs on a Au(111) substrate pose a very clean environment. Additionally, when evaporating single Co atoms onto this system, a fraction of the Co atoms adsorbs on the GNRs—and is therefore decoupled from the underlying Au surface. By contacting the GNRs with the STM tip and applying a voltage pulse, current was run through the GNR and the substrate and a motion of the Co atoms on the atomic scale could be observed.

All measurements presented in this chapter were performed in Regensburg, and most of them were done together with Sasha Vrbica. The evaluation of the data was shared. Ulrike Paap, a bachelor student, helped to perform and evaluate a part of the measurements [215]. This experiment is also treated in the PhD thesis of Sasha Vrbica [216].

In the following, a short overview of the theoretical fundamentals is given. After that, the sample preparation and the method of contacting the GNRs with the STM tip are introduced. Some exemplary cases for voltage pulses are shown. The pulses are analyzed under the aspect of finding electromigration forces. Last, the diffusion of Co atoms on GNRs and the Au(111) surface is discussed and temperature dependent measurements are presented.

5.1. Theoretical basics

First, an introduction into the basic concept of electromigration will be given. Then, the basics of diffusion in one and two dimensions are introduced. Last, the principles of Kelvin probe spectroscopy are explained.

5.1.1. Electromigration

As already mentioned, electromigration describes the displacement of atoms in a material caused by an electric field and the current flow through the material. Its first observation was reported by Gerardin in molten alloys in 1861 [213]. The resulting material transport can lead to failure of integrated circuits by the creation of hillocks and voids (c. f. Fig. 5.1) [211, 212]. On the other hand, one can also

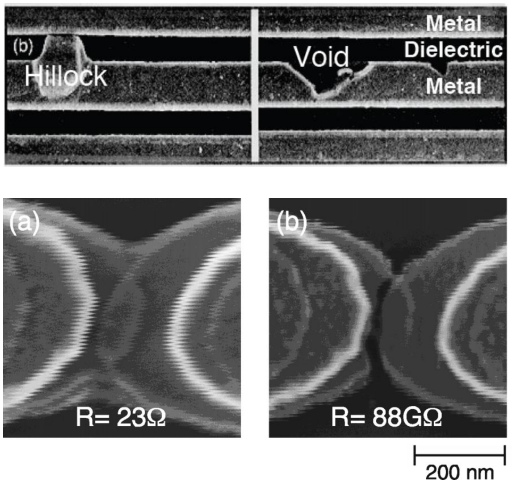

Figure 5.1.: **Examples for electromigration.** Top: Formation of hillocks and voids in Cu interconnects. From [217]. Bottom: Fabrication of Au contacts with nanometer separation by means of electroburning. From [218].

take advantage of electromigration by (re-)moving adsorbates on purpose [219]. As an example, one can mention the current-induced cleaning of graphene [2] where the removal of (charged) adsorbates helps to improve the performance of graphene based devices. Furthermore, the fabrication of very closely spaced contacts by electroburning [124, 218, 220] relies on electromigration as well. An example is shown in Fig. 5.1.

A thorough description of this phenomenon can be found in the reviews of Refs. [221, 222]. Here, only the basic principle is sketched.
The underlying theory was developed by Fiks [223] and Huntington and Grone [224] and employs a ballistic approach to determine the mechanisms of electromigration. The displacement of an atom that is free to migrate in or on the surface of a conductive material results from the interplay of two driving forces. One of them—the so-called *wind force*—is caused by the electrons flowing through the material. By scattering, the electrons transfer their momenta to the atom and lead to a force component pointing in the direction of the electron current. The second contribution—the direct electrostatic force, or simply *direct force*—stems from the applied electric field acting on the migrating atom.
The sketch in Fig. 5.2 illustrates this situation. A positively charged ion (blue) is

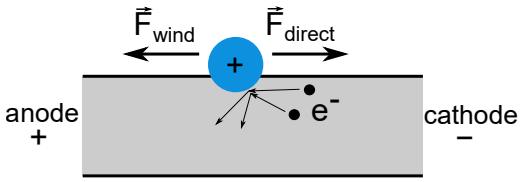

Figure 5.2.: **Principle of electromigration.** A positively charged ion (blue) on a conductor (gray) feels the direct force $\vec{F}_{direct}$ arising from the applied potential and the wind force $\vec{F}_{wind}$ stemming from scattering with electrons. After [216].

sketched on the surface of a conductor (gray). A potential drop is applied across the conductor. This leads to an electric field pointing from left to right and causing a direct force component $\vec{F}_{direct}$ on the ion. Additionally, electrons (black dots) move from right to left and transfer their momenta to the ion by scattering. The resulting force component $\vec{F}_{wind}$ is pointing in the opposite direction of the direct force. Depending on which force component prevails, the ion will get displaced to the left or the right[1].
The resulting force $\vec{F}_{res}$ can be described by [222]

$$\vec{F}_{res} = \vec{F}_{direct} + \vec{F}_{wind} = (Z - n_e \cdot l_{mfp} \cdot \sigma) \cdot e \cdot \vec{E} \tag{5.1}$$

where Z is the charge of the adsorbate, n_e the electron density in the conductor, l_{mfp} the mean free path of the electrons, σ the scattering cross section, e the elementary charge and $\vec{E}$ the electric field.
Therefore, the type of the adsorbate as well as the conductivity of the sample play an important role. This was addressed theoretically for different adsorbates on graphene and CNTs [225–227]. Experiments for electromigration of single adatoms on carbon-based materials, however, are scarce.
STM poses an ideal tool for the detection of electromigration on the atomic scale

[1]The theory is valid for neutral atoms as well. The contribution of the wind force does not depend on the charge of the atom. To model the influence of the direct force, Huntington and Fiks assumed the electric field to act on the bare positive charge of the ion core [222–224]. This is in line with the approach of viewing a metal as positively charged cores and an electron sea surrounding them.

since the high spatial resolution allows keeping track of the displacement of single atoms. Braun *et al.* [214] performed experiments in that context by probing the motion of single Au and Ag adatoms on a Ni(111) surface under the influence of current induced by an STM tip. They found that adatoms are pushed away from the tip below a certain voltage threshold whereas they are pulled towards the tip above.
However, more experiments recording the atomic displacement of adatoms on a current-carrying substrate are necessary to better understand electromigration on the atomic scale.

5.1.2. Thermally activated diffusion

There are two main techniques to experimentally monitor diffusion processes on a sample surface at the atomic scale. On the one hand, a field ion microscope [228] allows the real space observation of surfaces with atomic resolution. On the other hand, scanning probe microscopy can be used to follow the diffusion of single adatoms. Due to its lower tip-sample interaction, usually STM is preferred for diffusion studies of adatoms on conductive surfaces over AFM.
There are several methods to study atomic diffusion with an STM. For example, adsorbates can be directly tracked with the STM tip [229]. This method achieves high temporal resolution but the diffusion of the adsorbate might be influenced by the presence of the STM tip.
Another option is to monitor diffusion by taking a series of subsequent STM images. Using this approach, the tip influence on the diffusion behavior is reduced since the tip is positioned away from the adsorbate most of the times. The downside is that one might miss single diffusion events—like adatom jumps forth and back or displacement of the adsorbate outside the imaging frame.

Therefore, one has to look at the average motion of multiple adatoms. To this end, the average number of image-to-image diffusion steps $\bar{N}$ is defined as the product of the total[2] hopping rate ν (which describes the displacement of the adatom from one lattice site to an adjacent site and is also referred to as jump rate or diffusion rate) and the time Δt between two subsequent images [231]:

$$\bar{N} = \nu \cdot \Delta t \tag{5.2}$$

In the simplest approximation, the adatoms are thereby considered to jump only one lattice site at a time. For the 1-dimensional case, the probability that an adatom makes k steps in one direction is given by the Poisson distribution

$$P_k = \frac{e^{-\frac{\bar{N}}{2}} \left(\frac{\bar{N}}{2}\right)^k}{k!} \tag{5.3}$$

[2] *Total* hopping rate means that the hopping in all possible directions is considered. Sometimes, the hopping rate is defined for each lattice direction separately (c. f. Ref. [230]).

The probability to find an adatom m lattice sites away from the origin therefore reads [232]

$$P_m = e^{-\bar{N}} \sum_{i=0}^{\infty} \frac{\left(\frac{\bar{N}}{2}\right)^{2i+m}}{i!(i+m)!} = e^{-\bar{N}} I_m(\bar{N}) \tag{5.4}$$

with I_m being a modified Bessel function of the first kind.
Due to the stochastic nature of the process, the diffusion steps in 2 dimensions (2D) superimpose independently of each other. For diffusion on a 2D square grid, the probability to make steps in each of the two orthogonal directions is therefore equal. Since the total average number of diffusion steps is $\bar{N}$, the average diffusion in each of the two directions is $\bar{N}/2$. The probability for a displacement by m and n lattice sites in each of the directions is then given by [231]

$$P_{mn} = e^{-\bar{N}} I_m\left(\frac{\bar{N}}{2}\right) I_n\left(\frac{\bar{N}}{2}\right) \tag{5.5}$$

When considering only thermally promoted diffusion, the hopping rate can be determined in the framework of the transition state theory. Here, the adatom is considered to sit in a potential well on the surface and has to overcome a diffusion barrier E_D to diffuse to neighboring lattice sites. The hopping rate can be written as [230]

$$\nu(T) = \nu_0 \exp\left(\frac{-E_D}{k_B T}\right) \tag{5.6}$$

Hereby, T is the temperature of the system, k_B the Boltzmann constant and ν_0 is the so-called attempt frequency which takes on values of roughly 10^{13} Hz.

To determine the average distance an adatom moved on the surface after a certain number of jumps, the random walk model can be used. In the 1D case, an adatom sitting in the origin at site x_0 can leave its position and jump by one lattice site either to the left or to the right with equal probability. It can be shown that after $\bar{N}$ jumps, the mean square distance of the adatom from the origin is [230, 233]

$$\langle (x_j - x_0)^2 \rangle = \langle (\Delta x)^2 \rangle = l^2 \cdot \bar{N} \tag{5.7}$$

with l being the lattice constant. If one includes the possibility of long jumps [232, 234], the adsorbate can also jump several lattice sites at a time. In that case, the average jump distance $\bar{l}$ replaces the lattice constant l.
For a 2D square lattice, the probabilities to move along each space direction x and y superimpose statistically independent [230] and the mean square distance from the origin reads

$$\langle (\Delta r)^2 \rangle = \langle (\Delta x)^2 \rangle + \langle (\Delta y)^2 \rangle = \bar{l}^2 \cdot \bar{N} = \bar{l}^2 \nu \Delta t = 4D\Delta t \tag{5.8}$$

with the jump diffusion coefficient $D = \bar{l}^2 \nu / 4$. The diffusion coefficient for a triangular lattice—as in the case of a (111) surface—takes on the same value. Again,

the definition of the hopping rate ν as total number of jumps in *all* directions is important. For other definitions of the hopping rate, different values for D can appear in the literature (c. f. Ref. [230]). In general, D is inversely proportional to the dimensionality of the diffusion [233].

5.1.3. Kelvin probe force spectroscopy

Kelvin probe force spectroscopy (KPFS) is a method to determine the local contact potential difference (CPD) between two materials. It goes back to an observation made by Lord Kelvin in 1898 [235]. He experimented with two parallel plates that were electrically connected and brought in close vicinity, thus forming a plate capacitor. Upon moving one of the plates, he noticed the flow of a capacitively induced current that was connected to the different work functions of the two plates. The current could be minimized by applying an appropriate voltage across the plates.
In 1991, Weaver *et al.* [236] and Nonnenmacher *et al.* [237] extended this method to scanning probe microscopy in order to measure the local CPD between a conductive AFM tip and the sample surface. Its working principle is schematically illustrated in Fig. 5.3 by depicting the energy levels of sample and tip upon bringing them into contact.
Panel (a) shows the energy level alignment of sample and tip when they are still far apart. Their respective work functions—Φ_s for the sample and Φ_t for the tip—are aligned to the vacuum level E_V. Since sample and tip have different work functions, their respective Fermi energies, E_F^s and E_F^t, are unequal.

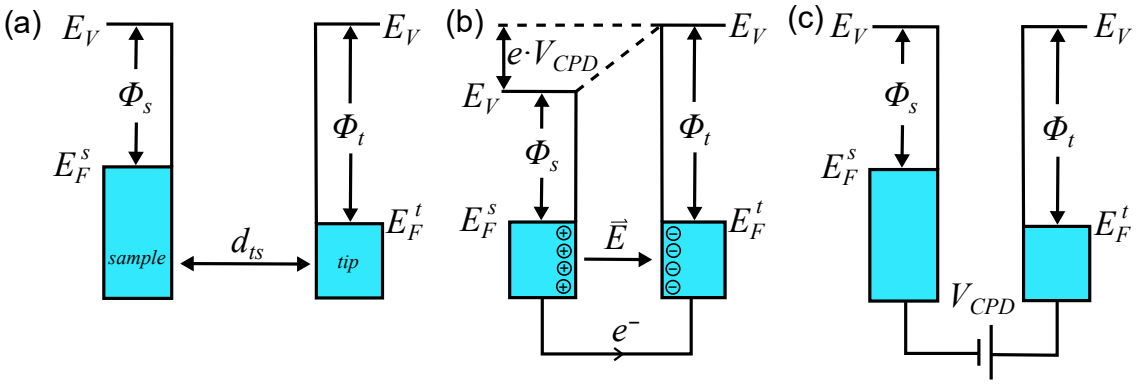

Figure 5.3.: **Energy level alignment for KPFS.** (a) Tip and sample are separated by a distance d_{ts} with no electrical contact. Their work functions, Φ_t and Φ_s, are different and aligned to the vacuum level E_V. (b) When tip and sample are in electrical contact, the Fermi levels of tip and sample, E_F^t and E_F^s, align and an electric field $\vec{E}$ forms in the junction. The vacuum level of the sample is lowered by the contact potential difference (CPD). (c) By applying a voltage V_{CPD}, the initial situation can be restored and the electrostatic interaction is minimized. After [238].

In panel (b), sample and tip are brought into electrical contact[3] by decreasing the tip-sample separation d_{ts}. Then, electrons will flow from the sample (with the lower work function and higher Fermi level) to the tip to equilibrate the two Fermi levels. Through that, charges will accumulate on the surfaces of tip and sample and an electric field $\vec{E}$ in the junction arises. The corresponding drop in potential is equal to the CPD. The electric field in the junction causes an electrostatic force between tip and sample. This attractive force can be sensed by means of AFM.
By applying a voltage between tip and sample, the Fermi levels can be shifted back. At a voltage V_{CPD}, the initial situation (for large d_{ts}) is restored. V_{CPD} is related to the difference in work functions by [237, 238]

$$V_{CPD} = \frac{1}{e}(\Phi_s - \Phi_t). \tag{5.9}$$

At this voltage, the electric field between tip and sample vanishes, and thus the electrostatic force in the junction is minimal.

To relate the measured frequency shift in a KPFS spectrum to the CPD, tip and sample can be approximated as a capacitor. This capacitor stores the energy

$$E_C = \frac{1}{2}V_{eff}^2 C \tag{5.10}$$

with the effective voltage $V_{eff} = V_{bias} - V_{CPD}$ and the capacity C.
Since the frequency shift Δf of the unperturbed AFM resonance frequency f_0 is proportional to the electrostatic force F_{es}, one can write

$$\begin{aligned} \Delta f &\propto \frac{\partial}{\partial z} F_{es} \\ &\propto \frac{\partial}{\partial z}\left(\frac{\partial}{\partial z} E_C\right) \\ &\propto \frac{1}{2}\frac{\partial^2 C}{\partial z^2}(V_{bias} - V_{CPD})^2 \end{aligned} \tag{5.11}$$

whereby z is the direction normal to the sample surface. When doing KPFS, the obtained $\Delta f(V_{bias})$ spectrum has thus the shape of a parabola[4].

5.2. Experimental procedure

The motion of Co atoms on GNRs was caused by contacting the GNR with the STM tip and ramping up the bias voltage for a short time. Thereby, the injected current heats the sample and enables motion of the adatoms. This section gives a brief overview of the sample preparation and explains the contacting procedure.

[3] This can either be direct contact or the case that d_{ts} is sufficiently small for electrons to tunnel.
[4] Deviations from this shape might arise, e. g., from charging processes.

5.2.1. Sample preparation

The sample preparation was carried out analogously to the previous chapter. That is why here only a short summary is presented. More details can be found in section 4.2.
After sputtering and annealing of a Au(111) single crystal, DBBA precursor molecules were thermally sublimed onto the Au surface. Subsequently, the 7-aGNR formation was triggered by two heating steps. In contrast to the previous chapter, no NaCl islands were grown this time. After cooling down the sample and transferring it into the STM chamber, Co atoms were added to the surface by electron beam evaporation. As already mentioned, a fraction of the Co atoms adsorbed on top of the GNRs. Compared to the previous chapter, a slightly higher Co coverage was chosen to increase the number of Co atoms on GNRs. Typical sample appearances can be seen in section 5.3.

5.2.2. Pulsing procedure

To run current through the GNRs and observe a motion of the adatoms, a reliable method to contact the GNRs with the STM tip is required. In the following, a procedure is introduced by which voltage pulses under reproducible, well-defined conditions could be performed. First, an overview STM image is taken and a suitable[5] GNR is selected. Then, the STM tip is positioned above the GNR and the feedback is switched off. This situation is illustrated in Fig. 5.4 (a). The tip is lowered and the tunneling current between tip and sample is recorded (shown as a red line in panel (d)). The distance by which the tip is lowered is labeled with z and is displayed by a blue line in panel (c). Note that $z = 0$ for the set point position. Increasing (positive) z values refer to a tip approach towards the sample surface. To establish a gentle contact, the tip is first lowered fast and then, when in close proximity to the GNR, slower. The tunneling current raises exponentially until a sudden increase can be observed in most current traces (here at roughly $z = 5.6\,\text{Å}$, marked with an arrow in panel (d) and especially clear in the logarithmic $I(z)$ plot in the inset). This rise in tunneling current is referred to as jump to point contact [239–242]. It marks the crossover between vacuum tunneling regime and direct tip-sample contact.
After this point is reached, the tip approach is continued for 0.2–0.3 Å to make sure tip and GNR are in good contact[6].
When the final tip height is reached, the voltage between tip and sample (green line

[5]Suitable means in this case that one or many Co atoms adsorbed on top of the GNR, but preferably not too close to the GNR ends.
[6]The approach distance necessary for establishing a contact between tip and GNR varies for different contact points due to surface corrugations on the atomic scale [241]. Therefore, an additional safety margin was added.

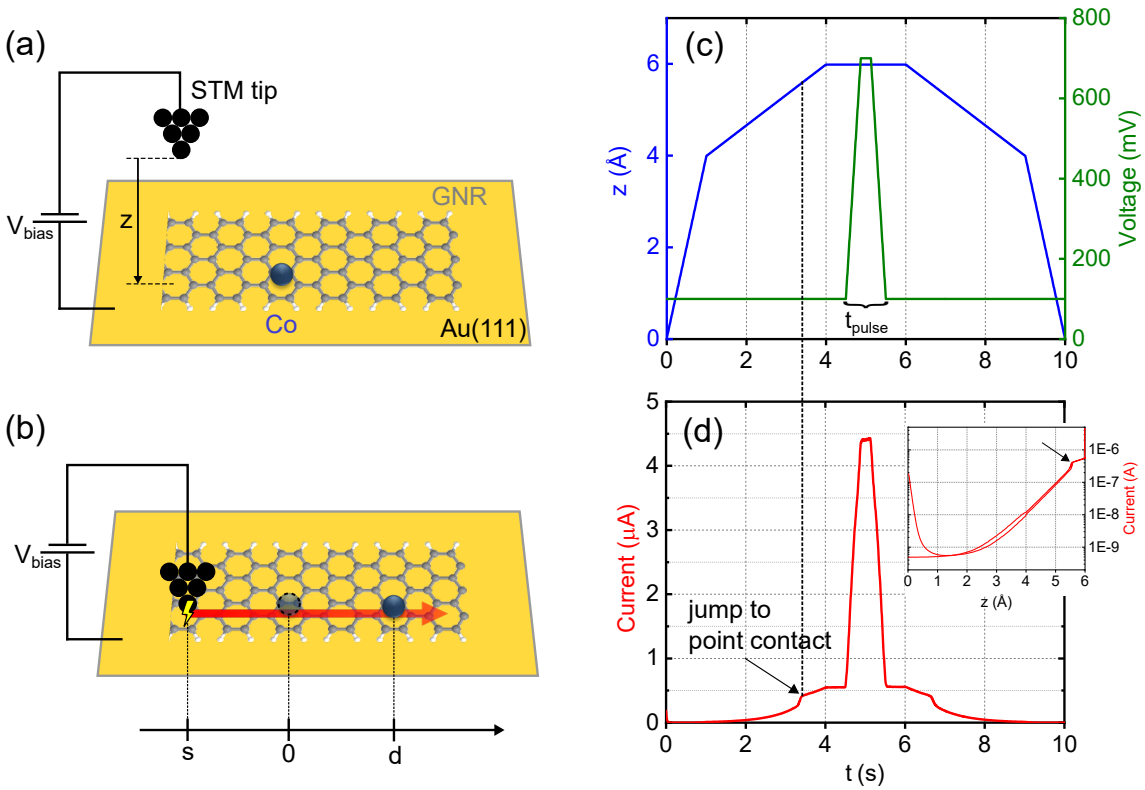

Figure 5.4.: **Pulsing procedure.** (a) Schematics of an STM tip above a GNR on a Au(111) surface with a Co atom adsorbed on it. (b) The STM tip is lowered by a distance z until a contact between tip and GNR is formed. Then the tunneling voltage V_{bias} is ramped up for a time t_{pulse} and current flows through GNR and substrate (symbolized by red arrow). Thereby, the Co atom is displaced. The initial separation between tip and Co atom is denoted by s and the displacement of the Co atom by d. (c) Typical example for a voltage pulse with 700 mV for a duration of 1 s (green line) used in experiment. The blue line indicates the tip approach towards the GNR. (d) Tunneling current recorded during the pulse in (c). The inset shows the current as a function of the tip approach z on a logarithmic scale.

in panel (c)) is increased for a short time t_{pulse}. This is referred to as voltage pulse[7] and a schematic is depicted in panel (b). Most pulses lasted for 0.5–1 s. During the voltage pulse, the current increases to its maximum value. The current spreading through the sample[8]—symbolized by the red arrow—may lead to a displacement of the Co atom. The separation between pulsing spot of the tip and initial center of the Co atom is labeled with s.

[7] One could also call it *current pulse* since it is actually the injected current that enables the motion of the adatoms through Joule heating of the system. As the voltage is easier to adjust on the instrumental side, the denotation *voltage pulse* will be used in the following, though.

[8] For reasons of clarity, only the fraction spreading through the GNR is sketched.

After the pulse, the tip is retracted and the feedback switched on again. Subsequently, another STM image is taken and compared to the previous one. By this method, the displacement d of the Co atom by the voltage pulse can be determined. A displacement away from the tip is registered with a positive sign whereas a displacement towards the tip is counted with a negative sign.

Regarding the direction of the Co displacement, the following considerations need to be taken into account. First of all, according to DFT calculations, Co atoms adsorbed on graphene are positively charged [243]. We assume that the same holds true for Co adatoms on GNRs.
Furthermore, one has to keep in mind that the bias voltage is applied to the sample. Thus, for a positive pulsing voltage—as in the example of Fig. 5.4—the electrons will flow from the STM tip into the sample. The wind force should therefore push the Co atom to the right hand side in the sketch. The direct force, resulting from the electric field between tip and sample should have the opposite sign, since the electric field lines are pointing from the positive sample to the grounded tip.
Hence, a displacement away from the tip ($d > 0$) indicates a dominating wind force, whereas a motion towards the tip ($d < 0$) means a prevailing direct force.
For pulses with a negative voltage, the signs for wind force and direct force are both reversed.

One has to note that the electromigration forces are small. Mainly local Joule heating helps to lift the adatoms from their adsorption sites and enables their motion [226, 227, 244]. The electromigration forces then result in a directional displacement. It is difficult to calculate the value of these forces because too many variables are unknown for this system. It should be noted, however, that the magnitude of the electromigration forces for various adatoms on CNTs was in the range of pN to nN [226, 227] and thus is comparable to the force needed to move single adatoms over metal surfaces[9] [245].

5.3. Sample characterization

In this section, the adsorption behavior of the Co atoms on the GNRs is treated. Different appearances of the adsorbed Co atoms are discussed and their adsorption positions on the GNR are examined. Last, exemplary cases for voltage pulses on GNRs and the resulting motion of the Co adatoms are shown.

[9]The force to move an atom depends on the substrate. The lateral force for moving Co over Pt(111) was reported to be 210 pN whereas it measures 17 pN for Co on Cu(111) [245].

5.3.1. Determination of Co adsorption position

Typical appearances of Co atoms adsorbed on a GNR and the bare Au(111) surface in experiment can be seen in Fig. 5.5. Panel (a) shows two partially overlapping GNRs and several Co atoms adsorbed on a GNR and the Au(111) surface. The longer GNR consists of two interconnected segments and is therefore kinked[10]. The Co adatoms adsorbed on the GNR are labeled with (I) and (II). They appear brighter and larger than the Co atoms on the Au surface. Whereas Co on Au(111) has an apparent height of 1.0 Å and a width of 13 Å, Co atoms on a GNR show typically apparent heights of 2.3 Å and widths of 15 Å. The reason for the difference is that—due to the GNR acting as a spacer—the tip needs to be closer to the on-top-adsorbed Co atoms to maintain a constant tunneling current. It should be underlined that a Co atom adsorbed on a GNR looks distinctly different from a Co atom buried underneath a GNR (c. f. Fig. 4.14).
One important point to consider is that the appearance of all structures depends on the STM set point parameters. Therefore, all values presented here refer to adatoms in images that were taken with $V_{bias} = 100\,\mathrm{mV}$ and $I_{tunnel} = 2\,\mathrm{pA}$.
Although both adsorbed on a GNR, Co atoms (I) and (II) look slightly different. Ad-

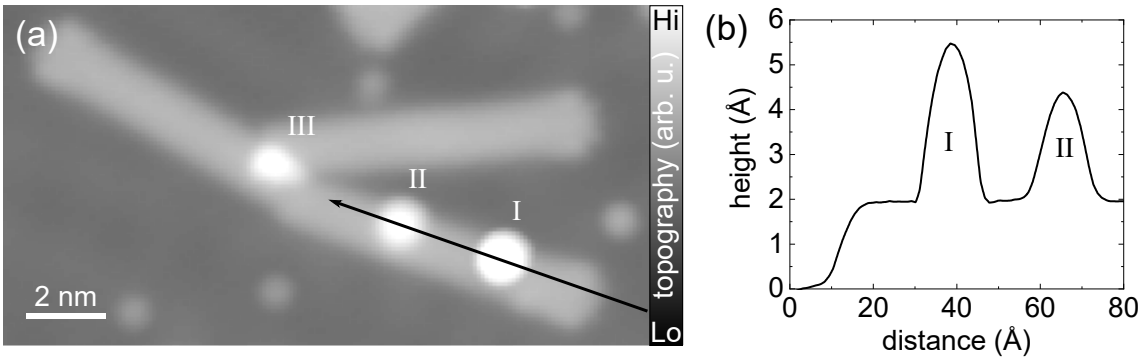

Figure 5.5.: **Different adsorption heights of adatoms.** (a) STM image of interconnected and overlapping GNRs. Co atoms are labeled with (I) and (II), the overlap between two GNRs is marked with (III). $V_{bias} = 100\,\mathrm{mV}$, $I_{tunnel} = 2\,\mathrm{pA}$. (b) Apparent height profile along the black arrow in (a).

sorbate (I) appears larger than adsorbate (II) in the STM image in Fig. 5.5 (a). Their apparent heights can be deduced from the line scan shown in panel (b). Whereas adsorbate (II) exhibits an apparent height of 2.4 Å and a width of 15 Å—close to what most of the adatoms show—adsorbate (I) has an apparent height of 3.5 Å but the same width of 15 Å. Only a small fraction of the adsorbates had this larger appearance.

[10]During the sample growth, two (or more) GNRs can fuse. Throughout this process, pentagon and heptagon defects can occur at the interconnection sites. A detailed study of interconnected 7-aGNRs can be found in Ref. [246].

There are various possible reasons for the different apparent heights of Co atoms on GNRs. First, Virgus *et al.* [247] predicted different adsorption sites—and correspondingly varying apparent heights—for Co atoms with different spin configurations adsorbed on graphene. They claim an equilibrium height of Co atoms over the graphene layer of 2.2 Å when Co is in the $3d^8 4s^1$ state and a height of 3.3 Å for Co in the $3d^7 4s^2$ configuration.
On the other hand, the larger adatom could actually be a dimer consisting of 2 Co atoms. For comparison, the apparent height of a single Co atom on Au(111) was found to be around 1.0 Å, that of a Co dimer on Au(111) roughly 1.3 Å.
Furthermore, an adsorbed hydrogen atom on top of the adatom(s) can also cause a height difference. The actual reason for the different heights could not be determined.

Last, one has also to distinguish the Co adatoms from inherent structural phenomena from the growth process, such as overlapping GNRs (labeled with (III) in Fig. 5.5 (a)) or a not fully polymerized GNR backbone (indicated by a black arrow in Fig. 4.7).

To study the motion of Co atoms on the GNRs, it is of interest to know their exact adsorption positions on the GNR. According to DFT calculations, Co atoms preferably adsorb at the center of the outer carbon hexagon rings of 7-aGNRs [197]. In our case, the determination of the exact Co adsorption position by means of AFM was not possible. For taking atomically resolved AFM images with functionalized tips, the tip has to be approached very closely to the structure to be investigated. This leads to strong interactions between tip and sample and resulted in a pick-up of the Co adatom by the tip. This is different to the previous chapter where the Co atoms were buried underneath the GNR and therefore protected from being picked up.
The adsorption position, however, can also be estimated by means of STM. Hereby, one has to keep in mind that, in general, STM overestimates the sizes of structures. Nonetheless, by assuming a symmetrical tip, the apparent center of a structure—like a GNR or a Co atom—is also its real center. Thus, by identifying the middle of the GNR and the middle of the adsorbed Co atom and overlaying the atomic lattice structure of the GNR, one can draw conclusions about the adsorption position of the Co adatom.

This is done in Fig. 5.6. Panel (a) shows a horizontally aligned GNR segment with a Co atom residing on it. There are also three Co atoms on the bare Au(111) surface close to the GNR. Panel (b) shows the procedure to determine the adsorption site. The black dashed line marks the center of the GNR. It was obtained by simply taking the middle between upper and lower GNR edge. The blue dashed line indicates the center of the Co adatom. Here, it has to be noted that the appearance of the Co atom—as seen in panel (a)—is asymmetrically broadened due to the fact that it is adsorbed off-center on the GNR.
To remove the contribution of the GNR from the image, one has to adjust the

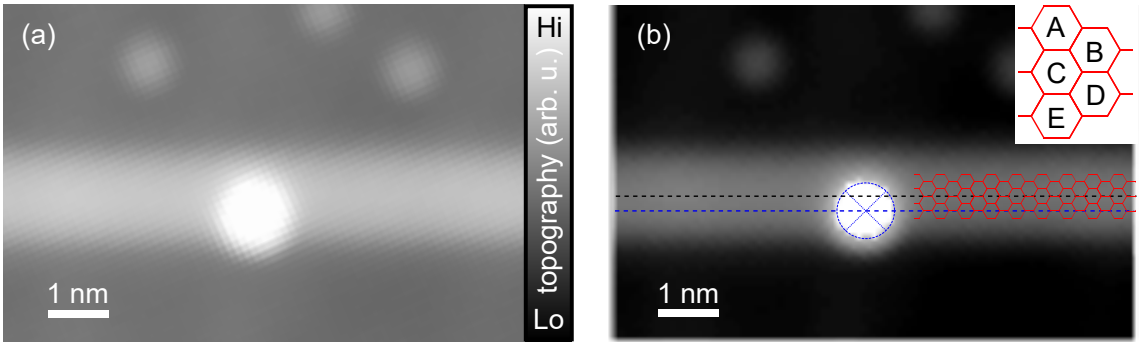

Figure 5.6.: **Determination of Co adsorption position.** (a) STM image of a GNR section with a Co atom adsorbed on top. Above the GNR, three Co atoms on the bare Au(111) surface can be seen. $V_{bias} = 100\,\mathrm{mV}$, $I_{tunnel} = 2\,\mathrm{pA}$. (b) Contrast modified version of the image in (a). The center of the GNR and the Co atom are marked with black and blue dashed lines, respectively. A true to scale model of the GNR lattice is overlaid in red. The inset declares the nomenclature of the hexagon rings across the GNR.

contrast until only the signal stemming from the Co atom is visible. In panel (b), this image was overlaid to the original image. The blue circle marks the Co atom as obtained by the contrast adapted image. One can clearly see that the appearance of the Co atom is asymmetrically broadened towards the GNR edge. In the right half of the image, a true to scale model of its lattice is overlaid to the GNR. The center of the Co atom coincides with the center of the outer carbon hexagon ring and therefore hints towards an adsorption at this site, as predicted by theory. To clarify the nomenclature of the adsorption position across the GNR, the inset assigns a letter to every hexagon ring across the GNR. Almost all Co atoms were adsorbed at the outer carbon rings, i. e. sites A or E.
One has to mention, however, that the position determination with STM is not ultimately conclusive, in particular because the tips in experiment are not always perfectly symmetric. Therefore, one can not rule out that some Co atoms might also adsorb at the centers of the inner hexagon rings B–D, or on bridge or top sites.

5.3.2. Lateral manipulation of GNRs with adsorbed Co adatoms

Even though the Co adatoms on the GNR get easily picked up when trying to image them by means of AFM, they are quite stably adsorbed on the GNR. This is evidenced by the fact that Co atoms do not fall off the GNR when laterally manipulating the GNR with the STM tip. They even adhere to their original adsorption site on the GNR while the GNR is moved. An example for a lateral manipulation of a GNR is shown in Fig. 5.7. Panel (a) depicts the initial situation. 2 Co atoms are adsorbed on a short GNR. For the lateral manipulation, the bias voltage is lowered

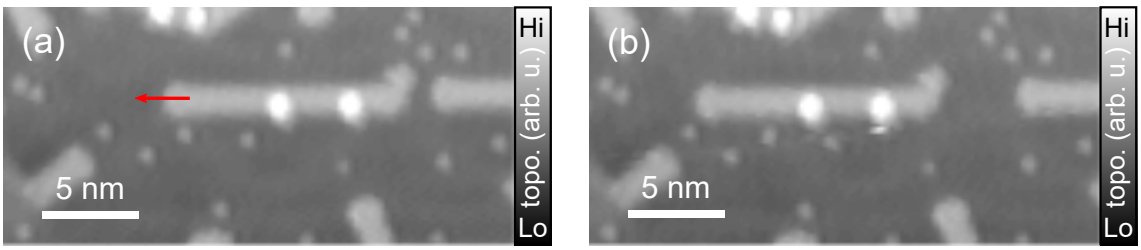

Figure 5.7.: **Lateral manipulation of GNR with Co atoms adsorbed on it.** (a) A GNR with 2 Co atoms on top is moved to the left by the STM tip. The red arrow describes the path of the STM tip during the manipulation process. (b) Final configuration. The adatoms did not change their adsorption positions on the GNR. $V_{bias} = 100\,\mathrm{mV}$, $I_{tunnel} = 2\,\mathrm{pA}$.

and the tunneling current is increased[11]. The red arrow represents the path the STM tip is taking during the manipulation process. Panel (b) shows that the GNR got displaced by 3 nm to the left, but the Co adatoms on the GNR did not move relative to the GNR.

5.3.3. Exemplary cases

In the following, some exemplary cases for voltage pulses on GNRs using different polarities will be given. Fig. 5.8 (a) shows three interconnected GNR segments with two Co atoms adsorbed on the longest segment. The Co atoms on the GNR are labeled with 1 and 2. The red cross indicates the spot at which the GNR was contacted by the STM tip to perform a voltage pulse. It is located at the corner of the longest GNR segment. The pulse was executed with a voltage of +700 mV and lasted for 1 s. The distances between tip and Co atoms were $s_1 = 13.5\,\mathrm{nm}$ and $s_2 = 8.2\,\mathrm{nm}$. In panel (b), the situation after the voltage pulse can be seen. The dashed circles indicate the original positions of the Co atoms on the GNR. As one can see, Co atom 1 moved away from the tip whereas Co atom 2 was displaced towards the tip. The motions were noted as $d_1 = 1.3\,\mathrm{nm}$ and $d_2 = -0.8\,\mathrm{nm}$. Additionally, both atoms are now adsorbed on the opposite GNR edge, i. e. they changed their adsorption sites from A to E (or vice versa).

Panel (c) shows another case of a pulsing event. One can see two interconnected GNRs with two Co atoms (labeled with 3 and 4) on the left GNR segment. This voltage pulse was performed with −1000 mV on the GNR segment without Co adatoms and lasted for 0.6 s. The distances between Co atoms 3 and 4 and STM tip were $s_3 = 10.2\,\mathrm{nm}$ and $s_4 = 15.3\,\mathrm{nm}$.
In the image after the pulse—shown in panel (d)—one can observe that Co atom 3

[11]Typical values for a lateral manipulation process are $V_{bias} = 50\,\mathrm{mV}$ and $I_{tunnel} = 200\,\mathrm{nA}$.

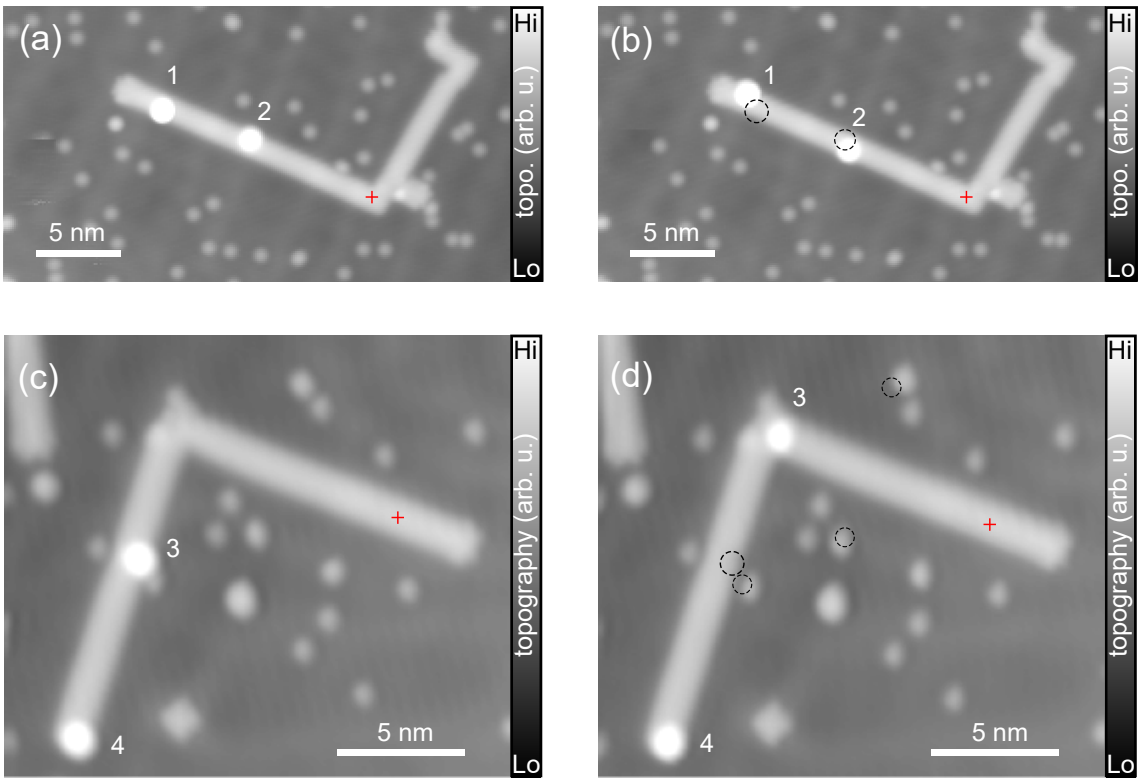

Figure 5.8.: **Exemplary cases for voltage pulses.** (a) Interconnected GNR segments with two Co adatoms (labeled 1 and 2) on the longest segment before a voltage pulse with +700 mV for 1 s. The red cross indicates the pulsing spot. (b) Situation after the pulse. The initial Co adsorption positions are indicated by dashed circles. $V_{bias} = 100\,\mathrm{mV}$, $I_{tunnel} = 2\,\mathrm{pA}$ for (a) and (b). (c) Interconnected GNR segments with two Co adatoms (labeled 3 and 4) before a voltage pulse with −1000 mV for 0.6 s. (d) Situation after the pulse. $V_{bias} = -100\,\mathrm{mV}$, $I_{tunnel} = 2\,\mathrm{pA}$ for (c) and (d).

moved by a quite large distance of $d_3 = -5.2\,\mathrm{nm}$. Co atom 4 did not move, therefore $d_4 = 0\,\mathrm{nm}$. It is also visible that some Co atoms on the bare Au surface got displaced, even though their motion is very small.

During the experiment, pulsing voltages ranging from −1000 mV to −500 mV and from +500 mV to +1200 mV were used. The current flowing during the pulse was mostly in the range of 1–10 µA. Voltage pulses with $|V_{bias}| < 500\,\mathrm{mV}$ turned out to rarely lead to an adatom displacement and were therefore not pursued.

5.4. Results and discussion

Since the tip can slightly change during a voltage pulse, the experimental conditions for all pulses are always very similar, but possibly not the same. For that reason, the result of many pulsing events has to be evaluated to obtain reliable conclusions from the evaluation of the Co motion.
In this section, the displacement of the Co atoms on the GNRs is tested with regard to the effects of electromigration forces. No clear dependence of pulsing voltage polarity and preferential direction of motion is found, though. However, GNRs pose a stage for 1-dimensional diffusion of Co atoms. This diffusion is investigated and the influence of various pulsing parameters is examined. Last, temperature dependent measurements are performed to attain the diffusion rate and barrier for Co atoms on the Au(111) surface.

5.4.1. Electromigration

The previous examples demonstrate that the motion of the Co adatoms is not unidirectional for a given polarity of the voltage pulse. In Fig. 5.8 (b), one Co atom moves away from the tip, the other one towards the tip. This, at a first glance, seems to contradict the expectations from the electromigration theory.
One has to note, however, that performing voltage (current) pulses provides the system with energy. Therefore, Joule heating as a source of motion has to be considered as well. The direction of this kind of thermal motion is random, though. To find a possible contribution from electromigration forces, a large number of pulsing events has to be considered. Since the direction of the thermal motion of the adatoms is random, their displacement should average to zero. Any remaining net displacement can thus be attributed to electromigration forces.

To this end, a large number of pulsing events was performed. In order to obtain unbiased statistics, however, certain adatoms had to be disregarded from the evaluation.
Co atoms that were adsorbed at the GNR termini (such as Co atom 4 in Fig. 5.8) were not counted because their motion on the GNR is limited a priori to one direction only—the center of the GNR. That would distort the statistics in favor of displacements towards the tip. Furthermore, it turned out during the experiment that Co atoms adsorbed at the GNR termini are very stable. They almost never moved upon pulsing, but stayed at their adsorption site[12]. A possible reason will be discussed later.
Similarly, adatoms adsorbed at the kinks of interconnected GNRs or at defect sites seemed to be pinned to their adsorption site and thus were disregarded as well.

[12]...or got picked up by the STM tip.

Total number of Co adatoms	1430	
Number of Co atoms that did not move	736	(51.5% / –)
Number of displaced Co atoms (including events below)	694	(48.5% / 100%)
Co moved along GNR	536	(37.5% / 77.2%)
Co fell off GNR	6	(0.4% / 0.9%)
Co moved to other edge (site A to E)	54	(3.8% / 7.8%)
Co atom vanished (pick up by STM tip)	98	(6.8% / 14.1%)

Table 5.1.: **Statistics for Co motion after a voltage pulse.** The first column describes the event and the second column the number of occurrences. The first percentage value refers to the portion with respect to the total number of Co atoms, the second one gives the portion with respect to the displaced atoms only.

Considering these restrictions, in total, around 900 voltage pulses were performed during which the motion of 1430 Co atoms was monitored.
Table 5.1 gives an overview of all pulsing events. Roughly half of the Co atoms got displaced. Most of them moved along the GNR. Only very few fell off the GNR during the displacement. Some only changed the adsorption site across the GNR (from A to E). A couple of adatoms vanished—that means they were not found in any subsequent STM image. This was interpreted as a pick up of the Co atom by the STM tip, i. e. the Co atom jumped (possibly due to the high electric field at the tip apex) to the tip.

To investigate the directionality of the motion, the displacement of each Co atom is plotted versus the pulsing voltage in Fig. 5.9. In this graph, Co atoms that did not move, only changed their adsorption site from A to E or vanished are not considered. The negative pulsing voltages (from $-1000\,\mathrm{mV}$ to $-500\,\mathrm{mV}$) are plotted in red and the positive ones (from $+500\,\mathrm{mV}$ to $+1200\,\mathrm{mV}$) in blue. As one can see, the displacement for both polarities of the pulsing voltage scatters and takes on both, positive and negative, values.
To find out about any preferential direction, the average displacement for the positive and negative voltage range is evaluated separately. For positive voltage pulses, the average displacement d_+ is $(0.2 \pm 1.0)\,\mathrm{nm}$. The uncertainty refers to the standard deviation. For the negative voltage range, $d_- = (0.1 \pm 1.5)\,\mathrm{nm}$ results. Both values are, within the experimental accuracy, not significantly different from each other and quite close to 0. That means that there is no net displacement and thus no prevailing wind or direct force. Also applying linear fitting curves to the data (applied to the entire voltage range and to positive and negative range separately) did not yield any indication for a preferential direction. That signifies that no electromigration forces could be observed in this experiment.
It is worth to mention, however, that there is very well displacement of Co adatoms. Neglecting the direction of the motion, the average displacement of an adatom is $(0.9 \pm 0.9)\,\mathrm{nm}$. That shows that the Co atoms get displaced by 3–4 graphene

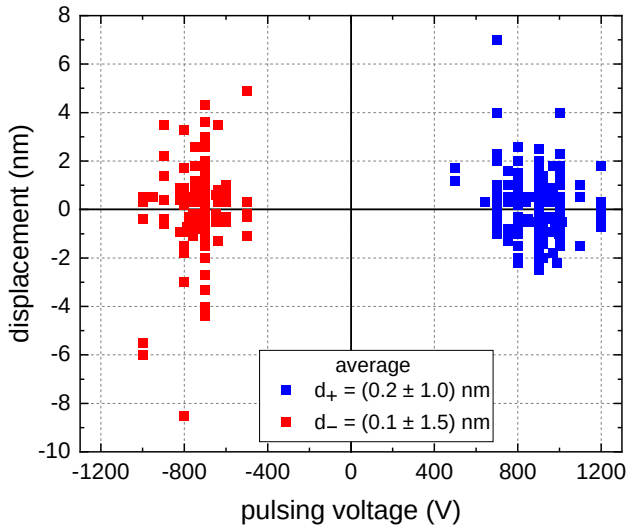

Figure 5.9.: **Adatom displacement after voltage pulse.** d_+ and d_- refer to the average displacement over the positive and negative pulsing range, respectively.

hollow sites in average, but the probability to move towards the tip or away from it is approximately equal.

Multiple reasons might be responsible why no signs of electromigration could be observed. The first one is related to the band structure of the 7-aGNRs. As mentioned in the previous chapter, 7-aGNRs on Au(111) exhibit a band gap of roughly 2.3 eV. Fig. 5.10 shows a differential conductance spectrum taken at the center of a 7-aGNR over a voltage range that covers conduction band (CB) and valence band (VB) onsets. The onsets of CB and VB are marked with dotted lines and are located at roughly −700 mV and +1500 mV, respectively. This yields a band gap of 2.2 eV and is therefore in agreement with literature values [28, 50, 127]. The CB is

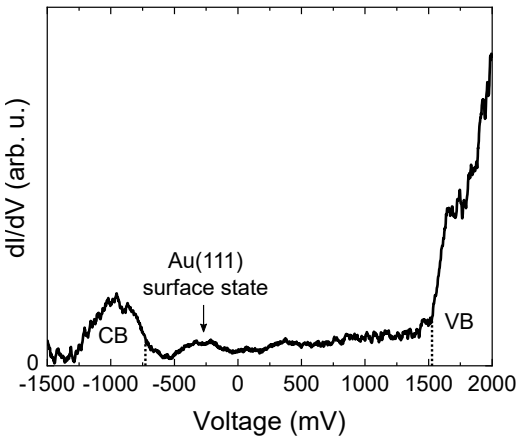

Figure 5.10.: **Differential conductance spectrum.** This spectrum was recorded at the center of a 7-aGNR. The onsets of conduction and valence band are indicated by dotted lines, the Au(111) surface state is marked with an arrow.

less pronounced because its detection is complicated by the vicinity to the Au(111) surface state [49] and the fact that the CB states for 7-aGNRs decay faster to the vacuum than the VB states [30].
In the gap region, the DOS does not fall to zero because of the substrate contribution from the Au surface. In particular, the Au(111) surface state (marked with an arrow) is prominent with its onset between −500 mV and −400 mV [131, 202, 208]. The comparatively low DOS of the GNR in the band gap region could nonetheless influence the electromigration test in the sense that less electrons will flow through the GNR but escape to the Au substrate instead[13]. This would diminish the probability for electrons to transfer their momenta to the Co adatom and therefore reduce the contribution of the wind force.
However, also pulses with voltages in the region of the CB, i. e. with −700 mV to −1000 mV, did not result in a directional motion of the Co atoms.

Another reason for the absence of electromigration could lie in the course of the electric field lines in the junction between STM tip and GNR during the pulsing events. To offer a feeling for the field strength in an STM junction, it is noted that electric field strengths of 1 V/nm at a bias voltage of 1 V can be reached under the apex [248]. Away from the center of the junction, the intensity decreases. Fig. 5.11 shows a schematic illustration for the paths the electric field lines could take during a voltage pulse[14]. For reasons of simplicity, the tip is depicted as a triangle. In the

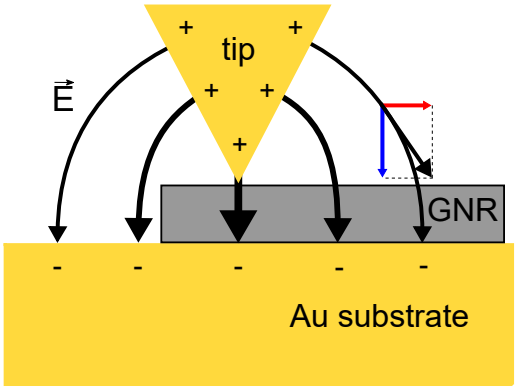

Figure 5.11.: **Electric field lines during voltage pulse.** This sketch shows an example for the paths of the electric field lines between tip and sample during a pulse with negative voltage. Off-center the tip apex, the electric field splits up in a component parallel (red arrow) and perpendicular (blue arrow) to the surface.

example, a negative voltage pulse is depicted, i. e. the electric field lines point from the tip to the Au surface—where the negative voltage is applied to. The electric field lines are assumed to penetrate the GNR, but field lines ending on the GNR would not affect the argumentation presented in the following. At the surface, the electric

[13] Koch *et al.* [127] found a higher conductance of 7-aGNRs when lifting them up with the help of an STM tip and applying voltages in the CB range than for voltages in the gap region.

[14] The role of the electric field caused by the charge of the injected electron is neglected here. The electric field caused by a single electron (assumed to be a point charge) in a distance of 1 nm is approximately 1 V/nm and thus of the same order as the electric field in the junction. However, the electron is expected to delocalize very fast in the sample (GNR or bulk gold). Therefore, the injected electrons might influence the vertical component of the electric field in the junction, but should not change the lateral field distribution qualitatively.

field is perpendicular to the sample plane but in between tip and sample, the field splits up in a component parallel (red arrow) and perpendicular (blue arrow) to the surface. This has consequences for the direct force which points in the direction of the electric field. A Co atom that is adsorbed on the GNR will not feel the full strength of the electric field in the junction, but only the fraction parallel to the surface. This effect is even enhanced, if the field lines end on the GNR[15].
As a side note, the fact that the electric field is (partially) perpendicular to the surface plane might enhance the pick up of Co adatoms by the STM tip.

Further possible influences on the Co displacement were tested. No difference for pulsing events on short GNRs in comparison to long GNRs could be detected. Furthermore, it apparently did not matter, if the Co atoms were adsorbed on single, isolated GNRs or on a bunch of interconnected GNRs[16]. The separation s between Co atom and tip during the pulse did also not affect the directionality of the displacement.

As a last point, it should be mentioned that the shape of the STM tip might play a role as well since it influences the electric field in the tunnel junction. The influence of the tip sharpness was not investigated explicitly here. Nonetheless, only relatively sharp tips were used for performing the voltage pulses. Slight changes at the tip apex due to the contacting procedure were compensated by performing a large number of pulses.

In conclusion, no electromigration forces could be detected during this experiment. Possibly, the current prefers to spread in the Au substrate instead of being confined to the GNR. Furthermore, the electric field lines are not parallel to the direction of Co adatom displacement along the GNRs. These points make the present setup not very suited for detection of electromigration. Clear traces of (random) displacement along the GNRs upon pulsing, on the other hand, could be detected.

5.4.2. One-dimensional diffusion

Even though no signs of directional electromigration could be found, the way the Co atoms move upon the voltage pulses is noteworthy. With 77.2% (536 out of 694), the majority of the displaced atoms moved along the GNR. Due to the limited width of the GNRs one can speak of a 1-dimensional motion of the Co adatoms along the GNR.
Remarkably, the Co atoms very rarely fell off the GNR onto the Au(111) surface—only in 0.9% (6 out of 694) of the cases. Even when pulsing "around the corner" of two interconnected GNRs (see Fig. 5.8 (c)), the Co displacement follows the course of the GNR. It seems like the GNR borders pose an energy barrier for the adatoms

[15] Due to the finite size of the Co atoms, the parallel component of the electric field sensed by the adatoms will not be exactly zero in this case.
[16] Apart from adsorption at defects at the interconnection sites which were especially stable.

that prevents them from dropping off to the Au substrate.
This can be understood in the framework of the Ehrlich-Schwoebel barrier which is known to form at step edges on crystal surfaces [249–251]. A possible scheme for an Ehrlich-Schwoebel barrier on the GNR is depicted in Fig. 5.12. Panel (a) shows

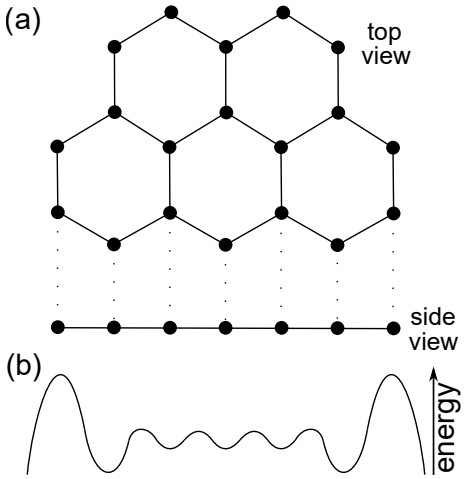

Figure 5.12.: **Hypothetical potential landscape across a 7-aGNR.** (a) Lattice structure of a 7-aGNR in top view (above) and side view (bottom). Black circles refer to carbon atoms. (b) Possible shape of the diffusion barriers for a Co adatom residing on the GNR. At the GNR edge, an Ehrlich-Schwoebel barrier prevents the Co from dropping to the surface.

the lattice structure of the GNR, both from top and side view. In panel (b), a possible contour of the diffusion barriers for adatoms across the GNR is illustrated. A minimum can be found at each hollow site across the GNR, separated by (small) energy barriers. The energy minima at the outermost hexagon ring centers are deeper, reflecting the increased probability to find adsorbed Co atoms at those sites. Since the transition to the Au(111) surface poses a step, its diffusion barrier is enhanced.

In this context, also the higher stability of Co atoms at certain GNR sites has to be discussed. Co atoms adsorbed at the GNR ends were less likely displaced. They might interact more strongly with the zigzag edge at the GNR terminus than Co atoms at the middle of a GNR with the armchair edges. An enhanced reactivity at zigzag sites, possibly paired with changes in the hydrogen termination of the GNR and its electronic structure[17], might lead to a pinning of the Co atoms at the GNR ends. This could also hold true for Co atoms at the kinks of interconnected GNRs or defect sites.
Here, it should be mentioned that DFT calculations for Au adatoms on GNRs yielded higher binding energies when the adatoms were adsorbed at zigzag sites than for armchair sites [252].
For these reasons, Co adatoms at the GNR termini, kinks and defect sites were excluded from the electromigration analysis.

Although certain adatoms could not be displaced laterally, they were not protected from being picked up by the STM tip upon voltage pulses. This vertical displacement

[17] see section 4.1.1 for the effect of an additional hydrogen atom at the GNR terminus to its π-system.

is an indication that no actual bond is formed between adatom and GNR terminus or defect site because otherwise it would not be possible to remove the adatoms by pulses with relatively low voltages.
During the experiment, we noted that around 14.1% (98 out of 694) of the displaced Co atoms vanished after a voltage pulse.
The probability for this pick up, however, was asymmetric with respect to the pulsing voltage. For negative voltage pulses, the pick up probability was 21.7%, whereas positive pulses led only in 8.7% to a vanishing of adatoms. Furthermore, the average separation between tip and Co atom during pulses that led to a pick up was larger for negative pulses ($s_- = 7.5\,\mathrm{nm}$) than for positive pulses ($s_+ = 5.6\,\mathrm{nm}$). Additionally, the average absolute voltage that resulted in picking up the Co atom was lower on the negative side with $V_- = -793\,\mathrm{mV}$ compared to $V_+ = +909\,\mathrm{mV}$ on the positive side. Apparently, pulses with negative bias are more effective in picking up Co adatoms.
A possible reason is given in the following. The pick up of Co atoms is promoted by the van der Waals force of the tip acting on the adatoms and the electric field in the junction. For both voltage polarities, the van der Waals portion is the same. Besides the electric field caused by the bias applied during the voltage pulses, there might be also a contribution stemming from different work functions of tip and sample (see section 5.1.3).
To determine the work function difference between tip and sample, Kelvin probe force spectroscopy was employed. Fig. 5.13 displays the resulting Kelvin parabola

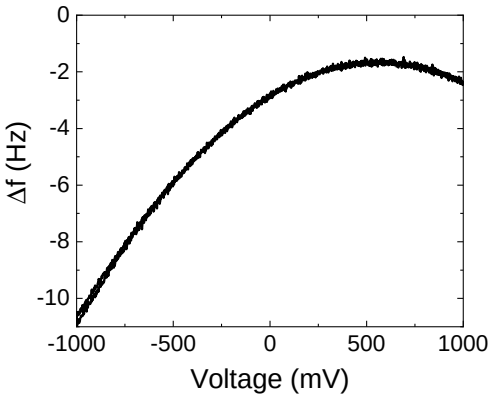

Figure 5.13.: **Kelvin parabola.** Frequency shift Δf recorded as a function of the applied bias voltage. The spectrum is taken above the clean Au(111) surface and has a parabolic shape. Its maximum is located at 560 mV.

with its maximum at a voltage of +560 mV. According to Eq. 5.9 this means that the work function of the sample is 560 meV higher than the one of the tip. Therefore, there is an inherent electric field in the unbiased junction in the tunneling regime. This inherent field leads to an enhancement of the perpendicular field component with negative pulses and to a weakening of the pulsing effect for positive pulses. That is why Co atoms get picked up more easily by negative pulses.

To evaluate the effectivity for a voltage pulse in terms of adatom displacement, the escape probability (EP) is introduced. The EP refers to the probability that an

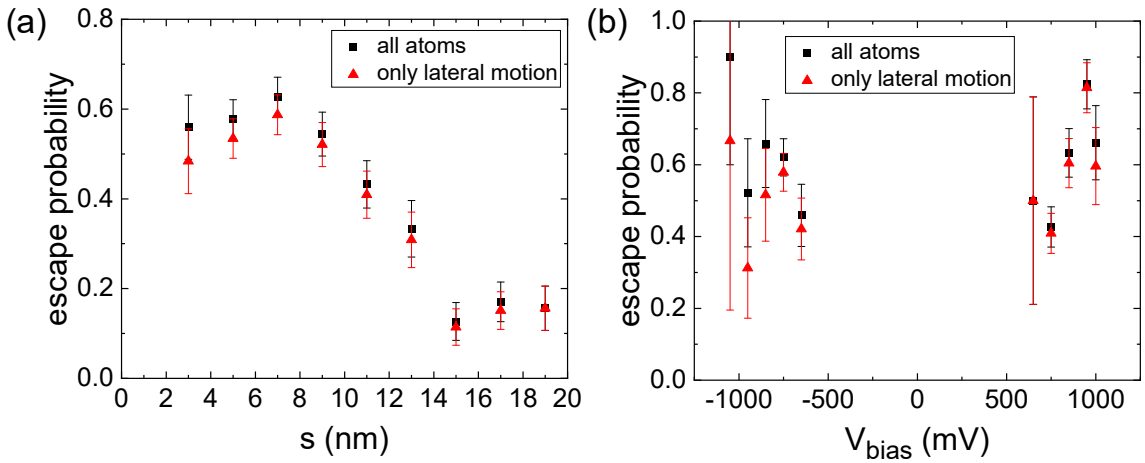

Figure 5.14.: **Escape probability.** (a) EP as a function of initial tip-adatom separation. (b) EP as function of pulsing voltage, only for pulses with $s < 10\,\mathrm{nm}$. Black squares consider all atoms, red triangles disregard picked up Co atoms. Data points represent intervals (see text). Error bars show the standard deviation.

adatom leaves its initial adsorption position. It is given by the number of displaced atoms divided by the total number of atoms.

In Fig. 5.14 (a), the EP as a function of tip-adatom separation before the voltage pulse, EP(s), is plotted. The black squares represent the EP for all displaced adatoms. Red triangles refer only to laterally displaced adatoms, i. e. Co atoms that got picked up during a pulse are disregarded. This was done to stress the effects of s on the lateral motion. For clarity, the events are grouped in the graph. Each data point represents an interval with a width of 2 nm. That means the data point at $s = 3\,\mathrm{nm}$ is the average of all pulsing events that were performed with a tip-sample separation between 2 nm and 4 nm.

Considering all displaced atoms, EP(s) is first roughly constant (around 50–60%) up to $s = 10\,\mathrm{nm}$. Then, it drops steadily to a value of 10–20% and becomes constant again. This means that atoms in a certain interval around the tip are more likely to be displaced.

One reason to explain this is that the GNR gets locally hot upon pulsing. The heat enables the diffusion of the adatoms. After a distance of roughly 10 nm away from the tip, the GNR might get colder and therefore the EP drops. A counter argument for this assumption is that adatoms should diffuse preferably from the hot side of the GNR to its cold side. However, no directional motion was observed.

Another reason for the initially constant and then dropping EP(s) might be that the electric field in the junction is highest directly underneath the tip apex and then weakens away from the center. The decay is, however strongly dependent on the geometrical shape of the tip. Thus, the direct force—promoted by the electric field—might enable the adatoms to leave their potential wells and diffuse along the GNR. After a certain tip-adatom distance, the field intensity drops and therefore

the displacement gets less likely.
The red triangles in Fig. 5.14 (a) depict EP(s) for lateral displacement only—i. e. without picked up Co atoms. Apart from the first few data points, EP(s) for both cases is very similar. Considering only lateral motion, EP(s) first increases for low tip-sample separations before it drops. This is, at a first glance, counter-intuitive. It reflects, however, that the pick up probability for small s is enhanced. Voltage pulses with low tip-sample separations led more frequently to a Co pick up. Furthermore, there is a certain threshold energy required to lift Co atoms out of their potential wells and enable motion. If the threshold is too high, i. e. the potential well is too deep, no lateral diffusion is possible. Increasing the electric field in the junction, however, eventually leads to a Co pick up.

To investigate the role of the pulsing voltage, EP is plotted as a function of V_{bias} in Fig. 5.14 (b). Since for small tip-adatom distances EP(s) is approximately constant, only pulses with $s < 10\,\mathrm{nm}$ were considered to emphasize the effects of V_{bias} on the EP. The data are grouped as well. Each point represents an interval of 100 mV. One can see a trend of increasing EP(V_{bias}) with increasing absolute value of the pulsing voltage. That means that—as mentioned above—the higher electric field in the junction causes the adatoms to diffuse more effectively. The fact that the difference between black squares (all displaced atoms considered) and red triangles (only lateral motion taken into account) grows with higher $|V_{bias}|$ tells that the pick-up probability increases for larger $|V_{bias}|$. This trend is more pronounced on the negative voltage side, reflecting that the pick up is more effective with negative voltages.

Another remarkable fact is that the displacement of Co atoms on GNRs by voltage pulses is quite effective. In Fig. 5.8 (d), it could be seen that sometimes—upon pulsing on a GNR—also the Co atoms on the bare Au(111) surface diffuse. This displacement, however, was not so frequent and mostly very small. To investigate the differences between diffusion of Co atoms on GNRs and on Au, we performed systematically pulses on the bare Au surface and compared the adatom displacement to the one of Co adatoms on GNRs.
The pulsing procedure was done in an analogous way to the pulsing on GNRs. However, no point contact was established since that led in most cases to dropping of tip atoms on the surface. The approach height was chosen in such a way that the current during the pulse was comparable to the one for pulsing on GNRs, i. e. in the range of roughly 1–10 µA.
For the evaluation of Co motion on Au(111), only atoms with $s \leq 7\,\mathrm{nm}$ were considered because this area was visible in most image frames of voltage pulses on GNRs[18]. Table 5.2 shows an overview of different pulsing scenarios. As already mentioned, 49% of the Co adatoms on GNRs get displaced during a voltage pulse on the GNR. However, only 6% of the nearby Co atoms on the Au(111) surface move when puls-

[18]It should be noted that Co atom displacement in some cases was also observed for $s > 7\,\mathrm{nm}$. To obtain reliable statistics, however, we stuck to restrict the area of interest to $s \leq 7\,\mathrm{nm}$.

Event	Displaced atoms
Displacement of Co on GNR after pulse on GNR	694/1430 (49%)
Displacement of Co on Au(111) after pulse on GNR	391/6331 (6%)
Displacement of Co on Au(111) after pulse on Au(111)	16/519 (3%)

Table 5.2.: **Comparison of Co motion on GNRs and Au(111) after pulsing on GNR and Au(111).** The first number in the right column refers to the displaced Co atoms, the second number to the total number of Co atoms in the area of interest.

ing on the GNR. Upon performing the voltage pulse on the Au(111) surface, only 3% of the Co adatoms on the Au substrate get displaced.
There is a significant difference between Co atoms on GNRs and on the Au substrate in terms of displacement. For the motion of Co atoms on the Au(111) surface, on the contrary, it only plays a minor difference if the pulse was executed on a GNR or directly on the Au surface. This indicates that diffusion for Co atoms on the GNRs is more effective. A possible reason for this observation is that the GNR might get hotter during the voltage pulse and thus promote Co displacement more readily. This will be discussed in more detail in the next section.

5.4.3. Temperature dependent measurements

In order to find out more about the diffusion of Co on the GNRs and on Au(111), we tried to determine the hopping rate ν. To this end, it was evaluated how many times the Co atoms on GNRs moved what distance. The result is plotted in a histogram in Fig. 5.15. Hereby, the bins have approximately the size of one lattice constant, i. e. from one outer hexagon ring to the next outer hexagon ring along the GNR armchair edge ($\approx 4.3\,\text{Å}$). The histogram shows that in most cases the adatoms are displaced by $|d| < 2\,\text{nm}$, but also large displacements are possible.
Note that only Co atoms that moved along the GNR are incorporated in the histogram. Due to their high count (736 in total), Co atoms that did not move were left out for clarity. The large number of adatoms with zero displacement can not simply be explained by jumps forth and back to the origin. Additionally, some adatoms might be pinned to their adsorption sites. This will be further discussed later in this section.
By fitting a 1D random walk function to the above distribution, one can extract the hopping rate (via Eqs. 5.4 and 5.2). This is not performed here, but was treated in the PhD thesis of Sasha Vrbica [216]. There, a value of $\nu \approx 5\,\text{Hz}$ was found[19].

As was pointed out before, the diffusion of the Co atoms on the GNRs might be due to heating of the GNR during the voltage pulse. To determine a temperature thresh-

[19]The large number of immobile Co atoms was taken into account by introducing a prefactor to the random walk function.

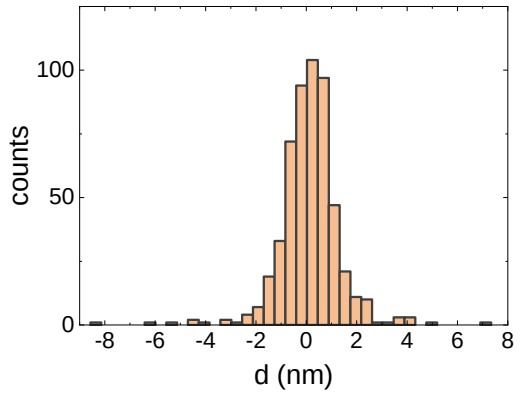

Figure 5.15.: **Distribution of Co displacement after voltage pulse.** Histogram of how many adatoms traveled what distance on the GNR after a voltage pulse. Only adatoms moving along the GNR were considered.

old, above which the Co atoms start to diffuse on the GNRs, variable temperature measurements were performed.

To this end, the sample was heated to different temperatures. This was done by warming the entire STM scan head—which is thermally weakly coupled to the He cooling bath—with a heating diode. Then, we waited until the temperature stabilized ($\pm 1\,\mathrm{K}$) and scanned the same sample area over and over again. Thereby, we looked for diffusion of Co atoms on the Au(111) surface and on the GNRs.

After the first heating step to 20 K, no motion of Co atoms could be detected. Therefore, we further elevated the temperature.

At 34 K, we observed that Co diffusion on the Au(111) surface started. Panels (a) and (b) of Fig. 5.16 show two subsequent scans of the same sample area. The time delay between the two subsequent images was $\Delta t = 171\,\mathrm{s}$. The thermal drift was corrected in hindsight by overlaying the images manually over each other. For this, the immobile herringbone reconstruction and the GNRs—which did not diffuse even at the highest temperatures tested—served as marker structures.
There are many Co atoms on the Au(111) surface. Their initial positions are marked with yellow circles. Some adatoms appear fuzzy. This is presumably due to an unstable tip, i. e. the front atoms at the tip apex might slightly rearrange during the scan. On the one hand, it can not be ruled out that the adatoms could also get pushed away by the STM tip or diffuse during the scanning at elevated temperatures. One can see that some of the adatoms moved in between the two images. We tracked the motion of every single Co atom and determined the average squared motion $\langle(\Delta r)^2\rangle$ for all adatoms. This was done for a series of subsequent images.
For diffusion at 34 K, an average squared motion of $\langle(\Delta r)^2\rangle = 0.6\,\mathrm{nm}^2$ was found. This value can be inserted into Eq. 5.8. By further inserting $\bar{l} = 4.1\,\text{Å}$ as the lattice constant of the Au(111) surface and $\Delta t = 171\,\mathrm{s}$, one obtains a value for the hopping rate of $\nu = (21 \pm 4)\,\mathrm{mHz}$. The uncertainty results from an averaging over different imaging sequences. This value is much lower than the hopping rate determined for Co on GNRs.

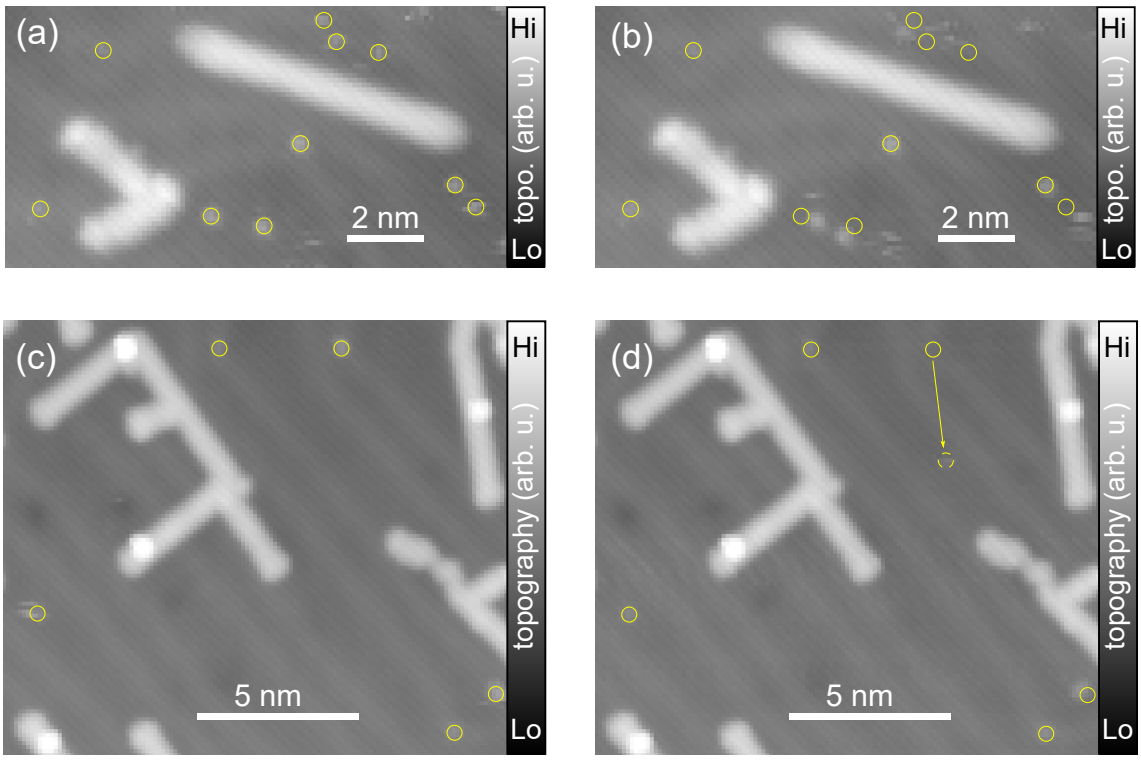

Figure 5.16.: **Co diffusion at elevated temperatures.** (a)–(b) Two consecutive images of the same sample area at $T = 34\,\mathrm{K}$ (corrected for thermal drift). The time Δt between the two images is 171 s. Yellow circles in both images mark the initial positions of the Co atoms. (c)–(d) Same as above, but for $T = 46\,\mathrm{K}$ and $\Delta t = 189\,\mathrm{s}$. The arrow marks the diffusion of one specific Co atom. $V_{bias} = 100\,\mathrm{mV}$, $I_{tunnel} = 1\,\mathrm{pA}$.

In the PhD thesis of Sasha Vrbica [216], the diffusion rate at 34 K was determined by fitting a 2D random walk function (Eq. 5.5) to a histogram obtained by evaluating image-to-image displacements of the Co atoms on Au(111) during two subsequent scans. From this evaluation, a diffusion rate of 25 mHz resulted which agrees with the value obtained here.

We further increased the temperature. Panels (c) and (d) of Fig. 5.16 show two subsequent images taken at $T = 46\,\mathrm{K}$. The time between the two images was $\Delta t = 189\,\mathrm{s}$. Here, less adatoms are visible. Furthermore, only one atom on the Au surface moved appreciably (motion highlighted with a yellow arrow). From another area on the sample with more adatoms (not shown here), we determined a hopping rate of $\nu = (5 \pm 2)\,\mathrm{mHz}$. Despite the higher temperature, this value is surprisingly lower than the one obtained at 34 K. A possible reason for this might be that certain sites on the Au(111) surface are more reactive—like the kinks of the herringbone reconstruction (c. f. Ref. [194])—and therefore Co adatoms might be adsorbed there more stably (see also Ref. [253]). It is possible that most of the freely moving adatoms

already migrated to step edges during the heating process. When we finally reached 46 K, potentially mainly Co atoms that are harder to move are still on the surface. Therefore, the diffusion rate seems to be lower.
Furthermore, it should be pointed out that the Co atoms on the GNR did not move.

The highest temperature tested was 79 K. Here, we did not observe any motion of Co adatoms, neither on Au(111) nor on the GNRs. Possibly, all mobile Co atoms on Au already diffused to step edges or defect sites on the Au surface and therefore we could not observe any displacement.
The lack of motion of Co on the GNRs probably means that the temperature of the GNR during a voltage pulse is (much) higher than 79 K. One could argue that the Co atoms on the GNRs might also have started diffusion and what we see now are only pinned atoms. However, we did not observe motion of Co on the GNRs at any tested temperature (9 K, 20 K, 34 K, 46 K, 62 K and 79 K), which makes that scenario rather unlikely.

As a next step, the diffusion barrier E_D was estimated. Usually, it is determined from the slope of the Arrhenius plot when the diffusion rate is plotted versus the inverse temperature [254]. Since the diffusion in our case showed an unexpected decrease in diffusion rate upon increasing the temperature—which might be related to a pinning of certain adatoms to defect sites—we calculated E_D for 34 K and 46 K separately. By reshaping Eq. 5.6,

$$E_D = -k_B T \ln\left(\frac{\nu}{\nu_0}\right) \tag{5.12}$$

results. When inserting $\nu_0 = 10^{13}$ Hz and the hopping rate determined above, one obtains $E_D = (107 \pm 4)$ meV at $T = 34$ K. The uncertainty margin stems from the propagation of uncertainty from the determination of ν on the one hand, and the uncertainty in temperature on the other hand—which was assumed to be ± 1 K, but might be even higher. The latter term has more weight in the determination of uncertainty, since ν enters logarithmically. As a side note, even when changing the so-called attempt frequency ν_0 by two orders of magnitude, only an additional uncertainty of ± 10 % in E_D results (which is not included in the uncertainty margin here).
The same procedure was repeated for the diffusion barrier at 46 K and a value of $E_D = (149 \pm 4)$ meV was obtained. According to the lower diffusion rate, also a higher diffusion barrier resulted at this higher temperature. Again, it is stressed that these unexpected values might result from a partial diffusion of freely moving Co adatoms to the Au(111) step edges and a higher ratio of pinned Co adatoms that could have distorted the determination of the diffusion rate.
It should be further noted that the uncertainty margins might be larger than indicated here. To obtain more precise results, one would have to wait longer for the measurement temperature to stabilize. The exact evaluation of E_D, however, was not in the main focus of this project. Still, both values obtained here are in line with literature predictions for Co diffusion on Au(111). Depending on the reconstruction

area on the Au(111) surface, barrier heights of 100–200 meV were found by theory [255].

As already mentioned, the Co atoms on the GNRs did not move even at the highest temperatures tested here. Thus, E_D for Co on a GNR could not be determined experimentally. Therefore, theoretical values obtained by DFT calculations were used to estimate the temperature the GNRs might reach during a voltage pulse. Typical values for the diffusion barrier for Co atoms on a single layer graphene were around $E_D \approx 0.5\,\mathrm{eV}$ [243, 256, 257] (see also further references in Ref. [243]). When putting this value into Eq. 5.12, further inserting $\nu = 5\,\mathrm{Hz}$ (determined for diffusion of Co on GNRs during the pulses [216]), and solving for T, one obtains a temperature of $T = 205\,\mathrm{K}$. It has to be noted that the theoretical values for E_D were determined as just the energy difference between high symmetry adsorption sites (hollow and top or bridge positions). A more accurate determination of E_D would require the calculation of the complete potential landscape [195] and might yield an even higher value for T. Thus, the GNRs could get considerably hotter than the temperatures tested here.

The higher diffusion barrier for Co on GNRs than for Co on the bare Au(111) surface might explain why we see motion of Co on Au(111) upon raising the temperature, but not on the GNRs.
The reason, why the displacement of Co on the GNRs upon pulsing is so much more effective than for Co on Au might be related to the temperature spread in the substrate. Whereas the heat can easily be transported to the bulk when pulsing on the Au(111) surface, the GNR is presumably not so strongly coupled to the Au substrate and therefore gets hotter.
To increase the effectivity of pulses on the Au(111) surface, one could try to use voltages in the range of -400 to $-500\,\mathrm{mV}$ to hit the resonance of the Au(111) surface state. This might keep a larger fraction of the current close to the surface and therefore lead to a larger displacement of Co atoms.

5.5. Conclusion and Outlook

In this chapter, 7-aGNRs were grown on a Au(111) surface in UHV and Co atoms were added. A fraction of the Co atoms adsorbed on top of the GNRs. The adsorption position of the Co atoms on the GNRs was estimated by means of STM. By contacting the GNRs with an STM tip and applying a bias voltage pulse, current was injected into the system and the adatoms started to diffuse.
The motion of the adatoms was tested for the influence of electromigration forces but no preferential direction of the displacement was found. Two reasons were offered to explain why no electromigration could be observed. On the one hand, most of the voltages used for pulsing were in the range of the band gap of the 7-aGNR, thus reducing the flow of electrons within the GNR and lowering the wind force.

On the other hand, the electric field lines in the junction are not parallel to the displacement of Co atoms along the GNR and therefore the contribution of the direct force is lowered.
Remarkably, almost all displaced Co atoms moved along the GNR. This was explained by the presence of an energy barrier that prevents the Co atoms from falling off the GNR and yields—due to the small width of the GNRs—a 1-dimensional motion. The chance of Co displacement on a GNR was expressed in terms of an escape probability and tested for the influence of the initial tip-adatom pulsing distance and the applied bias voltage.
Further, the displacement of Co atoms on Au(111) was compared to the motion of Co atoms on GNRs upon pulsing on Au and the GNRs. A much higher diffusion rate was found for Co atoms on GNRs.
Temperature dependent measurements were performed and the diffusion behavior of Co on the Au(111) surface was determined. However, some adatoms seemed to be pinned to defect sites on the surface which impaired the determination of the hopping rate, especially at higher temperatures.

One way to find electromigration forces for Co atoms on GNRs might be to lift up the GNR with an STM tip [127]. In this way, the GNR would be contacted on one end by the STM tip and on the other end by the sample surface, whereas its center would be decoupled from any substrate. The electric field in the junction would point along the GNR axis and thus maximize the influence of the direct force. Likewise, the contribution of the wind force would be enhanced since the electrons have to pass through the GNR instead of being able to tunnel directly into the substrate.
Instead of 7-aGNRs with a large band gap, one could also try to use GNRs with a lower (or vanishing) band gap, such as 5-aGNRs [258, 259], 9-aGNRs [30] or zGNRs [52]. In general, the 1-dimensional nature of GNRs offers an ideal proving ground for testing the directionality of electromigration.

6. Summary

Since the discovery of graphene, scientists try to explore new graphene-based technologies for future applications. Promising candidates for implementation in novel devices are GNRs because they can be fabricated in many different shapes with high precision. This allows to tailor their electronic properties like their band gap. Thanks to advances in solution chemistry, a manifold of different GNR structures is achievable. Many studies on the fabrication of new types of GNRs are carried out and some of them are also tested with regard to their transport properties.
While transport through GNRs is mainly researched on mesoscopic length scales, one has to keep in mind that modifications on the atomic scale can have an enormous influence on their electronic properties.
This thesis tried to connect the perspective of macroscopic transport characterizations with modifications on the atomic scale. In the preceding pages, different approaches of describing the electronic properties of GNRs were discussed. On the one hand, cGNRs synthesized in vitro were deposited on an insulating substrate and their transport properties were examined by contacting the cGNRs with metal leads. On the other hand, 7-aGNRs were grown from precursor molecules on a Au(111) substrate in an STM chamber. Single Co atoms were added and the effects of these adatoms on the electronic structure of the 7-aGNRs were studied. Finally, the current-induced diffusion of Co atoms adsorbed on the 7-aGNRs was investigated.

In order to deposit the polymerized cGNRs onto a substrate, they had to be brought into dispersion first. THF and chlorobenzene were found to be suitable solvents for this task. Upon drop-casting the dispersion onto hBN, the formation of ordered cGNR domains was observed by means of AFM. Taking advantage of the parallel cGNR orientation within the domains, contacts were prepared by employing EBL and metalization. The I-V-characteristics of 4- and 6-cGNR devices were measured and found to be dominated by Schottky barriers that form at the cGNR–metal interfaces. With the help of the thermionic field emission model, the Schottky barrier heights were estimated.
In an attempt to improve the contacts and protect the cGNRs from environmental influences, the ribbons were encapsulated with a second hBN flake and zero-dimensional contacts were fabricated. The reliability of this type of contact still needs to be improved, though, since the contacts failed after only few measurement cycles. One option to tackle this problem is to remove residues from the fabrication process that possibly persist at the cGNR–metal interface with an additional oxygen

etching step.
Despite the persisting issues in the fabrication of reliable contacts, the sample preparation method employed in this thesis shows that it is possible to deposit domains of parallel GNRs on an insulating substrate. This facilitates contacting a larger number of GNRs at once which is helpful for applications in electronic devices because it acts like a fail safe from single defective GNRs.

Addressing atomistic aspects, GNRs were grown on a Au(111) substrate in an STM chamber under UHV conditions by means of on-surface synthesis. Using DBBA precursor molecules, 7-aGNRs of high quality and purity resulted. After adding single Co atoms to the surface, two sets of experiments were performed.
In the first set, the Co atoms were manipulated underneath the 7-aGNRs with the help of an STM tip. Differential tunneling spectra taken at the intercalation sites revealed a peak whose shape was dependent on the Co intercalation position. Co atoms buried at the middle of the armchair edge displayed a narrow peak which was assigned to a Kondo resonance. Co atoms at the corners of the 7-aGNRs exhibited a slightly broader peak which presumably stems from a hybridization of Co atom states with the end state present at the zigzag termini of the 7-aGNRs. When placing the Co atom at an intermediate position (three carbon rings away from the zigzag edge), no signs of a Kondo resonance could be detected. Instead, the 7-aGNR end state seemed to be extended along the armchair edge up to the intercalation site. Kondo temperatures were extracted by manually fitting the differential conductance spectra.
Density functional theory and tight-binding calculations suggest different coupling scenarios between Co atom states and 7-aGNR end state for the different intercalation sites.
To further investigate the Kondo properties of the system, temperature and magnetic field dependent measurements are necessary.

In the second set of experiments on UHV-synthesized 7-aGNRs with Co adatoms, the current-induced diffusion of Co atoms that adsorbed on top of the 7-aGNRs was studied. To initiate the diffusion process, the 7-aGNR was contacted with an STM tip and current was injected into the sample. Due to Joule heating, the Co atoms started to diffuse. Interestingly, the displacement of the Co atoms took place mostly along the 7-aGNR. This one-dimensional motion was rationalized by the presence of an energy barrier at the 7-aGNR edges.
The diffusion of Co atoms on the Au(111) surface was tested for comparison and found to be much lower than the one of Co atoms adsorbed on the 7-aGNRs. By testing the Co displacement at different temperatures, the diffusion rates were estimated.
No preferential direction of the Co motion (towards or away from the tip) could be detected. The observation of electromigration forces might be possible by lifting up the 7-aGNRs with an STM tip or by using GNRs with lower band gaps.

There is still a long way ahead to fully understand how modifications on the atomic

scale change the transport properties on the mesoscopic scale and to combine the atomistic and mesoscopic worlds. Nonetheless, the versatility of GNRs and the feasibility of tailoring their electronic states by introducing adatoms to the GNRs are promising prospects for the future application of GNRs in novel devices.

A. Fitting of the Kondo temperature

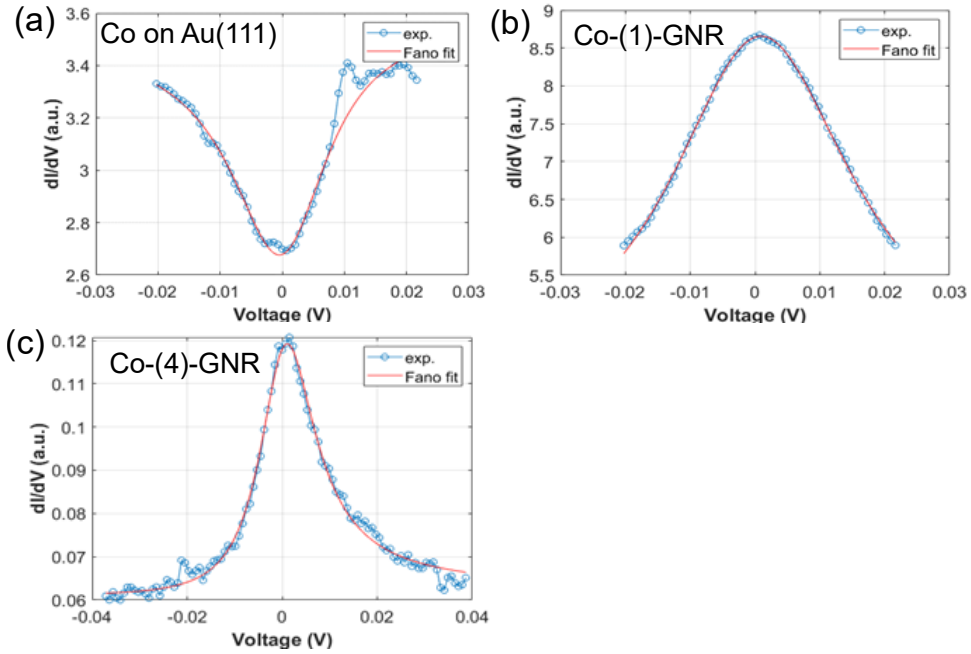

Figure A.1.: **Fano fits to experimental data.** Fano fits (red line) after Eq. 4.3 to the experimental dI/dV curves (blue dots) of (a) Co on Au(111), (b) a Co-(1)-GNR-complex and (c) a Co-(4)-GNR-complex.

Fig. A.1 shows the dI/dV spectra (blue dots) of (a) a Co atom on Au(111) (from Fig. 4.25), (b) a Co-(1)-GNR-complex (from Fig. 4.18) and (c) a Co-(4)-GNR-complex (from Fig. 4.14). The red curve is a non-linear least square fit of Eq. 4.3 to the experimental data.

panel	configuration	fitting range	T_K	q	E_K
(a)	Co on Au(111)	±20 mV	(106 ± 10) K	0.089	0.4 mV
(b)	Co-(1)-GNR-complex	±20 mV	(200 ± 7) K	57.1	0.6 mV
(c)	Co-(4)-GNR-complex	±40 mV	(78 ± 4) K	8.4	0.2 mV

Table A.1.: **Fitting parameters for Fig. A.1**

B. Measurement setups

Here, the different setups used for the sample characterization are described.

Ambient condition AFM

The formation of cGNR domains on hBN flakes was investigated with the Dimension Icon ambient condition AFM from Veeco Instruments employing the tapping mode. The setup is depicted in Fig. B.1. Samples were placed on a motorized stage. A coated Si cantilever served as AFM tip. It was driven by a piezo actuator and a laser was focused on the cantilever via an objective lens. The reflection of the laser signal was detected by a position sensitive photo sensor. Thus, the deflection of the AFM tip due to tip-sample interactions could be detected.

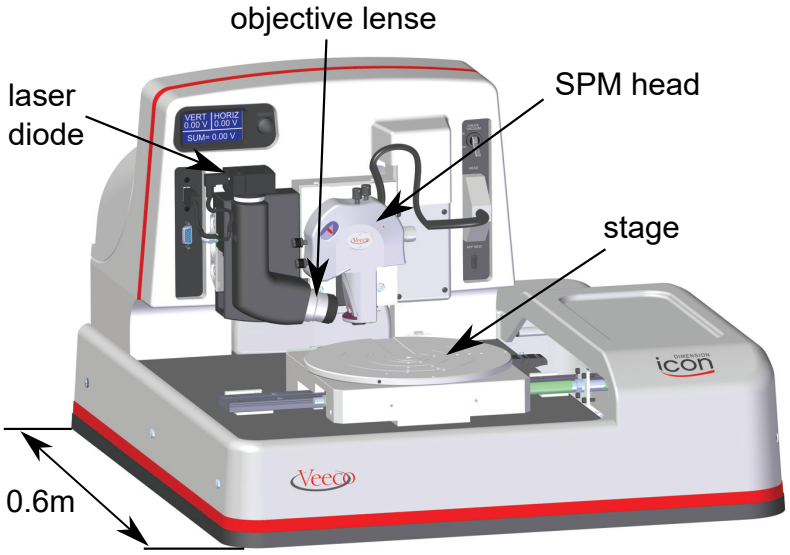

Figure B.1.: **Ambient condition AFM.** Schematics for the ambient conditions AFM setup used to identify cGNR domains on hBN. After [260].

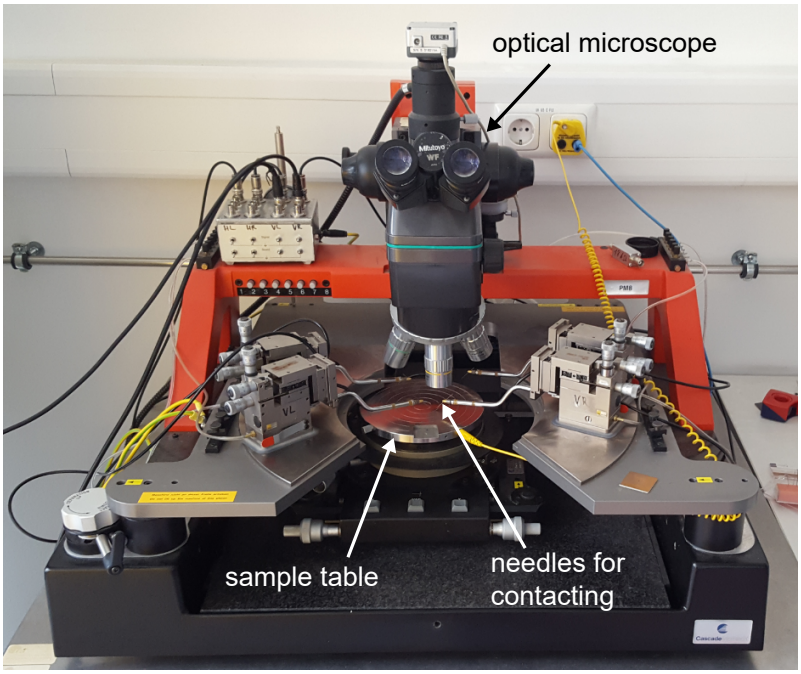

Figure B.2.: **Probe station.** Setup used for the transport characterization of the cGNR devices.

Probe station

After adding metal leads to the cGNRs, the I-V-characteristics of the devices were measured using a probe station (see Fig. B.2). The samples were placed on the movable sample table. Sharp metallic needles were lowered onto the metal leads to establish contact. The needles could be positioned with micrometer screws and were connected to the measurement devices.
A Yokogawa 7651 power supply was used to apply the source-drain voltage. The drain current was recorded using an Ithaco 1211 current preamplifier and an Agilent 34410 digital multimeter. The back gate voltage was applied with a Yokogawa GS200 voltage source.

Ultra high vacuum low temperature STM/AFM

Synthesis of 7-aGNRs and the corresponding experiments were performed in an ultra high vacuum low temperature combined STM/AFM. The setup follows the design from SPS-CreaTec and is depicted in Fig. B.3 (a). The entire vacuum system is placed on pneumatic dampers and consists of three chambers that are interconnected via gate valves. Samples are introduced to the machine via the load-lock which is pumped by a turbomolecular and a roughening pump. Single metal crystals are used as a substrate for 7-aGNR growth. They are placed on a sample holder (see panel

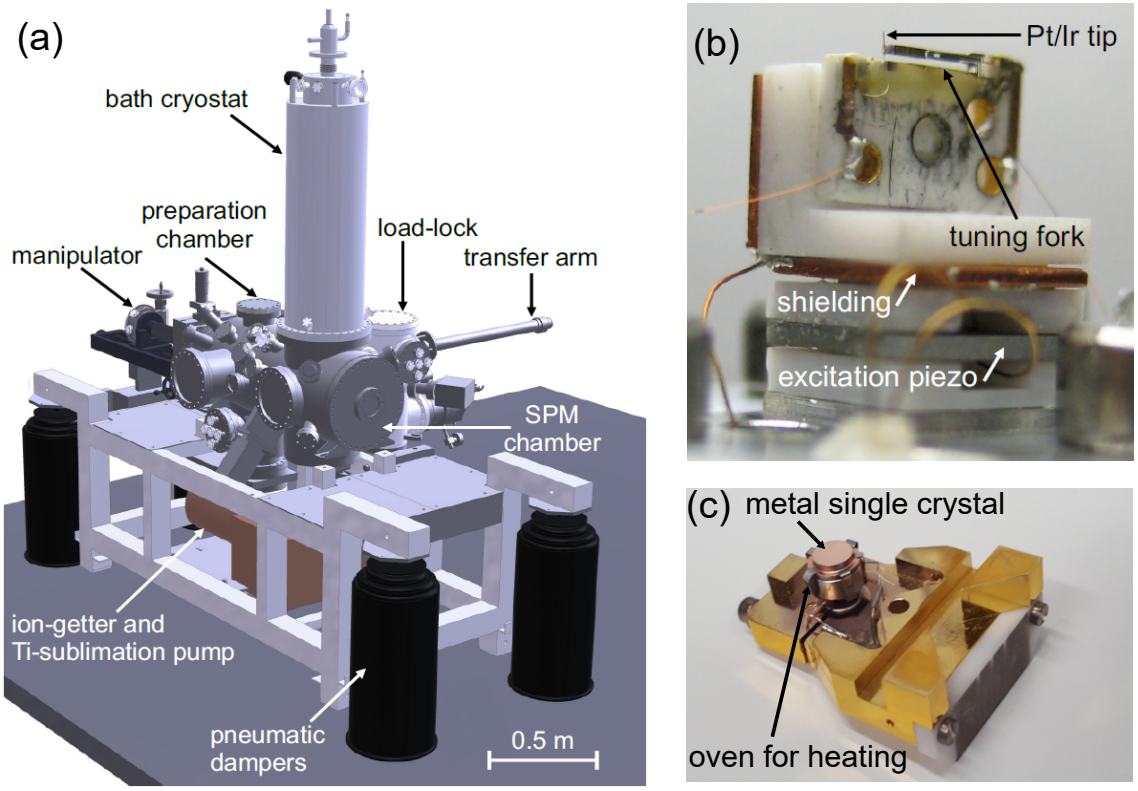

Figure B.3.: **UHV LT STM/AFM.** (a) Schematic drawing of the ultra high vacuum low temperature combined STM/AFM apparatus. (b) Picture of a mounted qPlus sensor. (c) Sample holder with metal single crystal. Images (a) and (b) from [261].

(c)) and can be heated by an oven. With a transfer arm, the sample holder can be brought into the preparation chamber where it is attached to the manipulator. Here, the samples are sputtered and annealed, the precursor sublimation and 7-aGNR growth takes place and NaCl islands are deposited. After sample preparation, the sample holder is transferred into the SPM chamber where the scan head is attached to a 5 K bath cryostat. Preparation chamber and SPM chamber are pumped by ion-getter and Ti-sublimation pumps yielding typical pressures below 10^{-10} mbar. Panel (b) shows a picture of a qPlus sensor (tuning fork with Pt/Ir tip) that is glued with one prong to a substrate. The sensor is driven by an excitation piezo. The mechanical oscillation of the sensor translates into an electrical signal because the tuning fork is composed of piezoelectric material.
The bias voltage in STM measurements is applied to the sample while the tip is kept grounded.

C. Experimental methods

Here, some details are added to the description of the sample preparation in the main text.

C.1. Fabrication of cGNR devices

Standard-contacted cGNR devices

Preparation of hBN samples First, a $4.5 \times 4.5\,\mathrm{mm}^2$ chip cut from a Si/SiO_2 substrate was cleaned by sonication in acetone, washing with isopropanol and plasma ashing in forming gas atmosphere at a pressure of 1.7 mbar for 4 min (at 40% plasma asher power). Afterwards, hBN crystals (mostly provided by Taniguchi and Watanabe) were mechanically exfoliated onto the chip using an adhesive tape (Nitto ELP BT-150-ECM from Nitto Denko). Suitable hBN flakes were identified with the help of an optical microscope. Here, the height of the hBN flakes could be estimated by the color of the flake in the microscope image.

Preparation of cGNR dispersion As described in the main text, tetrahydrofuran (THF) was used as solvent for the 4-cGNRs and chlorobenzene for the 6-cGNRs. A tweezers tip full of cGNR powder was put into a beaker glas half-filled with warm (60°C) solvent. The mixture was sonicated for at least one hour until it turned violet for the 4-cGNRs and gray for the 6-cGNRs.

Deposition of cGNR dispersion cGNRs were brought onto the hBN flakes by using two methods. One was drop-casting of the cGNR dispersion onto the sample (Si/SiO_2 chip with exfoliated hBN flake) lying on a 60°C hot plate. About 5 drops were dripped onto the sample using a glass pipette, waiting for the previous drop to evaporate before adding the next one. The second method was dipping the sample into the cGNR dispersion for 1 min and subsequently putting it on a 60°C hot plate for 5 min. In both cases, the sample chip was slightly tilted to keep residues from the evaporation process of the solvent at the edges of the sample chip.

Identification of cGNR domains The hBN flakes were investigated by means of AFM to check the success of the cGNR deposition. Hereby, also the orientation of the cGNR domains was determined.

Spin coating of e-beam resist E-beam resist was spin coated onto the samples with 3000 rpm for 5 s (step 1) and 6000 rpm for 60 s (step 2) with subsequent baking of the resist on a 150°C hot plate for 1 min. CSAR 62 4% and CSAR 62 9% were used as resists resulting in resist thicknesses of 80–110 nm and 200–240 nm, respectively.

Electron beam lithography The contact structures were patterned using EBL. For the fine contact fingers, the 30 µm aperture was used with a working distance of 10 mm and an area dose of 80–110 $\mu C/cm^2$. Fine and coarse wiring were structured with the 30 µm aperture, a working distance of 10 mm and an area dose of 110 $\mu C/cm^2$. The contact pads were patterned with the 120 µm aperture, a working distance of 10 mm and an area dose of 120 $\mu C/cm^2$.

The samples were developed by dipping them in the developer AR-600-546 for 60 s and subsequently two times in isopropanol for 30 s each.

Evaporation of contacts For metalization, most samples were put in the Univex B evaporator where the different metals are evaporated by e-beam at a pressure of 10^{-7}–10^{-6} mbar. Only the NiCr/Au contacts were evaporated thermally in the Univex A. The thickness of the contacts varied between 15–50 nm, depending on the thickness of the hBN flake used.

Lift-off For lift-off, the samples were put in warm AR 600-71 and placed onto the 60°C hot plate for 10–60 min.

***I-V*-characterization** The transport properties of the cGNR devices were measured at a probe station. A Yokogawa 7651 power supply was used to apply the source-drain voltage across the cGNRs and a 10 kΩ resistor to protect the cGNRs from high currents. The drain current was recorded using an Ithaco 1211 current preamplifier and an Agilent 34410 digital multimeter for readout. The back gate voltage was applied with a Yokogawa GS200 voltage source.

Encapsulated cGNR devices

The preparation of the hBN bottom flake, the deposition of the cGNR dispersion and the identification of cGNR domains were identical to the standard-contacted cGNR devices described above.

Subsequently, the cGNRs were encapsulated with a second hBN flake with the help of the stacking process which is described in detail in the PhD thesis of Martin Drienovsky [119].

After encapsulation, the sample was covered with the e-beam resist CSAR 62 9% by spin coating, contacts were patterned by EBL and the contacts were developed. All this was done with the same parameters as for the standard contacts.

Next, the sample was placed into a reactive ion etching (RIE) chamber. An etching step was performed with a mixture of 40 sccm CHF_3 and 6 sccm O_2 at a pressure of 55 mTorr and a power of 35 W for 70 s.

Afterwards, Cr/Au was deposited as a contact material by e-beam evaporation in the Univex B evaporator and the lift off was performed.

The samples were measured at a probe station with the same setup as described above.

C.2. Growth of 7-aGNRs on Au(111)

Preparation of Au(111) single crystals for molecule evaporation The Au(111) single crystal used as catalytic substrate was cleaned by repeated cycles of Ne^+ bombardment with an energy of 1 keV at a partial pressure of 10^{-5} mbar followed by annealing to 550°C. After the last sputtering sequence, the sputter gas was removed from the preparation chamber and the sample was annealed to 500°C at a pressure in the range of 10^{-10} mbar.

Sublimation of precursor molecules The sublimation of the precursor molecules took place in the STM preparation chamber using the load lock evaporator. DBBA (10,10´-dibromo-9,9´-bianthryl) molecules were put into a glass crucible and placed in the evaporator. The temperature of the crucible was monitored with a thermocouple. By slowly increasing the heating current, sublimation of the precursor molecules set in, which was monitored with a quartz micro balance (QMB). The final heating current was kept for at least an hour to ensure thermal equilibrium of the evaporator and a stable evaporation rate. Evaporating DBBA for 6 s at a rate of 13 mHz/s (equaling a total frequency shift of the QMB of $\approx$ 70 mHz) yielded the coverage shown in Fig. 4.7. The Au(111) sample was kept at 70°C during DBBA deposition.

Polymerization of the 7-aGNRs To form 7-aGNRs out of single DBBA precursor molecules, the sample was annealed—as described in the main text. The first annealing step at 200°C leading to a cleavage of the Br atoms from the DBBA molecules and to the formation of linear molecule chains lasted for 2 min. During the second

annealing step which was introduced for cyclodehydrogenation, the temperature was kept at 400°C for 4 min.

Growth of NaCl islands and deposition of CO molecules To facilitate the pick-up of CO molecules with the STM tip, thin NaCl islands were grown on the Au(111) surface. Since NaCl desorbs at the temperatures needed for 7-aGNR polymerization, the NaCl islands were grown after the 7-aGNRs. The NaCl deposition was done in the preparation chamber of the STM. The evaporation rate is monitored with a QMB. An amount of NaCl corresponding to a frequency shift of the QMB of 0.35 Hz was evaporated during which the sample was kept at 30°C.

Co evaporation Single Co atoms were added to the sample surface. For this purpose, an e-beam evaporator was used. The addition of Co atoms to the sample surface takes place through a pinhole shutter while the sample is resting in the STM chamber at a temperature of approximately 10 K. For Co evaporation, a heating current of 1.73 A and a high voltage of 2.0 kV were used. The evaporation times varied between 3 s and 10 s, depending on the desired Co atom coverage.

As a last step, CO molecules were added to the sample surface via the load lock after the sample was transferred into the STM chamber and cooled down to roughly 12 K.

C.3. Temperature dependent measurements

For the temperature dependent measurements, the entire STM scan head was warmed up by a heating diode. One has to note, that the piezo constant changes at higher temperatures and has to be adapted in the STM software for data evaluation. As a method for calibration, the dimensions of known structures (like the Herringbone reconstruction) can be measured.
Due to differently fast thermal expansion of sensor and sample, care has to be taken that tip and sample do not crash into each other before the thermal equilibrium is reached.

List of Tables

Bibliography

[1] K. S. Novoselov, A. K. Geim, S. V. Morozov, D. Jiang, Y. Zhang, S. V. Dubonos, I. V. Grigorieva, and A. A. Firsov. *Electric Field Effect in Atomically Thin Carbon Films.* Science **306**, 666–669 (2004).

[2] J. Moser, A. Barreiro, and A. Bachtold. *Current-induced cleaning of graphene.* Applied Physics Letters **91**, 163513 (2007).

[3] A. A. Balandin, S. Ghosh, W. Bao, I. Calizo, D. Teweldebrhan, F. Miao, and C. N. Lau. *Superior Thermal Conductivity of Single-Layer Graphene.* Nano Letters **8**, 902–907 (2008).

[4] F. Schwierz. *Graphene transistors.* Nature Nanotechnology **5**, 487–496 (2010).

[5] R. R. Nair, P. Blake, A. N. Grigorenko, K. S. Novoselov, T. J. Booth, T. Stauber, N. M. R. Peres, and A. K. Geim. *Fine Structure Constant Defines Visual Transparency of Graphene.* Science **320**, 1308 (2008).

[6] C. Lee, X. Wei, J. W. Kysar, and J. Hone. *Measurement of the Elastic Properties and Intrinsic Strength of Monolayer Graphene.* Science **321**, 385 (2008).

[7] K. S. Novoselov, V. I. Fal'ko, L. Colombo, P. R. Gellert, M. G. Schwab, and K. Kim. *A roadmap for graphene.* Nature **490**, 192–200 (2012).

[8] L. Yang, C.-H. Park, Y.-W. Son, M. L. Cohen, and S. G. Louie. *Quasiparticle Energies and Band Gaps in Graphene Nanoribbons.* Physical Review Letters **99**, 186801 (2007).

[9] A. Narita, X.-Y. Wang, X. Feng, and K. Müllen. *New advances in nanographene chemistry.* Chemical Society Reviews **44**, 6616–6643 (2015).

[10] J. Cai, Z. Hao, H. Zhang, Z. Ruan, C. Yan, and J. Lu. *Tuning Electronic Properties of Atomically Precise Graphene Nanoribbons by Bottom-up Fabrications.* ChemNanoMat (2020).

[11] Y.-W. Son, M. L. Cohen, and S. G. Louie. *Energy Gaps in Graphene Nanoribbons.* Physical Review Letters **97**, 216803 (2006).

[12] K. Nakada, M. Fujita, G. Dresselhaus, and M. S. Dresselhaus. *Edge state in graphene ribbons: Nanometer size effect and edge shape dependence.* Physical Review B **54**, 17954–17961 (1996).

[13] M. Fujita, K. Wakabayashi, K. Nakada, and K. Kusakabe. *Peculiar Localized State at Zigzag Graphite Edge.* Journal of the Physical Society of Japan **65**, 1920–1923 (1996).

[14] J. Björk, F. Hanke, and S. Stafström. *Mechanisms of Halogen-Based Covalent Self-Assembly on Metal Surfaces.* Journal of the American Chemical Society **135**, 5768–5775 (2013).

[15] L. Talirz, P. Ruffieux, and R. Fasel. *On-Surface Synthesis of Atomically Precise Graphene Nanoribbons.* Advanced Materials **28**, 6222–6231 (2016).

[16] P. B. Bennett, Z. Pedramrazi, A. Madani, Y.-C. Chen, D. G. de Oteyza, C. Chen, F. R. Fischer, M. F. Crommie, and J. Bokor. *Bottom-up graphene nanoribbon field-effect transistors.* Applied Physics Letters **103**, 253114 (2013).

[17] A. N. Abbas, G. Liu, A. Narita, M. Orosco, X. Feng, K. Müllen, and C. Zhou. *Deposition, Characterization, and Thin-Film-Based Chemical Sensing of Ultra-long Chemically Synthesized Graphene Nanoribbons.* Journal of the American Chemical Society **136**, 7555–7558 (2014).

[18] J. P. Llinas, A. Fairbrother, G. Borin Barin, W. Shi, K. Lee, S. Wu, B. Yong Choi, R. Braganza, J. Lear, N. Kau, W. Choi, C. Chen, Z. Pedramrazi, T. Dumslaff, A. Narita, X. Feng, K. Müllen, F. Fischer, A. Zettl, P. Ruffieux, E. Yablonovitch, M. Crommie, R. Fasel, and J. Bokor. *Short-channel field-effect transistors with 9-atom and 13-atom wide graphene nanoribbons.* Nature Communications **8**, 633 (2017).

[19] J. W. Hill and R. H. Petrucci. *General Chemistry.* Prentice Hall, Upper Saddle River, NJ, 2002, 3rd ed., 2002.

[20] M. I. Katsnelson. *Graphene: Carbon in Two Dimensions.* Cambridge: Cambridge University Press, 2012.

[21] R. Saito, G. Dresselhaus, and M. S. Dresselhaus. *Physical Properties of Carbon Nanotubes.* Imperial College Press, 1998.

[22] A. H. Castro Neto, F. Guinea, N. M. R. Peres, K. S. Novoselov, and A. K. Geim. *The electronic properties of graphene.* Reviews of Modern Physics **81**, 109–162 (2009).

[23] L. Pauling, L. O. Brockway, and J. Y. Beach. *The Dependence of Interatomic Distance on Single Bond-Double Bond Resonance1.* Journal of the American Chemical Society **57**, 2705–2709 (1935).

[24] L. Talirz. *Challenges in the characterization of bottom-up fabricated graphene nanoribbons addressed by ab initio simulations.* University of Zurich, PhD thesis, Zürich, 2015.

[25] P. R. Wallace. *The Band Theory of Graphite.* Physical Review **71**, 622–634 (1947).

[26] S. Reich, C. Thomsen, and J. Maultzsch. *Carbon Nanotubes: Basic Concepts and Physical Properties.* Wiley-VCH Verlag GmbH & Co. KGaA, 2007.

[27] T. Cao, F. Zhao, and S. G. Louie. *Topological Phases in Graphene Nanoribbons: Junction States, Spin Centers, and Quantum Spin Chains.* Physical Review Letters **119**, 076401 (2017).

[28] P. Ruffieux, J. Cai, N. C. Plumb, L. Patthey, D. Prezzi, A. Ferretti, E. Molinari, X. Feng, K. Müllen, C. A. Pignedoli, and R. Fasel. *Electronic Structure of Atomically Precise Graphene Nanoribbons.* ACS Nano **6**, 6930–6935 (2012).

[29] L. Brey and H. A. Fertig. *Electronic states of graphene nanoribbons studied with the Dirac equation.* Physical Review B **73**, 235411 (2006).

[30] L. Talirz, H. Söde, T. Dumslaff, S. Wang, J. R. Sanchez-Valencia, J. Liu, P. Shinde, C. A. Pignedoli, L. Liang, V. Meunier, N. C. Plumb, M. Shi, X. Feng, A. Narita, K. Müllen, R. Fasel, and P. Ruffieux. *On-Surface Synthesis and Characterization of 9-Atom Wide Armchair Graphene Nanoribbons.* ACS Nano **11**, 1380–1388 (2017).

[31] R. Gillen, M. Mohr, C. Thomsen, and J. Maultzsch. *Vibrational properties of graphene nanoribbons by first-principles calculations.* Physical Review B **80**, 155418 (2009).

[32] K. Wakabayashi, K.-i. Sasaki, T. Nakanishi, and T. Enoki. *Electronic states of graphene nanoribbons and analytical solutions.* Science and Technology of Advanced Materials **11**, 054504 (2010).

[33] T. Ando. *Theory of Electronic States and Transport in Carbon Nanotubes.* Journal of the Physical Society of Japan **74**, 777–817 (2005).

[34] P. Avouris, Z. Chen, and V. Perebeinos. *Carbon-based electronics.* Nature Nanotechnology **2**, 605 (2007).

[35] R. Saito, M. Fujita, G. Dresselhaus, and M. S. Dresselhaus. *Electronic structure of graphene tubules based on* C_{60}. Physical Review B **46**, 1804–1811 (1992).

[36] O. V. Yazyev. *Emergence of magnetism in graphene materials and nanostructures.* Reports on Progress in Physics **73**, 056501 (2010).

[37] M. Y. Han, B. Özyilmaz, Y. Zhang, and P. Kim. *Energy Band-Gap Engineering of Graphene Nanoribbons.* Physical Review Letters **98**, 206805 (2007).

[38] D. V. Kosynkin, A. L. Higginbotham, A. Sinitskii, J. R. Lomeda, A. Dimiev, B. K. Price, and J. M. Tour. *Longitudinal unzipping of carbon nanotubes to form graphene nanoribbons.* Nature **458**, 872–877 (2009).

[39] L. Jiao, L. Zhang, X. Wang, G. Diankov, and H. Dai. *Narrow graphene nanoribbons from carbon nanotubes.* Nature **458**, 877–880 (2009).

[40] L. Tapasztó, G. Dobrik, P. Lambin, and L. P. Biró. *Tailoring the atomic structure of graphene nanoribbons by scanning tunnelling microscope lithography.* Nature Nanotechnology **3**, 397–401 (2008).

[41] M. Y. Han, J. C. Brant, and P. Kim. *Electron Transport in Disordered Graphene Nanoribbons.* Physical Review Letters **104**, 056801 (2010).

[42] M. Evaldsson, I. V. Zozoulenko, H. Xu, and T. Heinzel. *Edge-disorder-induced Anderson localization and conduction gap in graphene nanoribbons.* Physical Review B **78**, 161407 (2008).

[43] D. Basu, M. J. Gilbert, L. F. Register, S. K. Banerjee, and A. H. MacDonald. *Effect of edge roughness on electronic transport in graphene nanoribbon channel metal-oxide-semiconductor field-effect transistors.* Applied Physics Letters **92**, 042114 (2008).

[44] J. Baringhaus, M. Ruan, F. Edler, A. Tejeda, M. Sicot, Taleb-IbrahimiAmina, A.-P. Li, Z. Jiang, E. H. Conrad, C. Berger, C. Tegenkamp, and W. A. de Heer. *Exceptional ballistic transport in epitaxial graphene nanoribbons.* Nature **506**, 349–354 (2014).

[45] L. Chen, L. He, H. S. Wang, H. Wang, S. Tang, C. Cong, H. Xie, L. Li, H. Xia, T. Li, T. Wu, D. Zhang, L. Deng, T. Yu, X. Xie, and M. Jiang. *Oriented graphene nanoribbons embedded in hexagonal boron nitride trenches.* Nature Communications **8**, 14703 (2017).

[46] L. Grill, M. Dyer, L. Lafferentz, M. Persson, M. V. Peters, and S. Hecht. *Nano-architectures by covalent assembly of molecular building blocks.* Nature Nanotechnology **2**, 687–691 (2007).

[47] J. Cai, P. Ruffieux, R. Jaafar, M. Bieri, T. Braun, S. Blankenburg, M. Muoth, A. P. Seitsonen, M. Saleh, X. Feng, K. Müllen, and R. Fasel. *Atomically precise bottom-up fabrication of graphene nanoribbons.* Nature **466**, 470–473 (2010).

[48] H. Zhang, H. Lin, K. Sun, L. Chen, Y. Zagranyarski, N. Aghdassi, S. Duhm, Q. Li, D. Zhong, Y. Li, K. Müllen, H. Fuchs, and L. Chi. *On-Surface Synthesis of Rylene-Type Graphene Nanoribbons.* Journal of the American Chemical Society **137**, 4022–4025 (2015).

[49] N. Merino-Díez, A. Garcia-Lekue, E. Carbonell-Sanromà, J. Li, M. Corso, L. Colazzo, F. Sedona, D. Sánchez-Portal, J. I. Pascual, and D. G. de Oteyza. *Width-Dependent Band Gap in Armchair Graphene Nanoribbons Reveals Fermi Level Pinning on Au(111).* ACS Nano **11**, 11661–11668 (2017).

[50] Y.-C. Chen, D. G. de Oteyza, Z. Pedramrazi, C. Chen, F. R. Fischer, and M. F. Crommie. *Tuning the Band Gap of Graphene Nanoribbons Synthesized from Molecular Precursors.* ACS Nano **7**, 6123-6128 (2013).

[51] H. Huang, D. Wei, J. Sun, S. L. Wong, Y. P. Feng, A. H. C. Neto, and A. T. S. Wee. *Spatially Resolved Electronic Structures of Atomically Precise Armchair Graphene Nanoribbons.* Scientific Reports **2**, 983 (2012).

[52] P. Ruffieux, S. Wang, B. Yang, C. Sánchez-Sánchez, J. Liu, T. Dienel, L. Talirz, P. Shinde, C. A. Pignedoli, D. Passerone, T. Dumslaff, X. Feng, K. Müllen, and R. Fasel. *On-surface synthesis of graphene nanoribbons with zigzag edge topology.* Nature **531**, 489 (2016).

[53] D. G. de Oteyza, A. García-Lekue, M. Vilas-Varela, N. Merino-Díez, E. Carbonell-Sanromà, M. Corso, G. Vasseur, C. Rogero, E. Guitián, J. I. Pascual, J. E. Ortega, Y. Wakayama, and D. Peña. *Substrate-Independent Growth of Atomically Precise Chiral Graphene Nanoribbons.* ACS Nano **10**, 9000–9008 (2016).

[54] J. Liu, B.-W. Li, Y.-Z. Tan, A. Giannakopoulos, C. Sanchez-Sanchez, D. Beljonne, P. Ruffieux, R. Fasel, X. Feng, and K. Müllen. *Toward Cove-Edged Low Band Gap Graphene Nanoribbons.* Journal of the American Chemical Society **137**, 6097–6103 (2015).

[55] G. D. Nguyen, H.-Z. Tsai, A. A. Omrani, T. Marangoni, M. Wu, D. J. Rizzo, G. F. Rodgers, R. R. Cloke, R. A. Durr, Y. Sakai, F. Liou, A. S. Aikawa, J. R. Chelikowsky, S. G. Louie, F. R. Fischer, and M. F. Crommie. *Atomically precise graphene nanoribbon heterojunctions from a single molecular precursor.* Nature Nanotechnology (2017).

[56] E. Carbonell-Sanromà, J. Hieulle, M. Vilas-Varela, P. Brandimarte, M. Iraola, A. Barragán, J. Li, M. Abadia, M. Corso, D. Sánchez-Portal, D. Peña, and J. I. Pascual. *Doping of Graphene Nanoribbons via Functional Group Edge Modification.* ACS Nano **11**, 7355–7361 (2017).

[57] P. S. Costa, J. D. Teeter, A. Enders, and A. Sinitskii. *Chevron-based graphene nanoribbon heterojunctions: Localized effects of lateral extension and structural defects on electronic properties.* Carbon **134**, 310–315 (2018).

[58] S. Kawai, S. Saito, S. Osumi, S. Yamaguchi, A. S. Foster, P. Spijker, and E. Meyer. *Atomically controlled substitutional boron-doping of graphene nanoribbons.* Nature Communications **6**, 8098 (2015).

[59] R. R. Cloke, T. Marangoni, G. D. Nguyen, T. Joshi, D. J. Rizzo, C. Bronner, T. Cao, S. G. Louie, M. F. Crommie, and F. R. Fischer. *Site-Specific Substitutional Boron Doping of Semiconducting Armchair Graphene Nanoribbons.* Journal of the American Chemical Society **137**, 8872–8875 (2015).

[60] C. Bronner, S. Stremlau, M. Gille, F. Brauße, A. Haase, S. Hecht, and P. Tegeder. *Aligning the Band Gap of Graphene Nanoribbons by Monomer Doping.* Angewandte Chemie International Edition **52**, 4422–4425 (2013).

[61] J. Cai, C. A. Pignedoli, L. Talirz, P. Ruffieux, H. Söde, L. Liang, V. Meunier, R. Berger, R. Li, X. Feng, K. Müllen, and R. Fasel. *Graphene nanoribbon heterojunctions.* Nature Nanotechnology **9**, 896 (2014).

[62] S. Linden, D. Zhong, A. Timmer, N. Aghdassi, J. H. Franke, H. Zhang, X. Feng, K. Müllen, H. Fuchs, L. Chi, and H. Zacharias. *Electronic Structure of Spatially Aligned Graphene Nanoribbons on Au(788).* Physical Review Letters **108**, 216801 (2012).

[63] M. Ohtomo, Y. Sekine, H. Hibino, and H. Yamamoto. *Graphene nanoribbon field-effect transistors fabricated by etchant-free transfer from Au(788).* Applied Physics Letters **112**, 021602 (2018).

[64] Z. Chen, W. Zhang, C.-A. Palma, A. Lodi Rizzini, B. Liu, A. Abbas, N. Richter, L. Martini, X.-Y. Wang, N. Cavani, H. Lu, N. Mishra, C. Coletti, R. Berger, F. Klappenberger, M. Kläui, A. Candini, M. Affronte, C. Zhou, V. De Renzi, U. del Pennino, J. V. Barth, H. J. Räder, A. Narita, X. Feng, and K. Müllen. *Synthesis of Graphene Nanoribbons by Ambient-Pressure Chemical Vapor Deposition and Device Integration.* Journal of the American Chemical Society **138**, 15488–15496 (2016).

[65] M. Kolmer, A. A. Ahmad Zebari, J. S. Prauzner-Bechcicki, W. Piskorz, F. Zasada, S. Godlewski, B. Such, Z. Sojka, and M. Szymonski. *Polymerization of Polyanthrylene on a Titanium Dioxide (011)-(2 × 1) Surface.* Angewandte Chemie International Edition **52**, 10300–10303 (2013).

[66] R. M. Jacobberger, B. Kiraly, M. Fortin-Deschenes, P. L. Levesque, K. M. McElhinny, G. J. Brady, R. Rojas Delgado, S. Singha Roy, A. Mannix, M. G. Lagally, P. G. Evans, P. Desjardins, R. Martel, M. C. Hersam, N. P. Guisinger, and M. S. Arnold. *Direct oriented growth of armchair graphene nanoribbons on germanium.* Nature Communications **6**, 8006 (2015).

[67] A. Narita, X. Feng, Y. Hernandez, S. A. Jensen, M. Bonn, H. Yang, I. A. Verzhbitskiy, C. Casiraghi, M. R. Hansen, A. H. R. Koch, G. Fytas, O. Ivasenko, B. Li, K. S. Mali, T. Balandina, S. Mahesh, S. De Feyter, and K. Müllen. *Synthesis of structurally well-defined and liquid-phase-processable graphene nanoribbons.* Nature Chemistry **6**, 126–132 (2014).

[68] U. Zschieschang, H. Klauk, I. B. Müller, A. J. Strudwick, T. Hintermann, M. G. Schwab, A. Narita, X. Feng, K. Müllen, and R. T. Weitz. *Electrical Characteristics of Field-Effect Transistors based on Chemically Synthesized Graphene Nanoribbons.* Advanced Electronic Materials **1**, 1400010 (2015).

[69] P. Fantuzzi, L. Martini, A. Candini, V. Corradini, U. del Pennino, Y. Hu, X. Feng, K. Müllen, A. Narita, and M. Affronte. *Fabrication of three terminal devices by ElectroSpray deposition of graphene nanoribbons.* Carbon **104**, 112–118 (2016).

[70] G. Binnig and H. Rohrer. *Scanning tunneling microscopy.* Surface Science **126**, 236–244 (1983).

[71] G. Binnig, C. F. Quate, and C. Gerber. *Atomic Force Microscope.* Physical Review Letters **56**, 930–933 (1986).

[72] J. Bardeen. *Tunnelling from a Many-Particle Point of View.* Physical Review Letters **6**, 57–59 (1961).

[73] J. Tersoff and D. R. Hamann. *Theory of the scanning tunneling microscope.* Physical Review B **31**, 805–813 (1985).

[74] C. J. Chen. *Introduction to Scanning Tunneling Microscopy.* Oxford University Press, 2nd ed., 2008.

[75] F. Queck-Scharrer. *Implementierung der Rastertunnelmikroskopie auf Isolatoren.* University of Regensburg, PhD thesis, 2019.

[76] F. J. Giessibl. *Advances in atomic force microscopy.* Reviews of Modern Physics **75**, 949–983 (2003).

[77] Q. Zhong, D. Inniss, K. Kjoller, and V. B. Elings. *Fractured polymer/silica fiber surface studied by tapping mode atomic force microscopy.* Surface Science **290**, L688–L692 (1993).

[78] C. B. Prater, P. G. Maivald, K. J. Kjoller, and M. G. Heaton. *TappingMode imaging applications and technology.* Veeco Application Notes **AN04** (2004).

[79] F. J. Giessibl. *The qPlus sensor, a powerful core for the atomic force microscope.* Review of Scientific Instruments **90**, 011101 (2019).

[80] T. Preis, C. Kick, A. Lex, D. Weiss, J. Eroms, A. Narita, Y. Hu, K. Müllen, K. Watanabe, and T. Taniguchi. *Graphene nanoribbons on hexagonal boron nitride: Deposition and transport characterization.* Applied Physics Letters **114**, 173101 (2019).

[81] A. Lex. *Charakterisierung von bottom-up synthetisierten Graphen-Nanoribbons auf Bornitrid.* University of Regensburg, Master's thesis, 2016.

[82] C. Kick. *Vergleich von Transportmessungen unterschiedlicher chemisch synthetisierter cove-type Graphen-Nanoribbons auf hexagonalem Bornitrid.* University of Regensburg, Master's thesis, 2018.

[83] S. M. Sze and K. K. Ng. *Physics of Semiconductor Devices.* John Wiley & Sons, 3rd ed., 2007.

[84] E. H. Rhoderick. *Metal-semiconductor contacts.* IEE Proceedings I - Solid-State and Electron Devices **129**, 1 (1982).

[85] J. Svensson and E. E. B. Campbell. *Schottky barriers in carbon nanotube-metal contacts.* Journal of Applied Physics **110**, 111101 (2011).

[86] A. Di Bartolomeo. *Graphene Schottky diodes: An experimental review of the rectifying graphene/semiconductor heterojunction.* Physics Reports **606**, 1–58 (2016).

[87] R. T. Tung. *The physics and chemistry of the Schottky barrier height.* Applied Physics Reviews **1**, 011304 (2014).

[88] W. Schottky. *Zur Halbleitertheorie der Sperrschicht- und Spitzengleichrichter.* Zeitschrift für Physik **113**, 367–414 (1939).

[89] N. F. Mott. *Note on the contact between a metal and an insulator or semiconductor.* Mathematical Proceedings of the Cambridge Philosophical Society **34**, 568–572 (1938).

[90] A. M. Cowley and S. M. Sze. *Surface States and Barrier Height of Metal-Semiconductor Systems.* Journal of Applied Physics **36**, 3212–3220 (1965).

[91] J. Bardeen. *Surface States and Rectification at a Metal Semi-Conductor Contact.* Physical Review **71**, 717–727 (1947).

[92] V. Heine. *Theory of Surface States.* Physical Review **138**, A1689–A1696 (1965).

[93] F. A. Padovani and R. Stratton. *Field and thermionic-field emission in Schottky barriers.* Solid-State Electronics **9**, 695–707 (1966).

[94] Z. Zhang, K. Yao, Y. Liu, C. Jin, X. Liang, Q. Chen, and L.-M. Peng. *Quantitative Analysis of Current-Voltage Characteristics of Semiconducting Nanowires: Decoupling of Contact Effects.* Advanced Functional Materials **17**, 2478–2489 (2007).

[95] Y. Liu, Z. Y. Zhang, Y. F. Hu, C. H. Jin, and L.-M. Peng. *Quantitative Fitting of Nonlinear Current-Voltage Curves and Parameter Retrieval of Semiconducting Nanowire, Nanotube and Nanoribbon Devices.* Journal of Nanoscience and Nanotechnology **8**, 252–258 (2008).

[96] D. J. Perello, S. C. Lim, S. J. Chae, I. Lee, M. J. Kim, Y. H. Lee, and M. Yun. *Thermionic Field Emission Transport in Carbon Nanotube Transistors.* ACS Nano **5**, 1756–1760 (2011).

[97] T. Nagano, M. Tsutsui, R. Nouchi, N. Kawasaki, Y. Ohta, Y. Kubozono, N. Takahashi, and A. Fujiwara. *Output Properties of C60 Field-Effect Transistors with Au Electrodes Modified by 1-Alkanethiols.* Journal of Physical Chemistry C **111**, 7211–7217 (2007).

[98] A. J. Chiquito, C. A. Amorim, O. M. Berengue, L. S. Araujo, E. P. Bernardo, and E. R. Leite. *Back-to-back Schottky diodes: the generalization of the diode theory in analysis and extraction of electrical parameters of nanodevices.* Journal of Physics: Condensed Matter **24**, 225303 (2012).

[99] S. Osella, A. Narita, M. G. Schwab, Y. Hernandez, X. Feng, K. Müllen, and D. Beljonne. *Graphene Nanoribbons as Low Band Gap Donor Materials for Organic Photovoltaics: Quantum Chemical Aided Design.* ACS Nano **6**, 5539–5548 (2012).

[100] I. Ivanov, Y. Hu, S. Osella, U. Beser, H. I. Wang, D. Beljonne, A. Narita, K. Müllen, D. Turchinovich, and M. Bonn. *Role of Edge Engineering in Photoconductivity of Graphene Nanoribbons.* Journal of the American Chemical Society **139**, 7982–7988 (2017).

[101] C. E. P. Villegas, P. B. Mendonça, and A. R. Rocha. *Optical spectrum of bottom-up graphene nanoribbons: towards efficient atom-thick excitonic solar cells.* Scientific Reports **4**, 6579 (2014).

[102] Y. Hu, P. Xie, M. De Corato, A. Ruini, S. Zhao, F. Meggendorfer, L. A. Straasø, L. Rondin, P. Simon, J. Li, J. J. Finley, M. R. Hansen, J.-S. Lauret, E. Molinari, X. Feng, J. V. Barth, C.-A. Palma, D. Prezzi, K. Müllen, and A. Narita. *Bandgap Engineering of Graphene Nanoribbons by Control over Structural Distortion.* Journal of the American Chemical Society **140**, 7803–7809 (2018).

[103] G. Soavi, S. Dal Conte, C. Manzoni, D. Viola, A. Narita, Y. Hu, X. Feng, U. Hohenester, E. Molinari, D. Prezzi, K. Müllen, and G. Cerullo. *Exciton-exciton annihilation and biexciton stimulated emission in graphene nanoribbons.* Nature Communications **7**, 11010 (2016).

[104] A. Narita, I. A. Verzhbitskiy, W. Frederickx, K. S. Mali, S. A. Jensen, M. R. Hansen, M. Bonn, S. De Feyter, C. Casiraghi, X. Feng, and K. Müllen. *Bottom-Up Synthesis of Liquid-Phase-Processable Graphene Nanoribbons with Near-Infrared Absorption.* ACS Nano **8**, 11622–11630 (2014).

[105] K. Watanabe, T. Taniguchi, and H. Kanda. *Direct-bandgap properties and evidence for ultraviolet lasing of hexagonal boron nitride single crystal.* Nature Materials **3**, 404–409 (2004).

[106] T. Taniguchi and K. Watanabe. *Synthesis of high-purity boron nitride single crystals under high pressure by using Ba-BN solvent.* Journal of Crystal Growth **303**, 525–529 (2007).

[107] C. R. Dean, A. F. Young, I. Meric, C. Lee, L. Wang, S. Sorgenfrei, K. Watanabe, T. Taniguchi, P. Kim, K. L. Shepard, and J. Hone. *Boron nitride substrates for high-quality graphene electronics.* Nature Nanotechnology **5**, 722–726 (2010).

[108] J. Xue, J. Sanchez-Yamagishi, D. Bulmash, P. Jacquod, A. Deshpande, K. Watanabe, T. Taniguchi, P. Jarillo-Herrero, and B. J. LeRoy. *Scanning tunnelling microscopy and spectroscopy of ultra-flat graphene on hexagonal boron nitride.* Nature Materials **10**, 282–285 (2011).

[109] W. Ouyang, D. Mandelli, M. Urbakh, and O. Hod. *Nanoserpents: Graphene Nanoribbon Motion on Two-Dimensional Hexagonal Materials.* Nano Letters **18**, 6009–6016 (2018).

[110] A. F. Holleman and N. Wiberg. *Anorganische Chemie 1 - Grundlagen und Hauptgruppenelemente.* Gruyter, Walter de GmbH, 2017. p. 997.

[111] Y. Fan, M. Zhao, Z. Wang, X. Zhang, and H. Zhang. *Tunable electronic structures of graphene/boron nitride heterobilayers.* Applied Physics Letters **98**, 083103 (2011).

[112] Y.-J. Li, Q.-Q. Sun, L. Chen, P. Zhou, P.-F. Wang, S.-J. Ding, and D. W. Zhang. *Hexagonal boron nitride intercalated multi-layer graphene: a possible ultimate solution to ultra-scaled interconnect technology.* AIP Advances **2**, 012191 (2012).

[113] Y. Guo, C. Liu, Q. Yin, C. Wei, S. Lin, T. B. Hoffman, Y. Zhao, J. H. Edgar, Q. Chen, S. P. Lau, J. Dai, H. Yao, H.-S. P. Wong, and Y. Chai. *Distinctive in-Plane Cleavage Behaviors of Two-Dimensional Layered Materials.* ACS Nano **10**, 8980–8988 (2016).

[114] U. Stöberl, U. Wurstbauer, W. Wegscheider, D. Weiss, and J. Eroms. *Morphology and flexibility of graphene and few-layer graphene on various substrates.* Applied Physics Letters **93**, 051906 (2008).

[115] R. Decker, Y. Wang, V. W. Brar, W. Regan, H.-Z. Tsai, Q. Wu, W. Gannett, A. Zettl, and M. F. Crommie. *Local Electronic Properties of Graphene on a BN Substrate via Scanning Tunneling Microscopy.* Nano Letters **11**, 2291–2295 (2011).

[116] S. Kawai, A. Benassi, E. Gnecco, H. Söde, R. Pawlak, X. Feng, K. Müllen, D. Passerone, C. A. Pignedoli, P. Ruffieux, R. Fasel, and E. Meyer. *Superlubricity of graphene nanoribbons on gold surfaces*. Science **351**, 957–961 (2016).

[117] L. Wang, I. Meric, P. Y. Huang, Q. Gao, Y. Gao, H. Tran, T. Taniguchi, K. Watanabe, L. M. Campos, D. A. Muller, J. Guo, P. Kim, J. Hone, K. L. Shepard, and C. R. Dean. *One-Dimensional Electrical Contact to a Two-Dimensional Material*. Science **342**, 614–617 (2013).

[118] J.-W. Huang, C. Pan, S. Tran, B. Cheng, K. Watanabe, T. Taniguchi, C. N. Lau, and M. Bockrath. *Superior Current Carrying Capacity of Boron Nitride Encapsulated Carbon Nanotubes with Zero-Dimensional Contacts*. Nano Letters **15**, 6836–6840 (2015).

[119] M. Drienovsky. *Übergittereffekte in eindimensional moduliertem Graphen*. University of Regensburg, PhD thesis, 2018.

[120] J. N. Han, X. He, Z. Q. Fan, and Z. H. Zhang. *Metal doped armchair graphene nanoribbons: electronic structure, carrier mobility and device properties*. Physical Chemistry Chemical Physics **21**, 1830–1840 (2019).

[121] F. Léonard and J. Tersoff. *Role of Fermi-Level Pinning in Nanotube Schottky Diodes*. Physical Review Letters **84**, 4693–4696 (2000).

[122] J. J. Palacios, A. J. Pérez-Jiménez, E. Louis, E. SanFabián, and J. A. Vergés. *First-Principles Phase-Coherent Transport in Metallic Nanotubes with Realistic Contacts*. Physical Review Letters **90**, 106801 (2003).

[123] F. Prins, A. Barreiro, J. W. Ruitenberg, J. S. Seldenthuis, N. Aliaga-Alcalde, L. M. K. Vandersypen, and H. S. J. van der Zant. *Room-Temperature Gating of Molecular Junctions Using Few-Layer Graphene Nanogap Electrodes*. Nano Letters **11**, 4607–4611 (2011).

[124] A. Candini, N. Richter, D. Convertino, C. Coletti, F. Balestro, W. Wernsdorfer, M. Kläui, and M. Affronte. *Electroburning of few-layer graphene flakes, epitaxial graphene, and turbostratic graphene discs in air and under vacuum*. Beilstein Journal of Nanotechnology **6**, 711-719 (2015).

[125] A. Candini, L. Martini, Z. Chen, N. Mishra, D. Convertino, C. Coletti, A. Narita, X. Feng, K. Müllen, and M. Affronte. *High Photoresponsivity in Graphene Nanoribbon Field-Effect Transistor Devices Contacted with Graphene Electrodes*. Journal of Physical Chemistry C **121**, 10620–10625 (2017).

[126] G. M. Paternò, Q. Chen, X.-Y. Wang, J. Liu, S. G. Motti, A. Petrozza, X. Feng, G. Lanzani, K. Müllen, A. Narita, and F. Scotognella. *Synthesis of Dibenzo[hi,st]ovalene and Its Amplified Spontaneous Emission in a Polystyrene Matrix*. Angewandte Chemie International Edition **56**, 6753–6757 (2017).

[127] M. Koch, F. Ample, C. Joachim, and L. Grill. *Voltage-dependent conductance of a single graphene nanoribbon.* Nature Nanotechnology **7**, 713–717 (2012).

[128] L. Talirz, H. Söde, S. Kawai, P. Ruffieux, E. Meyer, X. Feng, K. Müllen, R. Fasel, C. A. Pignedoli, and D. Passerone. *Band Gap of Atomically Precise Graphene Nanoribbons as a Function of Ribbon Length and Termination.* ChemPhysChem **20**, 2348–2353 (2019).

[129] J. B. Neaton, M. S. Hybertsen, and S. G. Louie. *Renormalization of Molecular Electronic Levels at Metal-Molecule Interfaces.* Physical Review Letters **97**, 216405 (2006).

[130] N. Kharche and V. Meunier. *Width and Crystal Orientation Dependent Band Gap Renormalization in Substrate-Supported Graphene Nanoribbons.* Journal of Physical Chemistry Letters **7**, 1526–1533 (2016).

[131] O. Deniz, C. Sánchez-Sánchez, T. Dumslaff, X. Feng, A. Narita, K. Müllen, N. Kharche, V. Meunier, R. Fasel, and P. Ruffieux. *Revealing the Electronic Structure of Silicon Intercalated Armchair Graphene Nanoribbons by Scanning Tunneling Spectroscopy.* Nano Letters **17**, 2197–2203 (2017).

[132] S. Wang, L. Talirz, C. A. Pignedoli, X. Feng, K. Müllen, R. Fasel, and P. Ruffieux. *Giant edge state splitting at atomically precise graphene zigzag edges.* Nature Communications **7**, 11507 (2016).

[133] J. Fernández-Rossier. *Prediction of hidden multiferroic order in graphene zigzag ribbons.* Physical Review B **77**, 075430 (2008).

[134] Y. Miyamoto, K. Nakada, and M. Fujita. *First-principles study of edge states of H-terminated graphitic ribbons.* Physical Review B **59**, 9858–9861 (1999).

[135] S. Okada, M. Igami, K. Nakada, and A. Oshiyama. *Border states in heterosheets with hexagonal symmetry.* Physical Review B **62**, 9896–9899 (2000).

[136] H. Lee, Y.-W. Son, N. Park, S. Han, and J. Yu. *Magnetic ordering at the edges of graphitic fragments: Magnetic tail interactions between the edge-localized states.* Physical Review B **72**, 174431 (2005).

[137] S. Blundell. *Magnetism in Condensed Matter.* Oxford University Press, 2001.

[138] L. Pisani, J. A. Chan, B. Montanari, and N. M. Harrison. *Electronic structure and magnetic properties of graphitic ribbons.* Physical Review B **75**, 064418 (2007).

[139] E. H. Lieb. *Two theorems on the Hubbard model.* Physical Review Letters **62**, 1201–1204 (1989).

[140] Y. Kobayashi, K.-i. Fukui, T. Enoki, K. Kusakabe, and Y. Kaburagi. *Observation of zigzag and armchair edges of graphite using scanning tunneling microscopy and spectroscopy.* Physical Review B **71**, 193406 (2005).

[141] C. Tao, L. Jiao, O. V. Yazyev, Y.-C. Chen, J. Feng, X. Zhang, R. B. Capaz, J. M. Tour, A. Zettl, S. G. Louie, H. Dai, and M. F. Crommie. *Spatially resolving edge states of chiral graphene nanoribbons.* Nature Physics **7**, 616 (2011).

[142] G. Z. Magda, X. Jin, I. Hagymasi, P. Vancso, Z. Osvath, P. Nemes-Incze, C. Hwang, L. P. Biro, and L. Tapaszto. *Room-temperature magnetic order on zigzag edges of narrow graphene nanoribbons.* Nature **514**, 608–611 (2014).

[143] Y. Y. Li, M. X. Chen, M. Weinert, and L. Li. *Direct experimental determination of onset of electron-electron interactions in gap opening of zigzag graphene nanoribbons.* Nature Communications **5**, 4311 (2014).

[144] J. van der Lit, M. P. Boneschanscher, D. Vanmaekelbergh, M. Ijäs, A. Uppstu, M. Ervasti, A. Harju, P. Liljeroth, and I. Swart. *Suppression of electron-vibron coupling in graphene nanoribbons contacted via a single atom.* Nature Communications **4** (2013).

[145] I. Tamm. *Über eine mögliche Art der Elektronenbindung an Kristalloberflächen.* Physikalische Zeitung der Sowjetunion **1**, 733–746 (1932).

[146] H. González-Herrero, J. M. Gómez-Rodríguez, P. Mallet, M. Moaied, J. J. Palacios, C. Salgado, M. M. Ugeda, J.-Y. Veuillen, F. Yndurain, and I. Brihuega. *Atomic-scale control of graphene magnetism by using hydrogen atoms.* Science **352**, 437 (2016).

[147] K. Sawada, F. Ishii, M. Saito, S. Okada, and T. Kawai. *Phase Control of Graphene Nanoribbon by Carrier Doping: Appearance of Noncollinear Magnetism.* Nano Letters **9**, 269–272 (2009).

[148] J. Jung and A. H. MacDonald. *Carrier density and magnetism in graphene zigzag nanoribbons.* Physical Review B **79**, 235433 (2009).

[149] G. Giovannetti, P. A. Khomyakov, G. Brocks, V. M. Karpan, J. van den Brink, and P. J. Kelly. *Doping Graphene with Metal Contacts.* Physical Review Letters **101**, 026803 (2008).

[150] Y. Wu, W. Jiang, Y. Ren, W. Cai, W. H. Lee, H. Li, R. D. Piner, C. W. Pope, Y. Hao, H. Ji, J. Kang, and R. S. Ruoff. *Tuning the Doping Type and Level of Graphene with Different Gold Configurations.* Small **8**, 3129–3136 (2012).

[151] M. Ijäs, M. Ervasti, A. Uppstu, P. Liljeroth, J. van der Lit, I. Swart, and A. Harju. *Electronic states in finite graphene nanoribbons: Effect of charging and defects.* Physical Review B **88**, 075429 (2013).

[152] J. Repp, G. Meyer, and K.-H. Rieder. *Snell's Law for Surface Electrons: Refraction of an Electron Gas Imaged in Real Space*. Physical Review Letters **92**, 036803 (2004).

[153] M. Golor, C. Koop, T. C. Lang, S. Wessel, and M. J. Schmidt. *Magnetic Correlations in Short and Narrow Graphene Armchair Nanoribbons*. Physical Review Letters **111**, 085504 (2013).

[154] X. Su, Z. Xue, G. Li, and P. Yu. *Edge State Engineering of Graphene Nanoribbons*. Nano Letters **18**, 5744–5751 (2018).

[155] L. Talirz, H. Söde, J. Cai, P. Ruffieux, S. Blankenburg, R. Jafaar, R. Berger, X. Feng, K. Müllen, D. Passerone, R. Fasel, and C. A. Pignedoli. *Termini of Bottom-Up Fabricated Graphene Nanoribbons*. Journal of the American Chemical Society **135**, 2060–2063 (2013).

[156] E. J. Clar. *The aromatic sextet*. J. Wiley, 1972.

[157] T. Wassmann, A. P. Seitsonen, A. M. Saitta, M. Lazzeri, and F. Mauri. *Clar's Theory, π-Electron Distribution, and Geometry of Graphene Nanoribbons*. Journal of the American Chemical Society **132**, 3440–3451 (2010).

[158] L. Gross, F. Mohn, N. Moll, P. Liljeroth, and G. Meyer. *The Chemical Structure of a Molecule Resolved by Atomic Force Microscopy*. Science **325**, 1110–1114 (2009).

[159] L. Gross, N. Moll, F. Mohn, A. Curioni, G. Meyer, F. Hanke, and M. Persson. *High-Resolution Molecular Orbital Imaging Using a p-Wave STM Tip*. Physical Review Letters **107**, 086101 (2011).

[160] M. Ternes, A. J. Heinrich, and W.-D. Schneider. *Spectroscopic manifestations of the Kondo effect on single adatoms*. Journal of Physics: Condensed Matter **21**, 053001 (2009).

[161] W. J. de Haas, J. de Boer, and G. J. van dën Berg. *The electrical resistance of gold, copper and lead at low temperatures*. Physica **1**, 1115–1124 (1934).

[162] J. Kondo. *Resistance Minimum in Dilute Magnetic Alloys*. Progress of Theoretical Physics **32**, 37–49 (1964).

[163] L. Kouwenhoven and L. Glazman. *Revival of the Kondo effect*. Physics World **14**, 33–38 (2001).

[164] S. M. Cronenwett, T. H. Oosterkamp, and L. P. Kouwenhoven. *A Tunable Kondo Effect in Quantum Dots*. Science **281**, 540 (1998).

[165] V. Madhavan, W. Chen, T. Jamneala, M. F. Crommie, and N. S. Wingreen. *Tunneling into a Single Magnetic Atom: Spectroscopic Evidence of the Kondo Resonance*. Science **280**, 567–569 (1998).

[166] J. Li, W.-D. Schneider, R. Berndt, and B. Delley. *Kondo Scattering Observed at a Single Magnetic Impurity.* Physical Review Letters **80**, 2893–2896 (1998).

[167] G. D. Scott and D. Natelson. *Kondo Resonances in Molecular Devices.* ACS Nano **4**, 3560–3579 (2010).

[168] P. W. Anderson. *Localized Magnetic States in Metals.* Physical Review **124**, 41–53 (1961).

[169] P. Nozières. *A "fermi-liquid" description of the Kondo problem at low temperatures.* Journal of Low Temperature Physics **17**, 31–42 (1974).

[170] K. Nagaoka, T. Jamneala, M. Grobis, and M. F. Crommie. *Temperature Dependence of a Single Kondo Impurity.* Physical Review Letters **88**, 077205 (2002).

[171] A. F. Otte, M. Ternes, K. von Bergmann, S. Loth, H. Brune, C. P. Lutz, C. F. Hirjibehedin, and A. J. Heinrich. *The role of magnetic anisotropy in the Kondo effect.* Nature Physics **4**, 847 (2008).

[172] M. Ternes. *Probing magnetic excitations and correlations in single and coupled spin systems with scanning tunneling spectroscopy.* Progress in Surface Science **92**, 83–115 (2017).

[173] M. Gruber, A. Weismann, and R. Berndt. *The Kondo resonance line shape in scanning tunnelling spectroscopy: instrumental aspects.* Journal of Physics: Condensed Matter **30**, 424001 (2018).

[174] V. Madhavan, W. Chen, T. Jamneala, M. F. Crommie, and N. S. Wingreen. *Local spectroscopy of a Kondo impurity: Co on Au(111).* Physical Review B **64**, 165412 (2001).

[175] U. Fano. *Effects of Configuration Interaction on Intensities and Phase Shifts.* Physical Review **124**, 1866–1878 (1961).

[176] H. O. Frota. *Shape of the Kondo resonance.* Physical Review B **45**, 1096–1099 (1992).

[177] N. Knorr, M. A. Schneider, L. Diekhöner, P. Wahl, and K. Kern. *Kondo Effect of Single Co Adatoms on Cu Surfaces.* Physical Review Letters **88**, 096804 (2002).

[178] J. Ren, H. Guo, J. Pan, Y. Y. Zhang, X. Wu, H.-G. Luo, S. Du, S. T. Pantelides, and H.-J. Gao. *Kondo Effect of Cobalt Adatoms on a Graphene Monolayer Controlled by Substrate-Induced Ripples.* Nano Letters **14**, 4011–4015 (2014).

[179] A. Zhao, Q. Li, L. Chen, H. Xiang, W. Wang, S. Pan, B. Wang, X. Xiao, J. Yang, J. G. Hou, and Q. Zhu. *Controlling the Kondo Effect of an Adsorbed Magnetic Ion Through Its Chemical Bonding*. Science **309**, 1542–1544 (2005).

[180] Y.-h. Zhang, S. Kahle, T. Herden, C. Stroh, M. Mayor, U. Schlickum, M. Ternes, P. Wahl, and K. Kern. *Temperature and magnetic field dependence of a Kondo system in the weak coupling regime*. Nature Communications **4**, 2110 (2013).

[181] V. Iancu, K.-F. Braun, K. Schouteden, and C. Van Haesendonck. *Inducing Magnetism in Pure Organic Molecules by Single Magnetic Atom Doping*. Physical Review Letters **113**, 106102 (2014).

[182] G. E. Pacchioni, M. Pivetta, L. Gragnaniello, F. Donati, G. Autès, O. V. Yazyev, S. Rusponi, and H. Brune. *Two-Orbital Kondo Screening in a Self-Assembled Metal-Organic Complex*. ACS Nano **11**, 2675–2681 (2017).

[183] C. Zhou, H. Shan, B. Li, A. Zhao, and B. Wang. *Engineering hybrid Co-picene structures with variable spin coupling*. Applied Physics Letters **108**, 171601 (2016).

[184] Y. Li, A. T. Ngo, A. DiLullo, K. Z. Latt, H. Kersell, B. Fisher, P. Zapol, S. E. Ulloa, and S.-W. Hla. *Anomalous Kondo resonance mediated by semiconducting graphene nanoribbons in a molecular heterostructure*. Nature Communications **8**, 946 (2017).

[185] J. Li, S. Sanz, M. Corso, D. J. Choi, D. Peña, T. Frederiksen, and J. I. Pascual. *Single spin localization and manipulation in graphene open-shell nanostructures*. Nature Communications **10**, 200 (2019).

[186] K. Simonov, N. Vinogradov, A. S. Vinogradov, A. Generalov, E. M. Zagrebina, N. Martensson, A. A. Cafolla, T. Carpy, J. P. Cunniffe, and A. Preobrajenski. *Effect of Substrate Chemistry on the Bottom-Up Fabrication of Graphene Nanoribbons: Combined Core-Level Spectroscopy and STM Study*. Journal of Physical Chemistry C **118**, 12532–12540 (2014).

[187] A. Batra, D. Cvetko, G. Kladnik, O. Adak, C. Cardoso, A. Ferretti, D. Prezzi, E. Molinari, A. Morgante, and L. Venkataraman. *Probing the mechanism for graphene nanoribbon formation on gold surfaces through X-ray spectroscopy*. Chemical Science **5**, 4419–4423 (2014).

[188] C. Bronner, J. Björk, and P. Tegeder. *Tracking and Removing Br during the On-Surface Synthesis of a Graphene Nanoribbon*. The Journal of Physical Chemistry C **119**, 486–493 (2015).

[189] F. Ullmann and J. Bielecki. *Über Synthesen in der Biphenylreihe*. Berichte der Deutschen Chemischen Gesellschaft **34**, 2174–2185 (1901).

[190] S. Blankenburg, J. Cai, P. Ruffieux, R. Jaafar, D. Passerone, X. Feng, K. Müllen, R. Fasel, and C. A. Pignedoli. *Intraribbon Heterojunction Formation in Ultranarrow Graphene Nanoribbons*. ACS Nano **6**, 2020–2025 (2012).

[191] C. Bronner, F. Leyssner, S. Stremlau, M. Utecht, P. Saalfrank, T. Klamroth, and P. Tegeder. *Electronic structure of a subnanometer wide bottom-up fabricated graphene nanoribbon: End states, band gap, and dispersion*. Physical Review B **86**, 085444 (2012).

[192] D. M. Eigler and E. K. Schweizer. *Positioning single atoms with a scanning tunnelling microscope*. Nature **344**, 524–526 (1990).

[193] J. A. Stroscio and D. M. Eigler. *Atomic and Molecular Manipulation with the Scanning Tunneling Microscope*. Science **254**, 1319 (1991).

[194] S. Mishra, D. Beyer, K. Eimre, S. Kezilebieke, R. Berger, O. Gröning, C. A. Pignedoli, K. Müllen, P. Liljeroth, P. Ruffieux, X. Feng, and R. Fasel. *Topological frustration induces unconventional magnetism in a nanographene*. Nature Nanotechnology **15**, 22–28 (2020).

[195] K. T. Chan, J. B. Neaton, and M. L. Cohen. *First-principles study of metal adatom adsorption on graphene*. Physical Review B **77**, 235430 (2008).

[196] A. Ishii, M. Yamamoto, H. Asano, and K. Fujiwara. *DFT calculation for adatom adsorption on graphene sheet as a prototype of carbon nanotube functionalization*. Journal of Physics: Conference Series **100**, 052087 (2008).

[197] H. Sevinçli, M. Topsakal, E. Durgun, and S. Ciraci. *Electronic and magnetic properties of* 3*d transition-metal atom adsorbed graphene and graphene nanoribbons*. Physical Review B **77**, 195434 (2008).

[198] A. D. Zdetsis and E. N. Economou. *Rationalizing and reconciling energy gaps and quantum confinement in narrow atomically precise armchair graphene nanoribbons*. Carbon **116**, 422–434 (2017).

[199] F. Mohn, L. Gross, and G. Meyer. *Measuring the short-range force field above a single molecule with atomic resolution*. Applied Physics Letters **99**, 053106 (2011).

[200] C. Q. Sun. *Relaxation of the Chemical Bond*. Springer Singapore, 2014.

[201] J. Li, W.-D. Schneider, R. Berndt, O. R. Bryant, and S. Crampin. *Surface-State Lifetime Measured by Scanning Tunneling Spectroscopy*. Physical Review Letters **81**, 4464–4467 (1998).

[202] J. Kliewer, R. Berndt, E. V. Chulkov, V. M. Silkin, P. M. Echenique, and S. Crampin. *Dimensionality Effects in the Lifetime of Surface States*. Science **288**, 1399–1402 (2000).

[203] R. Matzdorf. *Investigation of line shapes and line intensities by high-resolution UV-photoemission spectroscopy – Some case studies on noble-metal surfaces.* Surface Science Reports **30**, 153–206 (1998).

[204] P. M. Echenique, R. Berndt, E. V. Chulkov, T. Fauster, A. Goldmann, and U. Höfer. *Decay of electronic excitations at metal surfaces.* Surface Science Reports **52**, 219–317 (2004).

[205] D. Pines and P. Noziéres. *The Theory Of Quantum Liquids.* Benjamin New York, 1966.

[206] L. Bürgi, O. Jeandupeux, H. Brune, and K. Kern. *Probing Hot-Electron Dynamics at Surfaces with a Cold Scanning Tunneling Microscope.* Physical Review Letters **82**, 4516–4519 (1999).

[207] K.-F. Braun and K.-H. Rieder. *Engineering Electronic Lifetimes in Artificial Atomic Structures.* Physical Review Letters **88**, 096801 (2002).

[208] W. Chen, V. Madhavan, T. Jamneala, and M. F. Crommie. *Scanning Tunneling Microscopy Observation of an Electronic Superlattice at the Surface of Clean Gold.* Physical Review Letters **80**, 1469–1472 (1998).

[209] J. Tesch, P. Leicht, F. Blumenschein, L. Gragnaniello, M. Fonin, L. E. Marsoner Steinkasserer, B. Paulus, E. Voloshina, and Y. Dedkov. *Structural and electronic properties of graphene nanoflakes on Au(111) and Ag(111).* Scientific Reports **6**, 23439 (2016).

[210] Y. Li, W. Zhang, M. Morgenstern, and R. Mazzarello. *Electronic and Magnetic Properties of Zigzag Graphene Nanoribbons on the (111) Surface of Cu, Ag, and Au.* Physical Review Letters **110**, 216804 (2013).

[211] J. R. Black. *Electromigration–A brief survey and some recent results.* IEEE Transactions on Electron Devices **16**, 338–347 (1969).

[212] D. G. Pierce and P. G. Brusius. *Electromigration: A review.* Microelectronics Reliability **37**, 1053–1072 (1997).

[213] M. Gerardin. *De l'action de la pile sur les sels de potasse et de soude et sur les alliages soumis à la fusion ignée.* Comptes Rendus **53**, 727–730 (1861).

[214] K.-F. Braun, W.-H. Soe, C. F. J. Flipse, and K.-H. Rieder. *Electromigration of single metal atoms observed by scanning tunneling microscopy.* Applied Physics Letters **90**, 023118 (2007).

[215] U. Paap. *Wachstum von Grapheninseln und Untersuchung der Elektromigration.* University of Regensburg, bachelors thesis, 2017.

[216] S. Vrbica. *Applications of graphene in nanotechnology : 1D diffusion, current drag and nanoelectrodes.* Leiden University, PhD thesis, 2018.

[217] K.-H. Koo. *Comparison study of future on-chip interconnects for high performance VLSI applications.* Stanford University, PhD thesis, 2011.

[218] H. Park, A. K. L. Lim, A. P. Alivisatos, J. Park, and P. L. McEuen. *Fabrication of metallic electrodes with nanometer separation by electromigration.* Applied Physics Letters **75**, 301–303 (1999).

[219] B. C. Regan, S. Aloni, R. O. Ritchie, U. Dahmen, and A. Zettl. *Carbon nanotubes as nanoscale mass conveyors.* Nature **428**, 924–927 (2004).

[220] L. Martini, Z. Chen, N. Mishra, G. B. Barin, P. Fantuzzi, P. Ruffieux, R. Fasel, X. Feng, A. Narita, C. Coletti, K. Müllen, and A. Candini. *Structure-dependent electrical properties of graphene nanoribbon devices with graphene electrodes.* Carbon **146**, 36–43 (2019).

[221] P. S. Ho and T. Kwok. *Electromigration in metals.* Reports on Progress in Physics **52**, 301–348 (1989).

[222] R. S. Sorbello, H. Ehrenreich, and F. Spaepen. *Theory of Electromigration.* Solid State Physics **51**, 159–231 (1998).

[223] V. B. Fiks. *On the mechanism of the mobility of ions in metals.* Soviet Physics Solid State **1**, 14–28 (1959).

[224] H. B. Huntington and A. R. Grone. *Current-induced marker motion in gold wires.* Journal of Physics and Chemistry of Solids **20**, 76–87 (1961).

[225] D. Solenov and K. A. Velizhanin. *Adsorbate Transport on Graphene by Electromigration.* Physical Review Letters **109**, 095504 (2012).

[226] Y. Girard, T. Yamamoto, and K. Watanabe. *Quantum-Chemical Interpretation of Current-Induced Forces on Adatoms on Carbon Nanotubes.* Journal of Physical Chemistry C **111**, 12478–12482 (2007).

[227] N. Mingo, L. Yang, and J. Han. *Current-Induced Forces upon Atoms Adsorbed on Conducting Carbon Nanotubes.* Journal of Physical Chemistry B **105**, 11142–11147 (2001).

[228] E. W. Müller. *Das Feldionenmikroskop.* Zeitschrift für Physik **131**, 136–142 (1951).

[229] B. S. Swartzentruber. *Direct Measurement of Surface Diffusion Using Atom-Tracking Scanning Tunneling Microscopy.* Physical Review Letters **76**, 459–462 (1996).

[230] H. Ibach. *Physics of Surfaces and Interfaces*. Springer Berlin Heidelberg, 2006.

[231] J. Repp, W. Steurer, I. Scivetti, M. Persson, L. Gross, and G. Meyer. *Charge-State-Dependent Diffusion of Individual Gold Adatoms on Ionic Thin NaCl Films*. Physical Review Letters **117**, 146102 (2016).

[232] J. D. Wrigley, M. E. Twigg, and G. Ehrlich. *Lattice walks by long jumps*. The Journal of Chemical Physics **93**, 2885–2902 (1990).

[233] G. Kellogg. *Field ion microscope studies of single-atom surface diffusion and cluster nucleation on metal surfaces*. Surface Science Reports **21**, 1–88 (1994).

[234] D. C. Senft and G. Ehrlich. *Long Jumps in Surface Diffusion: One-Dimensional Migration of Isolated Adatoms*. Physical Review Letters **74**, 294–297 (1995).

[235] L. Kelvin. *V. Contact electricity of metals*. The London, Edinburgh, and Dublin Philosophical Magazine and Journal of Science **46**, 82–120 (1898).

[236] J. M. R. Weaver and D. W. Abraham. *High resolution atomic force microscopy potentiometry*. Journal of Vacuum Science & Technology B: Microelectronics and Nanometer Structures Processing, Measurement, and Phenomena **9**, 1559–1561 (1991).

[237] M. Nonnenmacher, M. P. O'Boyle, and H. K. Wickramasinghe. *Kelvin probe force microscopy*. Applied Physics Letters **58**, 2921–2923 (1991).

[238] W. Melitz, J. Shen, A. C. Kummel, and S. Lee. *Kelvin probe force microscopy and its application*. Surface Science Reports **66**, 1–27 (2011).

[239] J. K. Gimzewski and R. Möller. *Transition from the tunneling regime to point contact studied using scanning tunneling microscopy*. Physical Review B **36**, 1284–1287 (1987).

[240] L. Limot, J. Kröger, R. Berndt, A. Garcia-Lekue, and W. A. Hofer. *Atom Transfer and Single-Adatom Contacts*. Physical Review Letters **94**, 126102 (2005).

[241] J. Kröger, H. Jensen, and Berndt. *Conductance of tip-surface and tip-atom junctions on Au(111) explored by a scanning tunnelling microscope*. New Journal of Physics **9**, 153 (2007).

[242] J. Yang, D. Sordes, M. Kolmer, D. Martrou, and C. Joachim. *Imaging, single atom contact and single atom manipulations at low temperature using the new ScientaOmicron LT-UHV-4 STM*. European Physical Journal Applied Physics **73**, 10702 (2016).

[243] M. Manadé, F. Viñes, and F. Illas. *Transition metal adatoms on graphene: A systematic density functional study.* Carbon **95**, 525–534 (2015).

[244] B. N. J. Persson and P. Avouris. *Local bond breaking via STM-induced excitations: the role of temperature.* Surface Science **390**, 45–54 (1997).

[245] M. Ternes, C. P. Lutz, C. F. Hirjibehedin, F. J. Giessibl, and A. J. Heinrich. *The Force Needed to Move an Atom on a Surface.* Science **319**, 1066–1069 (2008).

[246] T. Dienel, S. Kawai, H. Söde, X. Feng, K. Müllen, P. Ruffieux, R. Fasel, and O. Gröning. *Resolving Atomic Connectivity in Graphene Nanostructure Junctions.* Nano Letters **15**, 5185–5190 (2015).

[247] Y. Virgus, W. Purwanto, H. Krakauer, and S. Zhang. *Stability, Energetics, and Magnetic States of Cobalt Adatoms on Graphene.* Physical Review Letters **113**, 175502 (2014).

[248] S. Mangel, M. Skripnik, K. Polyudov, C. Dette, T. Wollandt, P. Punke, D. Li, R. Urcuyo, F. Pauly, S. J. Jung, and K. Kern. *Electric-field control of single-molecule tautomerization.* Physical Chemistry Chemical Physics **22**, 6370–6375 (2020).

[249] G. Ehrlich and F. G. Hudda. *Atomic View of Surface Self-Diffusion: Tungsten on Tungsten.* Journal of Chemical Physics **44**, 1039–1049 (1966).

[250] R. L. Schwoebel and E. J. Shipsey. *Step Motion on Crystal Surfaces.* Journal of Applied Physics **37**, 3682–3686 (1966).

[251] R. L. Schwoebel. *Step Motion on Crystal Surfaces. II.* Journal of Applied Physics **40**, 614–618 (1969).

[252] W. H. Brito and R. H. Miwa. *Adsorption and diffusion of gold adatoms on graphene nanoribbons: An ab initio study.* Physical Review B **82**, 045417 (2010).

[253] E. Zupanič, R. Žitko, H. J. P. van Midden, I. Muševič, and A. Prodan. *Pinning of Adsorbed Cobalt Atoms by Defects Embedded in the Copper (111) Surface.* Physical Review Letters **104**, 196102 (2010).

[254] T. R. Linderoth, S. Horch, E. Lægsgaard, I. Stensgaard, and F. Besenbacher. *Surface Diffusion of Pt on Pt(110): Arrhenius Behavior of Long Jumps.* Physical Review Letters **78**, 4978–4981 (1997).

[255] H. Bulou. *Atomic diffusion on nanostructured surfaces.* Superlattices and Microstructures **44**, 533–541 (2008).

[256] X. Liu, C. Z. Wang, M. Hupalo, W. C. Lu, M. C. Tringides, Y. X. Yao, and K. M. Ho. *Metals on graphene: correlation between adatom adsorption behavior and growth morphology.* Physical Chemistry Chemical Physics **14**, 9157–9166 (2012).

[257] O. V. Yazyev and A. Pasquarello. *Metal adatoms on graphene and hexagonal boron nitride: Towards rational design of self-assembly templates.* Physical Review B **82**, 045407 (2010).

[258] A. Kimouche, M. M. Ervasti, R. Drost, S. Halonen, A. Harju, P. M. Joensuu, J. Sainio, and P. Liljeroth. *Ultra-narrow metallic armchair graphene nanoribbons.* Nature Communications **6**, 10177 (2015).

[259] J. Lawrence, P. Brandimarte, A. Berdonces-Layunta, M. S. G. Mohammed, A. Grewal, C. C. Leon, D. Sánchez-Portal, and D. G. de Oteyza. *Probing the Magnetism of Topological End States in 5-Armchair Graphene Nanoribbons.* ACS Nano **14**, 4499–4508 (2020).

[260] Veeco Instruments Inc., *Dimension Icon Instruction Manual*, (2010).

[261] G. Münnich. *Cross-Sectional Scanning Probe Microscopy on GaAs: Tip-Induced Band Bending, Buried Acceptors and Adsorbed Molecules.* University of Regensburg, PhD thesis, 2014.

Acknowledgment

I would like to express my deep gratitude to everyone who helped me during this thesis:

- PD Dr. Jonathan Eroms for his excellent supervision. Thank you for always finding time for discussions and answering my questions, your numerous suggestions to improve the sample fabrication process, your help in the lab and your sharp-minded comments concerning the evaluation of the data. Thank you for valuable comments on the composition and correction of this thesis.
- Prof. Dr. Jascha Repp for his excellent supervision. Thank you for always patiently answering all my questions, our weekly meetings in which I learned so much, your help and explanations in the lab and your motivating and instructive comments on my measurement projects. Thank you for valuable comments on the composition and correction of this thesis. Thanks for the pleasant atmosphere you created in your group and all the fun activities.
- Prof. Dr. Dieter Weiss for his consent to supervise this thesis, his interest in my research and the possibility to use all his facilities.
- Prof. Dr. Christoph Strunk and his group for the permission to use his lab equipment.
- Dr. Sasha Vrbica for joyful joint measurement sessions on the Co diffusion project and excellent cooperation regarding the acquisition and evaluation of the data. Thanks also to Prof. Dr. Jan van Ruitenbeek for proposing the electromigration experiment.
- Dr. Sujoy Karan for pleasant joint measurement times on our "GNRs+Co" project and for sharing his knowledge about STM with me. Thanks also to Dr. Tobias Frank for setting up DFT calculations in an attempt to explain our experimental observations, and to Prof. Dr. Jaroslav Fabian and Prof. Dr. Ferdinand Evers for joining in this project and sharing their theoretical expertise.
- My master student Christian Kick for pushing the characterization of cGNRs forward. My bachelor students Josef Amler, Adrian Skollik, Matthias Dietl and Ulrike Paap who helped to explore various projects during this PhD thesis. The student intern Dhruv Mittal for his help in fabricating and measuring encapsulated cGNR devices and DBOV-TDOP samples.

- All current and former members of the AG Repp, especially Florian Albrecht, Thomas Buchner, Sujoy Karan, Nemanja Kocic, Laerte Patera, Jinbo Peng, Andreas Pöllmann, Christoph Rohrer, Philipp Scheuerer, Sophia Sokolov and Fabian Queck-Scharrer, for a friendly working atmosphere, interesting discussions, helpfulness in the lab and amusing enterprises after the working hours.
- All current and former members of the graphene group, especially Andreas Sandner, Martin Drienovsky, Florian Oberhuber, Andreas Lex, Christian Kick, Robin Huber and Tobias Völkl for pleasant collaboration and exchanging many fabrication techniques.
- The members of the Lehrstuhl Weiss for making the working day enjoyable.
- Markus Ehlert, David Disterheft, Jan Bärenfänger and Niklas Hüttner for sharing the burden and the joy of caring for the SEMs.
- The technicians Daniel Pahl, Uli Gürster, Michael Weigl, Cornelia Linz and Thomas Haller for friendly support in the clean room, all other labs and with technical questions.
- Our secretaries Elke Haushalter and Clauida Moser for their always friendly and competent support in bureaucratic matters of all kind. You helped me to focus on the scientific problems only.
- Tobias Völkl, David Disterheft and Maxim Lapis for proofreading parts of this thesis and helping to improve it with valuable comments.
- Johannes Ziegler and Tobias Völkl for a pleasant atmosphere in the office, plenty of enriching discussions and funny distractions.
- Sabine, David, Walter, Rita and Veronika for their endless care, constant support and steady interest in what I am doing.